NANOSCALE MICROFABRICATION PROSPECTS USING PROXIMITY FOCUSED LIQUID METAL ION SOURCES

Radhakrishna A. Rao
B.Tech., University of Mysore, India, 1983
M.S., Oregon Graduate Center, 1986

A dissertation submitted to the faculty
of the Oregon Graduate Center
in partial fulfillment of the
requirements for the degree
Doctor of Philosophy
in
Electrical Engineering

December, 1988

The dissertation "Nanoscale Microfabrication Prospects using Proximity Focused Liquid Metal Ion Sources" by Radhakrishna A. Rao has been examined and approved by the following Examination Committee:

LYNWOOD W. SWANSON
Professor
Thesis Advisor

ANTHONY E. BELL
Associate Professor
Thesis Advisor

JONATHAN H. ORLOFF
Professor

JOHN ARTHUR
Professor
Oregon State University

ACKNOWLEDGEMENTS

I am most grateful to my advisors, Professor Lynwood Swanson and Dr. Anthony Bell for encouraging me to undertake this research and for their kindness and thoughtfulness in taking time to talk to me and point out many subtle points on this topic. I have benefited enormously from their informative discussions on liquid metal ion sources and field emission physics. I am also grateful for their support, which has included the opportunity to attend several conferences and discuss my work with other scientists. The opportunity to present my work at Stanford University on a regular basis is also greatly appreciated. These presentations stimulated numerous discussions on the applications of the proximity focused LMIS to lithography and microfabrication and helped me gain valuable perspective on the field. I also thank Professors Lynwood Swanson, Anthony Bell, Jon Orloff, and John Arthur at Oregon State University for serving on my examination committee.

I thank Professor Orloff for his encouragement and valuable advice during the entire course of this work. Professor John Arthur, both when I was at Oregon State University and later at OGC has been a source of support and encouragement and I thank him for it. I have benefited from many discussions with Professor Paul Davis, and I thank him for it. I thank Professors Calvin Quate and Fabian Pease at Stanford University for their kind interest and suggestions during the course of this research. Mark McCord and Doug Smith at Stanford University have always been very forthcoming and helpful

in all the discussions we have had over the course of this work.

I thank Greg Schwind and Shekar Rao for providing me with some of the graphs and figures used in this work. The excellent drafting of the figures by Barbara Ryall is gratefully acknowledged. To Joseph Puretz, thanks for all the times that we have had such interesting discussions. To my friend Michael Thorburn, at Oregon State University go many thanks for his understanding and encouragement. I also wish to thank Professor Jean Delord for his overall encouragement during the pursuit of this work.

Very special thanks go to my wife Suman for her love, faith and patience and to my parents for their years of support and encouragement. I thank my family and friends for having believed in me and for helping me make all this worthwhile.

To my beloved wife Suman, who above all else, has taught me how to face adversity and to beat it with courage.

Table of Contents

List of Tables

List of Figures

ABSTRACT

NANOSCALE MICROFABRICATION PROSPECTS USING PROXIMITY FOCUSED LIQUID METAL ION SOURCES

Radhakrishna A. Rao, Ph.D.

Oregon Graduate Center, 1988

Supervising Professors: Dr. Lynwood Swanson

Dr. Anthony Bell

The scanning tunneling microscope (STM) has in recent years provided us with a handle to achieve atomic resolution of surfaces. By replacing the electron source in an STM with a liquid metal ion source (LMIS), essentially a "proximity focused" technique, it has been found possible to do micromachining at close spacings. The current densities attained in such a close-spaced system are up to three orders of magnitude greater than currently available from focused ion beam (FIB) systems. Such high current densities provide the possibility of carrying out nanoscale microfabrication at speeds limited only by the mechanical deflection schemes.

Such enormous current densities and the resulting extremely rapid substrate changes led us to study the capability of the LMIS to operate at much lower currents than usual and led to the discovery of a new low current mode of operation of the LMIS. It has further turned out that these low

current LMIS have an application to the FIB technology, in terms of attaining the maximum current density possible in the focused beam spot.

The desire to image any nanoscale features produced from the proximity focused LMIS led to the investigation to obtain a highly confined beam of electrons from the LMIS by subjecting a frozen-in Taylor cone to a field build-up procedure. It now opens up the use of the LMIS as a dual source of ions and electrons in either a focusing column or in a STM environment. A use has also been found of the field electron emission from the LMIS for determining the source-target separation, based on solving Laplace's equation in cylindrical coordinates or in prolate spheroidal coordinates (the latter by A. M. Russell and Russell Young) and using the form obtained for the field emission voltage to determine the diode separations.

Finally the operation of the LMIS in a STM embodiment at emitter-target spacings of 100 nm or less, and also microfabrication features created on various targets will be described. It is seen that the threshold voltage for LMIS operation goes as the square root of the emitter-target spacing as would be expected from the Taylor theory.

CHAPTER 1

INTRODUCTION

Liquid metal ion sources (LMIS) have been used increasingly as a means of generating very high brightness sources of ions of a wide variety of elements. A LMIS consists of a low volatility liquid metal film which flows to the apex of a solid needle support structure. Subsequent application of a high electric field deforms the liquid and results in the formation of a conical protrusion known as the Taylor cone[1,2]. Taylor[3] showed that the balance of liquid surface tension and electrostatic stress results in a stabilized cone of half angle 49.3°. Emission of charged ions occurs through field evaporation, whereby singly charged species are evaporated over the Schottky barrier formed by field deformation of the potential well[4]. In recent years the advent of alloy LMIS has expanded the ion species to include volatile elements such as arsenic and high melting species such as boron[5]. Because of its very high brightness the LMIS is an excellent source for an ion microprobe and has found use in micro-milling[6], microcircuit fabrication[7], and high resolution SIMS[8].

The scanning tunneling microscope (STM) invented in the early 1980's by Gerd Binnig and Heinrich Rohrer[9] at IBM, works by positioning a very sharp tip (radius $\leq$100 nm) within a few angstroms of the surface using a three-dimensional piezoelectric scanner. A voltage (typically $<$1 V) applied between the tip and the sample, causes a tunneling current to flow. The

current is kept a constant using a feedback amplifier which monitors the current and adjusts the tip height accordingly. The tip is scanned over the surface in a raster fashion, and the tip height is used to build an image of the surface topography, often with atomic resolution. An important aspect of the operation of the STM has been the nondestructive nature of the technique. It has alternatively proved possible to intentionally induce local changes in the substrate and then use the tip as a probe for imaging the changes. Such changes could be wrought mechanically, electrically, thermally or be chemical in nature.

Mechanical deformations produced and imaged by an STM tip have been reported by Abraham et al.[10], and by van Kempen and van de Walle[11]. In the latter work, indentations were made which were some hundred Å deep. After each contact, the indentations were imaged with the tip and were found to be reproducible and pyramid-like, with relatively sharp edges.

Processes which are electrically induced, whether via the tunneling electron beam or via the high electric fields associated with it, are aimed at both structural and chemical modifications. They are envisaged as potentially useful for nanomachining, material deposition and removal, chemical and lithographic processing etc. Two efforts reported thus far pertain to inducing chemical modifications[12,13]. In the work by McCord and Pease[13], they used the STM tip to expose contamination resist (composed of hydrocarbon contamination), thin Langmuir-Blodgett films of docosenoic acid, metal halide films and PMMA polymer resist. Another technique was to use the STM to deposit metal directly from organometallic vapors that decompose on the

surface when bombarded with electrons[14]. All of these methods have achieved resolution ranging from 10 to 20 nm. Atomic-scale resolution has been achieved by pulsing the tip voltage to locally transfer individual atoms from the tip to atomically smooth crystals of germanium[15].

The purpose of the work presented in this dissertation has been to use the LMIS in an STM embodiment, to study the possibilities for micromachining and microfabrication, with what is essentially a proximity focused technique. In a focused ion beam (FIB) system, (see Fig. 1.1) a portion of the ions emitted from the source (as determined by an aperture) are focused in a focusing column using electrostatic lenses and scanned by means of an electrostatic deflector to perform ion beam micromachining. In the proximity focused case the micromachining with the ion beam would be achieved by the use of a close-spaced diode system comprising the source and the target as shown in Fig 1.2. The spot sizes attainable in a FIB system are ~ 0.3 μm with a single lens focusing column and ~ 500 Å with a twin lens focusing column. In a proximity focused mode, the beam diameter at the target would be of the same order of magnitude as the separation between the source and the target and could theoretically be at least as small as the Taylor cone apex (~ 50 Å) of the LMIS.

A typical beam current density at the target in the FIB case is about 1 A/cm^2 since only a very small fraction ($\sim 10^{-4}$) of the available current from the source is used in the focusing process. For the proximity focused LMIS, the entire current available is used, allowing exceedingly high current densities to be achieved at the target. For example, at 0.1 μm spacing of the

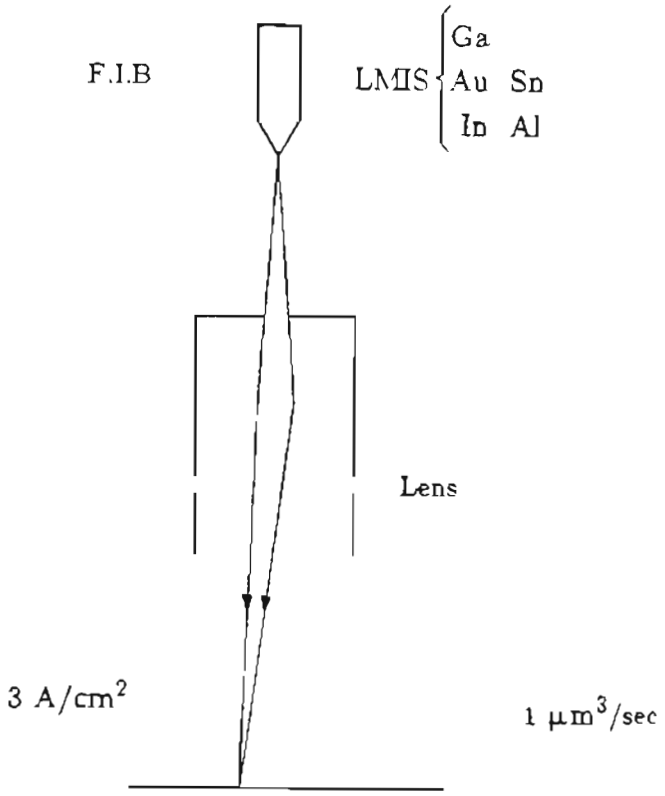

Ga LMIS Operating Voltage 5 - 10 kV
Accelerating Potential 15 - 25 kV
Needle Diameter ~ 1 mm
Emission Current 1 - 2 μA
Target Current 60 pA ~ $10^{-5}I_t$
Spot ~ 50 nm

Figure 1.1 : Schematic diagram of a Focused Ion Beam system.

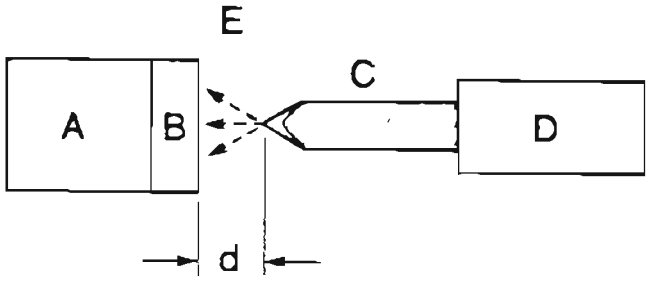

A XYZ Coarse Motion Device

B Substrate

C LMIS

D XYZ Piezo (Fine Motion Device)

E Ion Beam to Substrate

Figure 1.2 : Schematic diagram of a proximity focused LMIS system.

emitter from the target and assuming an emission half angle of 20°, a target current density of ~2300 A/cm^2 can be achieved for a Ga LMIS operating at 0.1 μA total current. At closer spacings or at higher total currents at the same spacing, the current densities would be correspondingly higher. Combining the LMIS with an STM embodiment then provides the possibility of carrying out nanometer fabrication at speeds limited only by the mechanical deflection schemes available.

The rapidity of the ion beam induced substrate changes (because of such high current densities) in the early stages of these "proximity focused" experiments, led us to conduct an investigation of the capability of the LMIS, to operate at much lower currents than usual. This led to the discovery of a new low current (and low voltage) mode of operation of the Ga LMIS. Currents as low as 1 nA were found possible instead of the normally observed current threshold values of 1 μA from the conventional LMIS. The threshold voltages at which LMIS operation commenced was as low as 2 kV compared to the normally 5 to 6 kV for the conventional LMIS. It has further turned out that these low current LMIS have an application to the FIB technology, in terms of attaining the maximum current density possible in the focused beam spot.

The desire to image any nanoscale features produced from the proximity focused LMIS led to an investigation to obtain a highly confined beam of electrons from the LMIS by subjecting a frozen-in Taylor cone to a field build-up procedure and reversing the polarity. It now opens up the use of the LMIS as a dual source of ions and electrons in either a focusing column

or in a STM environment.

References

1. D. R. Kingham and A. E. Bell, *31st Int'l Field Emission Symposium*, p. 65, Paris, 1984.
2. G. B. Assayag and P. Sudraud, *31st Int'l Field Emission Symposium*, p. 79, Paris, 1984.
3. G. I. Taylor, *Proc. R. Soc. Lond. A*, vol. 280, p. 383, 1964.
4. D. R. Kingham and L. W. Swanson, *31st Int'l Field Emission Symposium*, p. 59, Paris, 1984.
5. W. M. Clark, R. L. Seliger, M. W. Utlaut, A. E. Bell, L. W. Swanson, G. A. Schwind, and J. B. Jergensen, *J. Vac. Sci. Technol. B*, vol. 5, p. 197, 1987.
6. R. L. Reuss, D. Morgan, E. W. Greeneich, W. M. Clark, and D. B. Rensch, *J. Vac. Sci. Technol. B*, vol. 3, p. 62, 1985.
7. R. L. Seliger, J. W. Ward, V. Wang, and R. L. Kubena, *Appl. Phys. Lett.*, vol. 34, p. 310, 1979.
8. A. R. Waugh, A. R. Bayly, and K. Anderson, *Proc. 29th IFES, Eds. H. O. Anderson and H. Norden, Goteborg*, p. 409, 1982.
9. G. Binnig and H. Rohrer, *Helv. Phys. Acta*, vol. 55, p. 726, 1982.
10. D. W. Abraham, H. J. Mamin, E. Ganz, and J. Clarke, *IBM J. Res. Develop.*, vol. 30, p. 492, 1986.
11. H. van Kempen and G. F. A. van de Walle, *IBM J. Res. Develop.*, vol. 30, p. 509, 1986.

12. M. Ringger, H. R. Hidber, R. Schlogl, P. Oelhafen, and H.-J. Guntherodt, *Appl. Phys. Lett.*, vol. 46, p. 832, 1985.

13. M. A. McCord and R. F. W. Pease, *J. Vac. Sci. Technol. B*, vol. 4, p. 86, 1986.

14. E. E. Ehrichs, R. M. Silver, and A. L. deLozanne, *J. Vac. Sci. Technol. A*, vol. 6(2), p. 540, 1988.

15. R. S. Becker, J. A. Golovchenko, and B. S. Swartzentruber, *Nature*, vol. 325, p. 419, 1987.

CHAPTER 2

REVIEW OF SCANNING TUNNELING MICROSCOPY

1. Introduction

Wolfgang Pauli once remarked, "The surface was invented by the devil". One understands his frustration, when looking at the surface of a solid, one realizes that it serves as the boundary between the solid and the outer world, and is vastly different from the bulk or interior. An atom within a solid is surrounded by other atoms, whereas at the surface it can interact only with other atoms at the surface, with atoms immediately under it or with atoms beyond the surface. Hence the properties of the surface of a solid differ vastly from that of its interior, and these complexities have long thwarted efforts to derive precise theoretical and experimental descriptions of them.

The first successful attempts at imaging atomic structures came from the invention of the electron microscope, which in turn grew out of a basic discovery of quantum mechanics, that light and other kinds of energy exhibit the characteristics of both particles and waves. In particular the confirmation of the wave nature of the electron in 1927 by Clinton J. Davisson and Lester H. Germer of Bell Telephone Laboratories led directly to the invention of the electron microscope. With electron microscopy projections of atomic rows and even atomic orbitals in thin crystalline films have been

observed.

In the 1950's Erwin W. Muller invented the field ion microscope, a powerful tool for imaging the atomic structures of surfaces. The sample to be imaged is required to be either in the form of a very sharp needle, or must be placed at the tip of the needle. The sample must also be stable against the high electric fields characteristic of this technique.

The scanning tunneling microscope invented in the early 1980's by Gerd Binnig and Heinrich Rohrer[1] at IBM, has in the past several years developed into an imaging method for surfaces in real space on a scale which extends to atomic dimensions. Its initial purpose was perceived to be the imaging of the structure and electrical properties of insulating layers thin enough to permit electron tunneling. Its capabilities which include this local probing of surface structures, combined with its adaptability to various environments and the capacity to tune its low electron energies have allowed its use in diverse areas of science and technology.

2. Historical Background

Prince Louis de Broglie's dualistic matter-wave hypothesis, found expression in the definite form of Schrodinger's wave equation. A particle, say an electron, was assumed to be represented by a solution of this equation. Such solutions were found to have a continuous non-zero nature even in classically forbidden regions of negative kinetic energy, implying an ability to penetrate such forbidden regions and hence a non-zero probability to tunnel from one classically allowed region to another. Tunneling was believed to occur by the

distortion, lowering or thinning of a potential barrier under a high externally applied electric field.

Electron tunneling was first envisaged in connection with vacuum barriers, when Fowler and Nordheim[2] explained the main features of electron emission from cold metals by high external fields, which had been unexplained since its first observation by Lilienfeld[3] in 1922. Their one-dimensional model which confined the metal electrons in a potential well, of height equal to the work function ϕ and the Fermi energy, led, on the application of a high electric field to a substantial decrease in the wall thickness allowing electrons to tunnel through this potential well into vacuum as shown in Fig. 2.1, and to the derivation of the well-known Fowler Nordheim formula for the current density as a function of the electric field, F:

$$J = AF^2 \exp\left\{-4(2m)^{1/2}\frac{\phi^{3/2}}{3\hbar F}\right\} \tag{2.1}$$

An application of the tunneling theory as developed by Fowler and Nordheim[2] followed almost immediately in the form of an explanation of α decay as a tunneling process by Gamow[4] and Gurney and Condon[5] and subsequently was used to explain molecular dissociation by Rice[6]. Further important developments followed, wherein tunneling was invoked to understand transport properties of electrical contacts between two solid conductors, like the anomalous temperature independence of contact resistance between metals[7,8] and the interpretation of metal-semiconductor contacts-

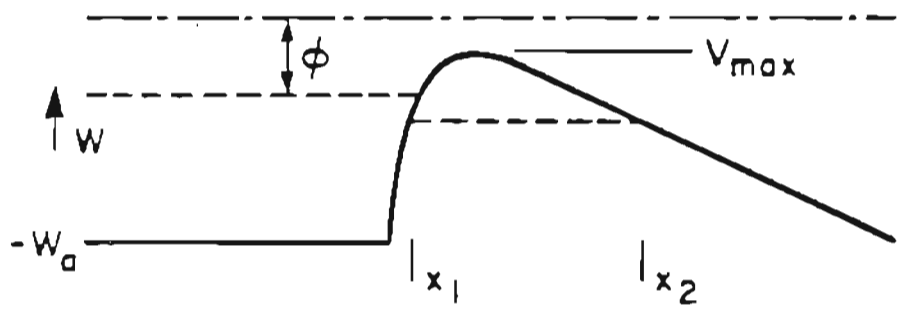

Figure 2.1 : Field emission tunneling diagram.

rectifiers such as those made from selenium or cuprous oxide[9-11] as also to understand interband tunneling or internal field emission otherwise known as the Zener mechanism[12] as an explanation for dielectric breakdown.

The next important development arose from the need to measure the microtopography of surfaces, and was the "Topographiner" invented by Russell Young and co-workers[13]. They developed a noncontacting instrument for measuring the microtopography of metallic surfaces, with a resolution of 30 Å perpendicular to the surface and about 4000 Å in the plane of the surface. They found the inherent noise in the perpendicular direction to be about 3 Å or one atomic layer. They were able to use this topographiner to obtain topographic maps of an infrared diffraction grating by using a field emitter with a radius of 100 Å. The instrument was shown to conform to the Fowler-Nordheim description of field emission while spaced at large distances from the surface but when moved to within 30 Å of the surface, the performance was seen to be compatible with Simmons' theory of metal-vacuum-metal (MVM) tunneling[14].

The scanning tunneling microscope (STM)[15] came soon after the topographiner, which was its precursor. The idea behind the STM was similar, a sharp needle brought to very close proximity ($<$ 20 Å) of a surface and scanned over it to obtain topographical information.

For scanning tunneling microscopy the voltages that come into consideration are very low, and we shall consider here, a form of Eq. (A.20) (from Simmons theory of MVM tunneling[14], developed in Appendix A):

$$J = J_0 \left\{ \bar{\phi} \exp(-A\bar{\phi}^{1/2}) - (\bar{\phi}+eV) \exp[-A(\bar{\phi}+eV)^{1/2}] \right\} \qquad (2.2)$$

For eV $\sim$ 0, β takes the value unity. Since $\bar{\phi} >> eV$, Eq. (2.2) can be written as

$$J = J_0 \left\{ \bar{\phi} - (\bar{\phi}+eV) \exp(-AeV/2\bar{\phi}^{1/2}) \right\} \times \exp(-A\bar{\phi}^{1/2}) \qquad (2.3)$$

Expanding $\exp(-AeV/2\bar{\phi}^{1/2})$, and neglecting terms containing V^2 and higher orders, Eq. (2.3) becomes

$$J = J_0 \left\{ \bar{\phi} - (\bar{\phi}+eV)(1-AeV/2\bar{\phi}^{1/2}) \right\} \exp(-A\bar{\phi}^{1/2})$$

$$= J_0 \, eV \left\{ (A\bar{\phi}^{1/2}/2) - 1 \right\} \exp(-A\bar{\phi}^{1/2}) \qquad (2.4)$$

Since $(A\bar{\phi}^{1/2}/2) >> 1$, Eq. (2.4) reduces to

$$J = J_L \, \bar{\phi}^{1/2} \, V \exp(-A\bar{\phi}^{1/2}) \qquad (2.5)$$

where

$$J_L = \left\{ (2m)^{1/2}/\Delta s \right\} (e/h)^2$$

Since eV is very small, $\bar{\phi}$ is considered to be the zero voltage mean barrier

height. Thus, in this case, Eq. (2.5) expresses the current density J as a linear function of V; that is the junction is ohmic for very low voltages.

Eq. (2.5) can be expressed in the following form

$$J = (e^2/\hbar) \cdot (\kappa_0/4\pi^2 s) \cdot V \cdot \exp(-2\kappa_0 s) \tag{2.6}$$

where $s = \Delta s$ is the effective tunnel distance in Å, κ_0 the inverse decay length of the wave function density outside the surface and given by the expression $2\kappa_0(\text{Å}) = 1.025\sqrt{\bar{\Phi}(\text{eV})}$, with $\bar{\Phi}$ the effective barrier height, V the applied voltage in volts, and $(e^2/\hbar)=2.44 \cdot 10^{-4}\Omega^{-1}$.

3. Physical Basis and Mode of Operation of the STM

Electron tunneling through two conductors separated by a vacuum barrier, which conceptually is the simplest of barriers, provides the underlying physical basis for the scanning tunneling microscope. The insulating layer, in this case a vacuum, acts as a potential barrier and the tunneling current, I is a measure of the overlap of the wave functions of the two conductors in the intervening gap. Therefore I is essentially a function of the separation of the conductors and the nature of the electronic states in the separating gap. For a planar conductor-insulator-conductor junction, (Fig. 2.2a,b, reproduced from Binnig and Rohrer[16]) considering free electrons tunneling through the barrier, the current density is given by Eq. (2.6). For a vacuum barrier, (Fig. 2.2c, from Binnig and Rohrer[16]) the total current I can not be expressed in a simple and closed form as in Eq. (2.6). Nevertheless, there is still essentially

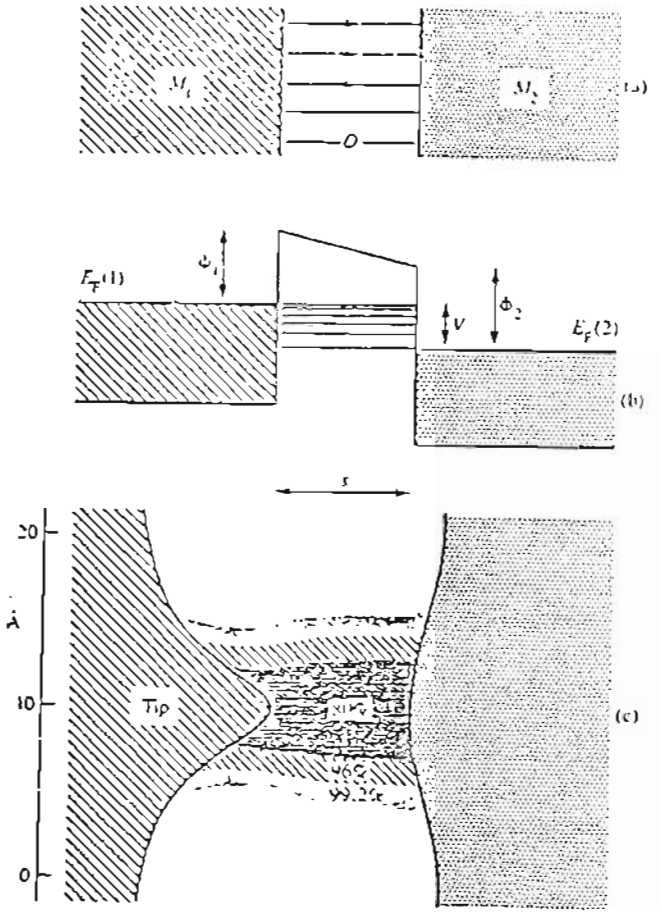

Figure 2.2 : (a) Planar metal-oxide-metal junction (M_1-O-M_2).

(b) Illustrative energy diagram for a tunneling junction having a trapezoidal barrier (ϕ_1,ϕ_2) of thickness s. (c) Calculated current density distribution for tunneling from a tip to a corrugated surface, assuming an effective barrier height of 2.41 eV, a tip radius of 1.7 Å, and s = 4 Å.

an exponential dependence of the current on tip-surface separation and barrier height. The prefactor, though, is altered due to density-of-state effects. The effective barrier height of a vacuum gap can be a expressed as the average of the work functions of the two conductors and is usually a few eV. Oxide barrier heights in typical planar metal-oxide-metal junctions are usually below 1 eV.

In the case of the scanning tunneling microscope, one of the electrodes is in the shape of a sharp tip, which is brought to within 20 Å or less of a conducting sample. Tunneling occurs when a few hundred millivolts is applied across the gap. The tunneling current is confined to a fine filament between the apex of the tip and the surface under investigation, and it decreases by about an order of magnitude for every 1 Å decrease in distance. By keeping the tip at a fixed distance above the surface, which in essence means keeping the tunneling current constant, one can obtain contours of constant tunneling current. For an electronically homogeneous surface, this can provide topographical images of the surface with a resolution dependent on the instrument's resolution. For an electronically inhomogeneous surface, the local electronic structure plays an important role in the variation of the tunneling current. Specific features in the I-V, V-s, or I-s characteristics as the tip is scanned, provide detail about the electronic and chemical properties of the surface under investigation. These manifest themselves in the voltage dependence of the tunneling current. Then, by recording the dI/dV or dI/ds one can in practise obtain electronic or chemical information on the surface. An illustration of such a "scanning tunneling spectroscopic image" is pro-

vided in Fig. 2.3 (reproduced from Binnig and Rohrer[16]). The images are of NiO on a Ni(100) surface. In (a), the strong peak at 0.8 V is attributed to NiO, being characteristic of that oxide. In (b), the STS (for scanning tunneling spectroscopy) and STM images are for bias voltages of 0.8 and 1.3 V. An oxide island is evident on the left of the STS image obtained at 0.8 V. The oxide island is hardly noticeable in the STM images.

Hence we see that the close relationship between the tip-sample spacing for constant tunneling current with the topography, while that of dI/dV with the local density of states and dI/ds with the local barrier height (or work function) allows us to obtain topographical or STM images, spectroscopic or STS images, and work function profiles respectively. A unique feature of these and other types of images obtainable with the STM is the apparent non-destructive nature of the process itself. On the other hand the STM technique can be used to intentionally modify or induce permanent structural modifications as the latter portion of this work will show.

4. STM Images: Experiment and Theory

In surface science applications, the STM has provided a means to achieve atomic resolution while imaging surfaces. This has led to theoretical studies, using the transfer Hamiltonian approach[17-19] and the direct transmission approach[20-22] which have given valuable insight into the physical basis of the STM and the lateral resolution that could be achieved. In the transfer Hamiltonian approach, the tunneling tip is regarded as tracing contours of constant wave-function density, evaluated at the center of the

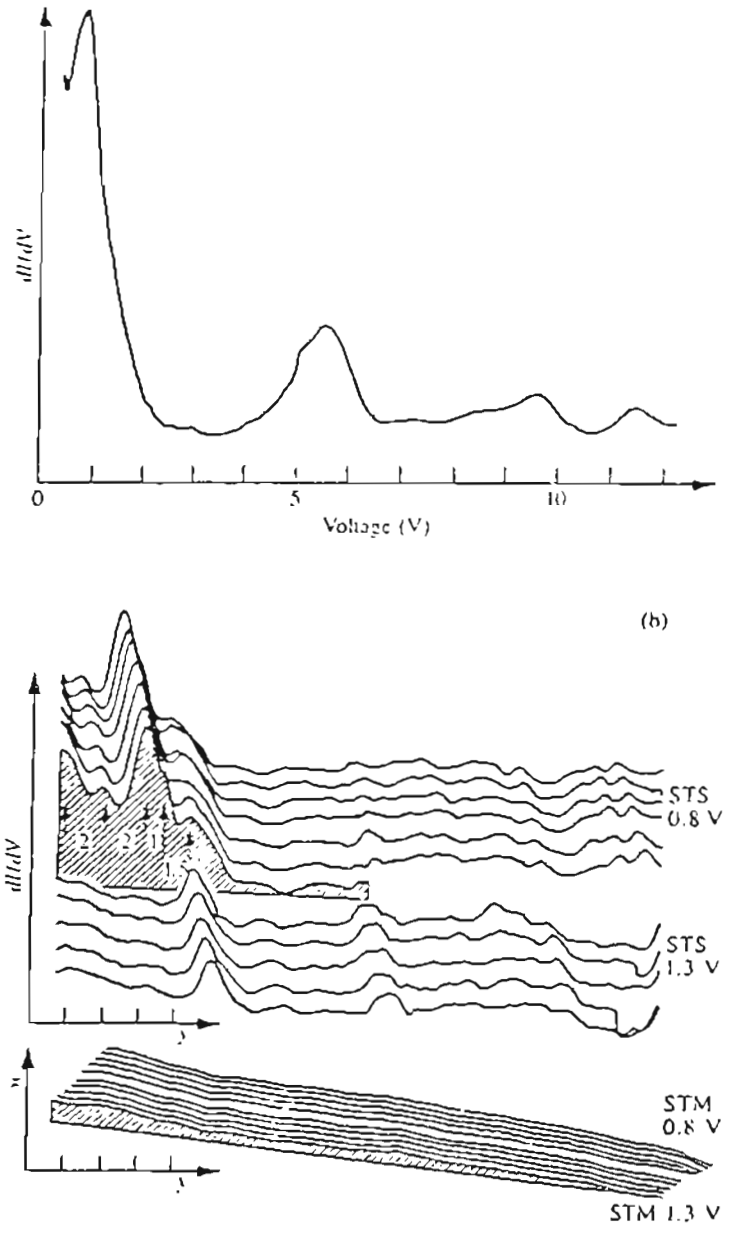

Figure 2.3 : Spectroscopic and structural imaging of NiO on a Ni(100) surface. Shown in (a) is dI/dV vs. V from an oxide covered region. The STS and STM images shown in (b) were obtained at indicated bias voltages of 0.8 and 1.3 V. Spatial separations in units of the NiO lattice spacings are indicated at the left. The divisions on the y and z axes correspond to spacings of 5 Å.

assumed spherical tip, while scanning a sample surface in the constant current mode; while the transmission approach not utilizing such simple physical concepts, provides an instructive view of the current distribution in the tunneling filament. Both approaches lead to similar expressions for the lateral resolution. In particular, the minimum periodicity, a_m, of a sinusoidal surface corrugation with amplitude c_s to be resolved is, for free electrons,

$$a_m = \sqrt{\pi/\ln A} \cdot L_{eff} <\leq \pi\sqrt{2/\ln A} \cdot \frac{\sqrt{r+s}}{\phi^{1/4}} \qquad (2.7)$$

where r is the radius of curvature of the tip, s is the average width of the tunneling gap, ϕ is the effective barrier height, $A = c_s/c_d$, with c_d the smallest observable corrugation of the equicurrent surface traced by the tip (or, in effect, the gap-width stability), and L_{eff} is the effective diameter of the tunneling current filament. The dominant factors are tip radius, gap width and barrier height; the vertical stability enters only logarithmically. Eq. (2.7) is expected to be a good approximation for a tip with a radius of curvature of 7 Å or more. If the image potential and non-uniform barrier heights are taken into consideration, it would result in a drastic reduction of ϕ at small gap widths and hence affect the resolution with the former and cause a change of barrier height at locations with strong curvatures due to smearing out of the electronic charge with the latter. STM experiments on cleaved graphite have yielded lateral resolution less than 2 Å and are believed to be due to an enhanced focusing effect occurring when imaging is done with a single, rather localized electron orbital as with an adsorbate atom at the apex of a metal

tip.

Surfaces prepared using standard surface-preparation procedures, when imaged with the STM, have looked quite rough with "terraces" and "flat lakes" embedded in a hilly landscape and not quite as flat as have always been assumed. These surfaces nevertheless retain their "ideal" surface structure and electronic properties, even on quite restricted flat regions and in the immediate vicinity of defects, defect areas and step-lines. This calls for necessary caution when interpreting data obtained with averaging surface analytical methods.

Topographical imaging of surfaces on the nanometer scale as opposed to atomic-resolution is of importance in applications relating to thin-film growth, technological preparation methods, new roughness standards for industrially important surfaces, and imaging of biological matter. The STM can with relatively simple instrumentation be employed for imaging with a lateral resolution in the nanometer range and a vertical resolution of 1 Å. An advantage of nanometer-scale imaging is the relatively little effect of the local chemical and electronic character of the surface under investigation which tend to predominate in atomic-resolution imaging.

A point of note in the imaging of high-resistance materials in the constant current mode is the variation of the potential drop $\Delta V = I \times R_s$ where R_s is the spreading resistance across the surface. This requires that the applied voltage be larger than ΔV everywhere on the portion of the surface under examination. The case in point is the imaging of the 7×7 reconstruction of the Si(111) surface, where the high voltage used could be attributed

to such a spreading resistance.

5. Spectroscopy with the STM

A powerful tool for obtaining electronic or chemical properties of surfaces, has been with the use of tunneling spectroscopy using the STM. Tunneling spectroscopy per se is concerned with density of state effects on the tunneling current which in turn manifests itself in an anomalous dependence of the voltage on the tunneling current. The spectroscopy is done experimentally by obtaining current-voltage characteristics or derivatives thereof.

STM spectroscopy differs from conventional spectroscopy by the fact that the tunneling barrier width is adjustable and its experimental control is crucial to obtaining meaningful tunneling spectra. The gap width is controlled by the tunneling current itself, either in the constant current mode or the constant resistance mode. The spectra are usually taken by superposing a small, fast modulation on the tunneling voltage while sweeping it slowly, as in conventional tunneling spectroscopy. Alternately, curves obtained with fast voltage sweeps or characteristics obtained with slow sweeps are also used to obtain spectroscopic information. The advantages to using fast sweeps are that the shapes of the spectroscopic features which are seen are not distorted by a changing gap width and are thus more familiar in their appearance, and that STM spectroscopy can be rendered insensitive to mechanical gap-width instabilities. An advantage to using slow sweeps is that the electric fields at the surface are prevented from becoming too high since, under the imposed condition of constant tunneling current, the gap width increases with

tunneling voltage. This can be particularly important in systems with loosely bound adsorbates or delicate molecules.

The scanning tunneling microscope provides images in a five-dimensional space, namely, in the three dimensional real space (x,y,z), the tunneling current I, and the tunneling voltage V. Hence, it is the selection of the dimensions of interest which determines the "imaging mode". For contours of constant wave-function overlap, we measure z as $z(x,y)$ at constant I and V, and call it a "topographical" image.

6. Local Modifications with the STM

An important aspect of the applications of the STM discussed thus far has been the nondestructive use of the tunneling-current tip. It has alternatively proved possible to intentionally induce local changes in the substrate and then use the tip as a probe for imaging the changes. Such changes could be wrought mechanically, electrically, thermally or be chemical in nature.

Mechanical deformations produced and imaged by an STM tip have been reported by Abraham et al.[23], and by van Kempen and van de Walle[24]. In the latter work, indentations were made which were some hundred Å deep. After each contact, the indentations were imaged with the tip and were found to be reproducible and pyramid-like, with relatively sharp edges.

Processes which are electrically induced, whether via the tunneling electron beam or via the high electric fields associated with it, are aimed at both structural and chemical modifications. They are envisaged as potentially useful for nanomachining, material deposition and removal, chemical and

lithographic processing etc. Two efforts reported thus far pertain to inducing chemical modifications[25,26]. In the work by McCord and Pease[26], they used the STM tip to expose both "contamination" resist (composed of hydrocarbon contamination) and a thin Langmuir-Blodgett film of docosenoic acid. They produced lines roughly 1 μm apart with widths of order 0.1 μm with both resists. Clearly the STM has the potential of doing lithography.

References

1. G. Binnig and H. Rohrer, *Helv. Phys. Acta*, vol. 55, p. 726, 1982.
2. R. H. Fowler and L. Nordheim, *Proc. R. Soc. Lond. A*, vol. 119, p. 173, 1928.
3. J. E. Lilienfeld, *Phys. Z.*, vol. 23, p. 506, 1922.
4. G. Gamow, *Z. Phys.*, vol. 51, p. 204, 1928.
5. R. W. Gurney and E. U. Condon, *Nature*, vol. 122, p. 439, London, 1928.
6. O. K. Rice, *Phys. Rev.*, vol. 34, p. 1451, 1929.
7. J. Frenkel, *Phys. Rev.*, vol. 36, p. 1604, 1930.
8. R. Holm and W. Meissner, *Z. Phys.*, vol. 74, p. 715, 1932.
9. A. H. Wilson, *Proc. R. Soc. Lond. A*, vol. 136, p. 487, 1932.
10. J. Frenkel and A. Joffe, *Phys. Z. Sowjetunion*, vol. 1, p. 60, 1932.
11. L. Nordheim, *Z. Phys.*, vol. 75, p. 434, 1932.
12. C. Zener, *Proc. R. Soc. Lond*, vol. 145, p. 523, 1934.
13. R. Young, J. Ward, and F. Scire, *The Rev. Sci. Instr.*, vol. 33, p. 999, 1972.
14. J. G. Simmons, *J. Appl. Phys.*, vol. 34, p. 1793, 1963.
15. G. Binnig, H. Rohrer, Ch. Gerber, and E. Wiebel, *Phys. Rev. Lett.*, vol. 49, p. 57, 1982.
16. G. Binnig and H. Rohrer, *IBM J. Res. Develop*, vol. 30(4), p. 353, 1986.

17. J. Tersoff and D. R. Hamann, *Phys. Rev. Lett.*, vol. 50, p. 1998, 1983.

18. J. Tersoff and D. R. Hamann, *Phys. Rev. B*, vol. 31, p. 801, 1985.

19. A. Baratoff, *Europhys. Conf. Abstr.*, 7B, p. 364, 1963.

20. E. Stoll, A. Baratoff, A. Selloni, and P. Carnevali, *J. Phys. C*, vol. 17, p. 3073, 1984.

21. N. Garcia, C. Ocal, and F. Flores, *Phys. Rev. Lett.*, vol. 50, p. 2002, 1983.

22. N. Garcia and F. Flores, *Physica*, vol. 127B, p. 137, 1984.

23. D. W. Abraham, H. J. Mamin, E. Ganz, and J. Clarke, *IBM J. Res. Develop.*, vol. 30, p. 492, 1986.

24. H. van Kempen and G. F. A. van de Walle, *IBM J. Res. Develop.*, vol. 30, p. 509, 1986.

25. M. Ringger, H. R. Hidber, R. Schlogl, P. Oelhafen, and H.-J. Guntherodt, *Appl. Phys. Lett.*, vol. 46, p. 832, 1985.

26. M. A. McCord and R. F. W. Pease, *J. Vac. Sci. Technol. B*, vol. 4, p. 86, 1986.

CHAPTER 3

CONSTRUCTION OF THE LMIS-STM EMBODIMENT

1. Introduction

The Scanning Tunneling Microscope (STM)[1] has provided surface scientists with a tool to image surfaces with atomic resolution. To obtain atomic resolution, a well-designed STM requires the tip-sample position control to be at least an order of magnitude smaller than the resolution desired[2]. For imaging of individual surface atoms, a resolution of about 0.1 Å is sought in the z-direction (i.e. normal to the sample surface) and about 1 Å in the x and y directions. This then requires the tip-sample position control to be

$$\Delta z = 0.01 \text{ Å} \tag{3.1a}$$

$$\Delta x, \Delta y = 0.1 \text{ Å} \tag{3.1b}$$

The tolerances stated above must be met in the presence of various disturbances such as building vibrations, acoustic noise and temperature drift as well as hysteresis and creep of the piezoelectric translation elements usually employed. Further they must be met in the presence of four other mechanical design requirements, viz.,

precision z distance regulation in the 0—1 μm range.

x and y scanning capability in the same range.

tip approach $\bar{z}$ from several mm to 100 nm range.

scan window selection $\bar{x}$, $\bar{y}$ in the same range.

The first two requirements result from the need for three dimensional tip translation capability for recording surface topography. The last two arise due to the need for convenient sample and tip loading, for reducing the tip-sample separation from macroscopic to tunneling distances, and for selecting an area of interest on the sample surface. Hence a complete STM incorporates six degrees of translational freedom. These translations have also to be performed with reasonable and coordinated speeds, not only to achieve efficient operation but also to minimize other disturbing influences such as thermal drift or surface modification by adsorption. Finally all the requirements have to be satisfied with UHV—compatible design elements.

In the case of the liquid metal ion source—scanning tunneling microscope embodiment, the tolerance requirements are not as severe as for the tunneling microscope itself, the reason being the operation of the liquid metal ion source (at least at the present time) is at separations that are at least an order of magnitude greater than the separations that are normally employed in conventional STM work, which are 20 Å or less.

During the operation of a liquid metal ion source (LMIS) there arises at threshold, a protusion commonly referred to as a Taylor cone of 49.3° half angle, from which field evaporation of (mostly) monomeric ions take place if

a pure element LMIS is used. The Taylor cone, for the purposes of the proximity focusing experiments can be considered to be of length approximately equal to the radius of the emitter supporting the liquid metal. The considerations then, during the operation of a LMIS in a STM embodiment, is the diameter of the ion beam at the target. Assuming an emission half angle of 20° for a LMIS operating at 0.5 μA threshold current, one can obtain theoretically, a beam diameter at the target proportional to the separation between the source and the target. It is conceivable then that a lower limit on this beam diameter at the target could be the diameter of the Taylor cone apex (~50 Å).

Hence for a well designed LMIS-STM embodiment the main issues to be considered are:

1. Coarse positioning (z) from several centimeters down to the 100 nm range.

2. Source translation capability over several centimeters of the sample both in the x and y directions.

3. The x,y,z piezoceramic drives for precision regulation for the directions normal to the sample surface and in the plane of the surface, in the range 0—10 μm.

4. The vibration isolation and damping stages.

5. Thermal effects.

We shall now consider these issues in more detail below.

2. Magnetically Driven Walker

In high resolution STM work it is essential to position a specimen and a very sharp tip to within several nanometers of each other from a range of a few centimetres. Such dynamic ranges of movement have usually been achieved using piezoelectric walkers or "louse" as they are commonly known. The piezoelectric walker works on the principle of expanding or contracting a piezoelectric plate while clamping the appropriate end. Steps ranging from a hundred to several thousand angstroms can be achieved. These steps are summed to provide the required large range of movement.

In the magnetically driven walker used in this work, the movement is generated by forces developed by current pulses through coils of copper wire in a magnetic field as introduced by Smith and Elrod[3]. The walker slides on a smooth low friction surface such as a microscope (glass) slide and does not require clamping as in the piezoelectric walkers. The geometry of a one-dimensional walker is shown in Fig. 3.1. The principle of operation is illustrated in Fig. 3.2 and is explained below.

About 300 turns of enamelled copper wire is wrapped around a rectangular support machined out of aluminum. The support has three teflon legs sharpened at the ends to fine points to reduce the coefficient of static friction but not so small as to prevent uniform motion by decreasing the coefficient of kinetic friction. This was done empirically until uniform reproducible motion was obtained as shown in Fig. 3.3. The magnetic field was provided by a permanent magnet and was of the order of 10^4 gauss. The

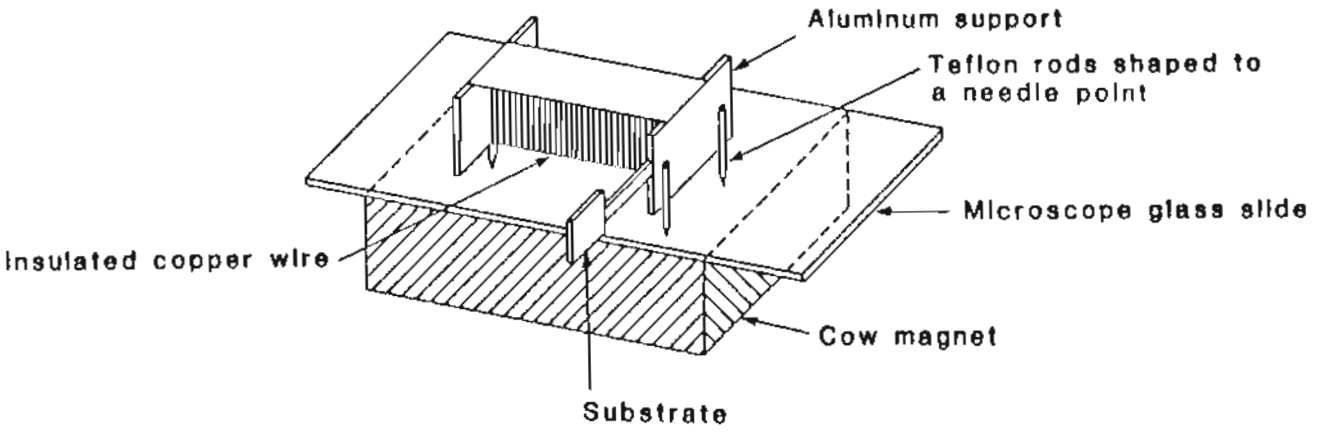

Figure 3.1 : Geometry of a one-dimensional magnetically driven walker used in the LMIS-STM.

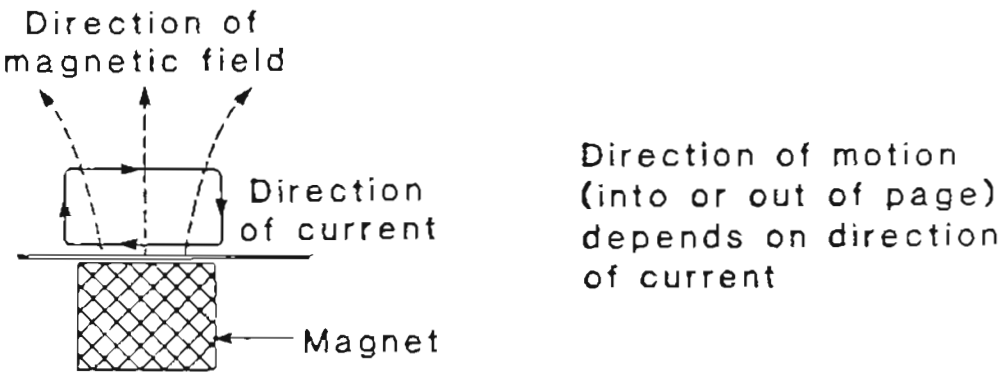

Figure 3.2 : Principle of operation of the magnetically driven walker.

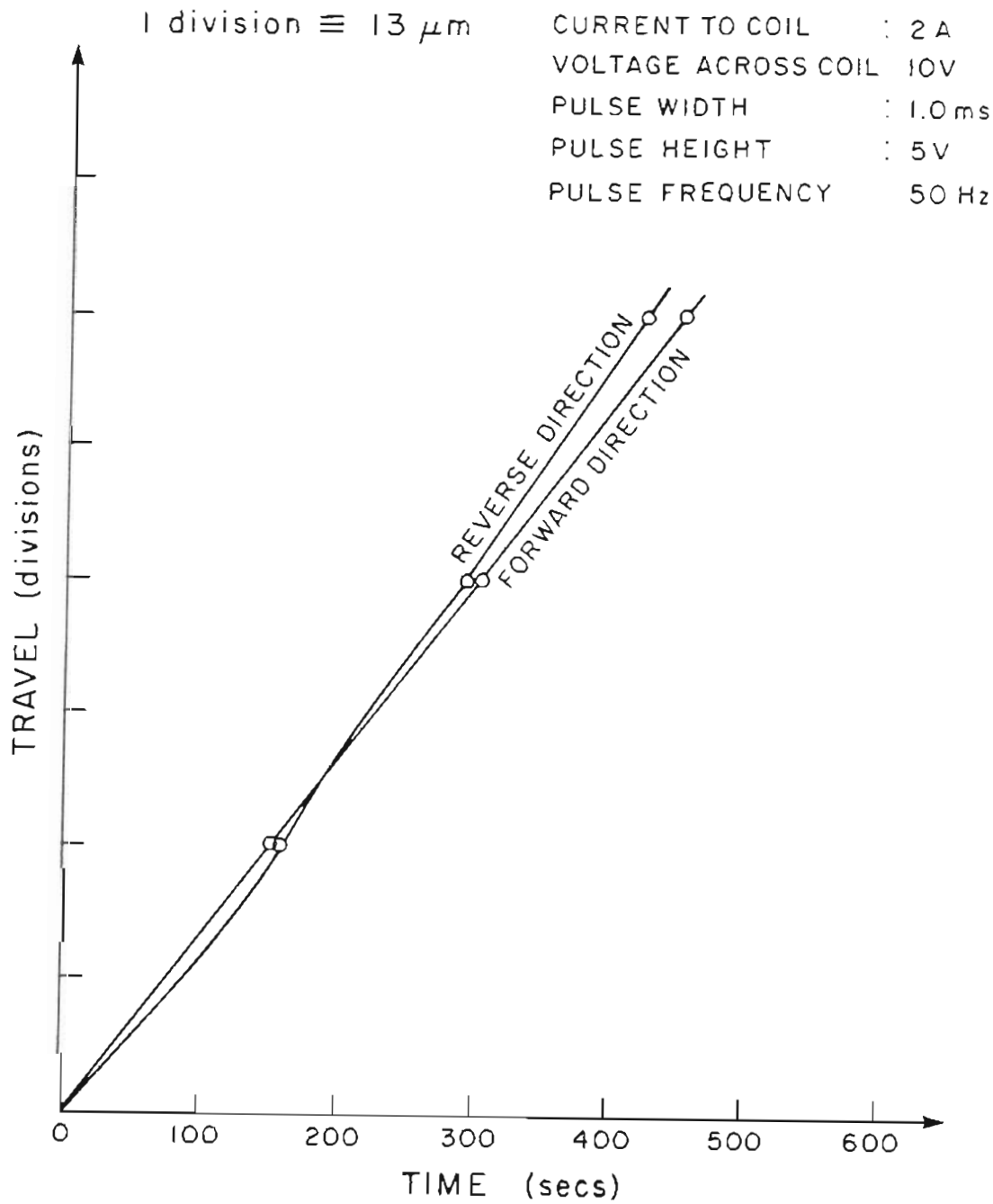

Figure 3.3 : Distance travelled versus time for the magnetically driven walker. The two curves represent forward and reverse motion over the same distance.

magnetic field is directed vertically as shown in Fig. 3.2. Current pulses ranging from 1.5 amperes to 5.0 amperes with voltages from 7 volts to 30 volts, (depending on the range of movement desired) are applied to the wound copper coils using a joystick type of controller. The current direction through the coil can be changed at the turn of a switch as also single current pulses can be applied to the walker to obtain single step capability. The electronic circuitry for the controller is sketched in Fig. 3.4. The copper wire is wound around the core such that when current flows through the coil, the portion of the coil nearest to the magnet ($\sim$1 to 2 mm from it) develops a force that is much greater than that developed by the portion of the coil farthest away from the magnet ($\sim$1 cm away from it) due to the dipole character of the magnetic field. It is also essential that the teflon legs be positioned such that the lower part of the coil is as close to the magnet as possible so that the difference in the forces generated be sufficient to propel the walker in the desired direction. The specimen mounted on the walker can then move forward or backward depending on the direction of the current in the coils. The range of movement is confined to the region of overlap between the coil and the magnet. Sideways motion of the walker was prevented by the use of teflon side rails. Front and end stoppers determine the total range of movement.

For use in vacuum, the walker was enclosed in a quartz tube sealed at both ends and with two copper feedthroughs at one end to supply the current to the coils. The first generation LMIS-STM embodiment (see Fig. 3.5) had coarse motion only in the z-direction and no source translation capa-

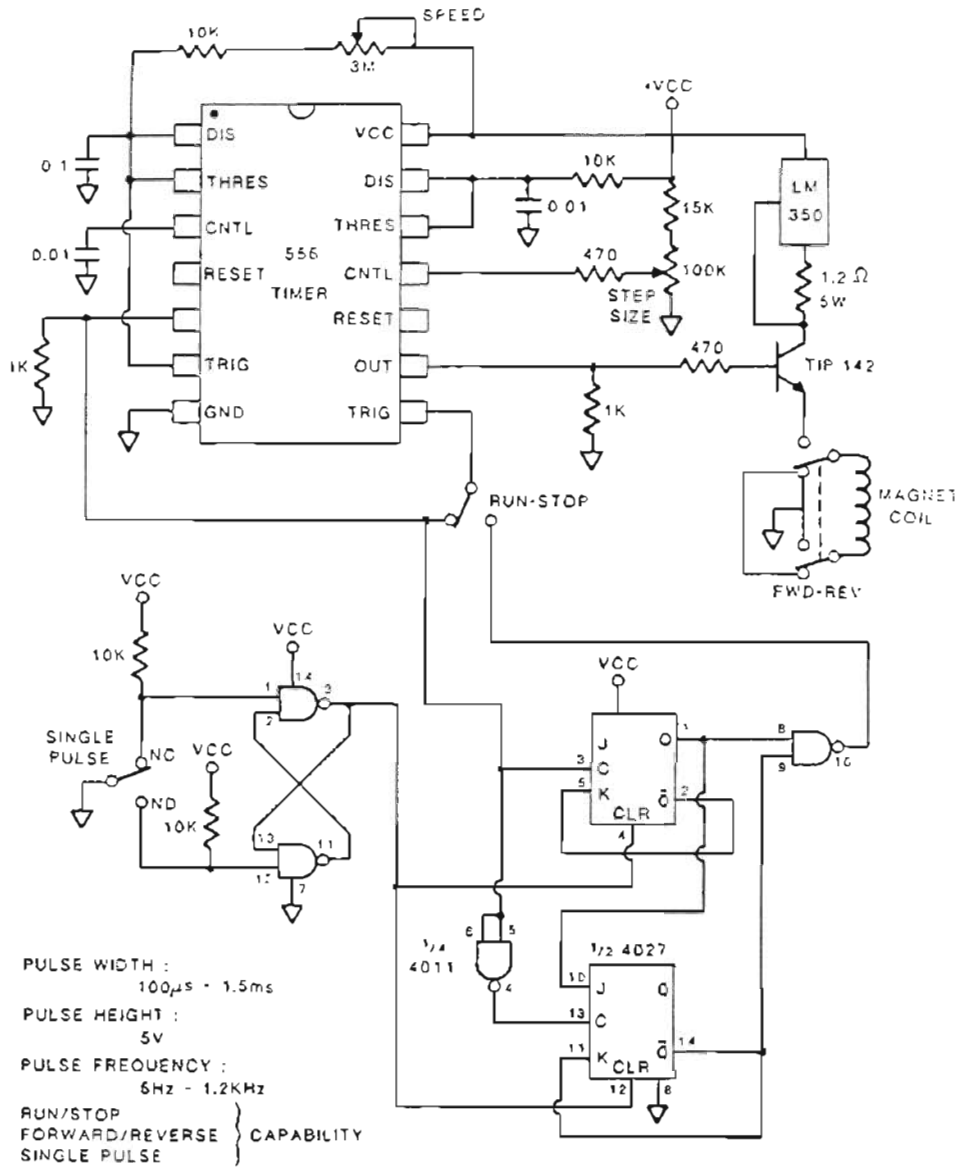

Figure 3.4 : Electronic circuitry for the controller used for the magnetically driven walker.

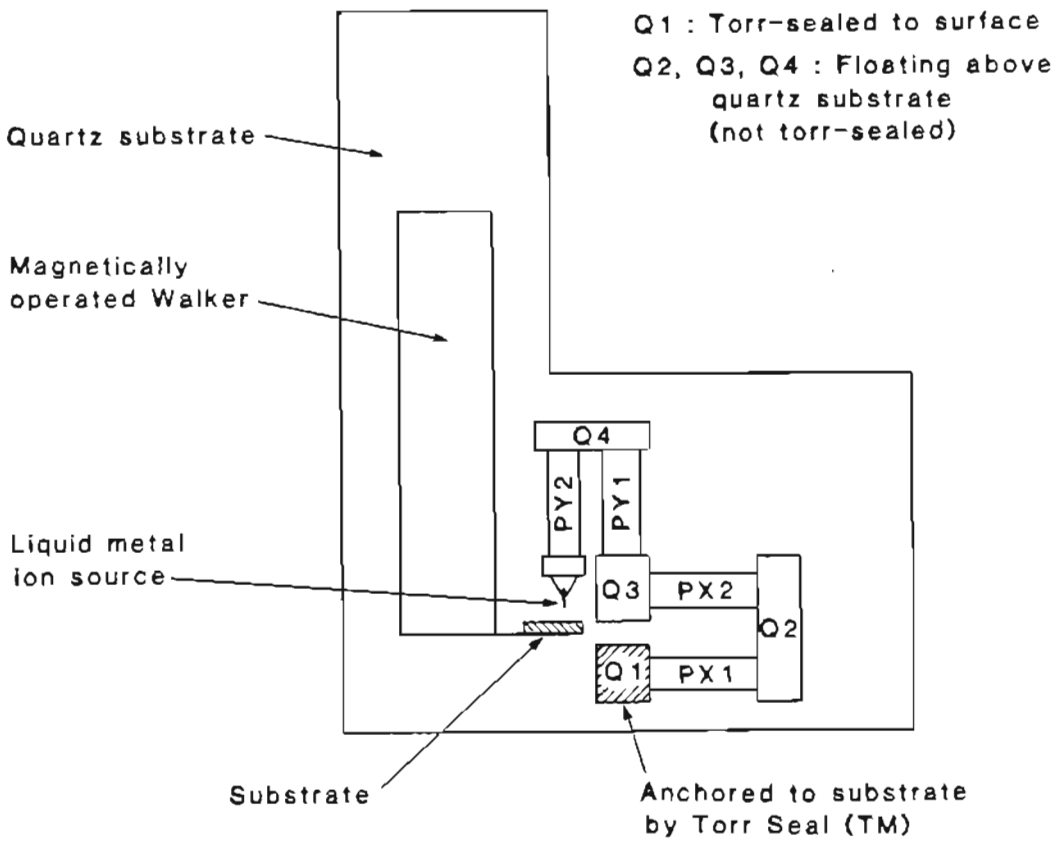

Figure 3.6 : Arrangement of the x-y piezodrives and walker on the quartz substrate for the first generation LMIS-STM. The piezoceramic tubes provide redundancy as well as first order thermal compensation.

bility in the x and y directions. In the second generation LMIS-STM embodiment (Fig. 3.6) this capability was provided by means of a screw thread attached to the base of the magnetically driven walker and operated from outside the vacuum chamber by means of a rotary feedthrough. Turning the screw thread would displace the magnetically driven walker sideways (x-direction) and the tip could then be brought within operating range using the motion of the walker. To provide for vibration isolation while using the screw thread, the rotary feedthrough did not directly couple to the screw thread but instead was brought to play by means of an L-shaped interlock which after the desired motion was accomplished could then be disengaged from the screw thread.

3. The X-Y-Z Piezodrives

The fine motion of the tip with respect to the substrate was achieved using piezoceramic tubes in the arrangement shown for the first generation LMIS-STM embodiment in Fig. 3.5. The piezoceramic tubes P_{x1} and P_{x2} provided movement in the x direction while P_{z1} and P_{z2} provided movement in the z direction. Of the four rectangular quartz pieces Q1, Q2, Q3 and Q4, only Q1 is anchored to the quartz substrate (which holds the STM) while the remaining three float above the substrate. The four piezoceramic tubes provided redundancy for the fine motion and first order thermal compensation. The piezoceramic tubes operate in the longitudinal mode and require a certain minimum length to provide the range of displacements required. The piezoceramic tubes used were Vernitron PZT-5H piezoceramics which are

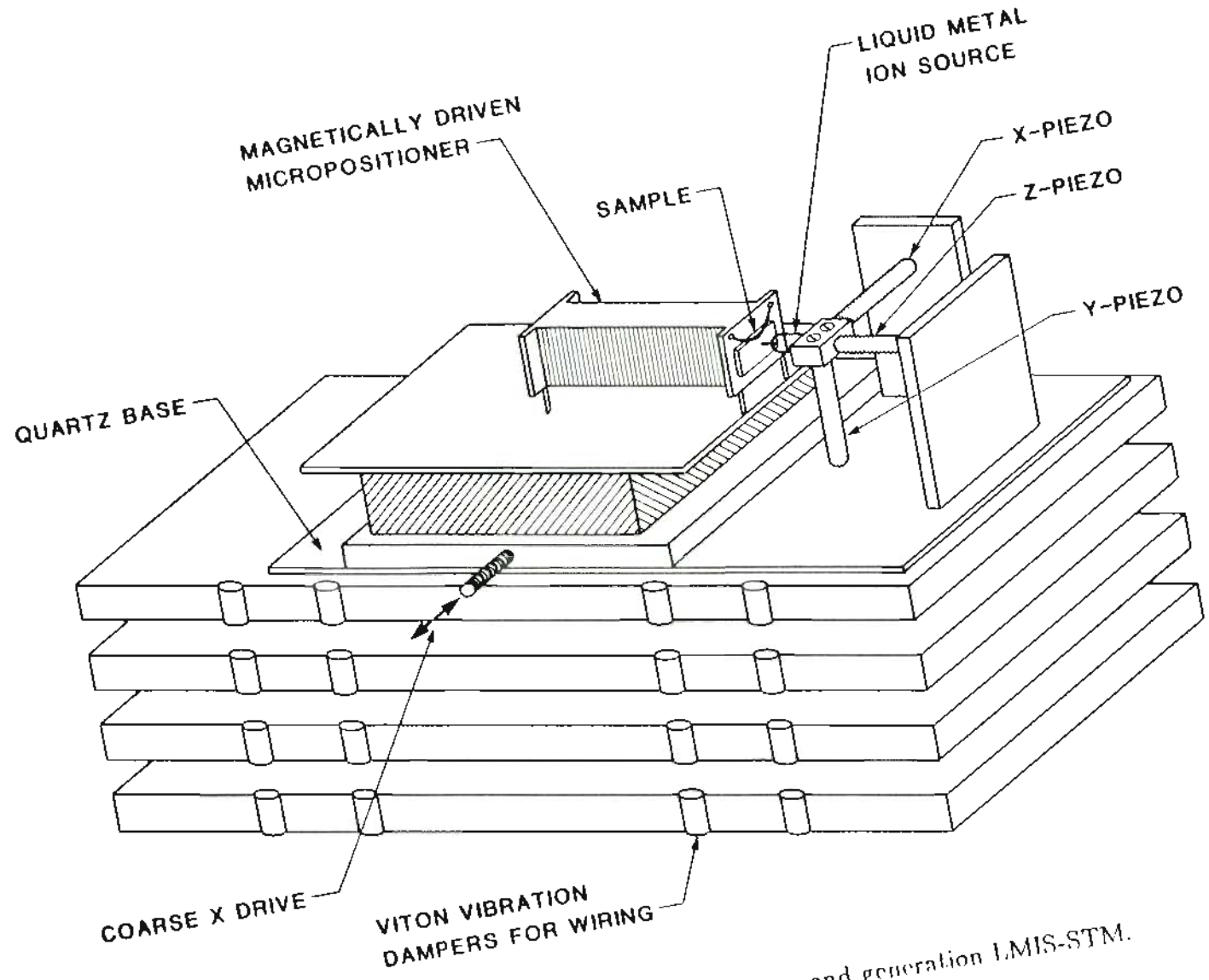

Figure 3.6 : Schematic diagram of the second generation LMIS-STM.

better suited for low frequency applications because of their increased permittivity, but have a reduced Curie point which restricts the working temperature range.

The displacement Δx versus voltage V relation for a piezotube is:

$$\Delta x = d_{31} \times V \times \left(\frac{L}{t} \right)$$

where the relevant parameters are:

$d_{31} = -274 \times 10^{-12}$ meters/volt

$= -2.74$ Å/volt

L = 0.5 inches = length of the piezoelectric tube.

t = 0.02 inches = wall thickness of the piezoelectric tube.

Hence,

$$\Delta x/\text{volt} = -2.74 \times (0.5/0.02)$$

$$= 68.5 \text{ Å/volt}$$

Here d_{31} is the relevant piezoelectric coefficient, and L and t are the lengths and the wall thickness of the piezoceramic tubes respectively.

We tested the x,z scan arrangement in the SEM at magnifications of 10,000X and higher. A motion of about 70 Å/volt was measured in both the x and z directions for positive voltages applied to the inside of the

piezoelectric tubes with the outsides being connected to ground.

For, the second generation LMIS-STM embodiment, the fine motion in the z direction as well as scanning in the x-y directions, orthogonal one inch piezoelectric (PZT-5A) tubes (Fig. 3.6), driven by a 800 volt scan signal, to provide $\sim 10 \times 10$ μm scan range, were chosen as the most practical way to achieve three dimensional electronically controllable motion on a nanometer scale.

The displacement Δx versus voltage V relation for the piezoelectric tubes (PZT-5A) works out to be:

$$\Delta x/\text{volt} = -1.71 \times (1.0/0.02)$$

$$= 85.5 \text{ Å/volt}$$

where the relevant parameters are:

$d_{31} = -171 \times 10^{-12}$ meters/volt

$= -1.71$ Å/volt

L = 1.0 inches = length of the piezoelectric tube.

t = 0.02 inches = wall thickness of the piezoelectric tube.

We tested the x-y scan arrangement using a Michelson interferometer (Fig. 3.7) with a He–Ne laser of wavelength 635.2 nm. Each movement of a fringe in this set-up represented a travel of 317.6 nm. It was seen that both

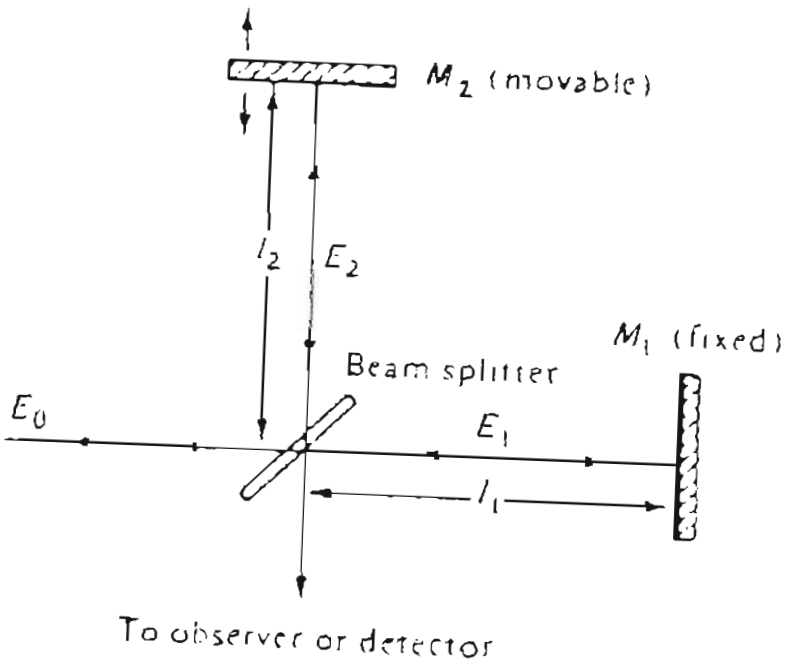

Figure 3.7 : Michelson interferometer set-up for calibrating the piezoceramic tubes for the LMIS-STM.

the x and y piezoelectric tubes showed motions of ~90 Å/volt while the z piezoelectric tube had a resolution of only 55 Å/volt. This reduction in the total displacement per volt of applied signal in the case of the z piezoelectric tube is probably due to the coupling between the orthogonal piezoelectric tubes which would restrict the total displacement possible with the individual piezoelectric tubes.

4. Tip and Sample Mount

The LMIS tips are mounted on the scanner using copper tip holders attached onto a small quartz block for electrical isolation from the piezoelectric transducers. The tips are held securely using set screws on the tip holders, and can be quickly changed. The sample mount is made of copper and has spring clips to hold the sample securely as also to provide electrical contact.

5. System Design

The STM embodiments were designed to be used in an ultra-high vacuum environment. An ultra-high vacuum (a few times 10^{-9} torr) environment was desired, for investigating both the proximity focused technique in the ion mode and field electron emission from the LMIS for imaging the features produced. This required that only ultra-high vacuum components be used while designing the STM system. Further all connections were made using "fluxless" solder, to rectangular pieces of quartz, the appropriate portions of which were nickel coated in a "Watts nickel plating bath" to provide

electrical contact. The portions of the quartz pieces which were not nickel coated served to provide electrical isolation between the coated portions as well as to minimize the effect of temperature on the performance of the STM. Another, quicker method used to provide areas of electrical contact on quartz was to "fire on" several layers of silver paint using a hydrogen flame on the desired areas. To render the STM even further insensitive to temperature variations, it was mounted on a quartz substrate which was attached rigidly to the top stage of the vibration isolation system.

As discussed by Pohl[2], the tolerance requirements in a well designed STM must be met in the presence of ill-defined disturbances like building vibrations, acoustic noise and thermal drift. These then have to be met with design rules for the optimization of damping and stiffness for the STM structure.

Low frequency vibrations, mainly due to buildings vibrating at frequencies ranging between 10 and 100 Hz with the largest maxima of the vibration-spectra (Fig. 3.8, from D. W. Pohl[2]) at 15 to 20 Hz, are of importance. The largest peak appears near 17 Hz with an amplitude of 0.2 μm. The peaks at 50 and 100 Hz are much less pronounced, probably because they are off-resonance with regard to the (lowest-order) floor eigenfrequency. The peak around zero is an instrumental artifact. The floor responce to irregular motions such as those caused by persons walking around are typically in the 1-3 Hz range, with amplitudes comparable to the 17 Hz peak. They are indicated by dashed bars in Fig. 3.8.

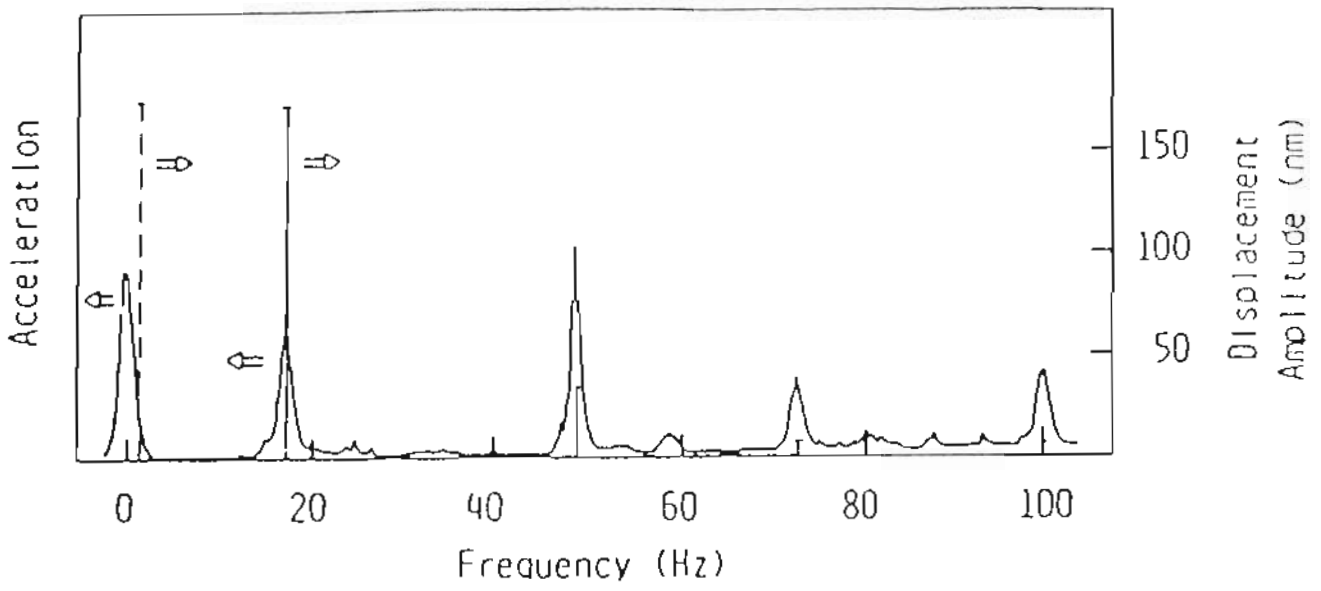

Figure 3.8 : Vibration spectrum of a typical floor in a laboratory. The curve depicts accelerometer output; the dashed bars depict the effects of walking in the laboratory.

These external pertubations discussed above tend to affect the tip-sample separation control and need to be reduced with vibration isolation systems and/or sufficient stiffness of the STM structure. The combined STM-vibration isolation system consist of elastic materials (viton rubber) supporting the mass of the STM, m_{STM}. The elastic elements are characterized by their elastic constant C_d(spring constant) and quality factor Q_d which is a measure of the amplitude enhancement at resonant frequency as well as the width of the resonant curve. The effectiveness of a damping system can be expressed by means of its transmittivity $\mathfrak{t}_d$, defined as the ratio of amplitudes of the supported STM structure, $|\hat{z}|$ and excitation $\hat{z}_e$ of the base. From harmonic oscillator theory we get for the transmittivity:

$$\mathfrak{t}_d(\Omega_d) = \left[(\Omega_d{}^2-1)^2 + \Omega_d{}^2/Q_d{}^2\right]^{-1/2} \tag{3.2}$$

where the frequency Ω_d is normalised to the (undamped) resonance frequency

$$\nu_d = \frac{1}{2\pi}\sqrt{C_d/m_{STM}}, \tag{3.3}$$

$$\Omega_d \equiv \nu/\nu_d \tag{3.4}$$

Equation 3.2 is plotted in Fig. 3.9 (reproduced from D. W. Pohl[2]) for two sets of parameters: Curve $\mathfrak{t}_{d1}$ results from $\nu_d = 3$ Hz, $Q_d = 3$, which is typical for damping systems with metallic springs and eddy-current attenuation; the respective values for curve $\mathfrak{t}_{d2}$ are $\nu_d = 5$ Hz, $Q_d = 15$, typical for damping systems with commercial antivibration pads made from caoutchouc.

There are three regions of frequency that can be recognised as seen in Fig. 3.9: (1) well below the resonant frequency the vibration isolation does nothing and the vibrations are transmitted with little or no amplification; (2) near the resonant frequency the vibrations are amplified substantially; and (3) well above the resonant frequency the vibrations are attenuated. The amount of amplification near resonance and attenuation above resonance depends on the damping. As seen from Fig. 3.9, for critical damping, the amplification has a maximum of less than 1.5, but the attenuation is only a factor of 5 for a frequency 10 times the resonant frequency. Typical rubber has a damping of order 0.05 of critical. This gives an amplification of 10 near resonance, but an attenuation of over 50 for a frequency 10 times the resonant frequency. Typical undamped steel springs have a damping of order 0.005 of critical. This gives an amplification of 100 near resonance and an attenuation of roughly 100 for a frequency 10 times its resonant frequency. Thus some damping is necessary; for the extra factor of 2 attenuation by undamped steel springs at $10\nu_d$ the price is a factor of 10 more amplification near resonance-but critical damping is usually too much. Between 0.2 and 0.02 of critical damping is often a good range. The lower the resonant frequency relative to the frequency of interest, the less damping is necessary.

To isolate the STM from building and other extraneous vibrations, a resonant frequency of $\nu_d < 1$ Hz would be desirable in view of the spectrum of Fig. 3.8. That is however difficult to implement since it implies a large static elongation Δ of the elastic element:

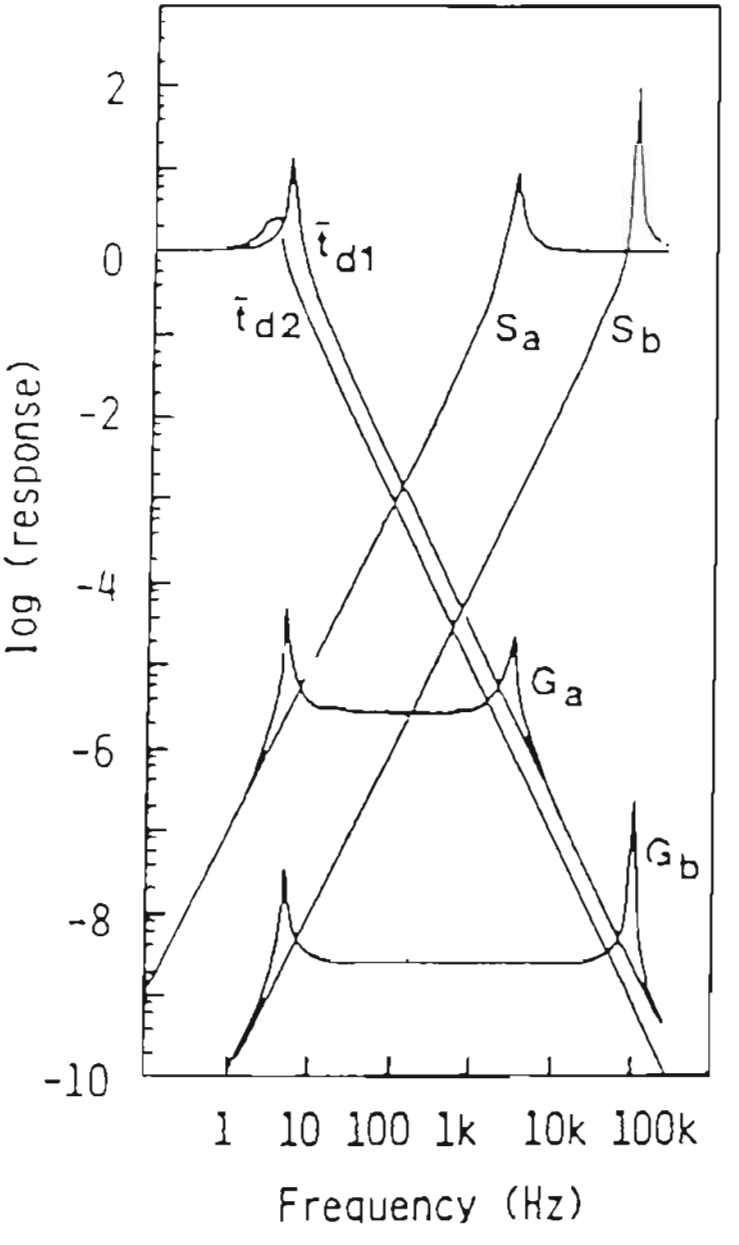

Figure 3.9 : Frequency characteristics of damping ($\bar{t}_{d_1}$,$\bar{t}_{d_2}$), stiffness ($S_a S_b$), and combination of ($\bar{t}_{d_1}$,$\bar{t}_{d_2}$), S_a,S_b, ($G_a G_b$).

$$\Delta = \frac{g}{2\pi \nu_d^{\,2}} \tag{3.5}$$

where $g = 9.81\ ms^{-2}$ is the earth acceleration constant. Thus a resonance of 1 Hz would require a static elongation of 2.5 m. Such large elongations, though feasible, involve inconveniences of design and operation. Most damping systems, for STM's as well as other sensitive machinery such as interferometers, therefore operate at $\nu_d = 2$ to 5 Hz.

The quality factor Q_d should not be too large to ensure that accidental excitations at ν_d attenuate within a reasonably short time. Its magnitude, though should not be too small in order to achieve efficient damping for frequencies $\nu > \nu_d$. For typical rubber type damping elements $Q_d = 10$—20.

The response to walking remains unattenuated using damping elements with a resonant frequency between 2 to 5 Hz. The 17 Hz resonance as well as the 50 and 100 Hz peaks and higher frequency pertubations can be efficiently isolated from the STM using the above criteria. This result is supported by the general experimental observation that noise in the tunnel current is dominated by low-frequency fluctuations.

Large-amplitude low-frequency perturbations which are relatively unaffected by conventional damping systems can jeopardize STM operation unless the STM structure possesses sufficient internal stiffness. Considering a stiffness transfer function:

$$S \equiv |\Delta \hat{z}_1| / |\hat{z}| \tag{3.6}$$

which for low frequencies reduces to

$$S(\Omega_1 - 0) \sim \begin{cases} \Omega_1/Q_1 &= \nu/\nu_1 Q_1 = \mathrm{Im}\hat{(}z_1/\hat{z}), \\ \Omega^2{}_1 &= (\nu/\nu_1)^2 = 1 - \mathrm{Re}\hat{(}z_1/\hat{z} \end{cases} \tag{3.7}$$

for the two cases considered (Re and Im denote real and imaginary parts respectively). This is the low frequency tail of the stiffness curves in Fig. 3.9. One recognises that a structure associated with S_a, about 3×10^{-5} of the 17 Hz excitation translates into a tip-sample distance disturbance, and 10^{-7} of the "walking" perturbation at 1 Hz. The respective data for S_b are 2×10^{-8} and 10^{-10} which is much more favorable.

The global instrument response to vibrations is obtained by multiplying the damping and stiffness transfer functions. The resulting curves G_a and G_b in Fig. 3.9 clearly indicate the frequency regimes which are problematic with regard to external perturbations.

For the pocket size STM, Figs. 3.5 and 3.6, that we have used to do our proximity focusing experiments the vibration isolation system consists of a stack of stainless steel plates with three (or more) viton rubber dampers between each set of steel plates. These were cut from a viton O-ring and are about 5 mm long and 2 mm in diameter. In such a vibration isolation system, each layer will contribute an additional 1/f damping for frequencies above a low frequency resonance characteristic of each layer combination. Hence such an arrangement will provide very effective isolation of the STM from externally induced high frequency vibrations, while averaging the

results of rapid scanning at rates of 1 kHz and above should overcome the problem of low frequency vibrations.

When the problem of isolating the STM from externally induced vibrations has been solved, the next case of interest is the vibration characteristics of the scanning needle. The needles in use in scanning tunneling microscopy are electrochemically etched or ground to a sharp point. For electrochemically etched needles, (see Appendix B) there are two basic shapes; one obtained using a d.c. etch technique with radii $\leq$500Å and cone half angles of $\sim$5 °, and the other from an a.c. etch technique with radii $\sim$1000 Å and cone half angles of 10 to 15°. We have evaluated the stiffness and lowest characteristic frequency of these two varieties of needle shapes, in Appendix C, with a view to providing guidance in the selection of needle shapes for scanning tunneling microscopy.

From the analysis of the vibration characteristics, i.e. the lateral deflections and the lowest mode frequencies for the two types of emitters, we find that the a.c. etched emitters are superior. They deflect a factor of $\sim$1000 less than their d.c. counterparts and their lowest mode frequencies of lateral vibrations are much higher.

References

1. G. Binnig and H. Rohrer, *Helv. Phys. Acta*, vol. 55, p. 726, 1982.

2. D. W. Pohl, *IBM J. Res. Develop.*, vol. 30(4), p. 417, 1986.

3. D. P. E. Smith and S. A. Elrod, *Rev. Sci. Instr.*, vol. 56, p. 1970, 1985.

CHAPTER 4

CONSIDERATIONS RELATIVE TO PROXIMITY FOCUSING OF THE LIQUID METAL ION SOURCE

Liquid metal ion sources (LMIS) have been used increasingly in those applications requiring a high brightness source of ions of a wide variety of elements. In recent years the advent of alloy LMIS has expanded the ion species to include elements such as arsenic which are highly volatile at their melting point and high melting species such as boron[1]. Because of its high brightness, the LMIS is an excellent source for an ion microprobe and has found use in micro-milling[2], microcircuit fabrication[3], and high resolution SIMS[4].

One of the main objectives in combining the techniques of the liquid metal ion source (LMIS) with the scanning tunneling microscope (STM) has been to build a proximity focused LMIS for micromachining and microfabrication, in many ways to perform tasks similar to a focused ion beam (FIB) system. The difference lies in the fact that in a FIB system, (see Fig. 4.40) a portion of the ions emitted from the source (as determined by an aperture) are focused in a focusing column using electrostatic lenses and scanned by means of an electrostatic deflector while in the proximity focused case, the micromachining with the ion beam would be achieved by the use of a close-spaced diode system comprising the source and the target. The spot sizes available in a FIB system are ~ 0.3 μm with a single lens focusing column

and ~500 Å with a twin lens focusing column. In a proximity focused mode, the beam diameter at the target would be of the same order of magnitude as the separation between the source and the target and could theoretically be atleast as small as the Taylor cone apex (~50 Å) of the LMIS.

The properties of the LMIS that make it useful to both the FIB and the proximity focused application are discussed below. For the FIB, the key source parameters are angular intensity (I′) and brightness (B). For proximity focusing, the key source parameters then are:

$$I' = \frac{J_s r^2}{m^2}$$

where $m = \frac{\alpha}{\theta}$ is the angular magnification (see figure below).

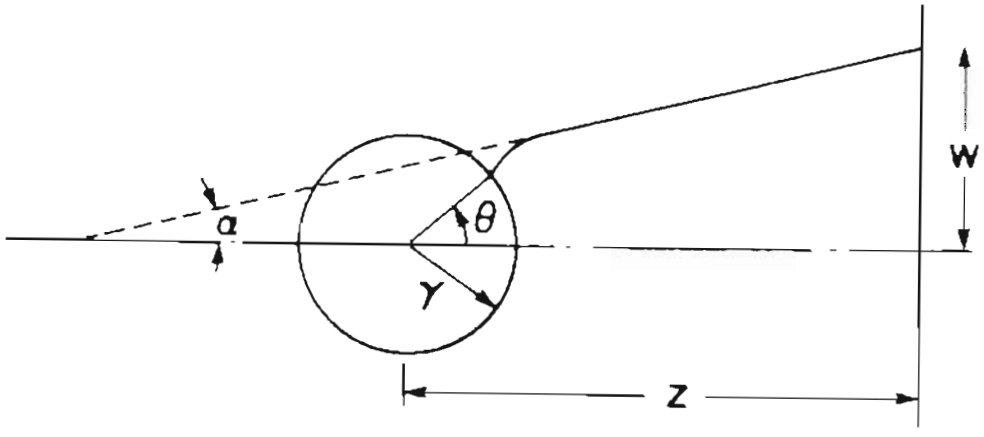

W = RESOLUTION
Z = DIODE SEPARATION

and

$$B = \frac{J_s}{\pi\alpha^2} = \frac{I'}{\pi r^2}$$

and

$$w = z \tan\alpha \sim z\alpha$$

The current density at the target at z, J(z) is then

$$J(z) = \frac{J_s r^2}{(mz)^2} = \frac{I'}{z^2} = \frac{I'm^2}{r^2} = \frac{I'\alpha^2}{w^2}$$

Thus we see that $w \propto z$, but z cannot be smaller than r. And $J(z) \propto I'$ and is also $\propto \frac{m^2}{r^2}$. Thus a large I' and small r favor large J(z) and these same source parameters favor large B. Hence we see that the key source parameters are the same for both the FIB and the proximity focused applications.

Some of the issues that arose during the proximity focusing experiments were

1. Emission instabilities of the LMIS due to back sputtered neutrals condensing on the source.

2. Physical contact between the Taylor cone of the LMIS and the substrate, in effect a "shorting" of the LMIS.

3. Reversing the polarity and obtaining electron emission from the LMIS for imaging the micro-features produced from the proximity focusing

experiments.

4. Current densities attainable at the target from the proximity focusing.

The first of the four issues, namely, the possible instabilities produced during the operation of the LMIS at close spacings will be considered in detail in Chapter 5.A.

A concern during the proximity focusing is the possibility of the Taylor cone of the LMIS making contact with the substrate while operating at close spacings. When that happens, the extraction voltage of the LMIS would change to $V_{EXT} = I \times R$, Ohm's law, and the current in the circuit would then be governed by that law. It could also result in pulling off, of a drop of liquid onto the substrate. Figure 4.1 shows schematically the shorting of the LMIS to the target when it is turned on at a diode separation that is less than or equal to the length of the Taylor cone protusion.

The last two considerations arose out of a need to image the micro-features produced with the proximity focused ion beam as also to obtain a measure of control from the enormous current densities that are available from this procedure. These issues are discussed in the next four sections.

The operation of the LMIS in the proximity focused mode, was done by positioning the LMIS and the substrate with a calibrated, magnetically driven micropositioner and piezoceramic drives. Large separations of the LMIS from the substrate were determined by use of a 30X binocular microscope with a calibrated reticule in the field of view. This was adequate down to separations of ~ 12 μm. Smaller distances were estimated by counting the

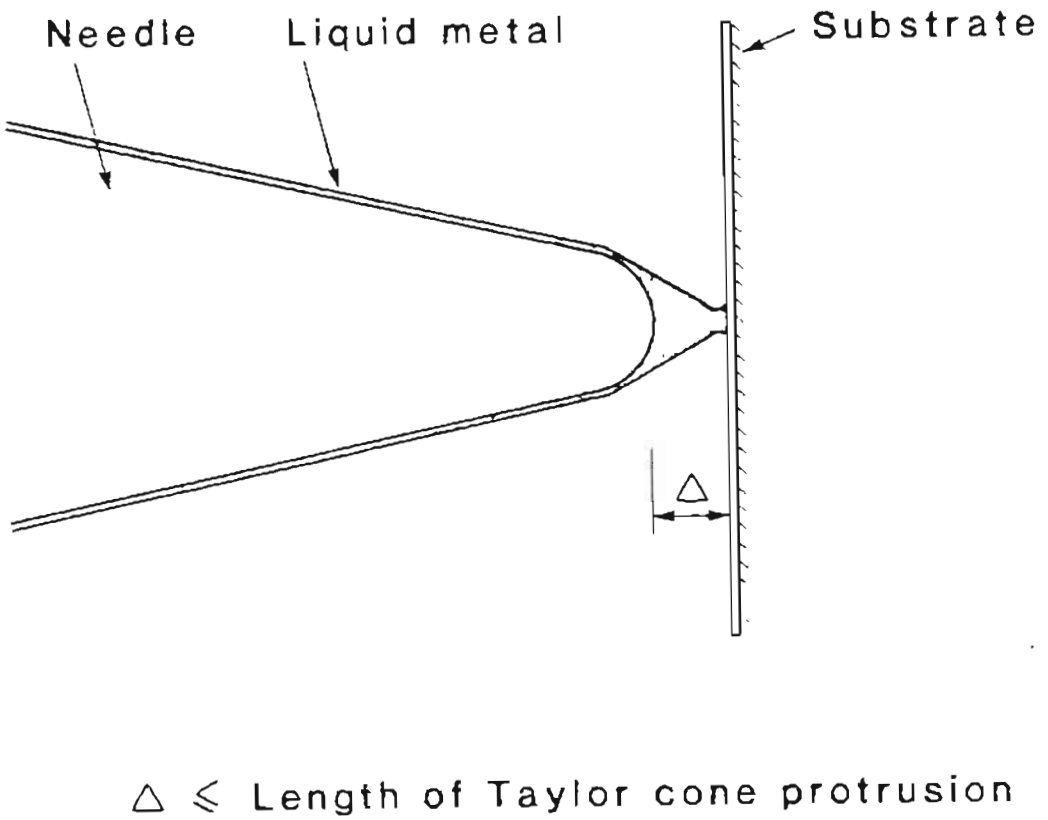

△ ⩽ Length of Taylor cone protrusion

Figure 4.1 : Schematic diagram of the "shorting" of the Taylor cone protrusion to the target.

number of electromagnetic pulses delivered to the magnetically driven micropositioner. The even closer approach was done using the x-y-z piezoceramic tubes. A 90X lens was also used in the binocular microscope, to visually note separations of the LMIS and the target below 12 μm. This lens could not be used for quantitative determination of the separation since it did not have a reticule in the field of view of the microscope.

The separation between the LMIS and the target would determine both the beam diameter and the current density at the target as described earlier. It was therefore felt desirable to develop a second method for determining the separations between the LMIS and the target besides using the calibrated magnetically driven micropositioner and piezoceramic combination. This could also serve as a check on the values of the separations obtained from the micropositioner/piezoceramic combination. It was felt that if electron emission could be obtained from the LMIS, this could be used to determine the emitter-substrate separations. (This is discussed in Chapter 4.B).

An investigation was conducted to try and determine if it was possible to obtain d.c. electron emission from a LMIS. If possible, then the electron emission from the LMIS could also be used to image the features produced (from the ion emission), in a STM mode, by monitoring the variation in tunneling current to obtain topographical information. Another possibility for imaging the substrate could be by withdrawing the LMIS away from the tunneling regime and using the field electron emission from it to profile the surface as demonstrated by Young et al.[5], with his topographiner. They estimated that a vertical resolution of 1 nm and a horizontal resolution of

~20 nm would be obtainable from an emitter placed at 10 nm from the substrate. Though not possessing as good a resolution as the STM, this technique could be used in addition to the STM mode, for imaging the substrate by simply using the emitter as a source of field emitted electrons and noting the variation of the emitted current as a function of emitter X-Y position to obtain surface topography.

The LMIS would then serve not only as a source of ions for possible proximity focused micromachining, but also as a source of electrons for imaging the microfeatures produced. A prospect for obtaining electron emission could be from freezing in the Taylor cone and field building-up the frozen-in cone to obtain a highly confined beam of electrons. This is discused in the next section.

A. A LIQUID METAL ELECTRON SOURCE

1. Introduction

The LMIS configuration consists of a needle wetted with the desired liquid metal and an extraction electrode placed in front of the needle. When a critical voltage of the order of 5 to 10 kV is applied to the needle the liquid metal is pulled outward by the electrostatic forces which compete with the surface tension forces to form a stable cone shaped structure (commonly referred to as the Taylor cone) and ion emission by field evaporation and ionization occur at the cone apex[6-9]. Since the static forces involved in the formation of the cone are polarity independent, one might speculate whether with reversed polarity one could obtain stable, d.c. field electron emission since the fields at the apex would be more than sufficient. Since solid field electron sources are known to undergo catastrophic destruction when an electric arc occurs[10, 11], the liquid metal electron source (LMES) would possess an obvious advantage.

With the above in mind Swanson and Schwind[12] investigated a Ga LMES and found that a Taylor cone, much like in the case of the LMIS is formed, and electron emission is obtained. The electron emission when examined in detail was found to consist of nanosecond pulses with large peak amplitudes of 200 to 300 A depending on the capacitance of the electrode structure. The frequency of the electron pulses was controlled by the RC time constant of the diode circuit. It was deduced that the apex radius decreased without limit as the liquid cone formed and led to sufficient

current that a regenerative explosive current pulse occurred leading to evaporation of the apex region of the cone and the cycle repeated as the cone reformed and the diode potential charged to the critical voltage. Under no circumstances could stable d.c. emission be obtained from the liquid, cone-shaped structure as observed in the case of ion formation with opposite polarity. This result is not unexpected in view of the more recent understanding of the role of dynamic factors in stabilizing the liquid cone in the case of liquid flow due to ion formation. Such dynamic flow is missing in the case of electron emission.

Mitterauer[13,14] and more recently Hata et al.[15,16], have reported d.c. electron emission from a wetted needle source configuration; however, unless the emission is investigated by high speed oscilloscope techniques such claims must be questioned. It is possible to obtain d.c. electron emission if sufficiently sharp needle substrates are used; in such cases the emission is not from a field stabilized liquid cone, but rather it is normal field electron emission as would be expected from such a solid emitter coated with a liquid layer. In some cases d.c. electron emission may occur from a solid whisker grown from the liquid layer in the presence of a high electric field.

Another prospect for obtaining d.c. electron emission from such a system is by forming a Taylor cone as in the normal case of ion emission from a LMIS and freezing in the cone shape by quenching the temperature below the liquid's melting point. If such a procedure were possible one could imagine a single source of both ions, as in the normal LMIS mode, and, by reversing the polarity, electrons from the frozen in solid cone. This study is an

investigation of the possibilities of obtaining d.c. electron emission (1) without forming a Taylor cone and (2) by forming the Taylor cone and freezing in the cone shape for a higher melting liquid such as indium. The practical consequences of a successful result would be a possible dual, high brightness source of both electrons and ions that could be used in a focusing column or in a proximity focusing diode system.

2. Experimental

The radii of the tungsten needles used as a substrate were less than the 4 to 5 μm normally used for the conventional LMIS. Figure 4.2 shows a SEM profile of an electrochemically etched needle used in this study. Typically they had apex radii of about 25 to 2000 nm and were electrochemically roughened in 2M NaOH solution for a few seconds at ~1 V a.c. Larger emitter radii could also be fabricated by a mechanical grinding process[17]. The needle was wetted with Ga or In by heating it to ~1000° K and then repeatedly dipping the needle into a pool of the molten liquid while gently heating the needle to ~1000° K) between dippings.

The emission studies were carried out in a field ion microscope (Fig. 4.3) in which a microchannel plate image intensifier was used in order to view the ion and electron emission patterns investigated. The base pressure for all measurements was 1×10^{-8} torr.

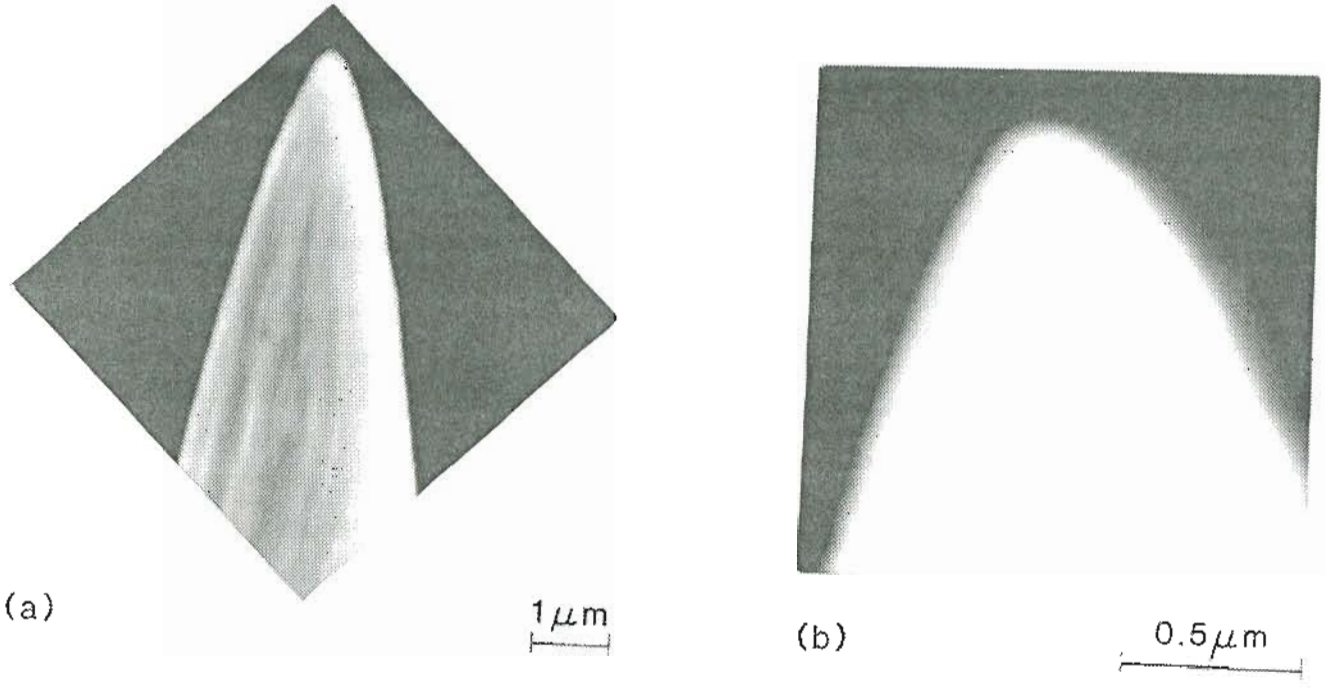

Figure 4.2 : SEM profile of a 180 nm radius tungsten needle etched by a d.c. drop-off technique: (a) low magnification showing part of shank and (b) high magnification of the apex region.

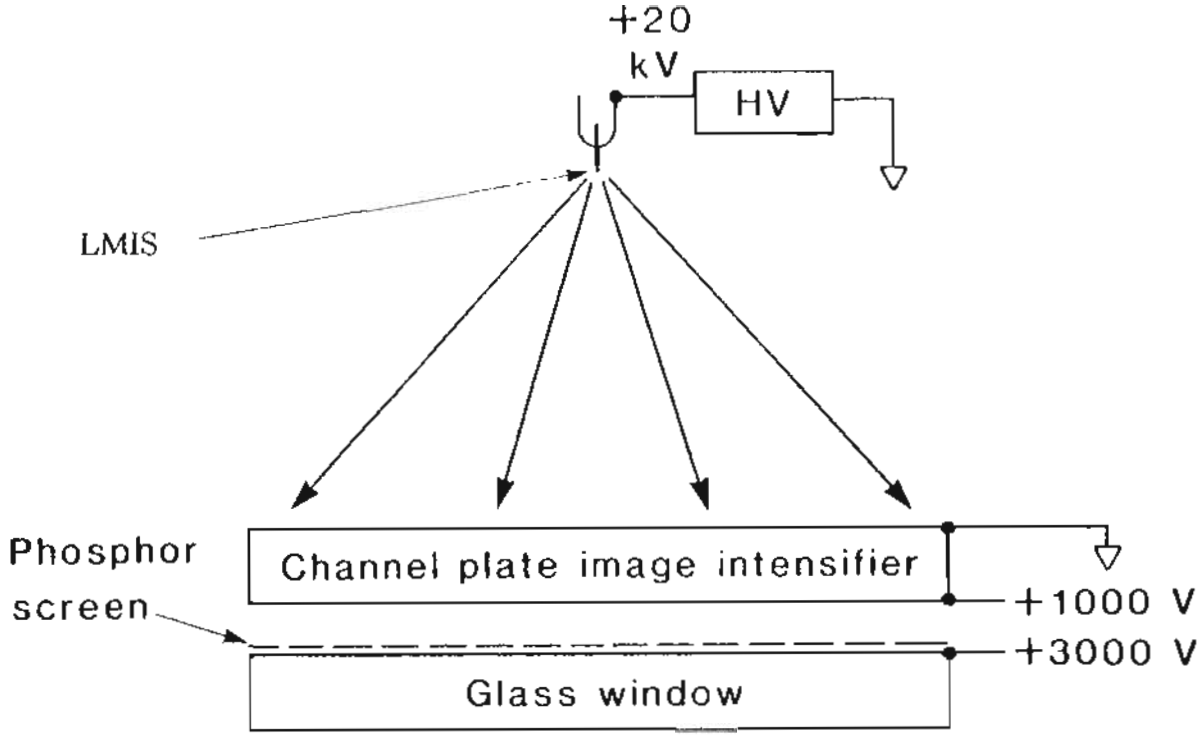

Figure 4.3 : Schematic diagram of field ion microscope with a microchannel plate image intensifier for viewing the ion and electron emission patterns.

3. Results

In this study the ion emission patterns and I(V) characteristics were obtained first by raising the emitter temperature (by resistively heating the emitter support filament) above the melting point of the liquid (for the case of In LMIS) and then increasing the extraction voltage to the threshold for the Taylor cone formation. The liquid cone was then solidified by slowly reducing the emitter heating current below the melting point of In at which point both the emitter heating current and the extraction voltage were quickly reduced to zero. Subsequent electron emission was obtained by thermal/field processing with both positive and negative fields. This procedure was carried out for small (50 nm to 1 μm) and large (1 to 2 μm) radii substrates. In addition, with the small radii substrates, it was possible to obtain field electron emission without first forming and freezing in the Taylor cone. These various results are described below.

3.1 Non-Taylor Cone Field Electron Emission

It is possible to obtain d.c. electron emission at a low extraction voltage V_e from wetted needle substrates if the emitter radius is sufficiently small. This emission is classic field emission from a sharp needle coated with a liquid metal film. Bell and Swanson[17] have shown that the electric field F_0 at the apex of a conical substrate of half angle α and apex radius of curvature ρ is given by:

$$F_0 = \nu_0 V_e / ((\rho x)^{1-\nu_0}[R_0^{\nu_0} - (\rho x)^{\nu_0}]) \qquad (4.1)$$

where R_0 is the emitter to extractor electrode spacing and

$$x = (1-\nu_0)/2$$

The parameter ν_0 is related to the cone half angle and the relation can be determined by using the equation

$$r = b/[P_{\nu_0}(\mathrm{Cos}\theta)^{1/\nu_0}] \tag{4.2}$$

to generate infinite cones with curved apexes (varying b and ν_0 to vary the radius and cone angle respectively of the resulting shape) which simulate LMI needle geometries as discussed by Bell and Swanson[17]. We assume that the emitter is an equipotential for which $b = r_0$ while the counterelectrode is generated by putting $b = R_0$, where R_0 is the distance from the apex of the cone equipotential to the on-axis point on the counterelectrode. A diagram of this electrode geometry generated from Eq. (4.2) is shown in Fig. 4.4 for $\nu_0 = 0.176$.

We find on generating the equipotentials that ν_0 is very nearly a linear function of α and to a good approximation is given by

$$\nu_0 = \nu_0' + m\alpha$$

where $\nu_0' = 0.068$ and $m = 10.796\times10^{-3}$ deg^{-1}. Thus for $\alpha = 10°$, $\nu_0 = 0.176$ while for $\alpha = 5°$, $\nu_0 = 0.122$.

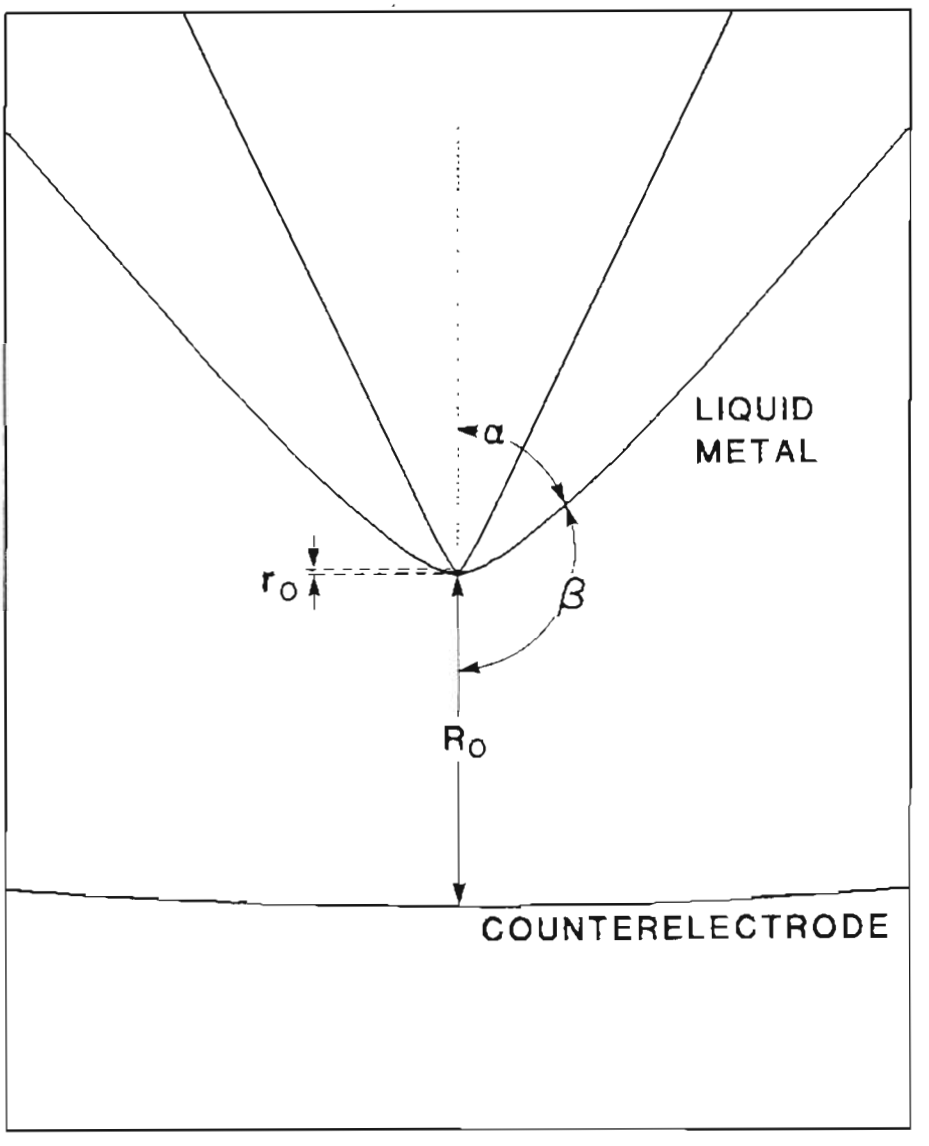

Figure 4.4 : Diagram of the equipotentials generated from Eq. (4.2) for $\nu_0 = 0.176$ and for the two equipotentials $b = r_0$ and R_0 representing an emitter shape and counterelectrode shape respectively.

It can also be shown that the condition for the onset of the Taylor cone formation is given by

$$F_0 = (4\gamma/\rho\epsilon)^{1/2} \tag{4.3}$$

where γ is the surface tension of the liquid film and ϵ is the vacuum permittivity. From Eqs. (4.1) and (4.3) one can calculate the relationship between the threshold voltage V_t for cone formation and emitter apex radius, ρ. Using $\gamma = 0.72$ N/m for Ga, $\alpha = 5°$ and $R_0 = 3$ mm, one can calculate that cone formation occurs at 2218 volts ($F_0 = 0.09$ V/Å) for $\rho = 200$ nm.

The values of threshold voltage V_t and field F_0 for various values of emitter apex radius ρ are given in Table 1 and 2 below for cone half angles $\alpha = 5°$ and 9° respectively.

Table 1. Threshold voltage V_t and apex field F_0 for various values of emitter apex radii ρ.
($\alpha = 5°$; $\gamma(Ga) = 0.72$ N/m; R = 3 mm)

$\rho(\mu m)$	V_t(volts)	$F_0(V/Å)$
0.01	851.60	0.570325
0.05	1482.99	0.255057
0.10	1874.61	0.180352
0.20	2361.74	0.127528
0.30	2698.69	0.104127
0.40	2963.96	0.090176
0.50	3185.85	0.080656
0.60	3378.20	0.073628
0.70	3548.92	0.068166
0.80	3702.99	0.063764
0.90	3843.81	0.060117
1.00	3973.79	0.057032

Table 2. Threshold voltage V_t and apex field F_0 for various values of emitter apex radii ρ ($\alpha = 9°$; γ(Ga) = 0.72 N/m; R = 3 mm)

$\rho(\mu m)$	V_t(volts)	F_0(V/Å)
0.01	1191.49	0.570325
0.05	1967.50	0.255057
0.10	2432.37	0.180352
0.20	2998.31	0.127528
0.30	3383.33	0.104127
0.40	3683.27	0.090176
0.50	3932.23	0.080656
0.60	4146.73	0.073628
0.70	4336.15	0.068166
0.80	4506.37	0.063764
0.90	4661.37	0.060117
1.00	4803.94	0.057032

We see from Tables 1 and 2 that the threshold voltage for cone formation V_t decreases with ρ. The field at the apex F_0, though, increases with smaller emitter radii. Thus we conclude that one is more likely to obtain field electron emission at or below the threshold voltage for cone formation from the solid emitter covered with a liquid layer as the emitter radius decreases.

Figure 4.5 shows an SEM profile of an electrochemically etched needle with apex radius of 0.16 μm and cone half angle $\alpha = 9°$. Figure 4.6a shows a plot of the ion emission current versus applied voltage for the emitter of Fig. 4.5. The threshold voltage for ion emission, $V_t = 2620$ V corresponds quite well with the value shown in Table 2. Figure 4.6b shows a plot of the field electron emission current versus applied voltage for the same emitter. The voltage at which electron emission commences is seen to be well below the critical voltage required to form the Taylor cone and must be attributed to normal field emission from the substrate which is to be expected from such a sharp emitter covered with a liquid layer. Figure 4.7 shows a Fowler Nordheim plot of the field electron emission. The linear relationship between $\log_{10}(I/V^2)$ and $(1/V)$ means that electrons are emitted by tunneling through the surface potential, that is, the normal field emission mechanism.

Figure 4.8a is a microchannel plate image of the field electron emission from a small radii emitter coated with liquid Ga. Figure 4.8b shows ion emission on applying the critical Taylor voltage to the same needle. Figure 4.9 shows plots of the emission current versus the applied voltage from the liquid metal source for both the electron and the ion mode. It is clearly seen again that in the electron mode the voltage at which electron emission commences

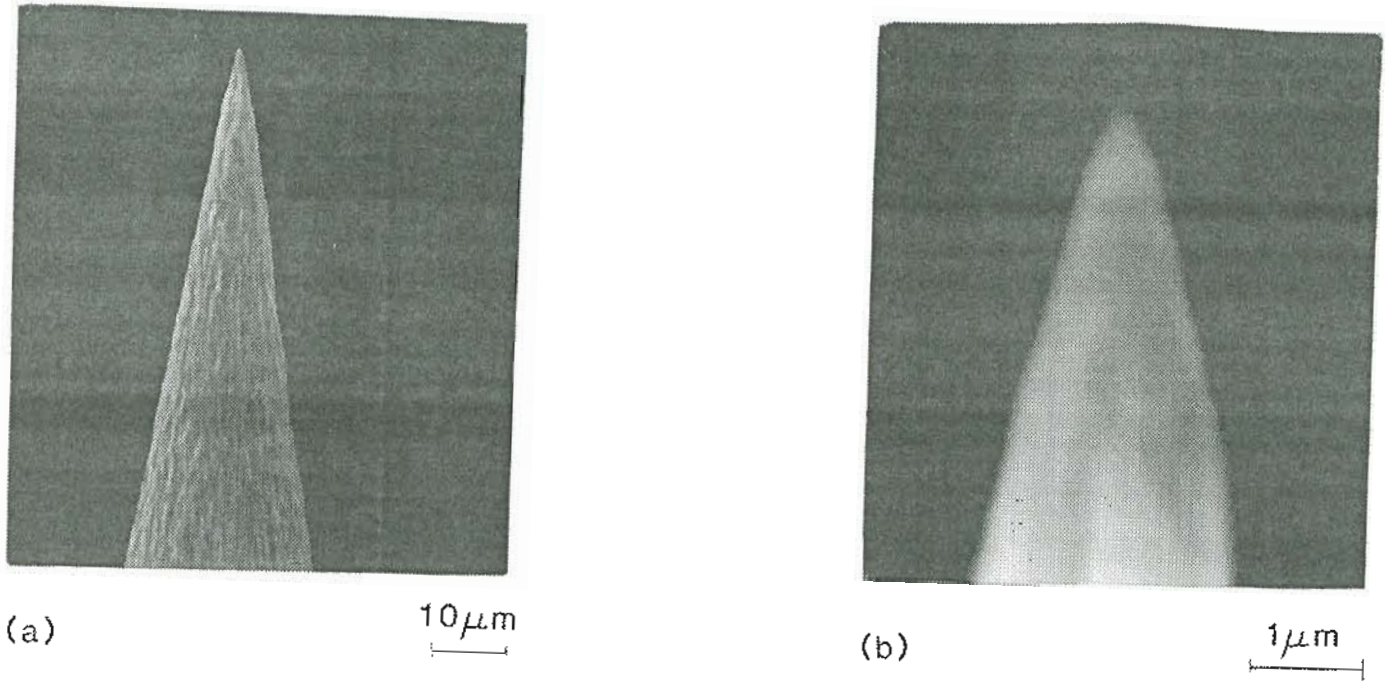

Figure 4.5 : SEM profile of a 160 nm radius tungsten needle etched by a d.c. drop-off technique: (a) low magnification showing part of shank and (b) high magnification of the apex region.

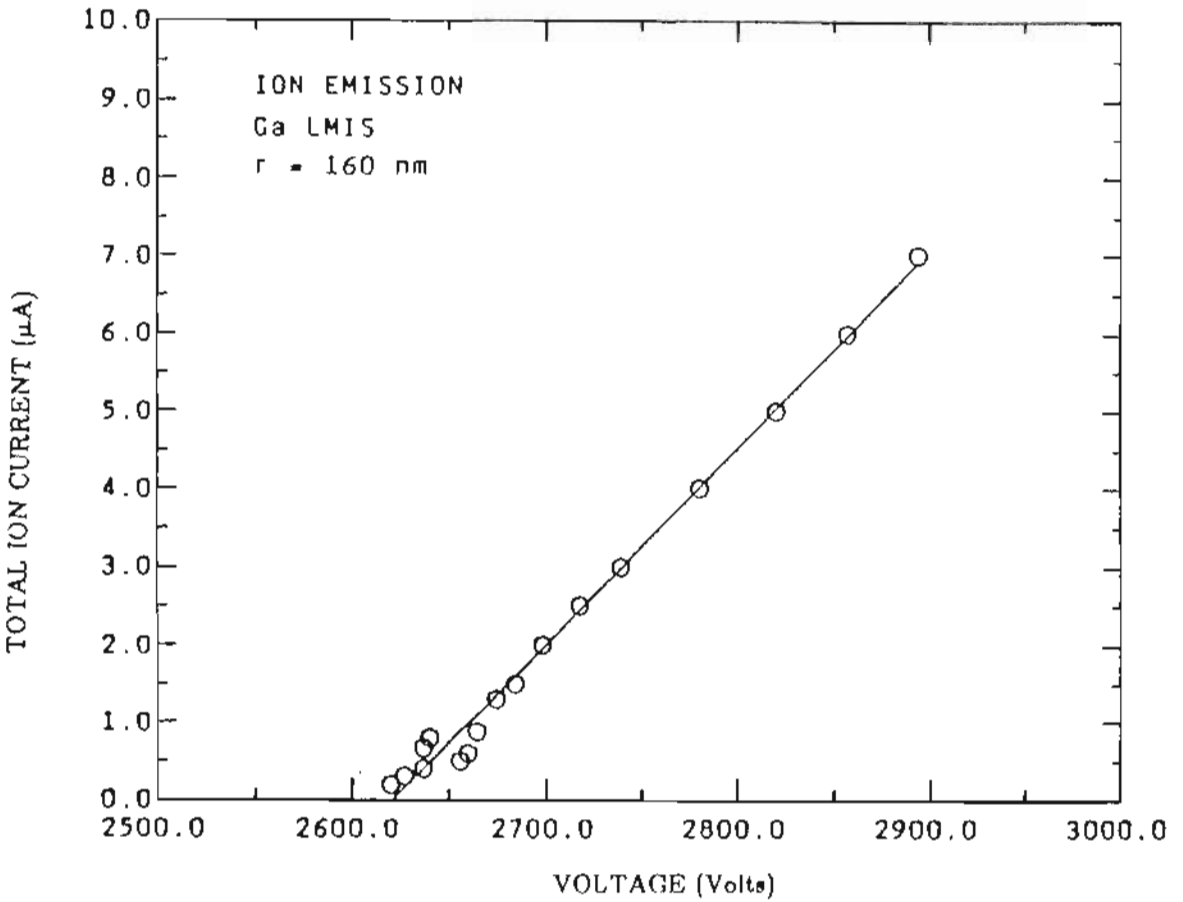

Figure 4.6(a) : Current/voltage plot for the Ga LMIS of Fig. 4.5. in the ion emission mode.

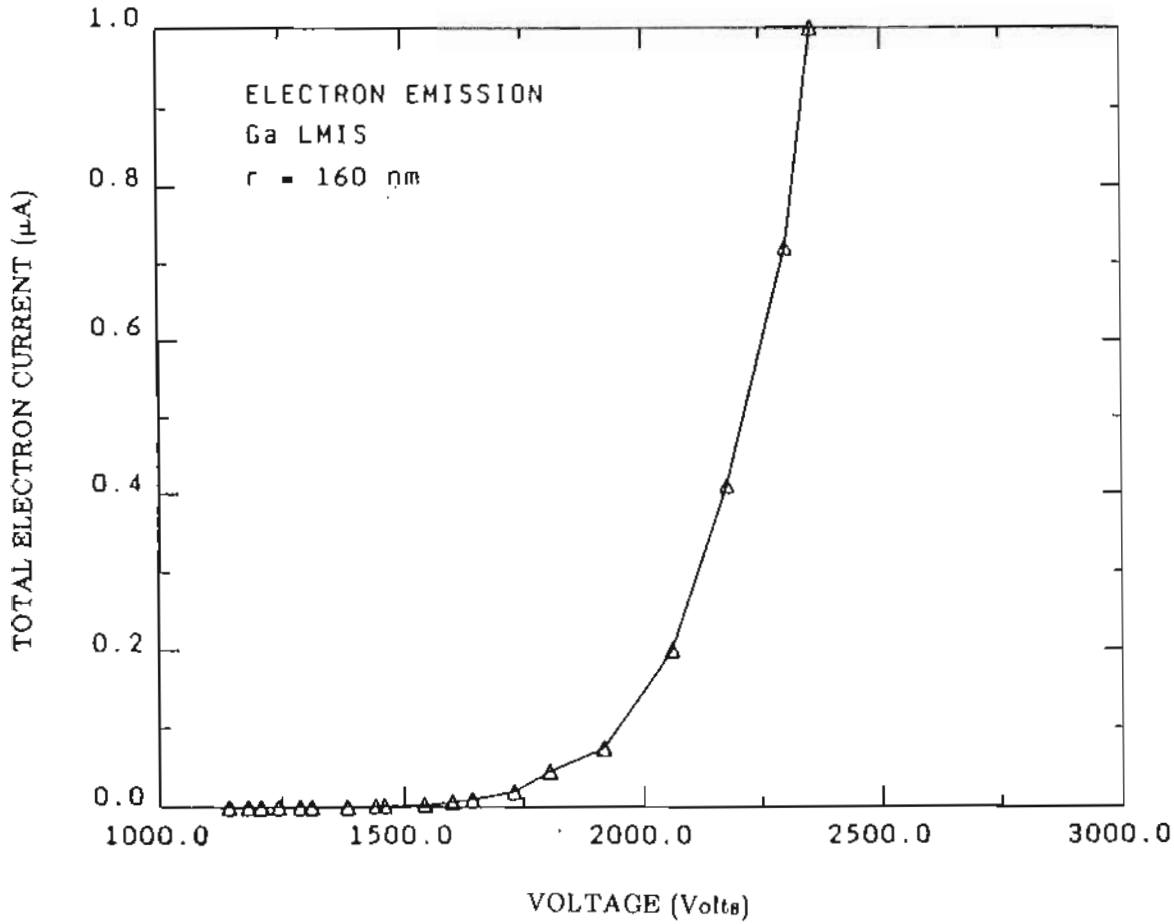

Figure 4.6(b) : Current/voltage plot for the Ga LMIS of Fig. 4.5. in the field electron emission mode.

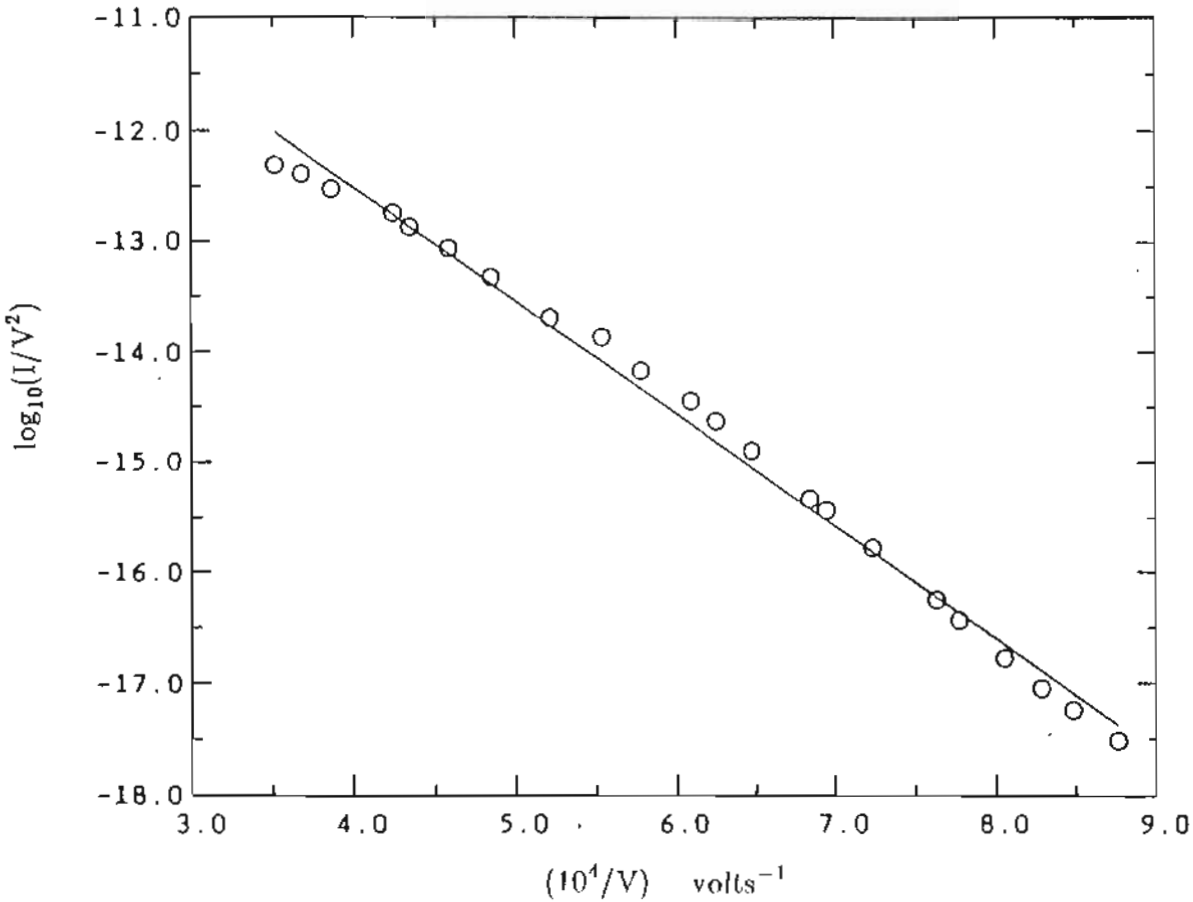

Figure 4.7 : Fowler-Nordheim plot for field electron-emission from the Ga LMIS of Fig. 4.5.

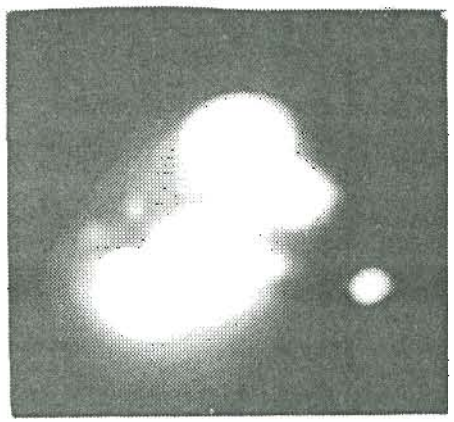

(a)

ELECTRON EMISSION
1900 V, 14 nA

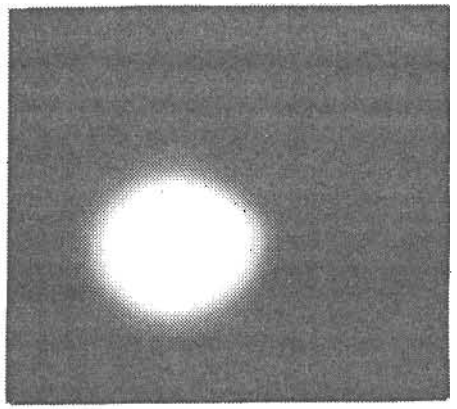

(b)

ION EMISSION
2830 V, 1 nA

Figure 4.8 : Microchannel plate images of the electron and ion beam patterns from a sharp needle Ga LMIS.

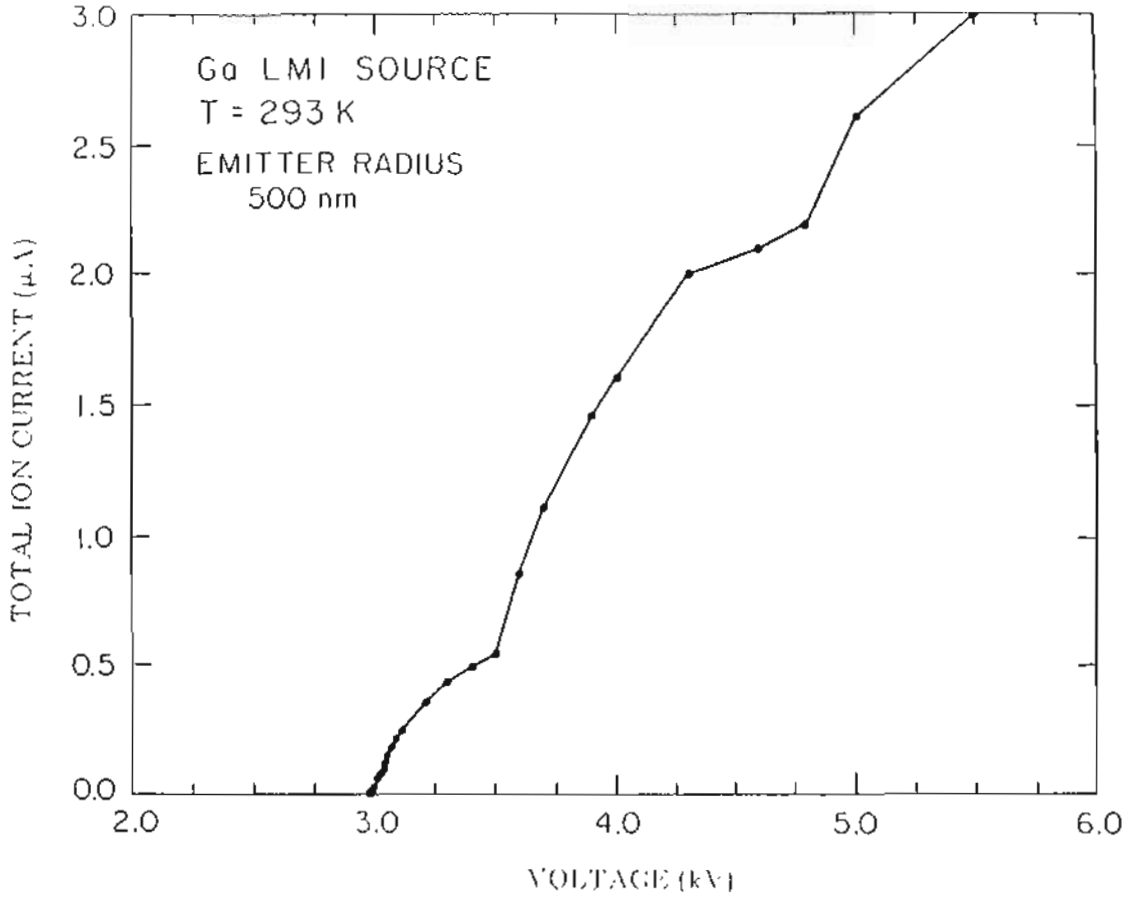

Figure 4.9(a) : Current/voltage plots in the ion emission mode, for the Ga LMIS whose microchannel plate images are shown in Fig. 4.8.

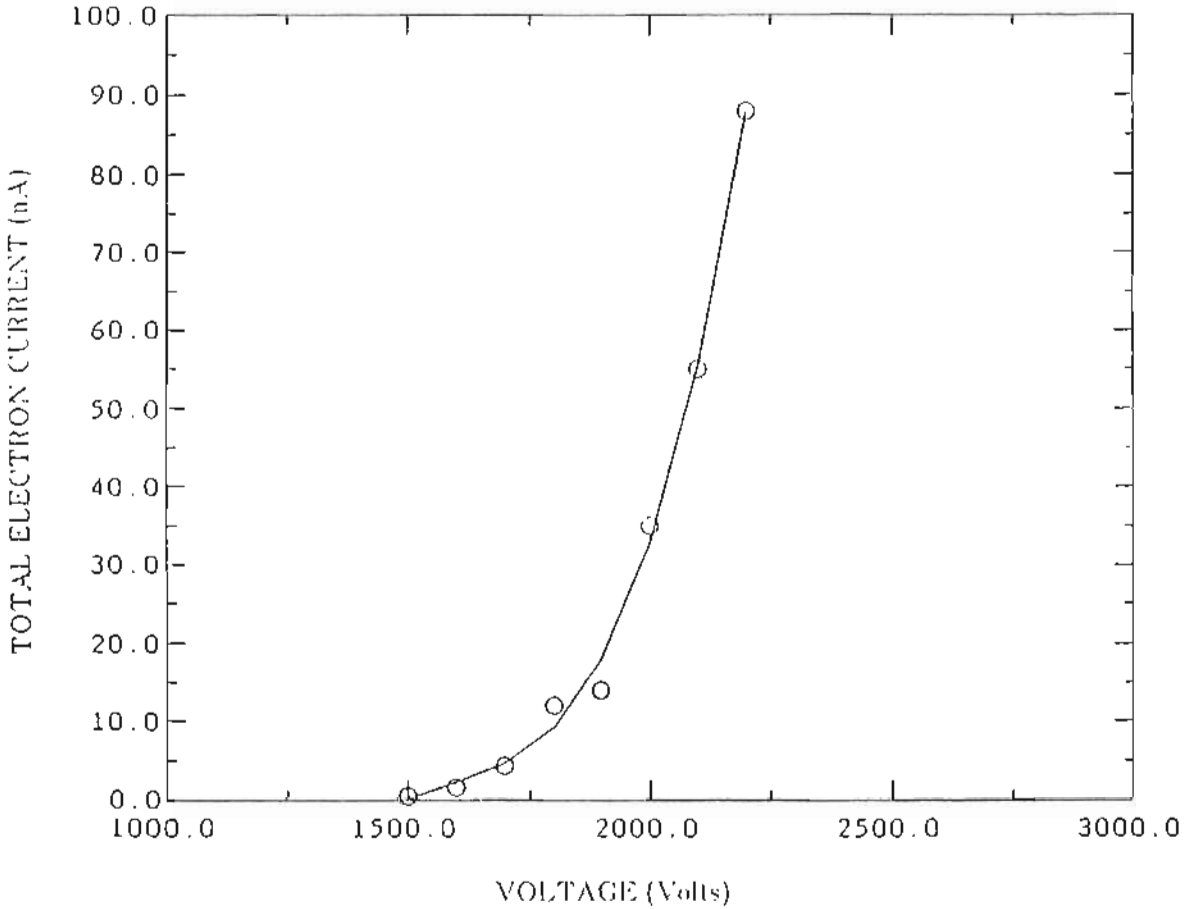

Figure 4.9(b) : Current/voltage plots in the field electron emission mode, for the Ga LMIS whose microchannel plate images are shown in Fig. 4.8.

is below the critical voltage required to form the Taylor cone. We plot in Fig. 4.10, a Fowler Nordheim plot of the field electron emission. The linear relationship again, between $\log_{10}(I/V^2)$ and $(1/V)$ is indicative of the field emission process.

Field emission was also obtained from a small radii needle wetted with In. Figure 4.11a shows a microchannel plate image of the In LMIS operating in the ion mode. Figure 4.11b is the microchannel plate image of the LMIS operating in the classic field electron emission mode as would be expected from such a sharp needle substrate.

When we increase the field electron emission voltage to the critical Taylor voltage, we find that as with Swanson and Schwind[12] this results in the explosive emission process and the evaporation of the cone apex. In the case of smaller radii emitters, this explosive emission also results in the destruction of the underlying substrate. Figure 4.12 shows an SEM profile of an electrochemically etched emitter. After wetting with Ga and operating in the ion emission mode, with a threshold V_t of 3.5 kV, the emitter was operated in the field electron emission mode at a voltage greater than the critical Taylor voltage. The emission was seen to be similar to that observed by Swanson and Schwind[12], and resulted in the destruction of the underlying emitter substrate as is clearly seen in Figure 4.13. We conclude that d.c. electron emission from a field stabilized Taylor cone is simply not possible regardless of the substrate radius.

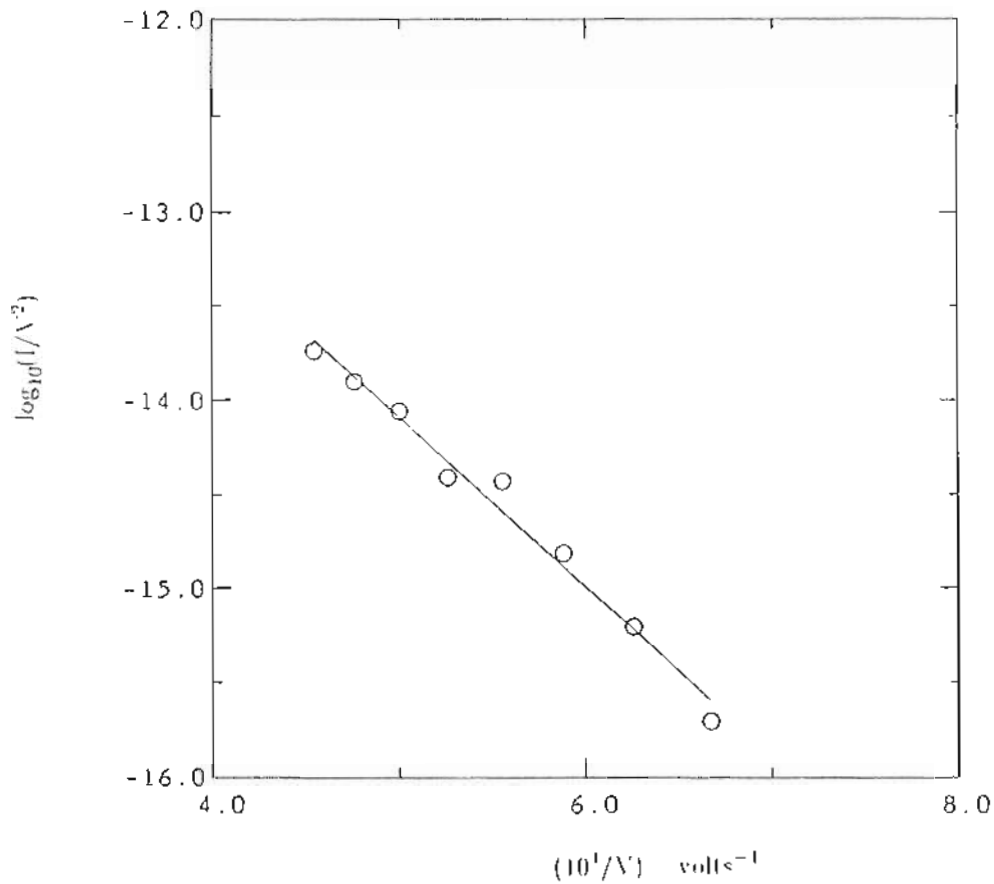

Figure 4.10 : Fowler-Nordheim plot for field electron-emission from the Ga LMIS of Fig. 4.9.

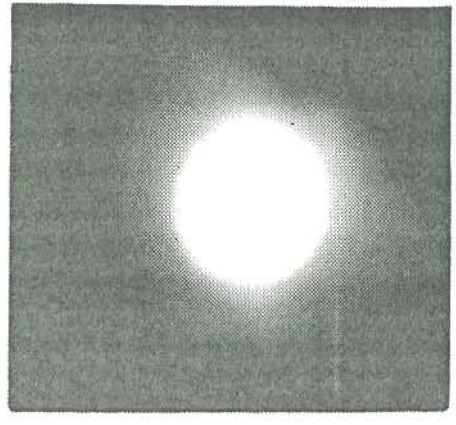

(a)

ION EMISSION
4700 V, 320 nA

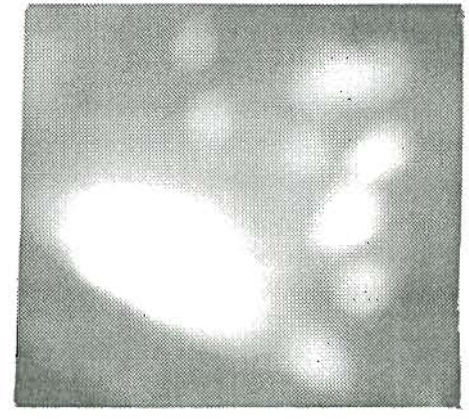

(b)

ELECTRON EMISSION
2500 V, 20 nA

Figure 4.11 : Microchannel plate images of (a) the ion beam pattern and (b) the electron beam pattern, for an indium LMIS.

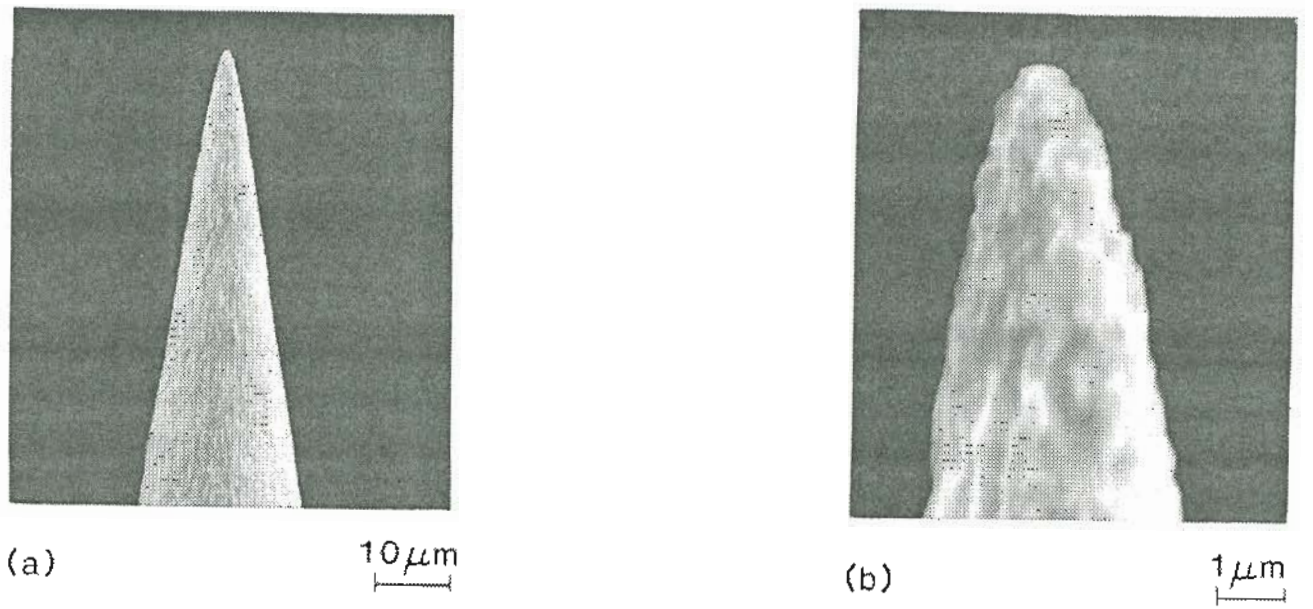

Figure 4.12 : SEM profile of a tungsten needle etched by a d.c. drop-off technique: (a) low magnification showing part of shank and (b) high magnification of the apex region.

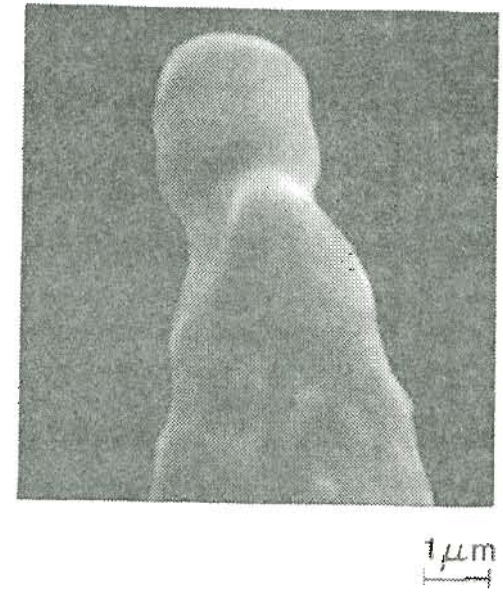

Figure 4.13 : SEM profile of the tungsten needle of Fig. 4.12 after operating in the field electron emission mode above the critical Taylor voltage.

3.2 Taylor Cone Electron Emission: Small Radius Emitters

A prospect for obtaining d.c. electron emission from a LMIS could be by forming a Taylor cone in the ion mode and freezing in the cone shape by quenching the temperature below the liquid's melting point (In, in this case). It may then be possible to carry out a field build-up process with either positive or negative fields at an elevated temperature in ordet to form the proper radius for electron emission.

An applied d.c. electric field on a field emitter at elevated temperatures causes "field build-up" to occur as seen in the early studies carried out by Dyke and coworkers[18]. The motivation for field build-up is the lowering of the thermodynamic chemical potential at the emitter tip which in turn motivates surface migration of the surface atoms towards the higher field regions of the emitter apex. The rate of this process can be given in terms of the rate of change of the emitter radius.

$$\left(\frac{dr}{dt}\right)_F = \left(\frac{dr}{dt}\right)_0 \left(1 - \frac{rF_2}{8\pi\gamma}\right) \tag{4.4}$$

and

$$\left(\frac{dr}{dt}\right)_0 = 1.25\gamma v_a D_0 \alpha \exp\left(-\frac{E_d}{kT}\right) \left(A_0 kTr^3\right)^{-1} \tag{4.5}$$

where

γ = surface tension (γ = 560 dyne/cm for In)

v_a = volume per atom

A_0 = surface area per atom

D_0 = diffusivity constant

E_d = activation energy for surface diffusion

α = emitter cone half angle.

It can be seen that dr/dt varies according to the following conditions:

$$\text{(a)}\ \frac{dr}{dt} > 0 \quad \text{if} \quad F < \left(\frac{8\pi\gamma}{r}\right)^{1/2}$$

$$\text{(b)}\ \frac{dr}{dt} = 0 \quad \text{if} \quad F_0 = \left(\frac{8\pi\gamma}{r_m}\right)^{1/2}$$

$$\text{(c)}\ \frac{dr}{dt} < 0 \quad \text{if} \quad F > \left(\frac{8\pi\gamma}{r}\right)^{1/2}$$

Case (a) leads to emitter dulling and hence to a decrease in emitted current with time. Case (b) ideally causes the emitter dulling due to surface tension forces to be balanced by the electrostatic force opposing the dulling force. This case is difficult to realize over the total emitting area due to the nonuniform field over the emitter surface. Case (c) is of the most interest since when it occurs, it motivates surface migration of surface atoms towards the higher field regions of the emitter apex in a complex process called "field build-up".

The In LMIS from the needle of Fig. 4.2, with a substrate radius of 180 nm was first operated in the ion emission mode with a threshold voltage of 3.5 kV. Figure 4.14 shows a plot of emission current versus applied voltage in the ion mode. That the current was due to emission from a Taylor cone is

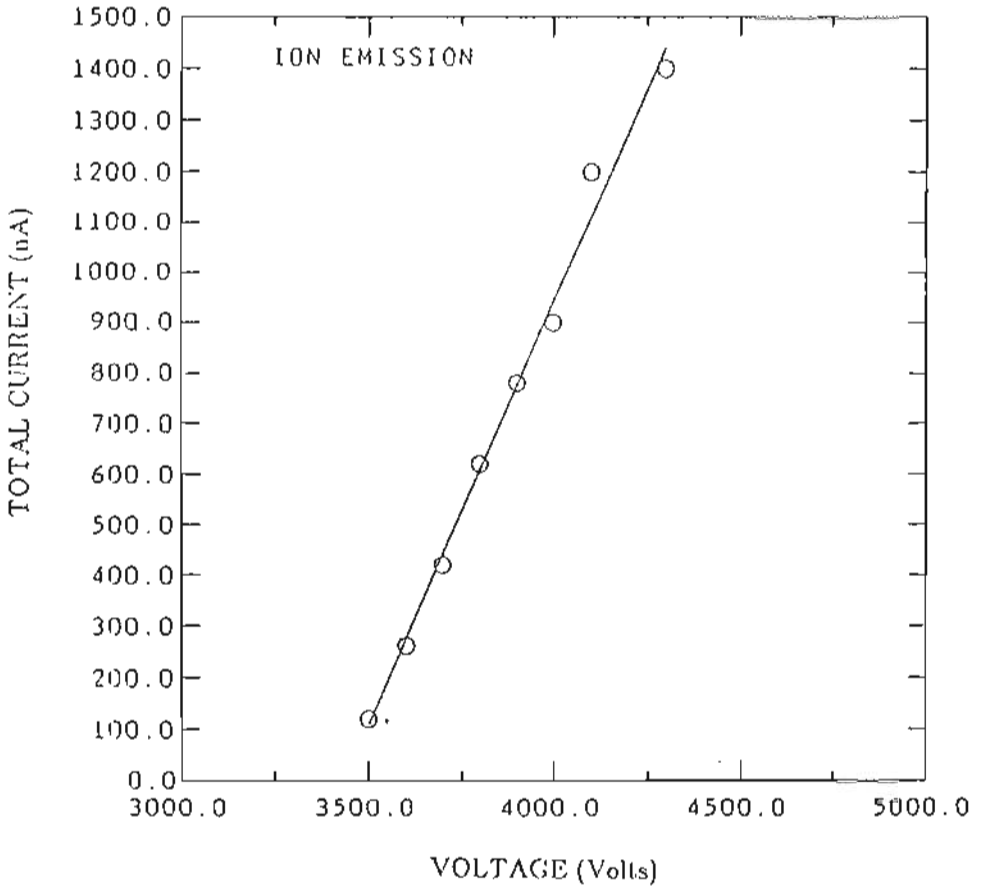

Figure 4.14 : Current/voltage plot for the In LMIS of Fig. 4.2 at an emitter-extractor spacing of ~1.5 mm. Substrate apex radius was 180 nm.

evident from the microchannel plate image shown in Fig. 4.15a. The image is the typical structureless pattern seen in normal LMIS operation. In addition below the threshold voltage, the emission current was characterized by pulses, the frequency of which increased with emission current, finally merging into d.c. at the threshold voltage. This is typical of LMIS behavior. After a stable pattern was obtained (usually at an extraction voltage slightly above threshold), the temperature of the liquid metal was quenched. As the temperature dropped below the liquid's melting point, it began to solidify. As this occurred, the emission current began to drop to zero due, presumably to lack of liquid-bourne replenishment of the metal, field evaporated at the apex of the cone. At this point the electric field to the LMIS was shut off. Leaving the field on though, for any length of time after the emission current begins to drop to zero, would result in field evaporation of the ions from the frozen-in Taylor cone of the LMIS and blunting back from the original sharp point of the cone. Hopefully the result, after quenching the liquid metal and shutting the applied field, is a Taylor cone-like structure frozen into place.

On reversing the polarity of the applied d.c. voltage to the LMIS, it was found possible to obtain normal field electron emission from the frozen-in structure. Figure 4.15b shows a microchannel plate image of the field emission pattern. A central emission spot was observed that overlaped the spot previously occupied by the ion emission, in addition several random emission spots were formed.

At this point the temperature of the now "solid" metal was gradually increased to slightly below the melting point (which in the case for In is 430

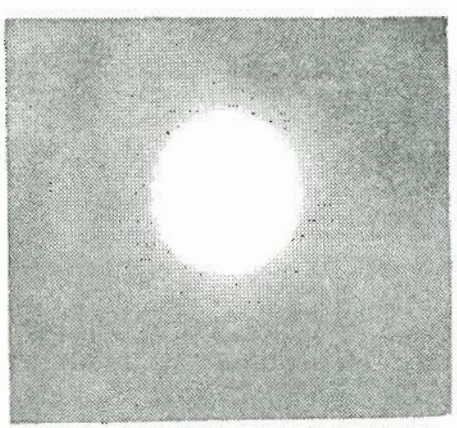

(a)

ION EMISSION
4600 V, 340 nA

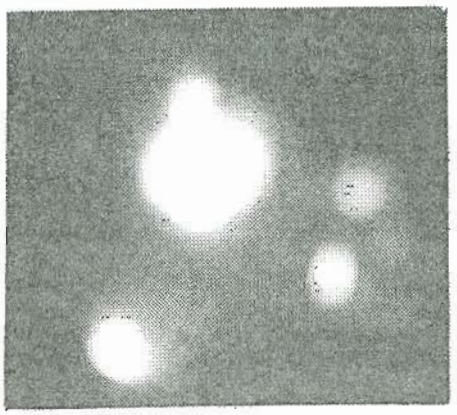

(b)

ELECTRON EMISSION
2090 V, 2 nA

Figure 4.15 : Microchannel plate images of the ion and electron beam patterns from the Fig. 4.2 In LMIS. (a) ion emission pattern (b) field electron emission after freezing in the Taylor cone of the LMIS, without doing a field build-up process.

K), in the presence of the applied negative field. Figure 4.16 shows the variation of the electron emission current with time during this process of heating in the presence of the applied field (i.e. a field build-up process). Within a few minutes ($\sim$3 to 4) there resulted a radical change in the emission pattern distribution with almost all the spurious emission spots disappearing leaving only the central field emission pattern. The emission current rapidly increased to the final value shown in the Fig. 4.16. Figures 4.17a and 4.17b are the microchannel plate images of the field emission pattern at the points marked in Fig. 4.16.

With the smaller radii emitters ($<$ 100 nm), it is possible to obtain the final single spot endform, by quenching the temperature and freezing in the Taylor cone without having to perform the field build-up process. Where the electron emission pattern displays random emission spots in addition to a single spot, if then, the emitter is subjected to the field build-up process, field, the random emission spots disappear to give rise to the single spot emission pattern.

To be sure beyond reasonable doubt, that the electron emission was occurring from the previously frozen-in Taylor cone structure, the In emitter of Fig. 4.2 was operated in the electron emission mode without first freezing in the Taylor cone in the ion mode. Figure 4.11 (earlier) shows the microchannel plate images of the ion and electron emission for this case. The electron emission pattern in this case, never converged to the single spot emission shown previously even on heating the emitter in the presence of an applied field. It was necessary to go back to the ion emission mode and freeze in the

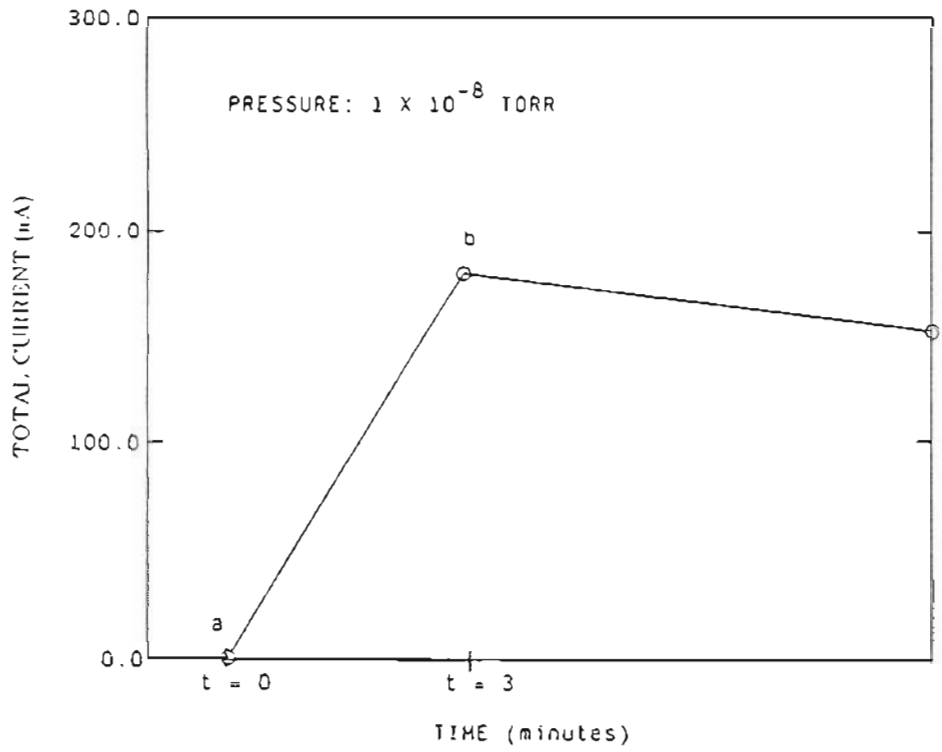

Figure 4.16 : Current versus time plot during the field build-up process for the In LMIS of Fig. 4.2. The applied negative voltage during the entire process was 2090 V. The emitter was heated during the time, t = 0 to t = 2. (a) and (b) are points at which photographs were taken.

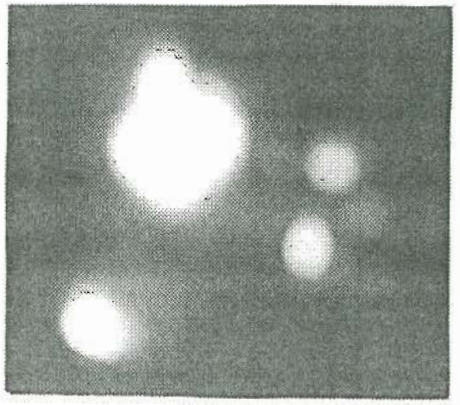

(a)

ELECTRON EMISSION
2090 V, 2 nA

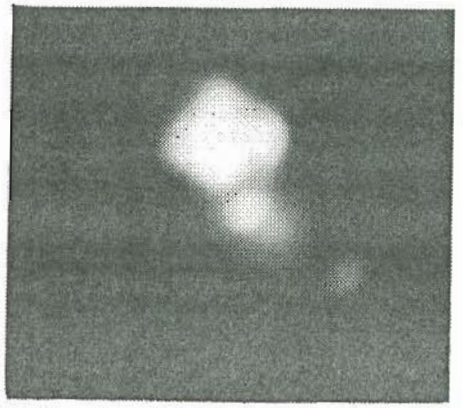

(b)

ELECTRON EMISSION
2090 V, 180 nA

Figure 4.17 : Microchannel plate images of the electron beam pattern at the points (a) and (b), indicated in Fig. 4.16.

Taylor cone again, to achieve the desired electron emission pattern. It was also seen that if, after achieving the desired electron emission pattern, the temperature of the emitter was increased to above the melting point of the metal, the emission pattern disappeared. This was interpreted to mean that the frozen-in Taylor cone structure had melted away. Figure 4.18 shows the sequence of emission patterns, of the ion emission, the electron emission after freezing in the Taylor cone and the electron emission on heating the emitter to a temperature above the melting point of indium, for a emitter with a substrate radius of about 1 μm.

In Fig. 4.19 we show the entire sequence of emission patterns (micro-channel plate images) for the In LMIS of Fig. 4.2, the ion emission, freezing into place the Taylor cone in the ion emission mode and field "electron" emission from the frozen in cone structure, and the process of heating the emitter in the presence of the applied field for the In LMIS. The circular emission pattern from the Taylor cone during ion emission is clearly shown in photo (a). Upon freezing in the Taylor cone and application of voltage of 2090 V to extract electrons at T = 300 K at a total emission current of 2 nA, the pattern, shown in photo (b) is seen to comprise of a central, some-what tetragonal structure with a couple of random emission spots around and below it. Going up in extraction voltage to 2290 V and an emission current of 5.8 nA, the central pattern is seen to have become brighter but with an increase in the random emission spots (see photo c). Upon increasing the extraction voltage to 2300 V and an emission current of 10 nA, and heating the emitter to a temperature slightly below T = 430 K for $\sim$1 minute

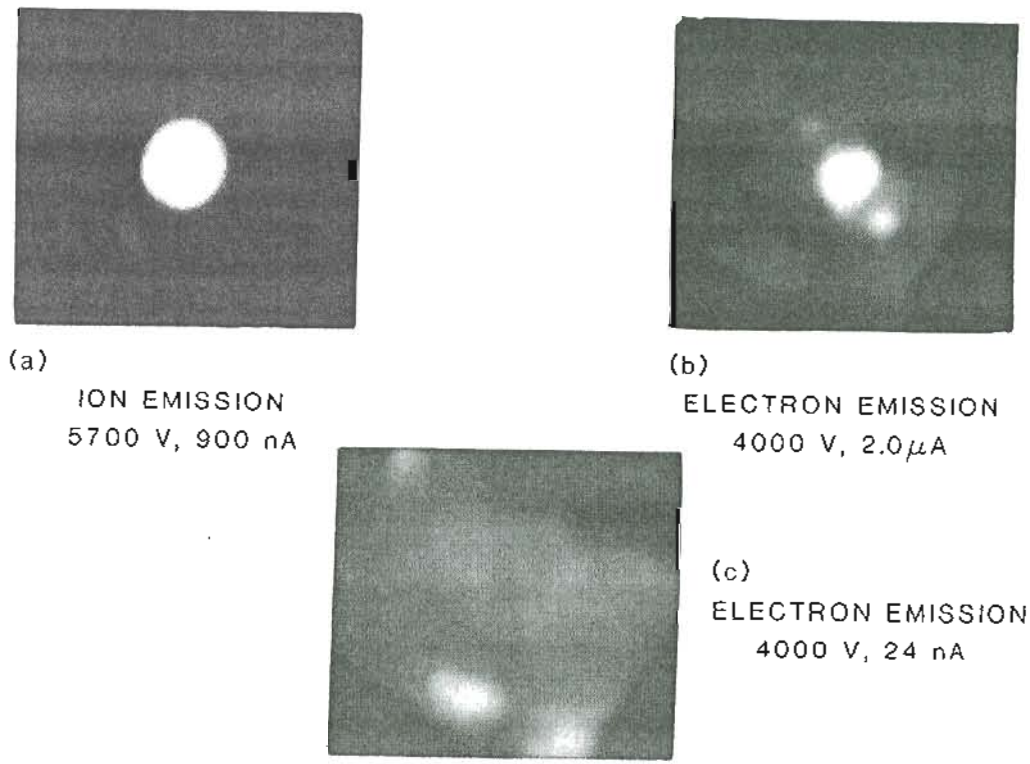

Figure 4.18 : Microchannel plate images of (a) the ion beam pattern (b) the electron beam pattern on freezing in the Taylor cone and (c) the electron emission pattern on later heating the emitter to a temperature greater than the melting point of the In liquid metal. The emitter radius was 1 μm.

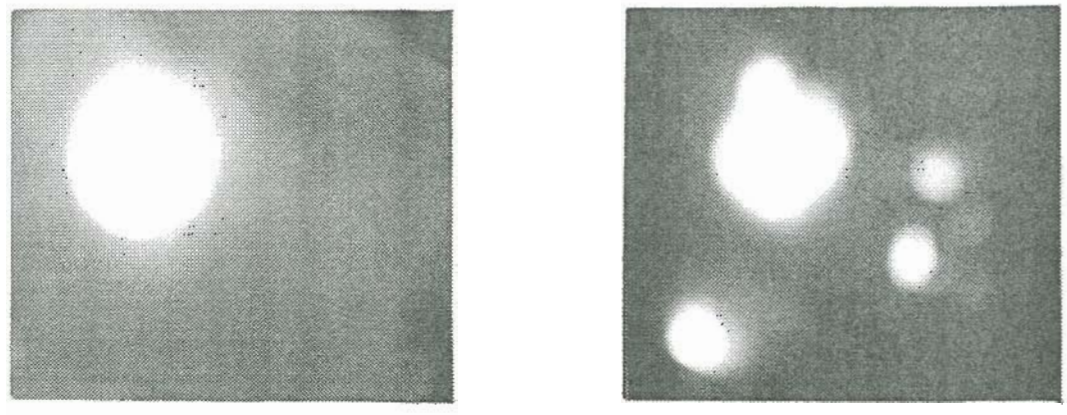

(a)

ION EMISSION
4000 V, 340 nA

(b)

ELECTRON EMISSION
2090 V, 2 nA

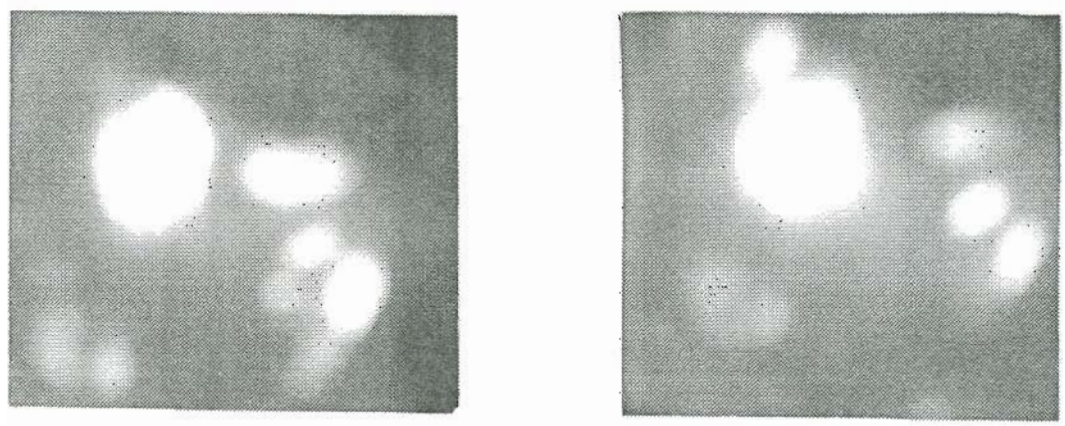

(c)

ELECTRON EMISSION
2290 V, 5.8 nA

(d)

ELECTRON EMISSION
2300 V, 10 nA

Figure 4.19(a-d) : Sequence of ion and field electron patterns after freezing in and subsequent field build-up of the In LMIS of Fig. 4.2 (a) ion emission pattern (b),(c) field electron emission patterns after freezing in the Taylor cone (d) field electron emission patterns during the field build-up process.

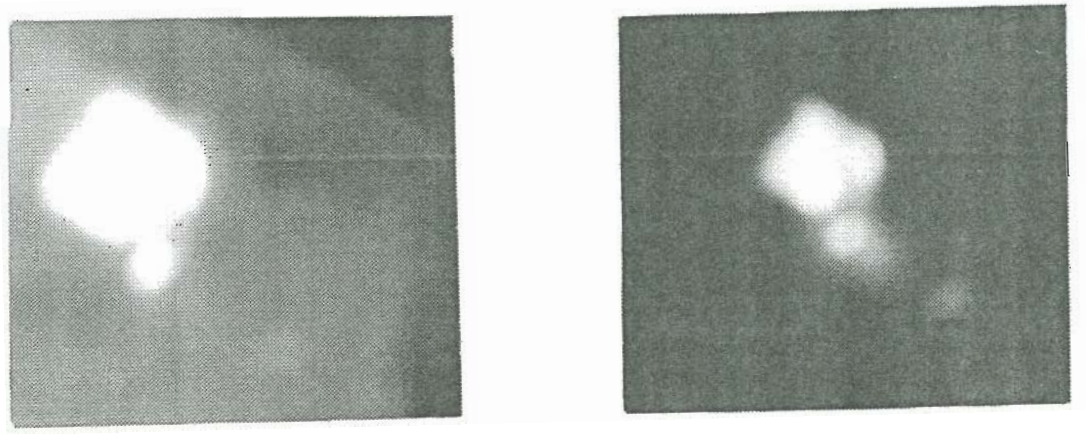

(e)
ELECTRON EMISSION
1800 V, 26 nA

(f)
ELECTRON EMISSION
2090 V, 180 nA

Figure 4.19(e,f) : Field electron emission patterns after the field build-up process (continuation of the process from Fig. 4.19d).

results in the central pattern becoming brighter and a few of the random emission spots disappearing, and is clearly shown in photo (d). Finally, after a few minutes of heating, the final bright emission spot shown in photo (e) is obtained. The extraction voltage was lowered in photo (e) to 1800 V at an emission current of 26 nA. Increasing the extraction voltage to 2090 V yields an emission current of 180 nA and the emission pattern seen in photo (f). This pattern sequence was reversible and reproducible.

Figure 4.20 shows the SEM profile of a tungsten emitter with an apex radius of about 1 μm, the emission patterns of which are shown in Fig. 4.21. Photo (a) shows the ion emission pattern at an extraction voltage of 5700 V and an ion emission current of 900 nA. Photos (b), (c), and (d) show the electron emission patterns at electron emission currents of 300 nA, 2.0 μA, and 3.5 μA. The extraction voltages for the patterns were respectively 3000 V, 4000 V, and 5000 V. It is interesting to note that even when the ion emission from the LMIS was off-axis and not confined to the center of the screen the electron emission pattern tended to overlap the ion emission pattern and is clearly shown in photos (a), (b) and (c) in Fig. 4.22.

Figure 4.23 shows SEM micrographs of the emitter of Fig. 4.20 after freezing in the Taylor cone and operating for several hours in the electron emission mode. The micrographs clearly show what appears to be a frozen in structure on the apex of the underlying emitter. The departure from a true Taylor cone shape could possibly be due to the field build-up process during the formation of the proper radius for the highly confined electron emission.

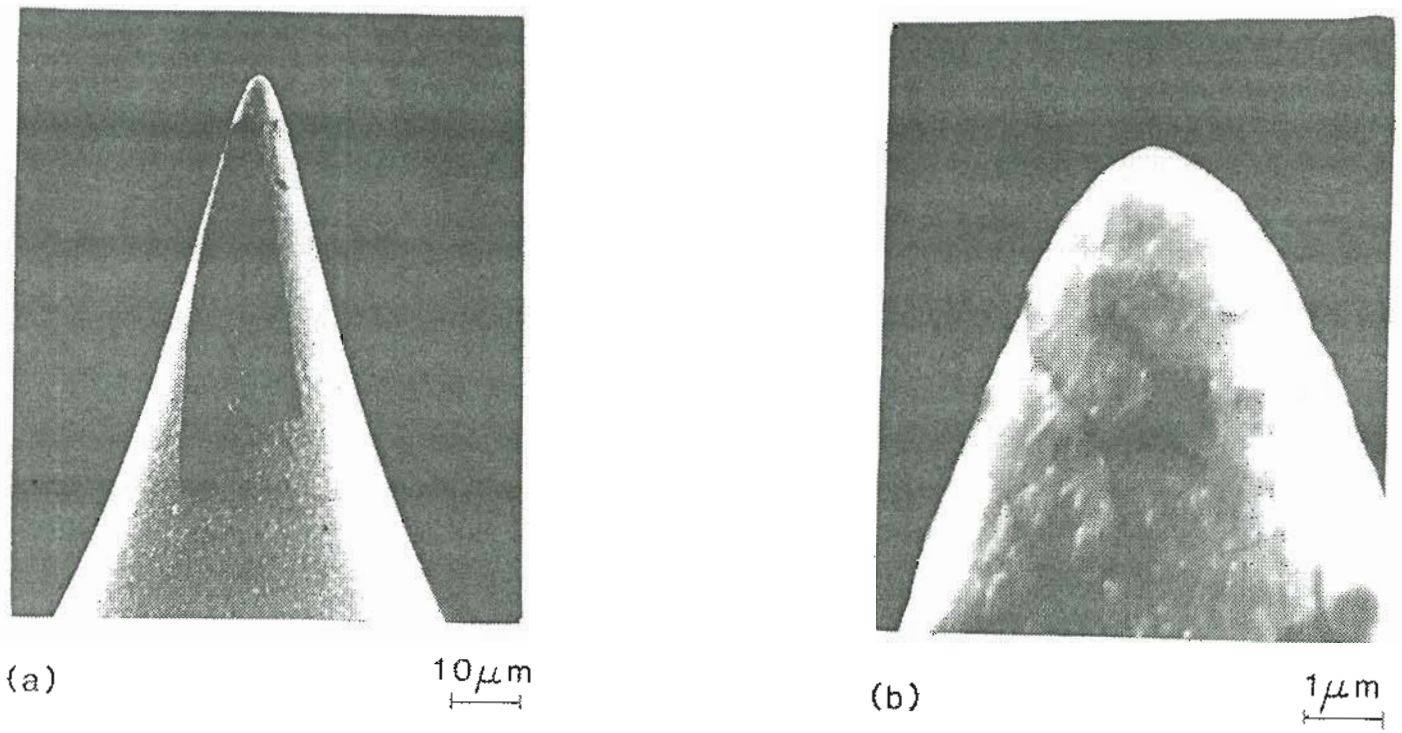

Figure 4.20 : SEM profile of a 1 μm radius tungsten needle etched by a d.c. drop-off technique: (a) low magnification showing part of shank and (b) high magnification of the apex region.

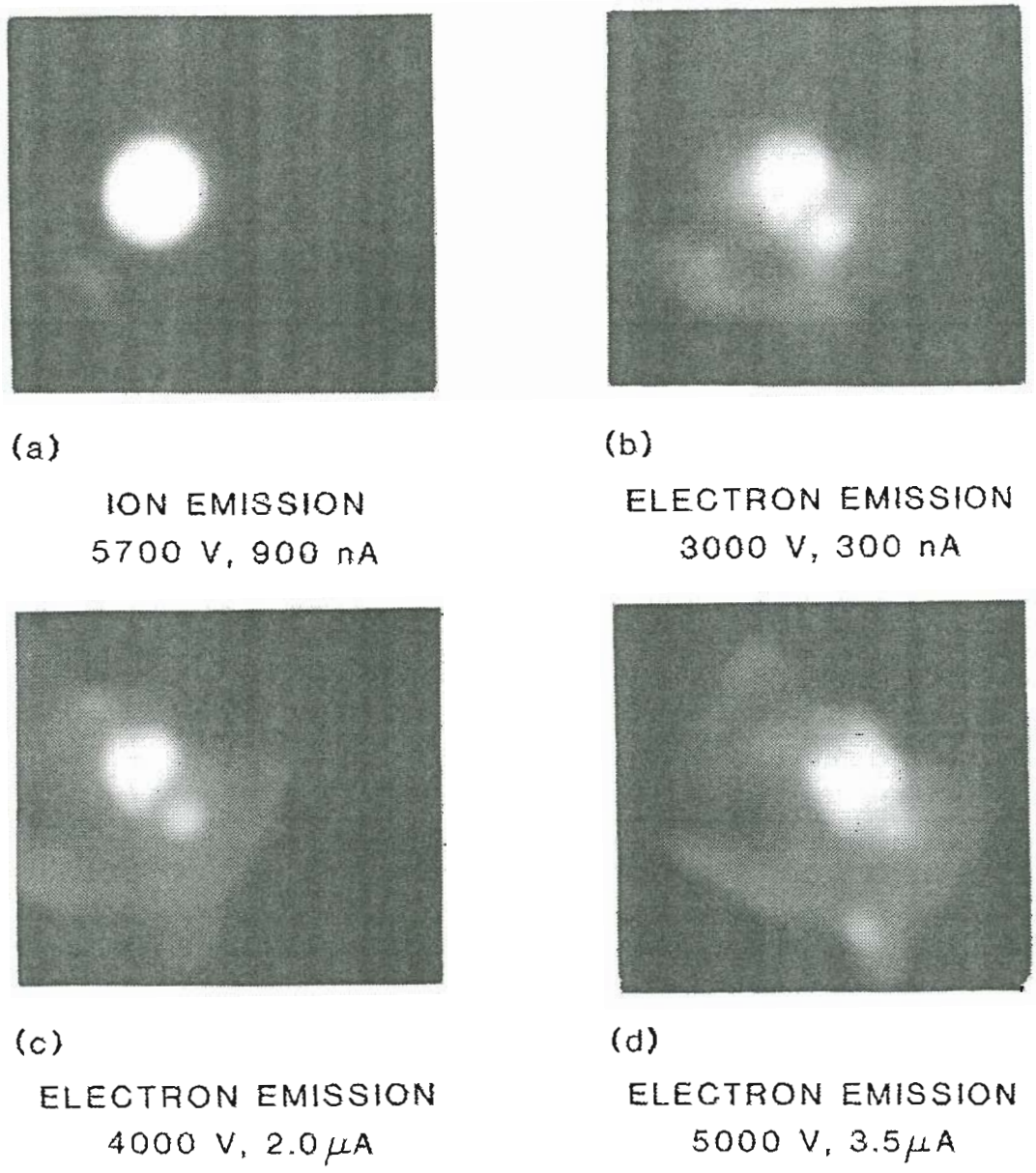

Figure 4.21 : Sequence of ion and field electron patterns after field build-up of the In LMIS of Fig. 4.20 (a) ion emission pattern (b),(c),(d) field electron emission patterns.

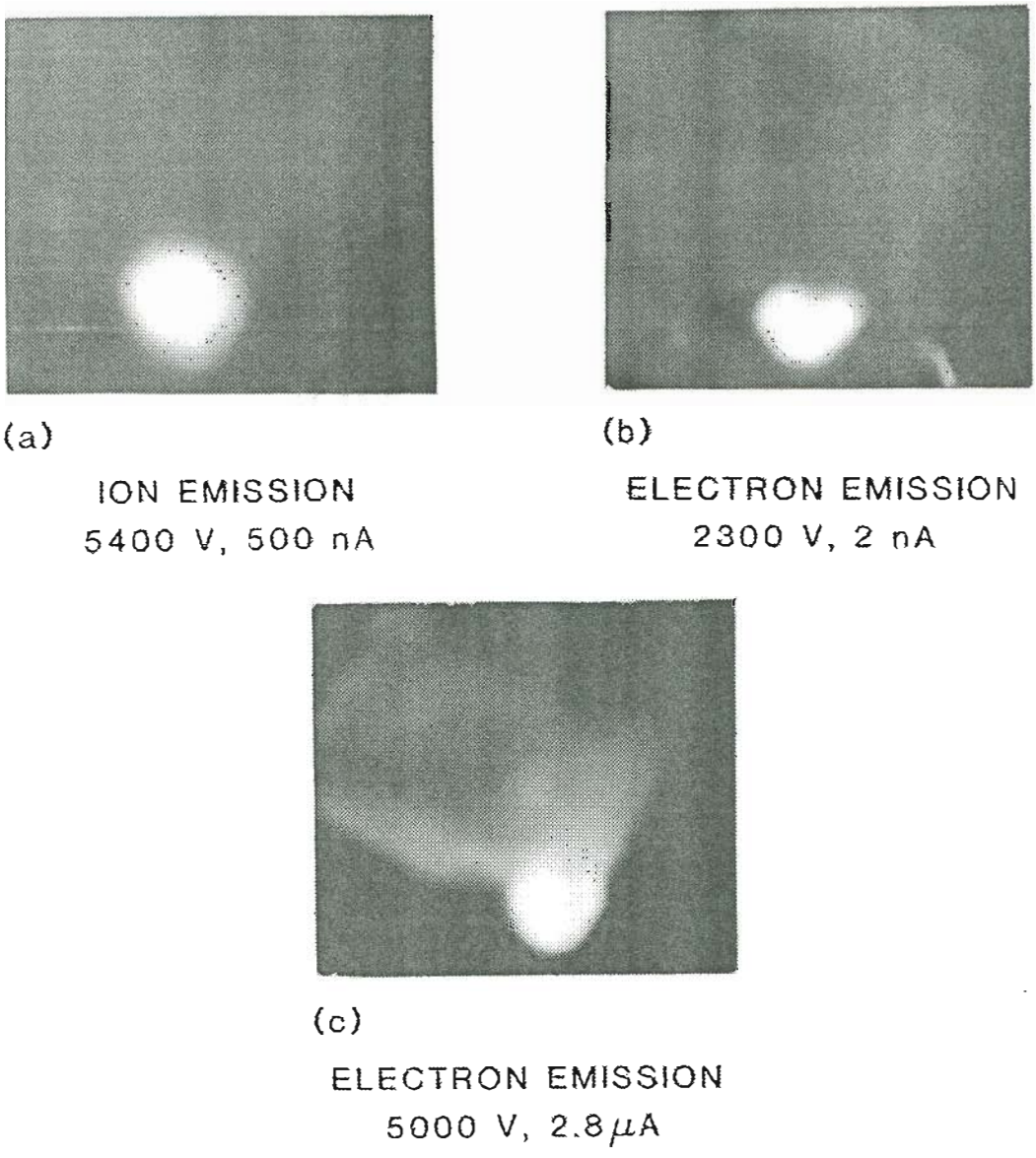

Figure 4.22 : Sequence of ion and field electron patterns after field build-up of an In LMIS where the ion emission was off-axis (a) ion emission pattern (b),(c) field electron emission patterns.

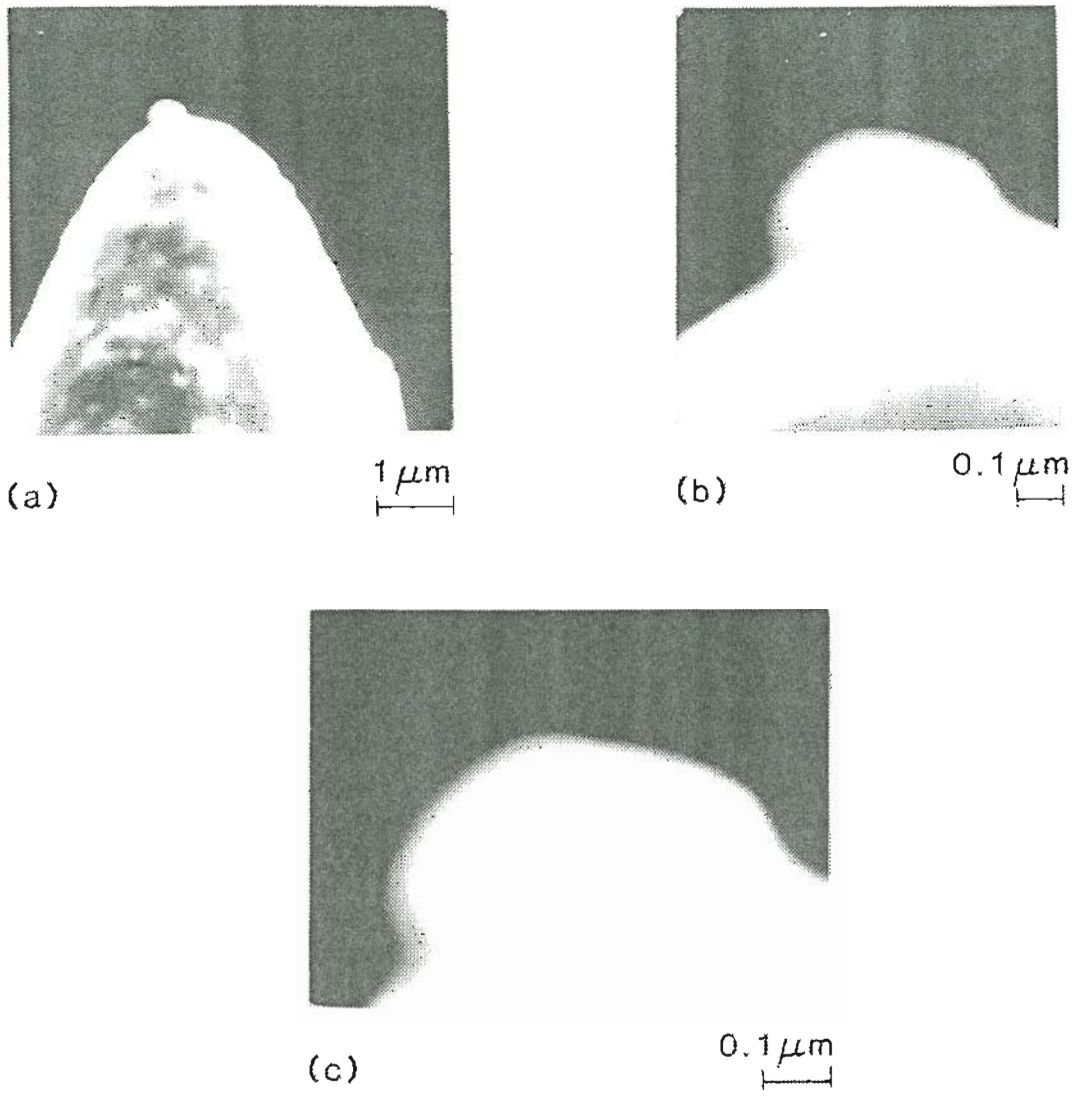

Figure 4.23 : SEM micrographs of the emitter of Fig. 4.20 after field build-up and operation as an electron emitter for several hours (a) at a magnification of 10,000X showing part of shank and (b) at a magnification of 55,000X and (c) at a magnification of 90,000X.

In order to further characterize this electron source we evaluated the emitting area for the In LMIS of Fig. 4.20 using a Fowler Nordheim plot and is discussed below.

If we consider a field electron-emission model based on the Fowler-Nordheim equation[19], we have the current density J given by

$$J = (1.54\times10^{-6}F^2/\phi)\exp(10.4/\phi) \times [\exp(-6.44\times10^{7}\phi^{3/2}/F)] \quad A/cm^2 \tag{4.6}$$

where J is in A/cm^2 when F is in V/cm, and the work function ϕ is in eV. The total current is then given by

$$I = J\,A \tag{4.7}$$

where A is the effective emitting area. Combining Eqs. (4.6) and (4.7) one obtains the total current as a function of area and work function.

$$I = (1.54\times10^{-6}A\beta^2V^2/\phi)\exp(10.4/\phi) \times [\exp(-6.44\times10^{7}\phi^{3/2}/\beta V)] \tag{4.8}$$

where $F = \beta V$. Equation (4.8) can then be written as

$$I/V^2 = (1.54\times10^{-6}A\beta^2/\phi)\exp(10.4/\phi) \times [\exp(-6.44\times10^{7}\phi^{3/2}/\beta V)] \tag{4.9}$$

Taking the logarithm of both sides, we obtain what is generally known as the Fowler-Nordheim equation

$$\log_{10}(I/V^2) = \log_{10}\left\{(1.54\times 10^{-6}A\beta^2/\phi)\exp(10.4/\phi)\right\} - \left\{\frac{6.44\times 10^7\phi^{3/2}}{\beta V}\times\log_{10}e\right\} \qquad (4.10)$$

where the first term on the left side is the Intercept in the $\log_{10}(I/V^2)$ vs $(1/V)$ plot, and the second term represents the slope in that plot. A Fowler-Nordheim plot of the field "electron emission" for the emitter of Fig. 4.20, with a correction applied for the protective resistance of 500 MΩ, is shown in Fig. 4.24. The linear relationship between $\log_{10}(I/V^2)$ and $(1/V)$ quite evident in the plot, is indicative of a field emission process. From the slope of the Fowler-Nordheim plot which is measured to be $m = -1.3534\times 10^4$ we obtain a value of the field factor $\beta = 1.71561\times 10^4$ cm^{-1}, and from the intercept which is measured to be -9.404, we estimate the effective emitting area to be of the order of 2.82×10^{-13} cm^2.

From the value of the emitting area, A, one can determine a value for the radius of the emitting structure, (obtained after the field build-up process) by using the equation

$$A = 2\pi r^2(1-\mathrm{Cos}\theta) \qquad (4.11)$$

where θ is related to the emission half angle α by the relation

$$\alpha = m\theta \qquad (4.12)$$

where m is the angular magnification and is usually taken to be equal to 0.5.

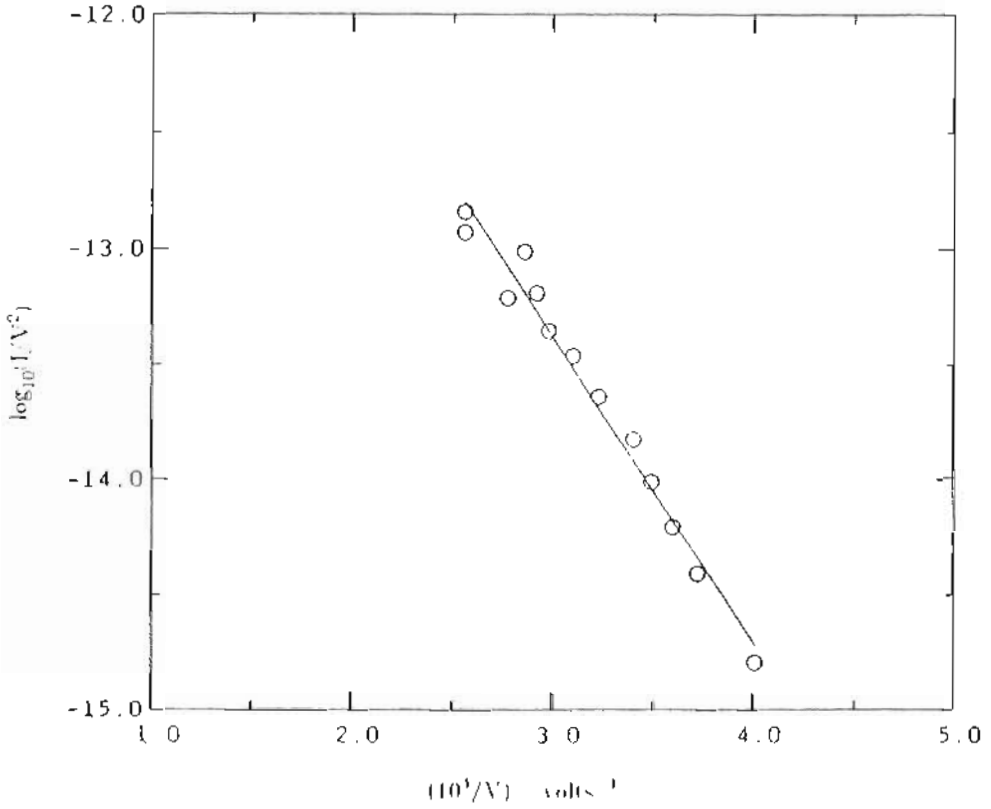

Figure 4.24 : Fowler-Nordheim plot for field electron-emission from the In LMIS of Fig. 4.20.

The emission half angle for the electron emission patterns after the field build-up process was measured to be 4.5°. Then, from Eqs. (4.11) and (4.12) and using the value of A obtained earlier from the Fowler-Nordheim plot, we get a value for the emitting radius to be 1.91×10^{-6} cm.

3.3 Taylor Cone Electron Emission: Large Radius Emitter

The process of freezing in the Taylor cone by quenching the temperature of the liquid metal and subsequent field build-up process was repeated, but with a positive field, for a much larger radius emitter (2 μm), the SEM profile of which is shown in Fig. 4.25. After wetting with indium, the LMIS was put in the field ion microscope chamber (Fig. 4.3). After operating in the ion emission mode, the Taylor cone was frozen in by quenching the temperature of the liquid metal. Rather than do a field build-up process with an applied negative field, it was decided to use a positive field slightly higher than the threshold for ion emission while heating the emitter to a temperature $\sim 1/3$ of its melting point. This was done because it was seen that unlike for the previous "smaller radii" emitters, the desired result, i.e. electron emission from preferably a single spot could not be achieved within a reasonable amount of time, by doing the field build-up process with a negative field. Increasing this field to a higher value to achieve the desired result was fraught with the possibility that this would result in an excessively high current density and the destruction of the emitter. Hence it was decided to heat the emitter in the ion mode but with the temperature low enough to prevent melting of the metal and hence ion emission. This was done for ~ 5

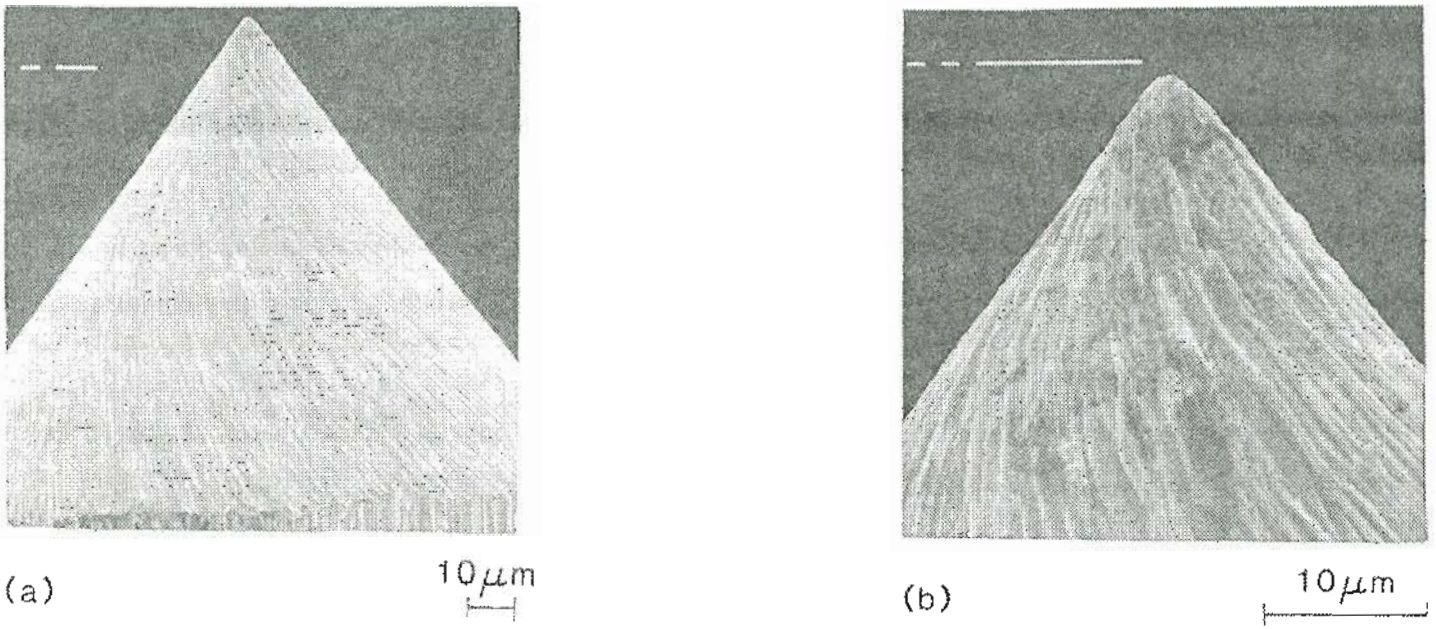

Figure 4.25 : SEM profile of a 2 μm radius tungsten needle (a) low magnification showing part of shank and (b) high magnification of the apex region.

minutes at 7100 volts. Figure 4.26 shows the variation in the electron emission current with time at the beginning and end of the field build-up process with a positive field. The data points were obtained at a field electron emission voltage of 3400 volts before and after completion of the field build-up process. At the end of the field build-up process the electron emission current was seen to have increased to its final value shown in Fig. 4.26. The electron emission pattern finally obtained is shown in photo (a) of Fig. 4.27. Photos (b) and (c) show the emission patterns at total electron currents of 450 and 550 nA respectively.

Angular intensities for emission currents in the electron mode in the range 0.6 nA to 700 nA were obtained for the emitter of Fig. 4.25 and are plotted in Fig. 4.28.

A Fowler Nordheim plot of the field electron emission from the emitter of Fig. 4.25 is given in Fig. 4.29. From the slope of the Fowler Nordheim plot which is measured to be $m = -1.19916 \times 10^4$ we obtain a value of the field factor $\beta = 1.93627 \times 10^4$ cm^{-1} and from the intercept which is measured to be -8.8, we estimate the effective emitting area from the Fowler Nordheim equation to be of the order of 8.90643×10^{-13} cm^2.

Using Eqs. (4.11) and (4.12) and the value of the emitting area from the Fowler Nordheim equation and again calculating a value for the radius of the emitting structure, we obtain 3.4×10^{-6} cm.

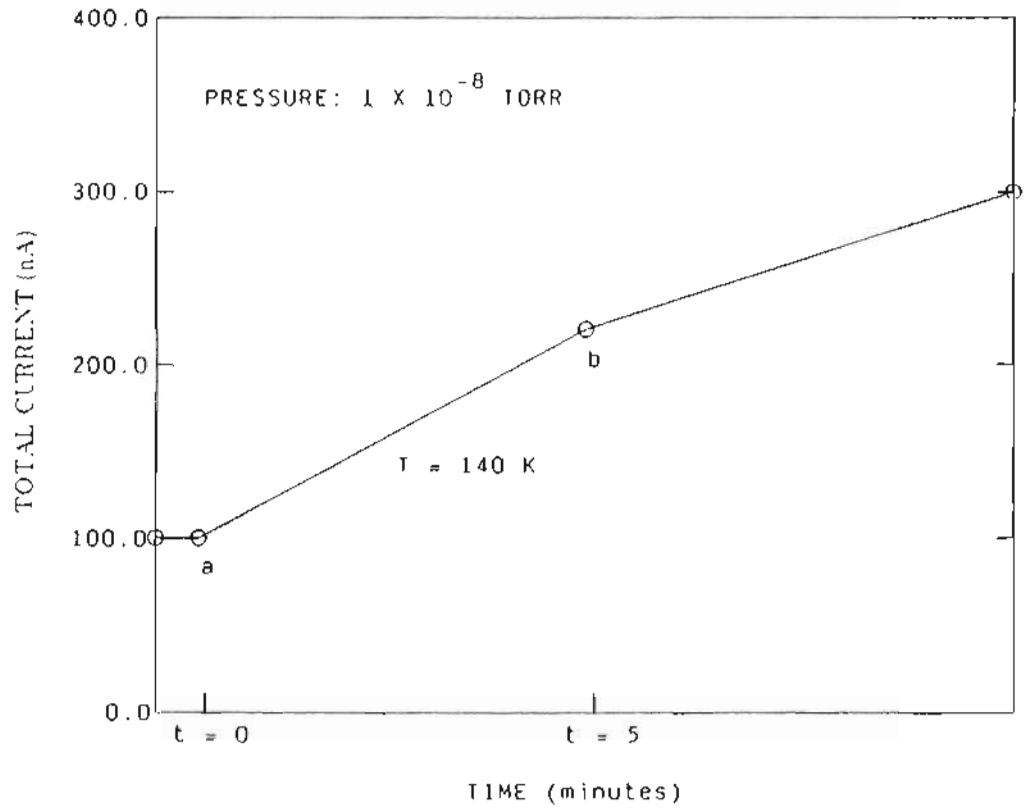

Figure 4.26 : Electron current at various times during the process of field build-up of the In LMIS of Fig. 4.25 with a positive field. The field build-up voltage during the entire process was 7100 V. The electron emission data points were taken at an electron voltage of 3400 V after cooling the emitter to 300 K.

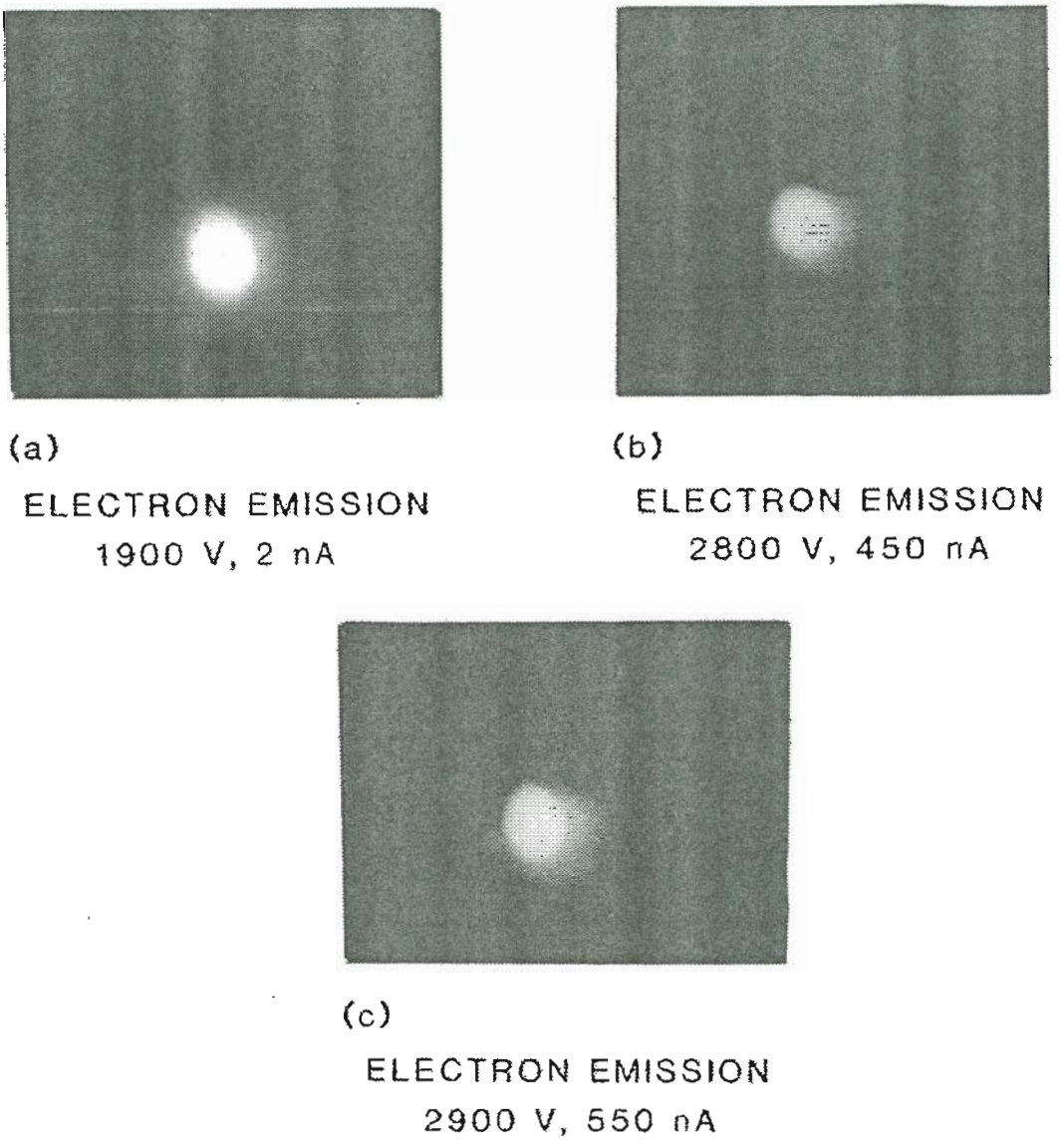

Figure 4.27 : Field electron patterns at various electron voltages after field build-up of the In LMIS of Fig. 4.25.

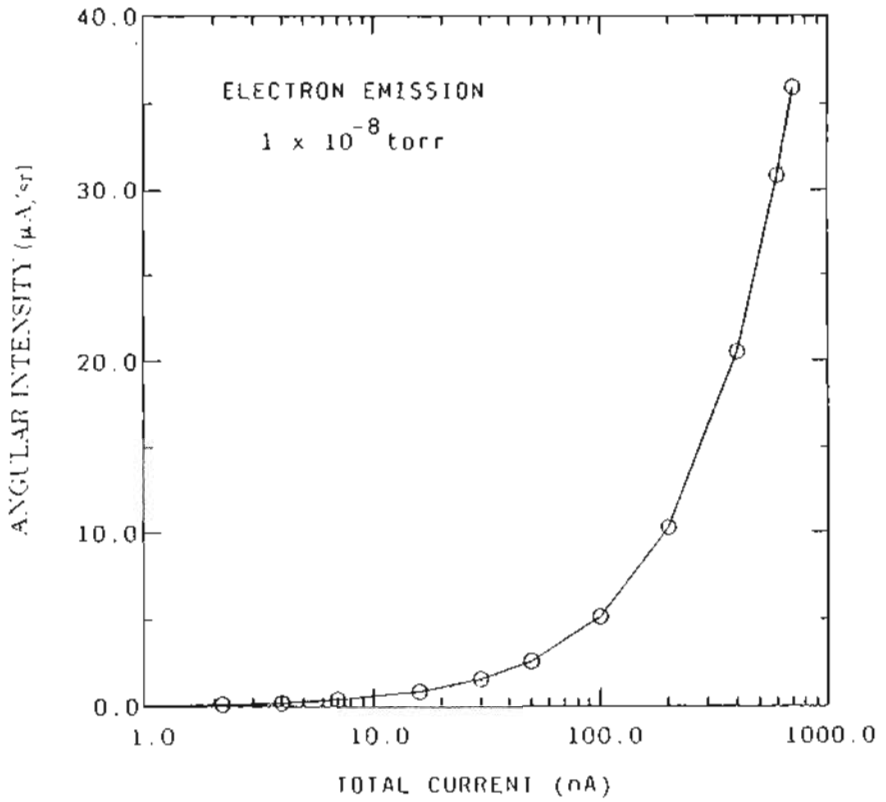

Figure 4.28 : Angular intensity as a function of total field electron current for the In LMIS of Fig. 4.25.

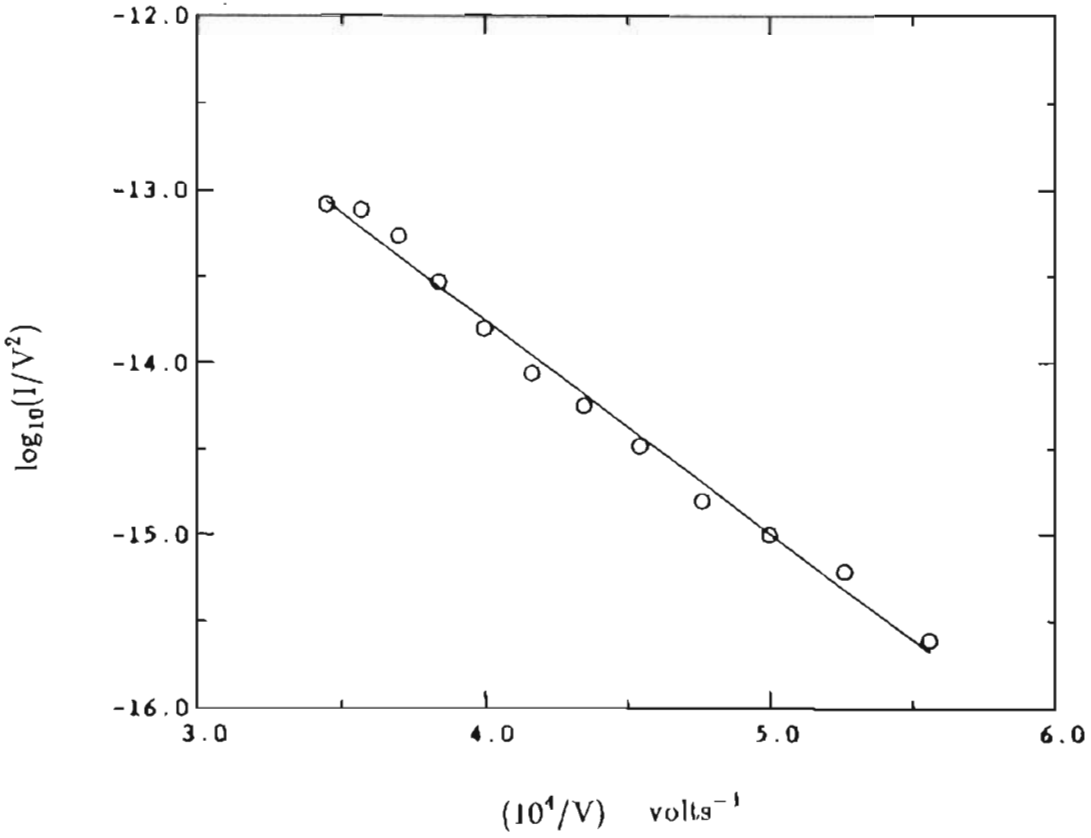

Figure 4.29 : Fowler-Nordheim plot for field electron-emission from the In LMIS of Fig. 4.25.

4. Summary

This study showed that it was possible to obtain d.c. electron emission from an LMIS either from the solid substrate covered with a layer of the liquid metal or by freezing in the Taylor cone shape and doing a thermal/field process to obtain a highly confined beam.

The electron emission from the solid needle was classic field emission from a small radii emitter and not from a field stabilized Taylor cone. Increasing the field electron voltage to the critical Taylor voltage resulted in a pulsed explosive emission process. For these small radii emitters it also resulted in the destruction of the underlying emitter substrate.

It was also found possible to obtain d.c. electron emission by freezing in the Taylor cone shape of the LMIS while operating in the ion mode and then doing a field build-up process on the frozen in structure at elevated temperatures. The electron angular emission distribution was highly confined and overlapped the ion emission distribution. The optimum substrate radius for easy field build-up and for obtaining on axis emission was 0.5 to 1.0 μm. The frozen-in Taylor cone electron emission could be easily restored after elimination of the Taylor cone by melting. The electron emission areas deduced were of the order of 10^{-13} cm^2 and the emission believed to arise from the same geometrical area as the ion emission.

B. EVALUATING SPACINGS IN THE LMIS-STM EMBODIMENT

1. Introduction

The object of this study was to develop a means for obtaining the separations between the LMIS and the target for the proximity focused LMIS. Two models were evaluated, with the aim towards establishing a relation between the field electron emission voltage from the LMIS and the emitter-target spacings. The values obtained for the emitter-target spacings from these models could also serve as a check on the emitter-target spacings obtained using the magnetically driven micropositioner and piezoceramic combination (see Chapter 3.2).

The first model, based on the work of A. M. Russell, Russell Young and others[5,20], establishes a relation between the emitter voltage for electron emission from a field emitter, the emitter-substrate spacing, and the emitter radius by solving Laplace's equation in the prolate spheroidal coordinate system. Russell Young used this model to evaluate emitter-target spacings in his work on the topographiner[5]. We have used this model in a similar attempt, to evaluate its usefulness in the proximity focused LMIS system.

The second model, uses a conical tip geometry to establish a relation between the emitter voltage for electron emission and the emitter-substrate separation by solving Laplace's equation in a polar coordinate system using Legendre polynomials.

We first of all develop the mathematical relationships between the electron emission voltage, the emitter radius and the emitter-target separations

for the two models and then see how well the mathematical predictions from these models correspond to experimental data.

2. Prolate Spheroidal Model (Model 1)

The idea of using field electron emission as a means of determining the emitter-substrate separation during operation at close spacings in the scanning tunneling microscope was attempted earlier by Young et al.[5], in their work on the topographiner based on earlier work by A. M. Russell[20] on electron trajectories in a field emission microscope. There they used the solution of Laplace's equation to determine a relationship between the emitter voltage, emitter-substrate spacing and the emitter radius. The emitter was assumed to be a hyperboloid and the prolate spheroidal coordinate system was used to obtain solutions of Laplace's equation. The appropriate diagram for the present calculation is shown in Fig. 4.30 (reproduced from Young et al[5].) where lines of constant ξ are the electric field lines, surfaces of constant η are equipotential surfaces, η_e is the equipotential corresponding to the emitter surface, and $\eta = 0$ is the flat anode surface. The potential then, in this coordinate system[5, 20], is:

$$V(\eta) = \frac{V_e}{\ln\left(\frac{1+\eta_e}{1-\eta_e}\right)} \ln\left(\frac{1+\eta}{1-\eta}\right) \qquad (4.13)$$

where V_e is the potential applied between the emitter and the substrate for field electron emission. The relationship between the emitter radius ρ at the

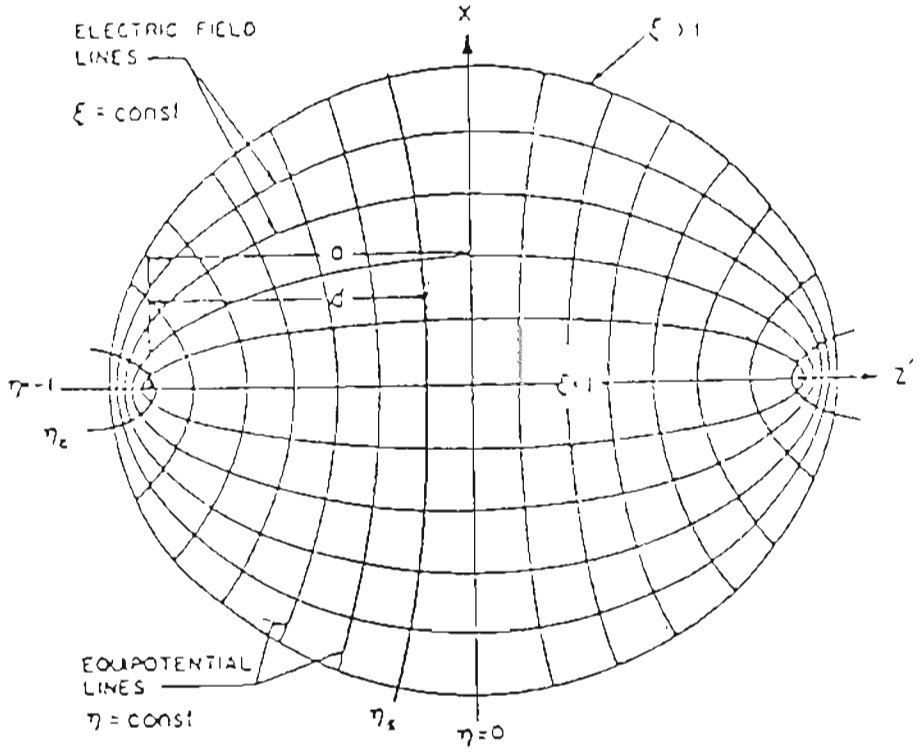

Figure 4.30 : Prolate spheroidal coordinate system. η_e is the equipotential contour corresponding to the emitter surface, $\eta = 0$ corresponds to the specimen or anode.

apex, and a, the distance between the focus of the hyperboloid and the origin ($\eta = 0$) in cartesian coordinates, and η_e is given by:

$$\rho = -\frac{a}{\eta_e}\,(1-\eta_e{}^2) \tag{4.14}$$

Solving for η_e in terms of ρ and a, we get

$$\eta_e = \frac{\frac{\rho}{a} \pm \left\{\frac{\rho}{a}+4\right\}^{1/2}}{2} \tag{4.15}$$

The field at the apex, is:

$$E = \frac{2V_e}{a\,\ln\left(\frac{1+\eta_e}{1-\eta_e}\right)}\;\frac{1}{1-\eta_e{}^2} \equiv E_0 \tag{4.16}$$

Rewriting Eq. (4.16), we get the following relationship between the emitter voltage and the emitter-target spacing:

$$V_e = \frac{aE_0}{2}\,[1-\eta_e{}^2]\;\ln\left(\frac{1+\eta_e}{1-\eta_e}\right) \tag{4.17}$$

where we consider only the negative root of Eq. (4.15) in Eq. (4.17).

3. Polar Model (Model 2)

In addition to solving Laplace's equation in prolate spheroidal coordinates, it can be solved in polar coordinates. Solutions of Laplace's equation for conical conductors would then take the form[17,21]

$$V = V_0 + \sum_{i=0}^{\infty} P_{\nu_i}(\mathrm{Cos}\theta)\left(A_{\nu_i} r^{\nu_i} + B_{\nu_i} r^{-\nu_i - 1}\right) \tag{4.18}$$

where the indices ν_i are in general non-integral. To ensure the correct behavior as r approaches zero, $B_{\nu_i} = 0$. For the special case when the equipotential shapes are generated by

$$r = b/[P_{\nu_0}(\mathrm{Cos}\theta)]^{1/\nu_0} \tag{4.19}$$

(as shown in Fig. 4.4, for $\nu_0 = 0.176$) V is reduced to a single term in r:

$$V = V_0 + A_{\nu_0} b^{\nu_0} \tag{4.20}$$

where V is chosen to be 0 at the emitter and equal to V_e at the counterelectrode. Hence we have, with $V = 0$ at the emitter, in Eq. (4.20):

$$0 = V_0 + A_{\nu_0} r_0^{\nu_0}$$

where $b \equiv r_0$ the axial position of the emitter apex. which gives us

$$V_0 = - A_{\nu_0} r_0^{\nu_0}$$

Hence the potential becomes:

$$V = A_{\nu_0}\left(b^{\nu_0} - r_0^{\nu_0}\right) \tag{4.21}$$

At the counterelectrode, $V = V_e$ so that

$$A_{\nu_0} = \frac{V_e}{\left(R_0^{\nu_0} - r_0^{\nu_0}\right)} \tag{4.22}$$

where R_0 is the distance from the apex of the cone equipotential to the on-axis point of the counterelectrode.

Substituting Eq. (4.22) in Eq. (4.21) we get, for the potential:

$$V = V_e\left(\frac{r^{\nu_0} - r_0^{\nu_0}}{R_0^{\nu_0} - r_0^{\nu_0}}\right) \tag{4.23}$$

The electric field E_r is given by:

$$E_r = (\partial V/\partial r)_\theta = V_e\ \nu_0\left(\frac{r^{\nu_0 - 1}}{R_0^{\nu_0} - r_0^{\nu_0}}\right) \tag{4.24}$$

where ν_0 for the needles typically used in this study (cone half angle $\sim$10 °) is 0.176. Here r_0 is not the radius of curvature of the emitter apex but is related to it by the expression:

$$r_0 = \frac{\rho(1-\nu_0)}{2} \tag{4.25}$$

where ρ is the radius of curvature of the emitter apex.

The electric field on-axis at the apex ($r = r_0$ and $\theta = 0$) is

$$E_0 = \left(\frac{V_e \nu_0}{r_0^{1-\nu_0}(R_0^{\nu_0} - r_0^{\nu_0})} \right)$$

This can be written as

$$E_0 = \frac{V_e \nu_0}{r_0 \left(\left\{ \frac{R_0}{r_0} \right\}^{\nu_0} - 1 \right)}$$

If we assume $R_0 = d + r_0$, where d is the emitter-target separation, we get

$$E_0 = \frac{V_e \nu_0}{r_0 \left(\left\{ \frac{d+r_0}{r_0} \right\}^{\nu_0} - 1 \right)}$$

which is

$$E_0 = \frac{V_e \nu_0}{r_0 \left(\left\{ 1 + \frac{d}{r_0} \right\}^{\nu_0} - 1 \right)} \tag{4.26}$$

Rewriting Eq. (4.26), we get the following relation between the voltage for electron emission and the emitter-target spacing:

$$V_e = \frac{E_0}{\nu_0} r_0 \left(\left\{ 1 + \frac{d}{r_0} \right\}^{\nu_0} - 1 \right) \tag{4.27}$$

4. Experimental

The emitters used for this investigation were much sharper than the 4 to 5 μm radii emitters used for the conventional LMIS. Figure 4.2 from an earlier section, shows a SEM profile of an electrochemically etched needle typically used in this study. Typically they had apex radii of about 25 to 500 nm and were electrochemically roughened in 2M NaOH solution for a few seconds at ~1 V a.c.

The emission studies were carried out in a LMIS-STM embodiment described earlier (Chapter 3). The experiments were concerned with determining the field electron emission characteristics of the small needle radii LMIS at various diode spacings in the LMIS-STM embodiment. An I(V) in the field electron emission mode was obtained at various separations.

The larger separations, of the LMIS from the substrate were determined by using a 30X binocular microscope with a calibrated reticule in the field of view. This was adequate down to separations of ~12 μm. Smaller distances were estimated by counting the number of electromagnetic pulses delivered to the calibrated magnetically driven micropositioner. A 90X lens was also used (in the binocular microscope) to visually note separations of the LMIS

and the substrate below 12 μm. This lens could not be used for quantitative determination of the separations since it did not have a reticule in the field of view of the microscope. Further a check on the distances estimated from the number of electromagnetic pulses delivered to the micropositioner, were done with respect to the substrate which was used as the reference point after the LMIS made direct contact with it, at which time the ion extraction voltage of the LMIS would drop to $V_{ext} = I \times R$ where R was the external resistor in the circuit and the current in the circuit would then be governed simply by that relation.

5. Results

It was first found essential to determine the value of the electric field at the emitter apex from both the models for a particular value of the field electron emission current, 1 nA. To determine the value of the electric field, we used Eq. (4.16) of the prolate spheroidal model, with the emitter-target separation, a, obtained from the magnetically driven micropositioner and piezoceramic combination, and the field electron emission voltage V_e of the LMIS at an electron current of 1 nA, for that separation. The same calculation, to determine the electric field, was done using Eq. 4.26 for the polar model with $\nu_0 = 0.176$. (See Section A.3.1 in Chapter 4) The values of the electric field obtained have been tabulated in Table 3.

Table 3. Values of the electric field at the emitter apex, E_0

Field Electron Emission Voltage (Volts)	Diode Spacing using Micro Positioner and Piezo (μm)	Electric Field at Apex (Prolate Spheroidal Model) (V/Å)	Electric Field at Apex (Polar Model) (V/Å)
-35	0.07	0.14206	0.1
-82	0.116	0.1646	0.114
-200	0.3	0.163	0.156
-250	0.56	0.142	0.142
-400	1.24	0.162	0.161
-725	4.0	0.211	0.189
-900	10.6	0.214	0.174
-1250	25.4	0.256	0.189

A plot of the electron emission voltage (for a current of 1 nA) versus the emitter-target spacing, can be done using the values of the electric field obtained for the two models, from Table 3. Such a plot is shown in Fig. 4.31.

From Fig. 4.31 we see that the plot for the prolate spheroidal model tends to level off and consequently would be expected to be inaccurate at spacings $\geq 10\mu m$. The polar model, seems to provide the more accurate values for spacings upto $\sim 25\ \mu m$. At very large spacings both models would be expected to become inaccurate. Below about 5 μm, both models would converge and be expected to be in good agreement with experimental values. Hence for the reason that the polar model is probably the more accurate of the two, upto spacings of $\sim 25\ \mu m$, we shall, for the remainder of this section consider only the polar model to evaluate the emitter-target spacings in the proximity focused LMIS.

From the values obtained for the electric field (for the polar model) an average value can be calculated.

$$E_0 = 1.5 \times 10^7 \ \ V/cm$$

Equation (4.27) can now be used to determine a value for d, the emitter-target separation, using the field electron emission voltage obtained at that spacing in the LMIS-STM embodiment. As an example, using the field electron emission voltage, $V_e = 200$ volts obtained at a micropositioner spacing of 3000 Å, we find the separation predicted from the polar model to be $d = 2300$ Å. Alternately we can use the plot of field electron voltage

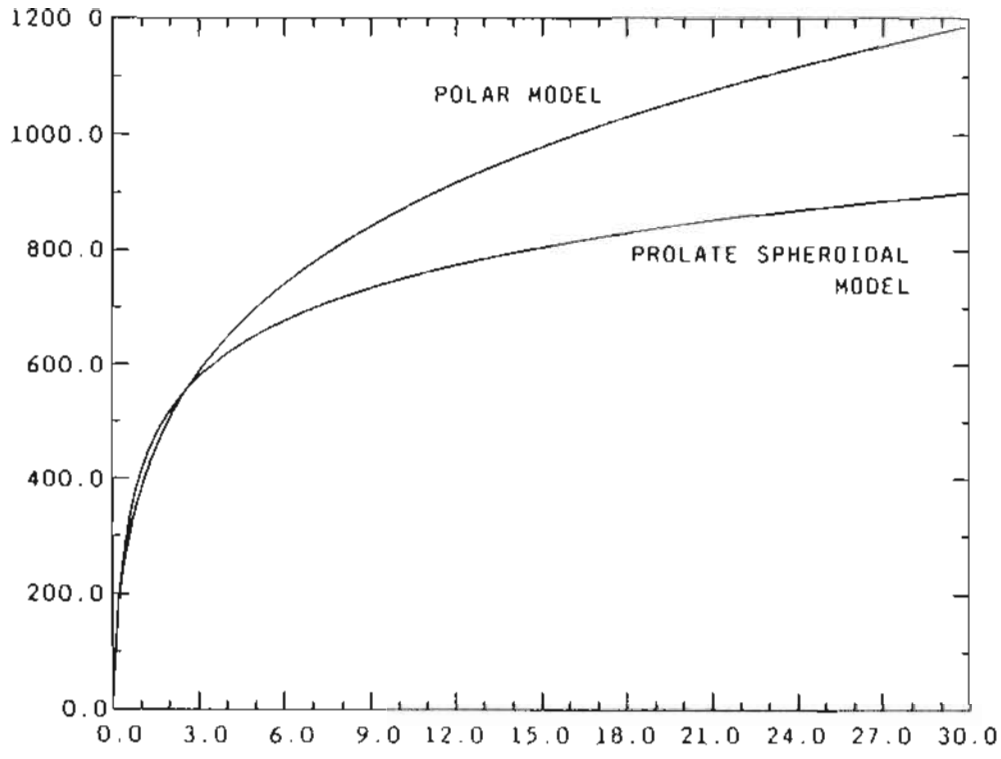

Figure 4.31 : Plot of the electron emission voltage versus emitter-target separation for an emitter radius of 1500 Å from the prolate spheroidal model and the polar model.

versus diode separation (Fig. 4.31) for the polar model and directly read off the diode separation for the field electron emission voltage.

Table 4 on the next page compares the values for the emitter-target separations obtained using the polar model, with the values from the micro-positioner and piezoceramic combination.

Table 4. Comparison of the methods used to determine the emitter-target separation

Electron Emission Voltage (Volts)	Diode Spacing using Polar Model (μm)	Diode Spacing using Micro Positioner and Piezo (μm)
-35	0.023	0.07
-82	0.062	0.116
-200	0.23	0.3
-250	0.343	0.56
-400	0.90	1.24
-725	4.17	4.0
-900	8.03	10.6
-1250	23.96	25.4

6. Summary

It is seen that for diode separations below about 25 μm, the polar model is in reasonably agreement with the diode separations determined using the calibrated micropositioner and the piezoceramic tubes as seen in Table 4. Hence for spacings ≤ 25 μm one can rely on the polar model as a predictor of the spacing. Larger separations can be determined quite easily by using a 30X binocular microscope with a calibrated reticule in the field of view. This is useful down to separations between the source and the target of ~12 μm.

C. A LOW CURRENT LIQUID METAL ION SOURCE

1. Introduction

As the spacing between the LMIS and the substrate becomes very small for the proximity focused LMIS, the current density due to the LMIS at the substrate becomes very large. This may result in either rapid sputter erosion of the substrate by ion bombardment or deposition of gallium (the principle liquid metal used in this study) at ion energies below the sputtering threshold. For example, at 0.1 μm spacing of the emitter from the substrate and, assuming an emission half angle of 20°, a target current density of ~2300 A/cm^2 can be achieved for a Ga LMIS operating at 0.1 μA total current. This is equivalent to about 2×10^7 ions/surface atom/sec, which for a sputtering yield of unity, would result in surface erosion taking place at the rate of $\sim10^7$ monolayers per second. Alternatively, if the LMIS operation is occuring at voltages where net deposition of gallium is taking place, that is below the sputtering threshold, then build up of gallium rather than sputtering would conceivably occur also at extremely rapid rates.

These high current densities posed experimental difficulties because of the rapidity of ion beam induced substrate changes at the early stage of these "proximity focused" experiments. (Conceivably, such enormous current densities could be harnessed at a later stage and would directly translate into higher processing speeds for micromachining). Hence for the reason of lack of manageability of such high current densities, an investigation of LMIS, capable of operating at much lower currents than usual, was carried out.

This was successful and a new low current (and low voltage) mode of operation of the Ga LMIS was discovered. Currents as low as 1 nA were found possible instead of the normally observed current threshold values of 1 μA from the conventional LMIS. The threshold voltages at which LMIS operation commenced for larger emitter/extractor separations was as low as 2 kV compared to the normally 5 to 6 kV for the conventional LMIS.

2. Experimental

The tungsten needles used as a substrate for the low current gallium LMIS were much sharper than the 4 to 5 μm radius normally used for the conventional LMIS. Typically they had apex radii of about 25 to 500 nm and were electrochemically etched in 2 M NaOH using a d.c. voltage of about 10 to 15 volts. The process is shown in Fig. 4.32 and is described in Appendix B. The emitters were roughened somewhat before use in 2 M NaOH solution for a few seconds at ~1 V a.c. Care was taken that the roughening procedure was not carried to excess so that the emitter apex did not blunt back. Figure 4.33 shows an SEM profile of an electrochemically etched needle used in this study. The needle was wetted with Ga in the usual manner by heating to 1000° K and then dipping the needle repeatedly into a pool of molten Ga at room temperature while gently heating ($<$ 1000° K) the needle between dippings. The measurements were carried out in a field ion microscope (see Fig. 4.3) in which a microchannel plate image intensifier was used in order to view the ultra low current ion emission patterns investigated. The base pressure for all measurements was 1×10^{-8} torr.

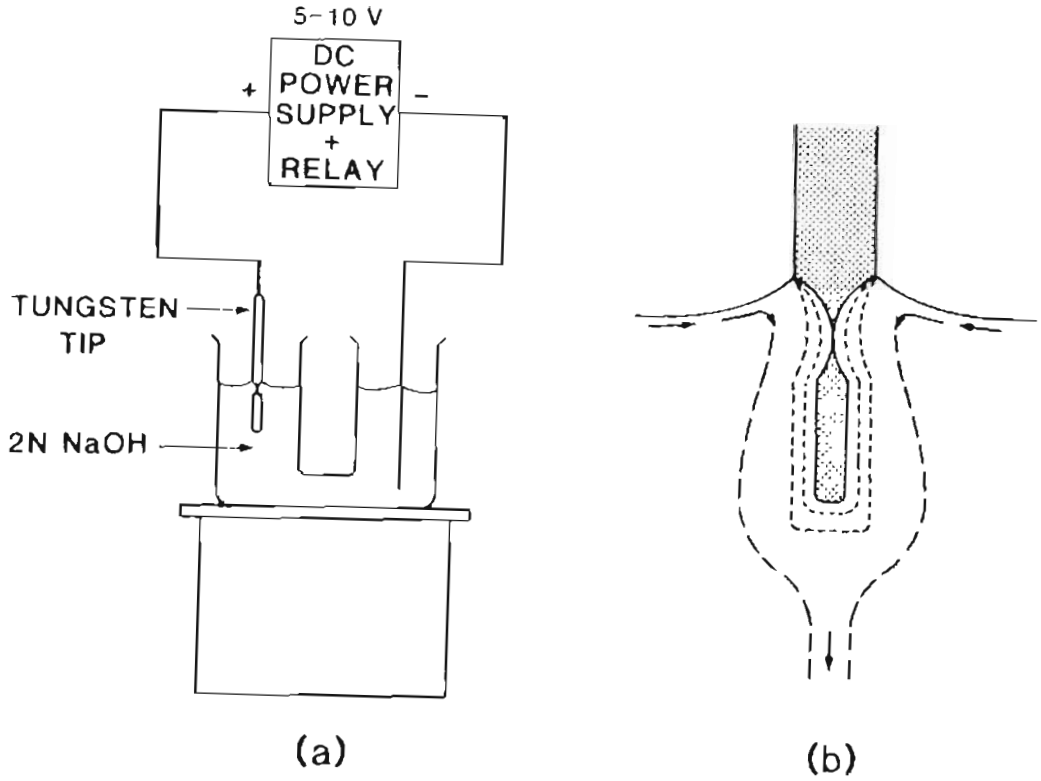

Figure 4.32 : D.C. drop-off technique to produce sharp emitters.

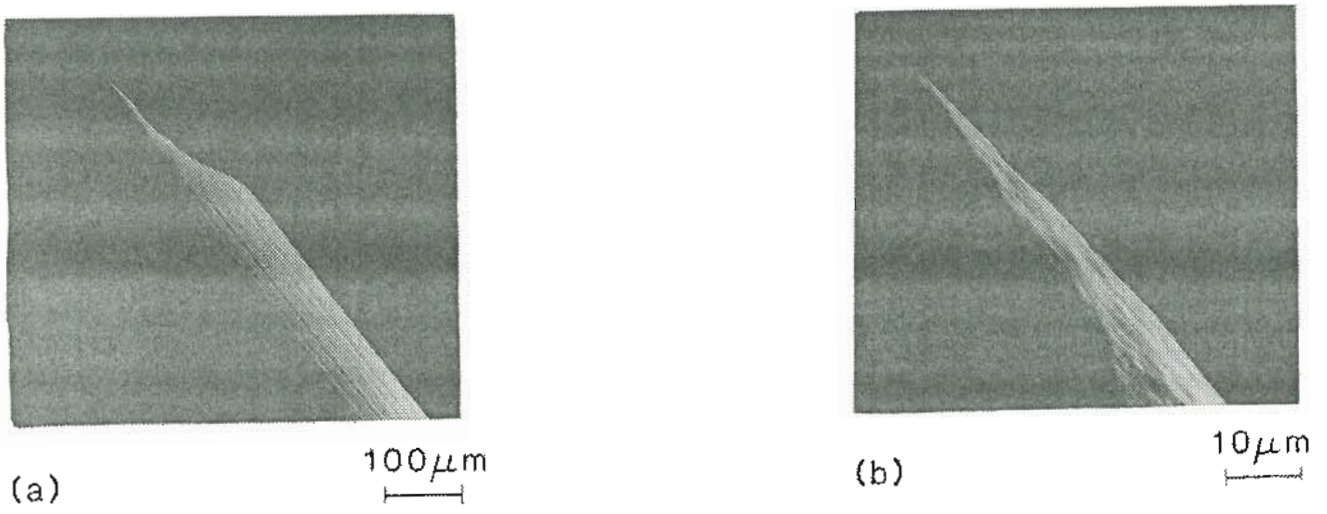

Figure 4.33 : SEM photos of an electrochemically etched needle with a d.c. etch technique: (a) low magnification showing part of shank and (b) high magnification of the apex region.

3. Results

In this study, the ion emission patterns and I(V) characteristics for Ga, were obtained by increasing the extraction voltage to the threshold for Taylor cone formation, at which point, ion emission commenced from the LMIS. In the case of indium, the temperature of the emitter had to be raised to above the melting point of the metal, before applying the extraction voltage to obtain ion emission.

Figure 4.34 shows a plot of ion emission current versus applied voltage for the Ga wetted needle LMIS of Fig. 4.33. The threshold voltage for the onset of emission was 3.0 kV.

That the current was due to emission from a Taylor cone is evident from the microchannel plate images which are shown photographed in Fig. 4.35 for the emitter of Fig. 4.33. These images are the typical structureless patterns seen in normal LMIS operation. In addition, below a very low threshold voltage the emission current was characterized by pulses, the frequency of which increased with emission current, finally merging into d.c. at the threshold voltage. This is typical of LMIS behavior. Figures 4.35B and 4.35C show what appears to be ion emission from two and four Taylor cones respectively as the voltage is increased. The susceptibility of these low current LMIS to multiple Taylor cone formation may be due to the critical electric field for onset of ion emission which goes as $r^{-1/2}$, being sufficiently high not only at the needle apex but also for a considerable portion along the sides of these sharp emitters.

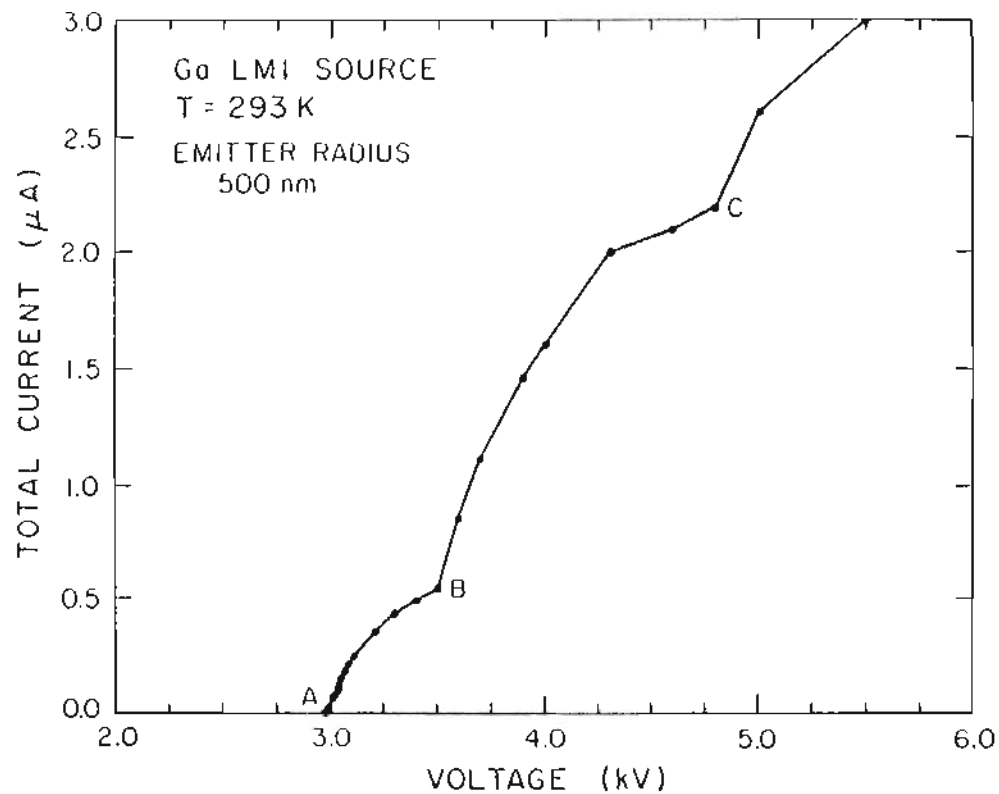

Figure 4.34 : Total emission current versus emitter/extractor potential difference for the Ga wetted needle LMIS shown in Fig. 4.33.

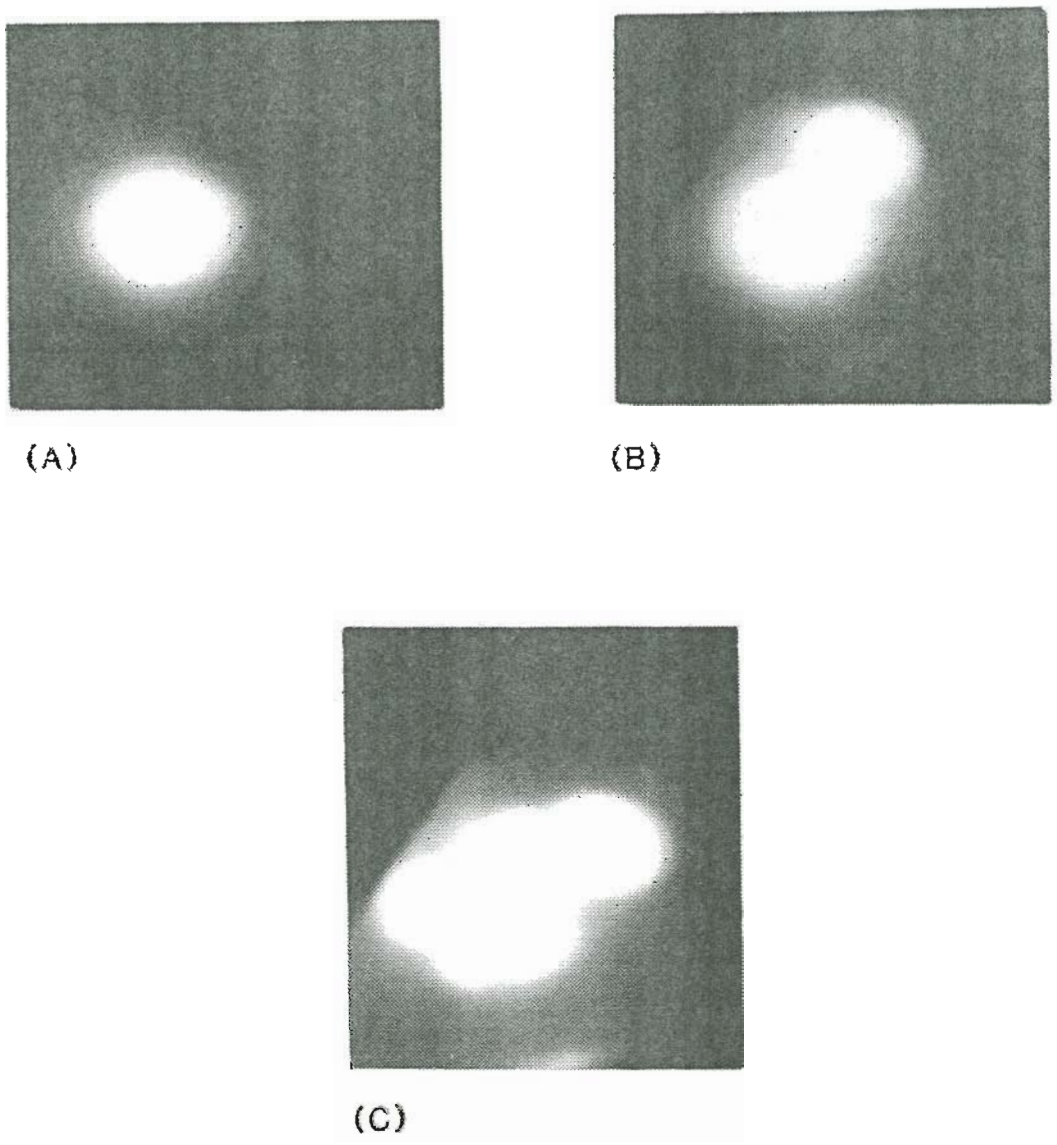

Figure 4.35 : Microchannel plate images of the ion beam from the Fig. 4.33 low current Ga LMIS. Images were photographed at the indicated currents in the I(V) plot in Fig. 4.34.

The appearance of multiple Taylor cones coupled with off-axis emission has been a troubling factor throughout, for these low current LMIS. These problems tend to disappear somewhat if the substrate needles used are of larger radii, approaching that of 500 nm and sometimes even as large as 1 μm; though at the larger radii the threshold currents initially starting out as low as 50 nA tend to creep up to 0.5 to 1 μA over a period of time, with the result that the source is no longer a low current source.

Another drawback in these low current LMIS, having sharp needles as substrates is that they tend to become supply limited during operation. An I(V) plot taken in a vacuum chamber with a microchannel plate image intensifier showed the I(V) to flatten out in a plateau (Fig. 4.36) and was seen to correspond to the ion image on the phosphor screen becoming smaller, as well as somewhat reducing in intensity. This in all probability is due to a supply limitation which would lead to an inability to draw currents more than a few μA from these sharp needle LMIS. Again, using emitter radii between 300 and 500 nm seemed to somewhat solve this problem.

Figure 4.37 shows an SEM profile of an electrochemically etched tungsten needle, with an apex radius of 50nm. Figure 4.38 shows a plot of ion emission current versus applied voltage for the needle of Fig. 4.37 after wetting with indium. In an earlier experiment molybdenum was used as the substrate and it was seen then, that indium wet molybdenum much better than tungsten, except that over a period of time the indium tended to alloy with the substrate leading to progressively higher melting temperatures to turn on the ion source. This did not happen when tungsten was used as the

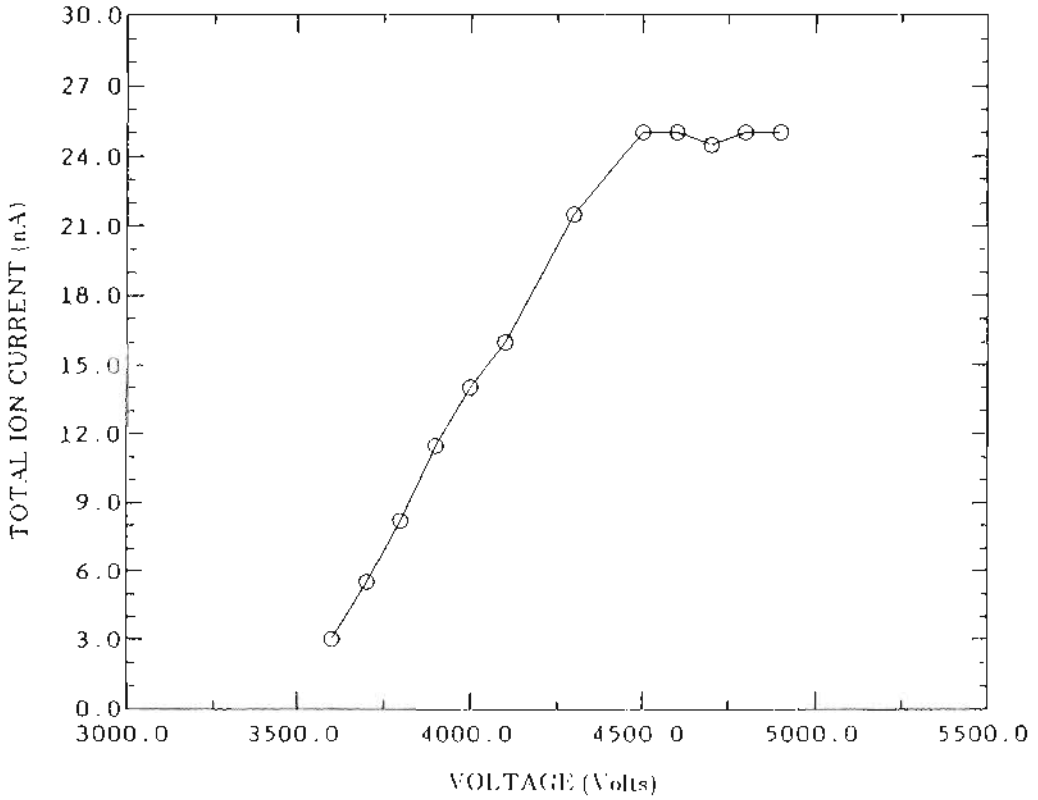

Figure 4.36 : Total emission current vs emitter/extractor potential difference for a low current gallium LMIS showing a levelling off in the ion emission current.

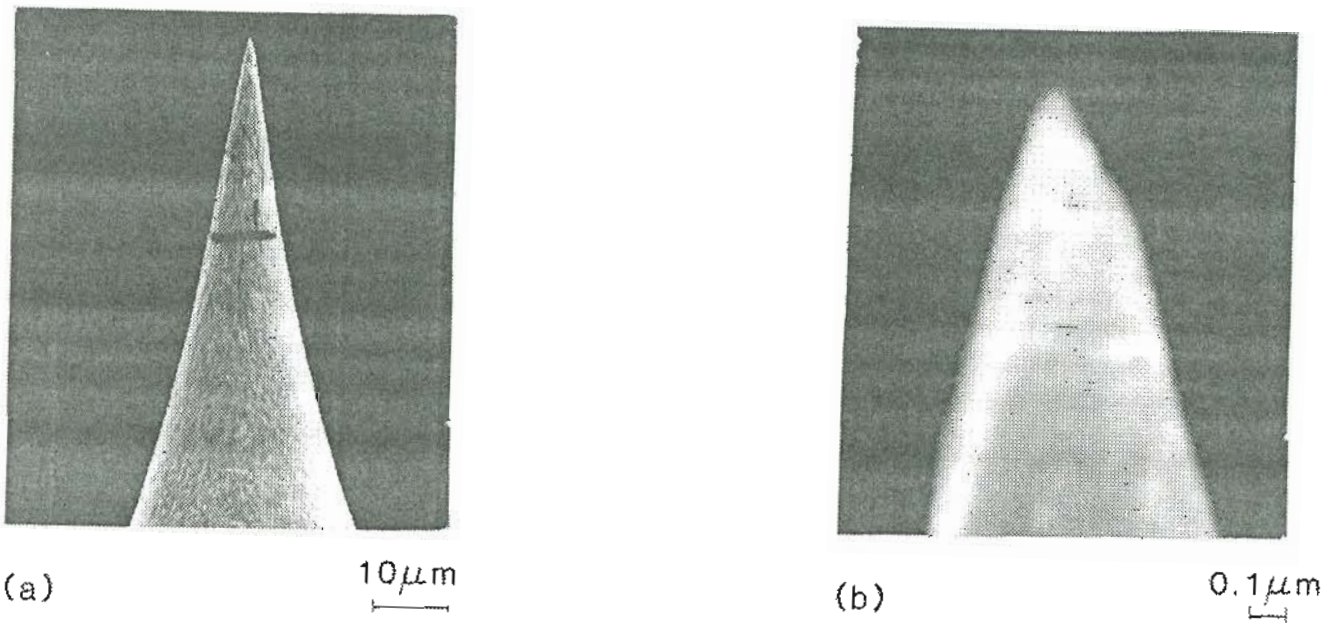

Figure 4.37 : SEM photos of an electrochemically etched needle with a d.c. etch technique: (a) low magnification showing part of shank and (b) high magnification of the apex region. Apex radius of the emitter is ~50 nm.

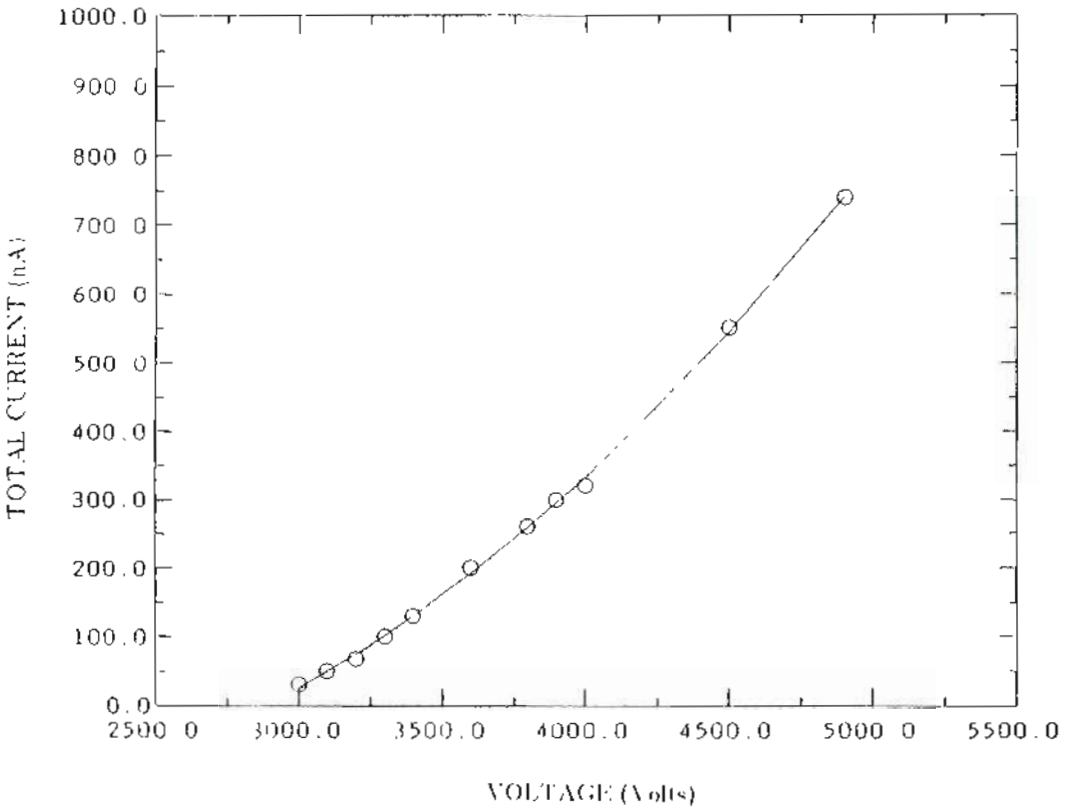

Figure 4.38 : Total emission current versus emitter/extractor potential difference for the indium wetted needle LMIS shown in Fig. 4.37.

substrate. The threshold voltage, as in the case for the Ga LMIS is 3.0 kV with a threshold current of 30 nA.

4. Discussion and Summary

For LMIS with needle radii of 2 to 5 μm the emission current turns on abruptly at a threshold value of about 0.5 to 1.0 μA. At emitter voltages below that corresponding to the threshold current, the Taylor cone collapses and current either ceases or pulses, the frequency of which increases as the voltage is increased towards the threshold value. At threshold the current merges into d.c. The fact that one is able to obtain lower threshold currents with smaller emitter radii may be due to the fact that the equilibrium radii of the Taylor cone is also smaller. Kingham and Swanson[7] showed that the electric field required to stabilize the Taylor cone shape for a dynamic model of the LMIS is given by

$$F = \left(\frac{4\gamma}{\rho\epsilon} + \rho_d v^2 \right)^{1/2} \tag{4.28}$$

where $\rho = \rho_{T.C}$ is the radius of the Taylor cone, ρ_d is the liquid density, γ is the surface tension, and v is the fluid velocity. The condition for onset of Taylor cone formation for the case of a needle substrate covered with a liquid layer, is given by Eq. (4.3), which is reproduced below.

$$F = \left(\frac{4\gamma}{\rho\epsilon} \right)^{1/2} \tag{4.3}$$

where for this case, $\rho = \rho_s$ is the radius of the underlying needle substrate.

Eqs. (4.3) and (4.28) then, differ only in the term $\rho_d v^2$ which in the analysis by Kingham and Swanson[7] takes into consideration the emission of ions during the operation of a LMIS i.e, the dynamic case. We will consider only the static case and ignore the term $\rho_d v^2$ in our calculations.

It has also been well established (Kingham and Swanson[8]) that field evaporation is the primary mechanism of ion formation which, for Ga, implies that a field strength at the Taylor cone apex of ~ 2 V/Å. It can be seen from Table 2 in Section 3.1A (earlier) that if an emitter radius of 200 nm and cone half-angle of 9° are used, the turn on voltage must be ~ 3000 V. In order to achieve a field of ~ 2 V/Å at 3000 V the radius must therefore be ~ 6 nm — perhaps even smaller since the Taylor cone half-angle is larger than 9°. In contrast, if the emitter radius is 1 μm, the turn-on voltage must be ~ 4800 volts. At this voltage a somewhat larger Taylor cone emitter radius of ~ 12 nm will suffice to provide the required field evaporation electric field of ~ 2 V/Å. The larger emitting area associated with the latter emitter will obviously lead to a larger threshold current.

As noted by Bell and Swanson[17] for a cone half-angle $\alpha = 49°$, there is a remarkably small dependance of the threshold voltage for cone formation on the emitter radius. A greater dependance of the threshold voltage on the emitter radius was noticed for LMIS of narrower cone angles. This can be shown by plotting Eq. (4.3) for cone half-angles of 5°, 9°, 20°, 30° and 49° and has been done in Fig. 4.39. We see then, from Fig. 4.39 that the difference between the threshold voltage for Taylor cone formation (for a

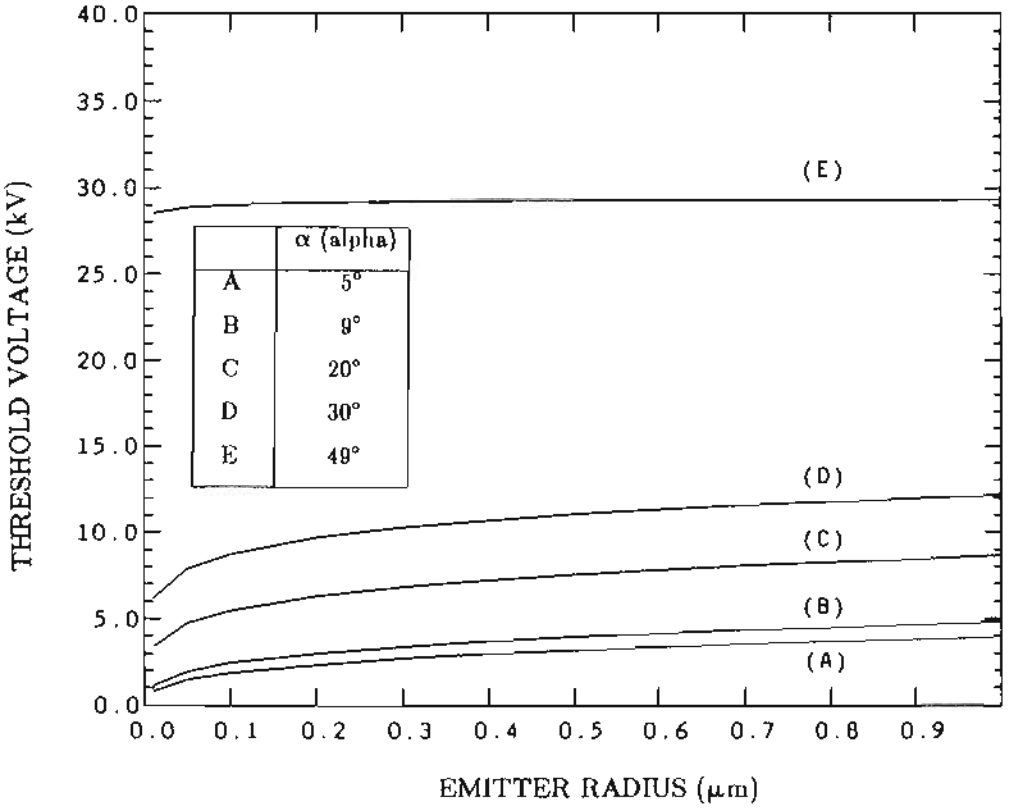

Figure 4.39 : Plot of the threshold voltage vs emitter radius for a LMIS with the indicated cone half-angles.

needle substrate of radii 1.0 μm) and the voltage for stabilization of the Taylor cone (assuming a Taylor cone radius of $\sim$10 nm) gets smaller as we go from cone half-angles of 5° to 30° and upto 49°. This then shows that if it were possible to fabricate emitters with small radii ($\leq$ 1.0 μm) and cone half-angle approaching 49°, these emitters would in all likelihood provide more stable operation as a LMIS than the currently used emitters with much narrower cone half-angles of 5 to 10°.

D. APPLICATION OF THE LOW CURRENT LMIS TO THE FOCUSED ION BEAM TECHNOLOGY

1. Introduction

Focused ion beam machines use one or more "lenses" to focus ions generated from the liquid metal ion source in an operation analogous to a series of optical lenses which focus a source of light in one plane onto another plane[22,23]. Hence one speaks of ion optics or ion lenses in a focused ion beam column.

The lenses used to deflect electrons in electron microscopes and electron beam lithography machines often employ magnetic fields. To do the same operation for ions would require higher magnetic fields (the ions being more massive and travelling more slowly) and consequently would be more difficult to generate. Ion lenses are therefore usually electrostatic and consist of two (or more) very precisely machined washer-shaped electrodes at some high potentials as shown in the schematic of an ion column in Fig. 4.40. The optics for the ion focusing column is schematically depicted in Fig. 4.41. The beam passes through the center of these concentric electrodes and is deflected and accelerated by the electric fields. Since the structure and fields are cylindrically symmetric about the axis of the beam, and since the deflection of the beam by the electric field is proportional to the distance from the axis, the lenslike operation results.

One of the properties which limits the operation of a simple optical lens is chromatic aberration, i.e., the lens has a different focal length for different

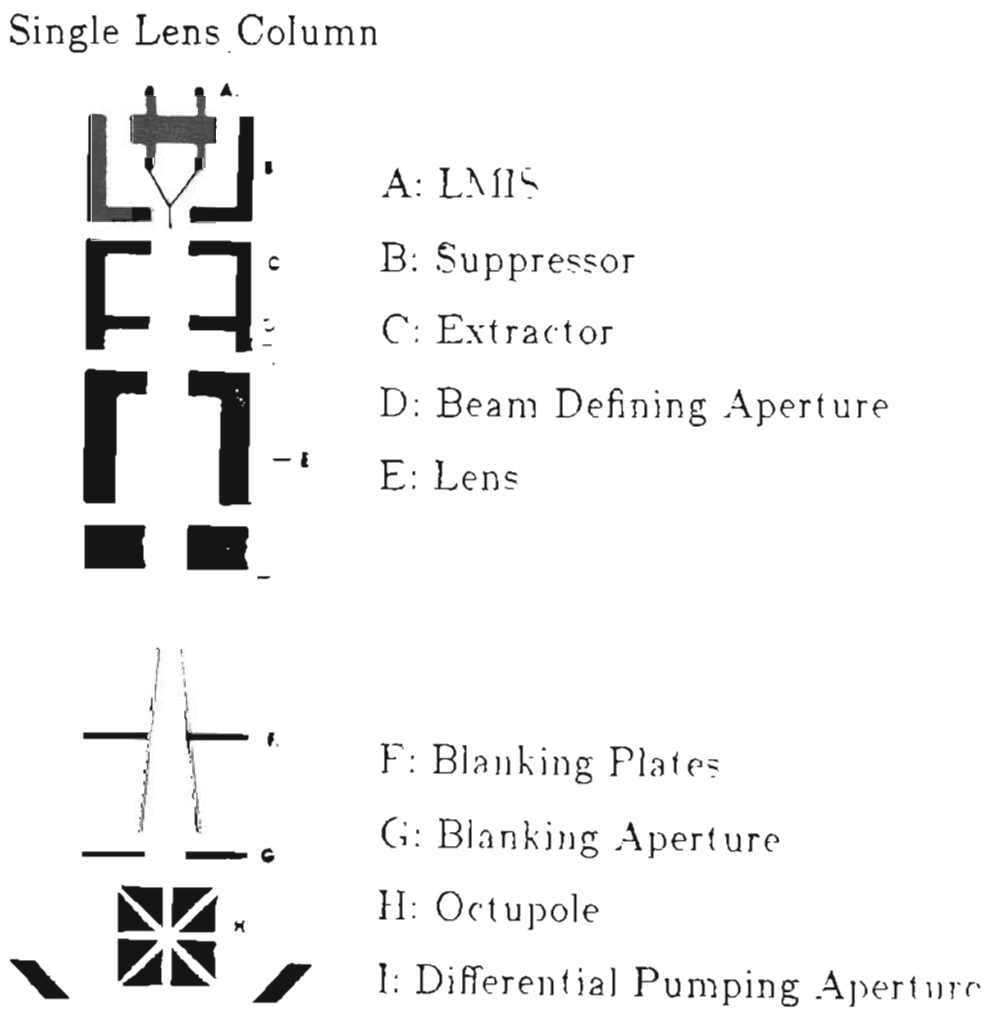

Figure 4.40 : Schematic of a focused ion beam system.

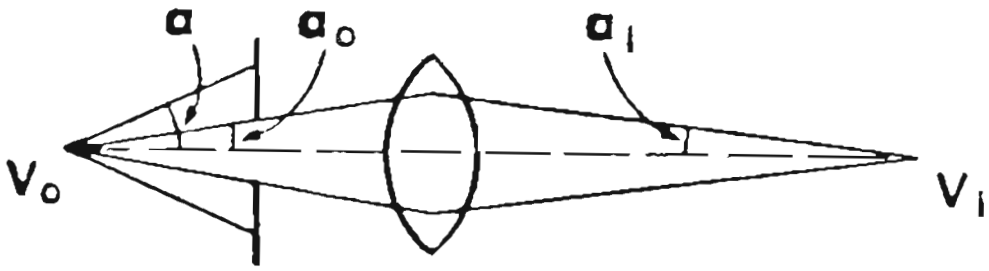

Figure 4.41 : Schematic diagram for the optics in an ion focusing column.

wavelengths of light. Similarly an electrostatic lens has a focal length which depends on the energy of the ions. The most serious practical limitation to the performance of most present focused ion beam columns is this chromatic aberration. The chromatic aberration would cause an otherwise zero diameter beam to have a diameter d_c given by

$$d_c = MC_c\alpha_0(\Delta V/V_0) \tag{4.29}$$

where M is the magnification of the lens system, C_c is the chromatic aberration coefficient, α_0 is the object side aperture half-angle, ΔV is the energy spread, and V_0 the emitter extraction voltage. (This expression refers to the sample or object side of a lens. A similar expression can be written for the image side.) The beam energy spread for the ions appears to be a fundamental property of the liquid metal ion source. The origin of this spread is due to the statistical nature of the ion emission and the mutual electrostatic repulsion between the ions[24].

Another effect which results in a change in the beam diameter is spherical aberration. Spherical aberration arises from the nonideal radial dependance of the focusing fields of a lens, i.e., the focal length of a lens for a particular ion depends on how far the ion trajectory is off axis. The contribution to the beam diameter from spherical aberration is given by

$$d_s = \frac{1}{2}MC_s(\alpha_0)^3 \tag{4.30}$$

where C_s is the spherical aberration coefficient.

Equations (4.29) and (4.30) hold for individual lenses or for combinations of lenses, provided that the coefficients are correctly added[25]. The values of the aberration coefficients C_c and C_s may be obtained by a computer calculation of the fields and ion trajectories in a lens system[26-28].

The other important effect which contributes to the finite beam diameter is the virtual source diameter or the Gaussian source size d_v which for a LMIS is ~500 Å[29]. Then as discussed by Swanson[29], when the performance of LMIS in FIB is limited by aberration effects, the total diameter of the beam spot at the image side of the column d_i is given by

$$(d_i)^2 = \left[(d_v)^2 + (d_c)^2 + d_s)^2\right] \tag{4.31}$$

where d_c and d_s, depend on the beam acceptance half-angle α_0 and can be reduced at the expense of beam current, by reducing the beam defining aperture.

If the spherical aberration term is neglected in Eq. (4.30) i.e.,

$$(d_s)^2 < (d_v)^2 + (d_c)^2 \tag{4.32}$$

then Eq. (4.31) reduces to

$$(d_i)^2 = \left[(d_v)^2 + (d_c)^2\right] \tag{4.33}$$

which, using Eq. (4.29) can be written as

$$(d_i)^2 = M^2 \left[(d_v)^2 + \frac{(C_c)^2 \Delta V^2 (\alpha_0)^2}{(V_0)^2} \right] \tag{4.34}$$

Rewriting Eq. (4.34) we get

$$(\alpha_0)^2 = \left[\frac{(d_i)^2}{M^2} - (d_v)^2 \right] \left[\frac{V_0}{C_c \Delta V} \right]^2 \tag{4.35}$$

The total current at the target is given by

$$I = \frac{dI}{d\Omega} \pi (\alpha_0)^2$$

and using Eq. (4.35), we obtain

$$I = \frac{dI}{d\Omega} \pi \left[\frac{(d_i)^2}{M^2} - (d_v)^2 \right] \left[\frac{V_0}{C_c \Delta V} \right]^2 \tag{4.36}$$

where $\frac{dI}{d\Omega}$ is the angular intensity of the source. The current density at the target will then be given by

$$J_i = \frac{I}{\frac{\pi (d_i)^2}{4}} \tag{4.37}$$

which becomes

$$J_i = \frac{4}{\pi (d_i)^2} \frac{dI}{d\Omega} \pi \left[\frac{(d_i)^2}{M^2} - (d_v)^2 \right] \left[\frac{V_0}{C_c \Delta V} \right]^2$$

Hence the relationship between the focused beam current density J_i and beam size d_i is given by

$$J_i = \left[\frac{1}{M^2} - \frac{{d_v}^2}{(d_i)^2} \right] \left[2V_0 / |C_c \Delta V| \right]^2 I' \tag{4.38}$$

where $I' = \frac{dI}{d\Omega}$.

If

$$\frac{1}{M^2} > \frac{(d_v)^2}{(d_i)^2}$$

then we get

$$J_i = 4Cf \tag{4.39}$$

where the column properties are contained in the first part of the above expression i.e.,

$$C = \frac{(V_0)^2}{(MC_c)^2}$$

while the source properties are represented by the last part as

$$f = \frac{I'}{(\Delta V)^2}$$

This latter expression may be regarded as a source figure of merit. The value of f generally decreases as the emission current increases, almost without exception, because the increase in angular intensity is more than offset by an accompanying increase in the ΔV^2 term in the denominator of f. Hence to maximize focused beam performance according to Eq. (1.38) one must maximize $\frac{I'}{(\Delta V)^2}$. We thus see the importance of energy spread in determining the properties of chromatically limited FIB systems. A curious conclusion we are left with is that to increase the current density at a fixed beam diameter one must operate the source at the lowest possible current.

Conventional wetted needle type LMIS exhibit an abrupt cut-off of the angular intensity at about 10 to 20 μA/sr which occurs at the threshold current of about 0.5 μA. Above this value the angular intensity increases linearly with emission current[30]. This feature of the angular intensity behavior coupled with the inverse square dependence of f on energy spread, as discussed above, results in f having a maximum value at the lowest emission currents attainable with conventional LMIS[31]. An LMIS capable of operation at emission currents that are less than the low current threshold values of the conventional LMIS could provide a larger value of f. Hitherto the lowest LMIS threshold currents reported were approximately 0.1 μA[32].

It has been seen that the spread in the energy of the ions varies with increasing (total) ion current. Swanson et al.[33], showed that the energy

spread (full width at half maximum, ΔV) for a gallium beam ranged from about 5 eV at 1 μA emission current to about 30 eV at 25 μA (Fig. 4.42, reproduced from Swanson et al[33].). These values further varied with the temperature of the source as seen in Fig. 4.43, (reproduced from Swanson et al[33].). The peak position of the energy distribution also is seen to vary with emission current and temperature, being at an energy deficit of around 4 eV at 2 μA, this deficit reducing with increasing ion current, Fig. 4.42. Varying the temperature of the source, tended to reduce the peak height of the energy distribution and move the peak position to smaller energy deficits, Fig. 4.43.

If field evaporation is the dominant emission mechanism, the minimum energy spread of the liquid metal ion source is expected to be about 1 eV or less. For gas-phase field ionisation over regions of space with strong enough fields, energy spreads of about 1 to 2 eV would be expected. The energy spreads though, observed for gallium sources at the onset of emission are around 5 eV (see Fig. 4.44, reproduced from Mair et al[32].). The increase in the energy spread has been attributed by Mair et al.[34], to Coulomb interactions between ions in the high current density region near the emitter tip. The variation of the full width half maximum, ΔV, with emission current, I, for collision dominated Coulomb interactions is predicted to have the form

$$\Delta V \propto I^{1/2} \tag{4.40}$$

Knauer[24] in an analysis of the energy spread in beams produced by field emission point sources, attributed the energy exchange mechanism to be that

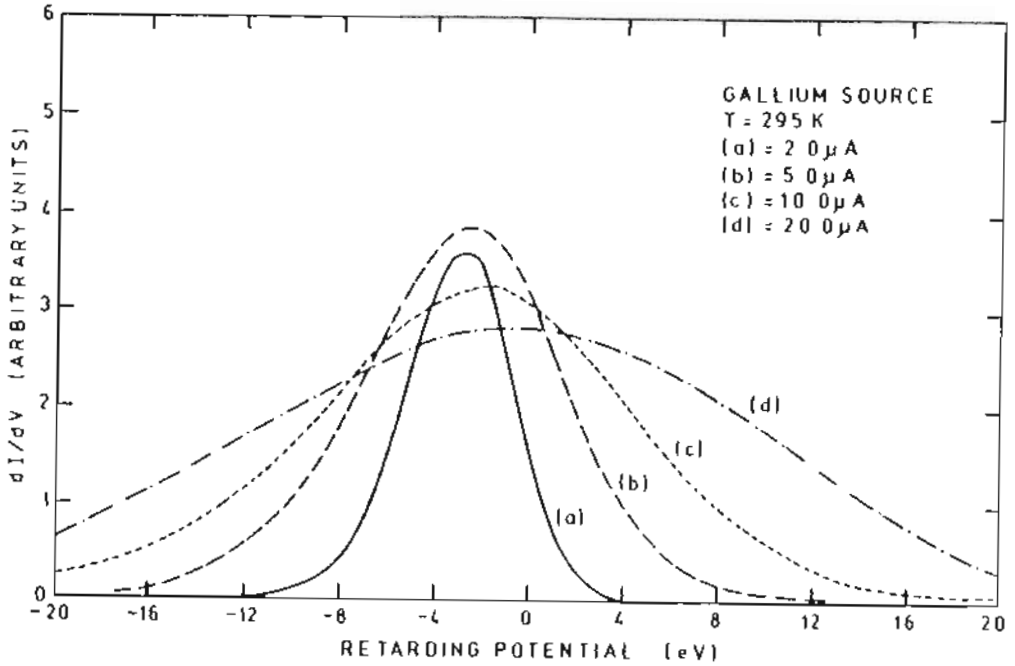

Figure 4.42 : Variation of the total energy distribution versus total emission current for a gallium source, with an applied voltage range of 3.9-4.8 kV.

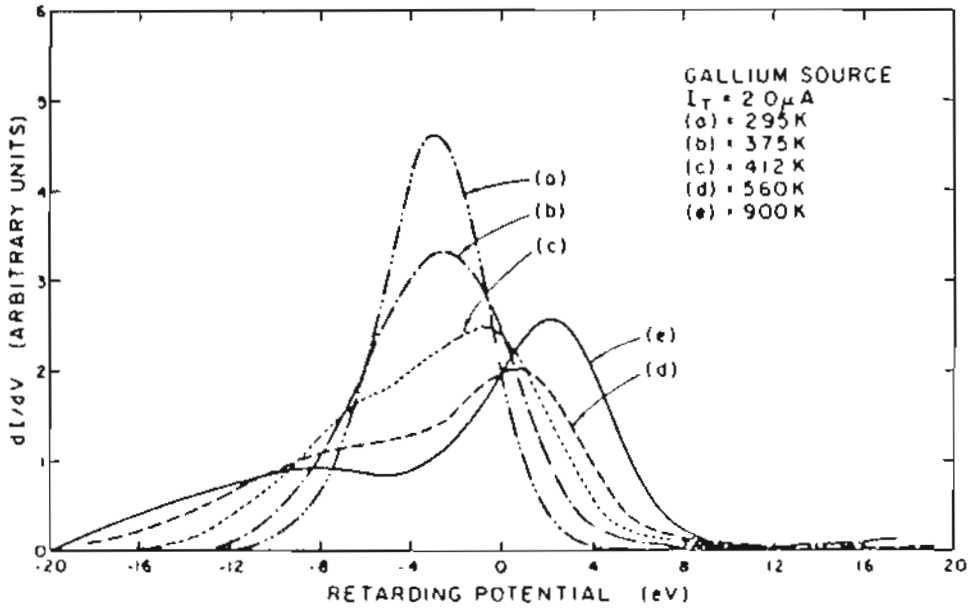

Figure 4.43 : Variation of the total energy distribution versus temperature for a gallium source.

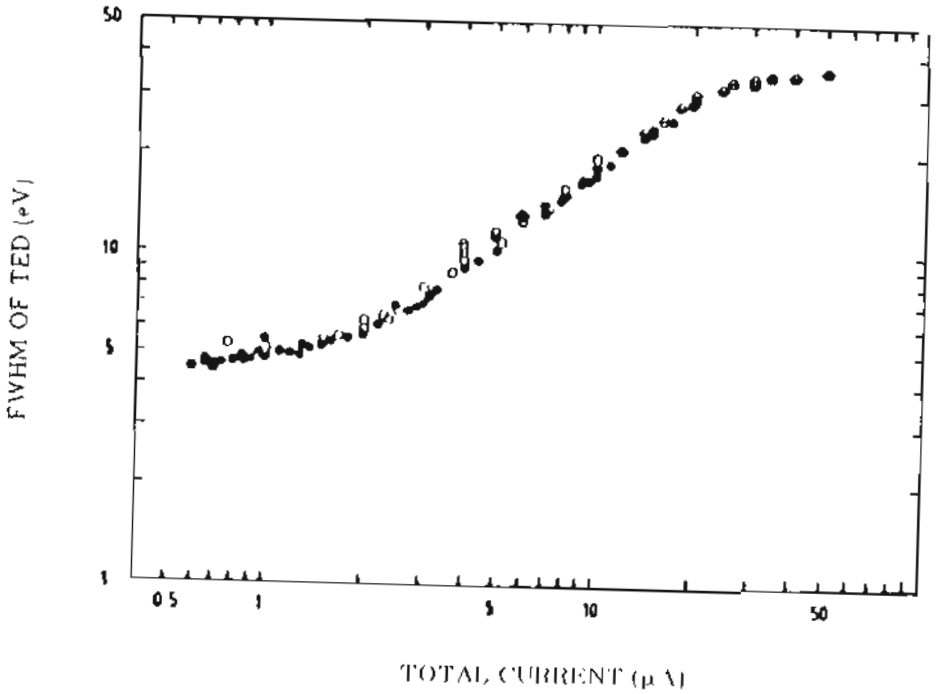

Figure 4.44 : Full Width at Half-Maximum (FWHM) values vs total current measured from the energy distribution curves for gallium at 293° K.

of steady Coulomb repulsion between neighbouring particles unlike the collision dominated models wherein the energy exchange mechanism is that due to the conversion of transverse kinetic energy to axial kinetic energy through collisions. Knauer obtained a formalism for the energy spread, given as

$$\Delta V \propto I^{2/3} \tag{4.41}$$

Swanson et al.[33], had in their paper observed the relation

$$\Delta V \propto I^{0.7} \tag{4.42}$$

The energy spreads for Ga - the most studied LMIS - have tended to decline only to 4.5 eV as the emission current decreases. This value is triple the value found by Culbertson et al.[31], in a study of the energy spreads at very low emission current where the emission mode was field evaporation of Ga from the solid substrate at 78° K. It is naturally of interest to search for an emission current of a LMIS operating in the Taylor cone mode at which the energy spread value would converge to that of the Culbertson value. In the Culbertson experiment Ga ions were formed by field evaporation from layers of Ga adsorbed on a W emitter while for a conventional LMIS they are formed in the high field region at the end of a field supported Taylor cone. In both cases field evaporation is thought to be the mechanism of ion formation[7,31], so that a convergence of energy spread values is thought likely at sufficiently low currents.

2. Experimental

The tungsten needles (Figs. 4.45, 4.46) used for this study had apex radii between 25 and 500 nm. They were electrochemically etched using a d.c. voltage between 10 to 15 volts and were roughened somewhat before use by etching in 2 M NaOH solution for a few seconds at ~1 V a.c. The needle was wetted with Ga in a wetting chamber, in the usual way.

A retarding potential analyzer (Fig. 4.47) was used for ion angular intensity, I(V) and energy spread measurements. The extractor electrode contained a 2 mm diameter aperture located 1 mm from the emitter. The base pressure for all measurements was 2×10^{-8} torr.

3. Results

A plot of the Full Width At Half Maximum (FWHM) of the energy distribution is shown in Fig. 4.48 for two emitter apex radii together with data obtained with a larger radius emitter. As with the energy spread data of Mair, et al.[32], the data has been plotted on a logarithmic scale so that the current in Fig. 4.48 spans a four order of magnitude range. As can be seen, the leveling off in the energy spreads, which were already apparent in the data obtained from the larger radii LMIS, was affirmed by the new measurements at the lower current. The average of 17 measurements was 4.5 ± 0.33 eV. This was a surprising result considering the fact that the lowest currents investigated in this work were comparable with those studied by Culbertson, et al.[31], who obtained energy spreads as low as 1.5 eV.

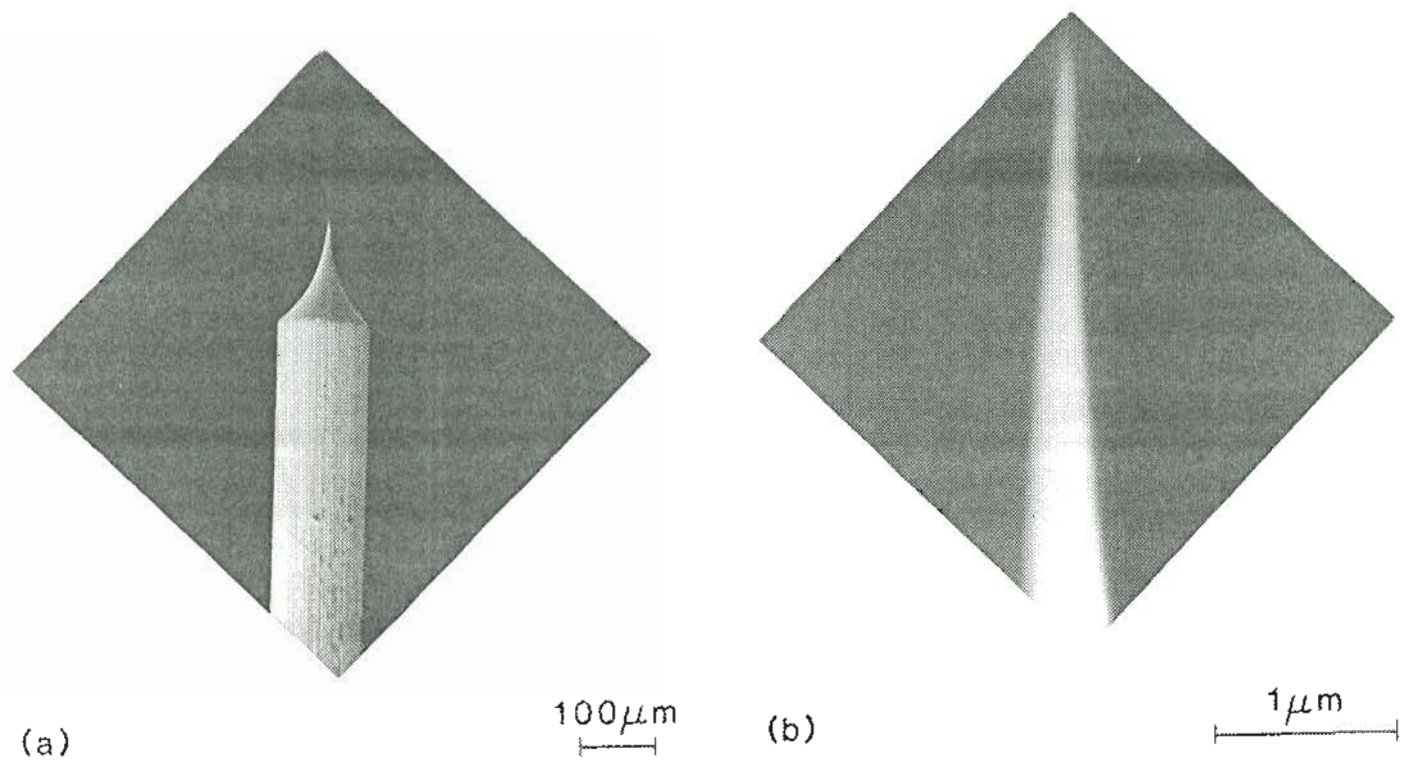

Figure 4.45 : SEM photos of an electrochemically etched needle with a d.c. etch technique: (a) low magnification showing part of shank and (b) high magnification of the apex region. Apex radius of the emitter is 25 nm.

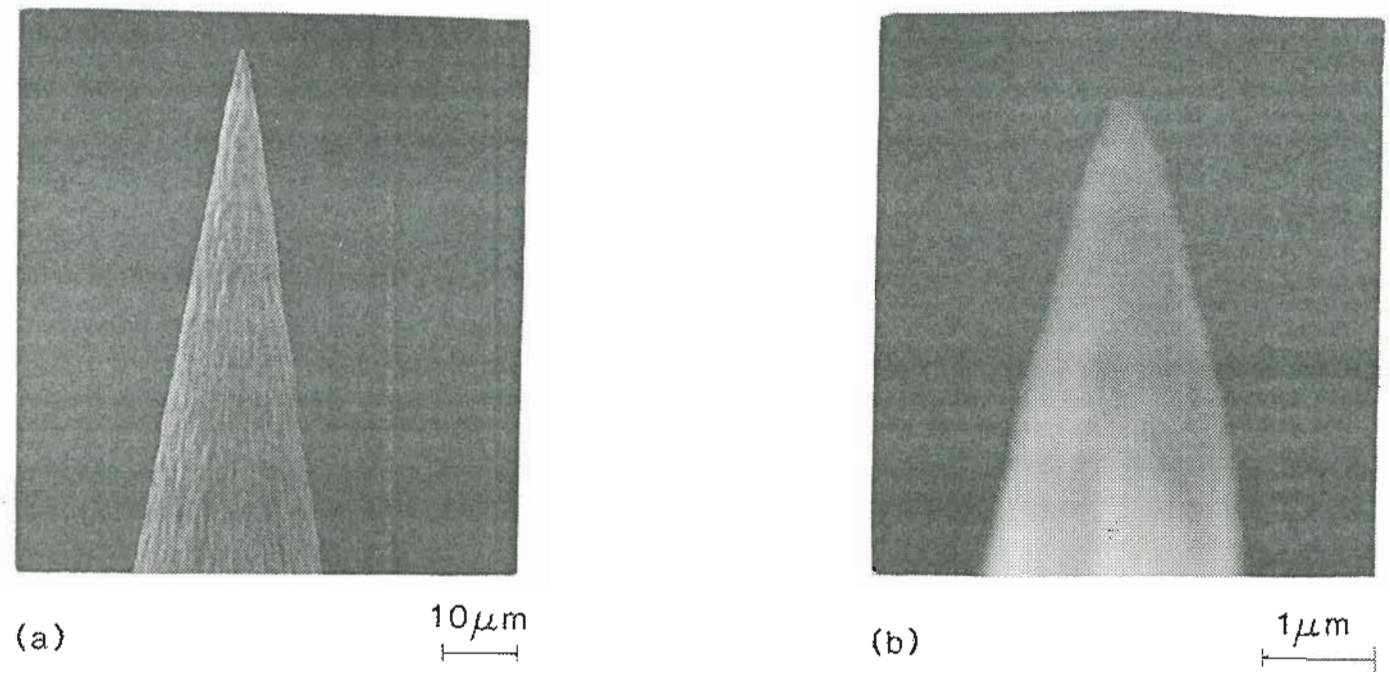

Figure 4.46 : SEM photos of an electrochemically etched needle with an a.c. etch technique: (a) low magnification showing part of shank and (b) high magnification of the apex region. Apex radius of the emitter is 160 nm.

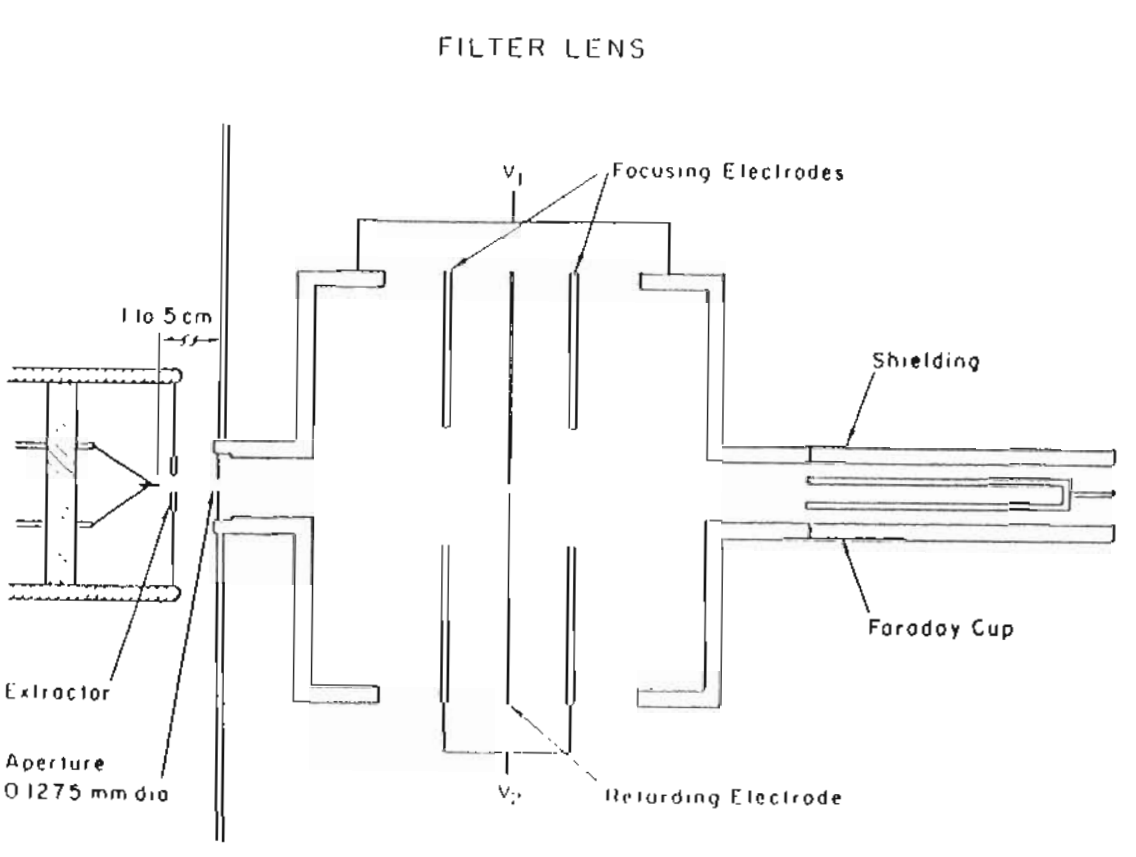

Figure 4.47 : Diagram of the saddle potential retarding energy analyzer used to measure the total energy distribution.

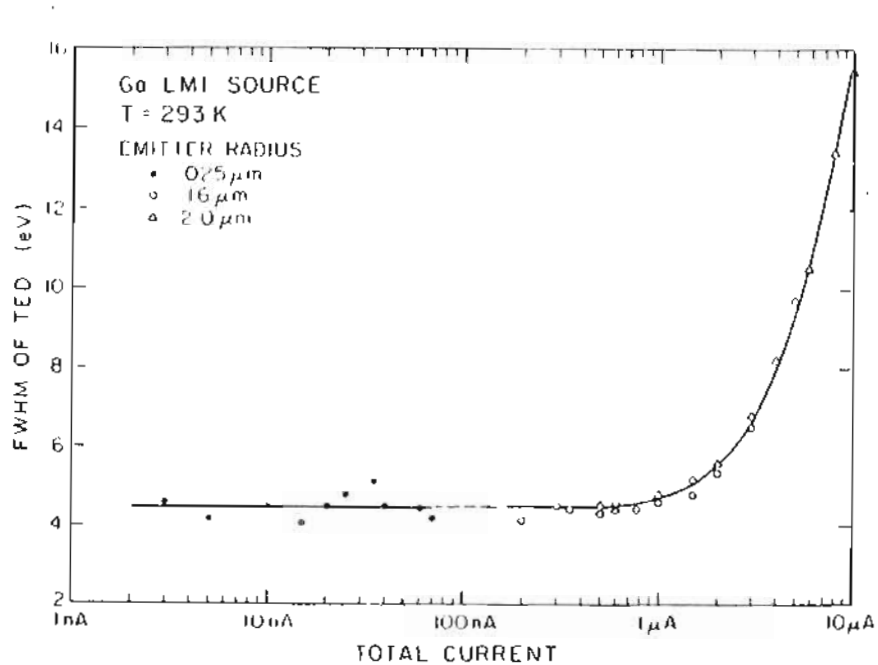

Figure 4.48 : FWHM of Total Energy Distribution as a function of total current for three Ga LMIS. The energy analyzer samples a solid angle of 1.7 μsr. Dashed line is interpolated.

Angular intensities for emission currents in the range 1 nA to 10 μA are plotted in Fig. 4.49 for the various emitter radii used in this study. In previous studies[30] it was shown that for emitters of varying geometry the value of I′ for a constant I varied linearly with the extraction voltage. Here the values of I′ have been normalized to an extraction voltage of 5 kV. For the small emitter radii LMIS a maximum in the axial current was noted as a second Taylor cone formed (see Fig. 4.50). The formation of the second cone would be expected to alter the fields at the site of the first Taylor cone and hence the emission current. It could also change the supply of liquid to the first cone and consequently affect the emission.

A plot of the figure of merit versus I as described by Eq. (4.38) is shown in Fig. 4.51. As stated earlier, the combination of a fixed energy spread coupled with a declining angular intensity results in the figure of merit reaching a maximum value at the total emission current of 1 μA.

4. Discussion

The leveling off of the energy spread at 4.5 eV as emission currents fall below 1 μA, seems, at first glance, to rule out ion-ion interactions as the source of the energy spread in excess of the 1.5 eV values found for field evaporation of Ga from tungsten needles at 78° K[31]. Since ion-ion interactions should diminish as the ion current declines, it seems likely that some other mechanism should be invoked to explain the 3 eV difference. On the other hand, theoretical formulations of the energy broadening ΔV_c due to stochastic charged particle interactions are generally of the form[24]

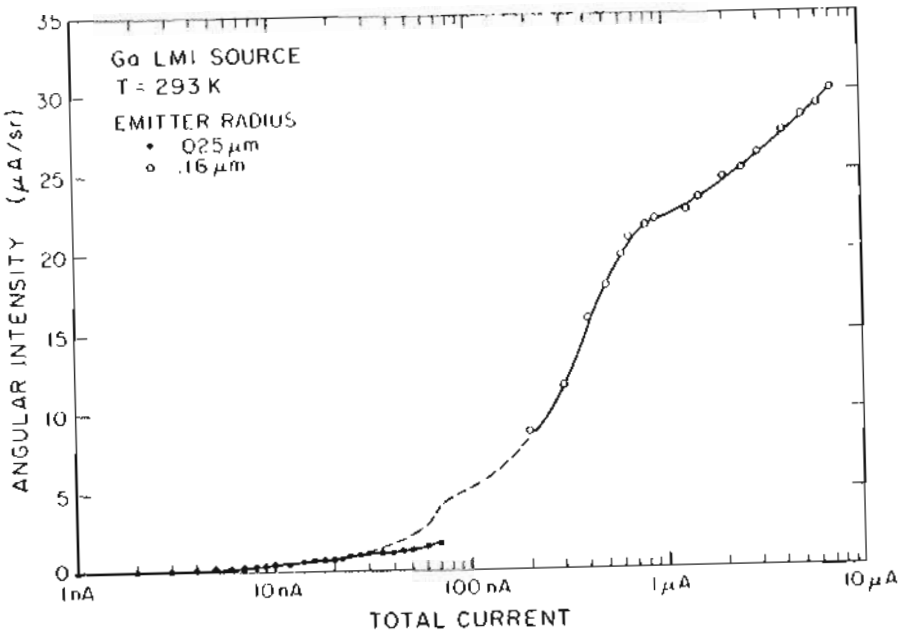

Figure 4.49 : Angular intensity, normalized to that from an emitter operating at 5 kV, as a function of total current for Ga LMIS with the indicated radii. Dashed line is interpolated.

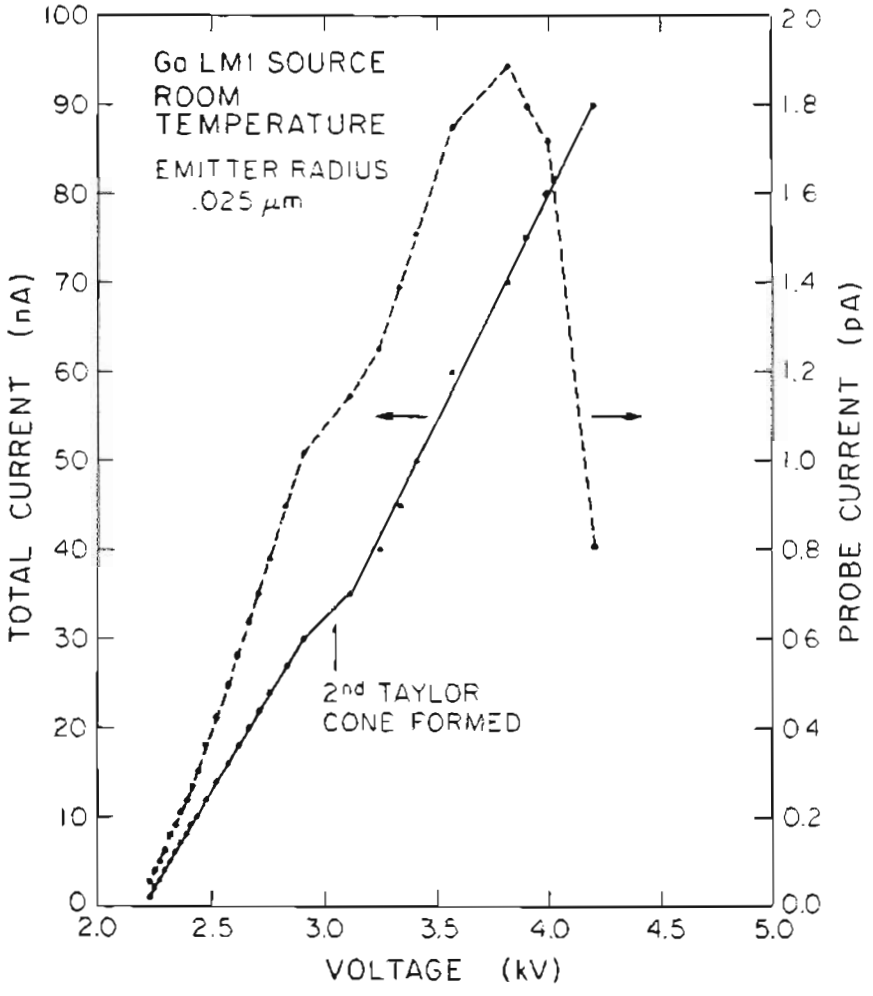

Figure 4.50 : Total current and probe current as a function of voltage for a low current Ga LMI source. Aperture half angle for the probe current is 0.705 mrad.

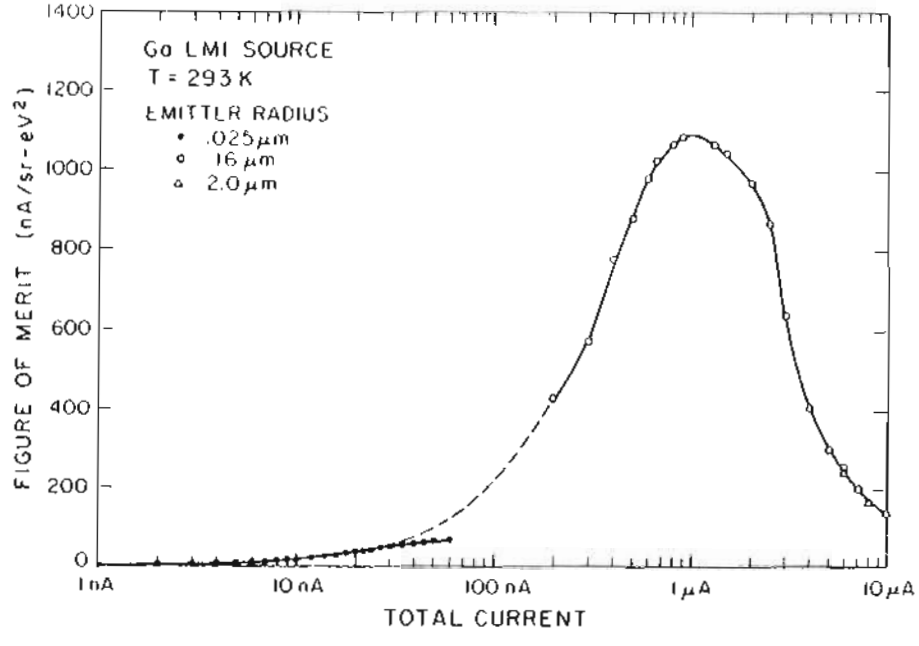

Figure 4.51 : Figure of merit for the indicated room temperature Ga LMI source, normalizing the angular intensities to that from an emitter operating at 5 kV. Dashed line is the interpolated data region.

$$\Delta V_c \propto \frac{I^n}{r^m} \tag{4.43}$$

where, in this case r is the radius of the Taylor cone apex. It has been shown theoretically[7] that r decreases with I for the Taylor cone model with dynamic terms included. Thus, one can envison the possibility of ΔV_c becoming independent of I if $r \propto I^{n/m}$ for $I <\sim 1\ \mu A$.

As to whether it is possible to attain FWHM values of the energy spread below 4.5 eV for Ga LMIS it is interesting to examine the results of Mayer and Gaukler[35] who reported energy spreads declining to 2.3 eV at 0.5 μA emission current. The low energy spread results were attributed to changes in the flow impedance associated with smaller radii emitters. Although flow impedance variations may account for the low threshold currents observed, we cannot reproduce the low energy spreads (and higher figure of merits reported by Mayer and Gaukler).

An important practical consequence of this work is to underscore the usefulness of operating the Ga LMIS at ~1 μA since, according to Fig. 4.51 this current level gives the maximum value of the figure of merit. For example, a current of 3 μA results in a figure of merit 43% lower than the value at 1 μA. Equally important is the fact that source life with respect to Ga utilization will increase by a factor of 3.

5. Summary

It is possible to operate the Ga LMIS in the Taylor cone mode at

currents down to a few nA using small radii emitters (< 0.5 μm). However, off-axis emission and multiple Taylor cone emission is more prevalent. The sought after lower value of energy spread at these lower currents is not realized but, instead, bottoms out at 4.5 eV as the current is decreased below 1 μA.

The figure of merit, $\frac{I'}{\Delta V^2}$, maximizes at or near 1 μA total current. This leads to a motivation to choose an emitter radius and shape so as to give stable operation at $\sim$1 μA. In this way emitter life and focused ion beam current density is maximized.

References

1. W. M. Clark, R. L. Seliger, M. W. Utlaut, A. E. Bell, L. W. Swanson, G. A. Schwind, and J. B. Jergensen, *J. Vac. Sci. Technol. B*, vol. 5, p. 197, 1987.

2. R. L. Reuss, D. Morgan, E. W. Greeneich, W. M. Clark, and D. B. Rensch, *J. Vac. Sci. Technol. B*, vol. 3, p. 62, 1985.

3. R. L. Seliger, J. W. Ward, V. Wang, and R. L. Kubena, *Appl. Phys. Lett.*, vol. 34, p. 310, 1979.

4. A. R. Waugh, A. R. Bayly, and K. Anderson, *Proc. 29th IFES, Eds. H. O. Anderson and H. Norden, Goteborg*, p. 409, 1982.

5. R. Young, J. Ward, and F. Scire, *The Rev. Sci. Instr.*, vol. 33, p. 999, 1972.

6. D. R. Kingham and L. W. Swanson, *Vacuum*, vol. 34, p. 941, 1984.

7. D. R. Kingham and L. W. Swanson, *Appl. Phys. A*, vol. 34, p. 123, 1984.

8. D. R. Kingham and L. W. Swanson, *Appl. Phys. A*, vol. 41, p. 157, 1986.

9. L. W. Swanson and D. R. Kingham, *Appl. Phys. A*, vol. 41, p. 223, 1986.

10. W. W. Dolan, W. P. Dyke, and J. K. Trolan, *Phys. Rev.*, vol. 91, p. 1054, 1953.

11. W. P. Dyke, J. K. Trolan, E. E. Martin, and J. P. Barbour, *Phys. Rev.*, vol. 91, p. 1043, 1953.

12. L. W. Swanson and G. A. Schwind, *J. Appl. Phys.*, vol. 49, p. 5655, 1978.

13. J. Mitterauer, *Proc. 28th IFES, Eds. L. Swanson and A. E. Bell, Portland, Oregon*, p. 75, 1981.

14. J. Mitterauer, *Proc. 31st IFES, Eds. P. Sudraud and P. Ballongue, Paris, France*, pp. C9-185, 1984.

15. K. Hata, S. Nishigaki, M. Watanabe, T. Noda, H. Tamura, and H. Watanabe, *J. de. Physique*, vol. C7, p. 375, 1986.

16. K. Hata, R. Ohya, S. Nishigaki, H. Tamura, and T. Noda, *Japan J. Appl. Phys.*, vol. 26, p. L896, 1987.

17. A. E. Bell and L. W. Swanson, *Appl. Phys. A*, vol. 41, p. 335, 1986.

18. J. P. Barbour, F. M. Charbonnier, W. W. Dolan, W. P. Dyke, E. E. Martin, and J. K. Trolan, *Phys. Rev.*, vol. 117, p. 1452, 1960.

19. L. W. Swanson and N. A. Martin, *J. Appl. Phys.*, vol. 46, p. 2029, 1975.

20. A. M. Russell, *J. Appl. Phys.*, vol. 33, p. 970, 1962.

21. A. E. Bell and L. W. Swanson, *Nucl. Instr. Meth. Phys. Res. B*, vol. 10/11, p. 783, 1985.

22. R. Levi-Setti, *Adv. Electron. Electron Phys. Suppl. A*, vol. 13, p. 261, 1980.

23. J. Melngailis, *J. Vac. Sci. Technol. B*, vol. 5(2), p. 469, 1987.

24. W. Knauer, "Optik," *Optik*, vol. 59, p. 335, 1981.

25. J. Orloff, *Optik*, vol. 63, p. 369, 1983.

26. E. Munro, *Image Processing and Computer-aided Design in Electron Optics, Ed. P. W. Hawkes*, p. 284, Academic, New York, 1973.

27. H. Paik, G. N. Lewis, E. J. Kirkland, and B. M. Siegel, *J. Vac. Sci. Technol. B*, vol. 3, p. 75, 1985.

28. W. Thompson, I. Honjo, M. Utlaut, and H. Enge, *J. Vac. Sci. Technol. B*, vol. 1, p. 1125, 1983 .

29. L. W. Swanson, *Nucl. Instr. Meth.*, vol. 218, p. 347, 1983.

30. A. E. Bell and L. W. Swanson, *Appl. Phys. A*, vol. 34, p. 123, 1984.

31. R. J. Culbertson, T. Sakurai, and G. H. Robertson, *J. Vac. Sci. Technol.*, vol. 16, p. 574, 1979.

32. G. L. R. Mair, R. G. Forbes, R. V. Latham, and T. Mulvey, *Microcircuit Engineering*, p. 171, Academic Press, 1983.

33. L. W. Swanson, G. A. Schwind, and A. E. Bell, *J. Appl. Phys.*, vol. 51, p. 3453, 1980.

34. G. L. R. Mair, D. C. Grindod, M. S. Mousa, and R. V. Latham, *J. Phys. D: Appl. Phys.*, vol. 16, p. L209, 1983.

35. H. P. Mayer and K. H. Gaukler, *J. de. Physique*, vol. 47, pp. C7-365, 1986.

CHAPTER 5

A PROXIMITY FOCUSED LMIS SYSTEM

The principle of LMIS operation is based on a needle substrate whereon a liquid metal (commonly gallium) flows. Without any electric field the liquid has a meniscus shape; however, when a high voltage is applied between the emitter and the extractor plate (typically several kV), the electric field and the surface tension forces compete and, for a critical voltage value, form a conical equilibrium shape, the well-known "Taylor cone", with a 49.3° half angle. Furthermore, a small protusion also occurs on the apex of the cone whose size depends on the emission current, being about 20 Å in radius and about 300 Å in length for an emission current of 10 μA[1,2]. As in field electron emission the beam is very divergent (20° half angle for 1-2 μA).

One of the main objectives of this research project has been the investigation of the LMIS in a STM set-up at spacings from 100 μm down to a few hundred angstroms or less. Electron sources have been used in the scanning tunneling microscope for imaging the surface[3] and for modifying the surface through electron beam lithography[4,5]. The argument for investigating LMIS in a STM has been to use these ion sources for micromachining and microfabrication in what is essentially a proximity focused mode as has been discussed earlier in Chapters 1 and 4. It could also be feasible to use these sources in the STM embodiment for deposition at voltages below the sputtering threshold. The LMIS could also be operated in the reverse polarity as an

electron emitter (see Chapter 4.A and 4.B) for mapping the surface topography in an application similar to scanning tunneling microscopy.

Some of the potential problems and issues that arose during the proximity focusing have been discussed in Chapter 4. The emission instabilities of the LMIS that arose due to the back sputtered neutrals condensing on the source is discussed in the next section as also the close spaced investigations that were carried out with the LMIS.

A. CLOSE-SPACED INVESTIGATIONS WITH A CONVENTIONAL LIQUID METAL ION SOURCE

1. Threshold Voltage Considerations

Before discussing the close spaced investigations in the LMIS-STM it may be worthwhile to develop the Taylor theory and its extension to very small spacings between the LMIS and the target, especially the variation in threshold voltage of the LMIS with diode spacing as predicted by the theory.

Taylor[6], showed that there is a unique geometry for which the electrostatic stress and surface tension stress balance one another over the entire surface of the liquid. This shape is that of a cone of half angle 49.3°. Solutions of Laplace's equation for conical conductors take the form[7]:

$$V = V_0 + \sum_{i=0}^{\infty} P_{\nu_i}(\mathrm{Cos}\theta)(A_{\nu_i} r^{\nu_i} + B_{\nu_i} r^{-\nu_i - 1}) \tag{5.1}$$

where the indices ν_i are in general non-integral. To ensure the correct behavior as r approaches zero, $B_{\nu_i}=0$. For the special case when a counterelectrode of shape generated by:

$$r = R_0/[P_{\nu_0}(\mathrm{Cos}\theta)]^{1/\nu_0} \tag{5.2}$$

is selected, V is reduced to a single term in r:

$$V = V_0 + A_{\nu_0} r^{\nu_0} P_{\nu_0}(\mathrm{Cos}\theta), \tag{5.3}$$

where V is chosen so that $P_{\nu_0}(\mathrm{Cos}\theta) = 0$ on the cone surface when $\theta = \beta$, where β is the cone exterior half angle, A_{ν_0} is a constant which depends on the geometry of the electrodes, V_0 is the potential of the cone, R_0 is the axial distance from the cone apex to the counterelectrode, and r is the axial position of the emitter apex as seen in Fig. 4.4. On the counterelectrode, $V = V_{CE}$ so that

$$A_{\nu_0}=(V_{CE}-V_0)/R_0{}^{\nu_0}. \tag{5.4}$$

The electric field E_θ, perpendicular to the cone surface may be found from

$$E_\theta = (\partial V/\partial\theta)_r\, r^{-1} = A_{\nu_0} r^{\nu_0-1} P'_{\nu_0}(\mathrm{Cos}\theta) \tag{5.5}$$

If we seek a balance between the electrostatic stress σ_e and the surface tension stress σ_s on the surface of a liquid cone of half angle α we have:

$$\sigma_e=\sigma_s \tag{5.6}$$

where $\sigma_e=E^2{}_\theta/8\pi$ and $\sigma_s=(\gamma\mathrm{Cot}\alpha)/r$, so that

$$(1/8\pi)A^2{}_{\nu_0}\left(r^{\nu_0-1}\right)^2[P'_{\nu_0}(\mathrm{Cos}\beta)]^2 = (\gamma\mathrm{Cot}\alpha)/r \tag{5.7}$$

As shown by Taylor[6], if ν_0 is taken to equal 1/2, a value of A_{ν_0} may be chosen so that $\sigma_e = \sigma_s$ for all values of r i.e. at all points on the surface of the cone. Substituting ν_0=0.5 in $P_{\nu_0}(\mathrm{Cos}\beta) = 0$, we obtain $\beta = 180\text{-}\alpha =$

130.7° corresponding to an internal cone half angle of $\alpha = 49.3°$; in this case $P'_{0.5}(\text{Cos}\beta) = 0.974$ and the counterelectrode shape is derived from $r = R_0 \{P_{0.5}(\text{Cos}\theta)\}^{-2}$. By noting that at the counterelectrode axial position $r = R_0$ and obtaining $A_{0.5}$ from Eq. (5.7) then, following Taylor, one may derive an expression for the counterelectrode/cone potential difference $V_{CE} - V_0$ required to stabilize the cone, i.e.,

$$V_{CE} - V_0 = \Delta V_s = 1.432 \times 10^3 (R_0 \gamma)^{0.5} \quad [V], \tag{5.8}$$

where R_0 is in cm and γ is in dyne/cm.

To determine the variation in the threshold voltage V_t with the diode spacing R_0 we write:

$$\Delta V_s = k \times (R_0)^{0.5} \tag{5.9}$$

$$\frac{(\Delta V_s)_1}{(\Delta V_s)_2} = \left[\frac{(R_0)_1}{(R_0)_2} \right]^{0.5} \tag{5.10}$$

Considering (from experiments) $\Delta V_s = V_t = 9.0$ kV for a counterelectrode/cone separation R_0 of 0.05 cm, we can arrive at various values of $\Delta V_s = V_t$ for various separations. Some selected values are provided on the next page.

Table 5. Threshold voltages V_t for various diode spacings for a liquid metal ion source. (γ = 720 dynes/cm)

Diode Spacing (cm)	Diode Spacing	V_t (volts)
1.0e-08	1.00 Å	4.02
1.0e-07	10.00 Å	12.72
1.0e-06	0.01 μm	40.25
3.0e-06	0.03 μm	69.71
5.0e-06	0.05 μm	90.00
1.0e-05	0.10 μm	127.28
5.0e-05	0.50 μm	284.60
1.0e-04	1.00 μm	402.49
2.0e-04	2.00 μm	569.21
3.0e-04	3.00 μm	697.14
5.0e-04	5.00 μm	900.00
1.0e-03	10.00 μm	1272.79
2.0e-03	20.00 μm	1800.00
3.0e-03	30.00 μm	2204.54
4.0e-03	40.00 μm	2545.58
5.0e-03	50.00 μm	2846.05
6.0e-03	60.00 μm	3117.69
7.0e-03	70.00 μm	3367.49
8.0e-03	80.00 μm	3600.00
9.0e-03	90.00 μm	3818.38
1.0e-02	100.00 μm	4024.92

A plot of the threshold voltage versus (diode spacing)$^{1/2}$ derived from the Taylor theory and shown in the table on the previous page, is given in Fig. 5.1.

2. Experimental

For the close spaced LMIS investigations, two approaches were tried for fabricating the emitter; the first one being the "a.c. method of electrolytic shaping of emitters" and the second one by "grinding the emitters" to a sharp point. The emitters fabricated by grinding a tungsten wire blank to a sharp end point of radius between 2-4 μm performed much better with regard to stability of the LMI source, i.e. the current emitted at constant voltage remains virtually unchanged over long periods of time. The onset of LMIS operation, too seems to occur generally at lower currents $\sim$0.5 μA for "ground" emitters as compared to "electrochemically etched" emitters. Both types of emitters were roughened in 2N NaOH for $\sim$1 - 2 secs after fabrication. This was done to facilitate smooth flow of the liquid to the apex of the emitter. Figures 5.2 and 5.3 show typical SEM micrographs of electrochemically etched and ground emitters. Also attached, Fig 5.4, is a typical I-V characteristic for a gallium LMIS, the source most used in our close-spaced investigations.

After wetting with Ga in the wetting chamber, the emitter is turned on by applying the appropriate extraction voltage and the emission current is noted. The emission pattern is also observed for centering and if not, it is centered by gently heating and/or applying an overvoltage while in the

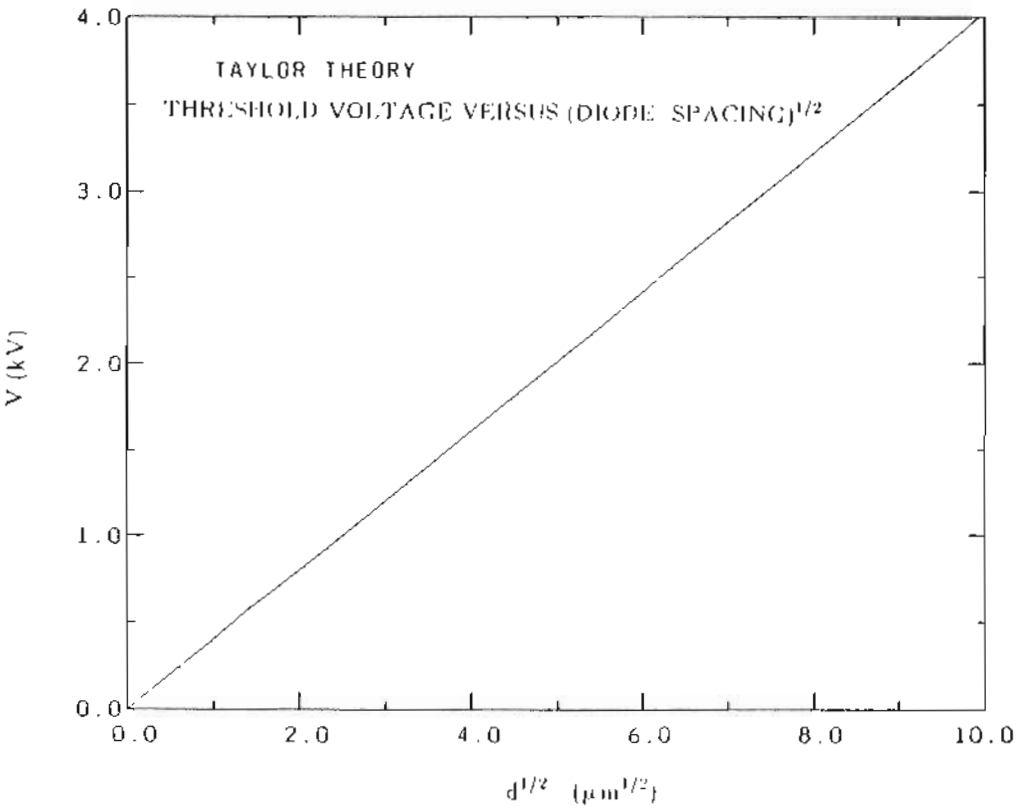

Figure 5.1 : Plot of variation in threshold voltage versus (diodespacing)$^{1/2}$ for a liquid metal ion source from the Taylor theory.

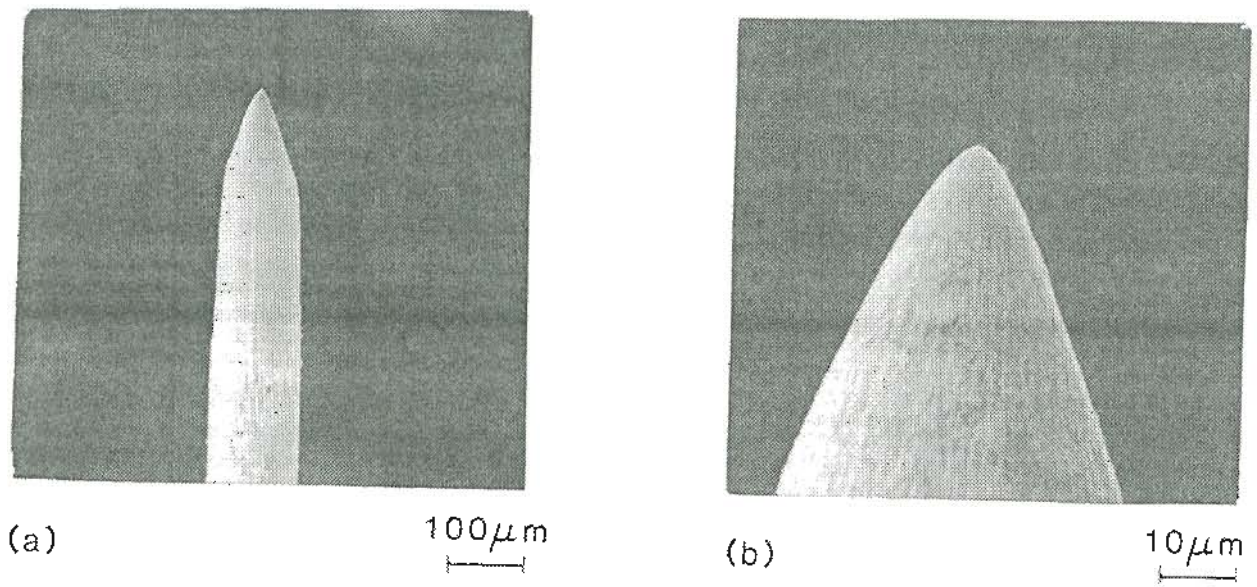

Figure 5.2 : Electrochemically etched W LMIS needle shape: (a) 100X magnification; (b) 1000X magnification; the emitter has been electrochemically roughened.

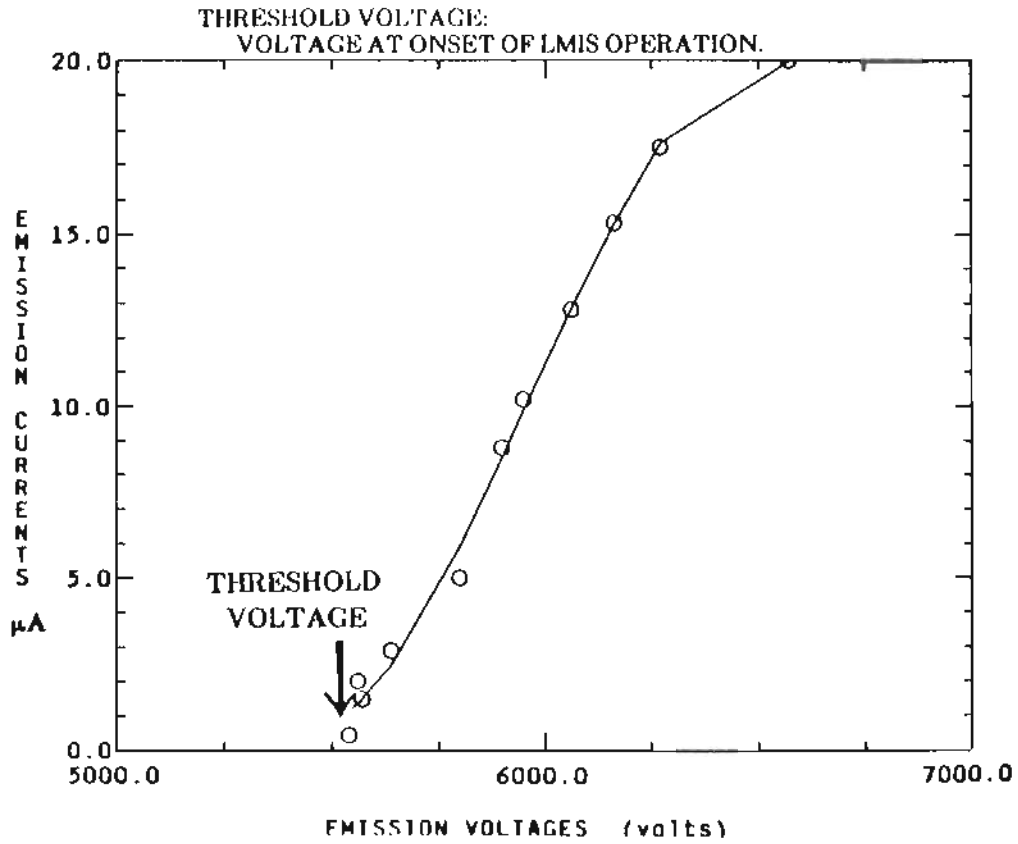

Figure 5.4 : Total emission current versus emitter – extractor potential difference for a conventional Ga LMIS and W needle.

process of emission.

The LMI source is then transferred to the source holder in the STM set-up described earlier. The initial experiments were concerned with determining the close spaced emission characteristics for a gallium LMIS and a n+ GaAs substrate doped with silicon. A GaAs substrate was used initially, in the hope that back sputtered material returning to the gallium source during close spaced operation would not result in instability of the LMIS as probably would, with some other target material. It was later seen that close spaced ion emission worked as well with other targets like silicon, chrome on Glass, and some II-VI compounds like MnTe, MnCdTe etc. Instability of the LMIS did occur at separations of 2 - 3 mil, but the source operated more and more stably as the separation between the LMIS and the target decreased below 2 mil.

The larger separations, d, of the LMIS from the substrate were determined as has been discussed earlier in Chapter 4.B. A resistor of value 50 MΩ was provided in the circuit to prevent damage to the power supply when the LMIS made physical contact with the substrate when operating at close spacings. The smallest distances measured were uncertain by an amount equal to the length of the Taylor cone protusion which is believed to extend by about 1 μm. Hence actual needle - substrate separations were less than those recorded by about the size of the Taylor cone.

3. Results

The dependence of the threshold voltage V_t for LMIS operation as a function of d were initially plotted on logarithmic scales (Fig. 5.5) for the a.c. etched emitter of Fig. 5.2 and for the mechanically ground emitter of Fig. 5.3 since both the threshold voltages and the diode separations spanned a three order of magnitude range. The closest spacings that were obtained for the two plots were 6.7 μm and 1.7 μm respectively. Figure 5.6 shows the above graphs replotted on a linear—linear scale in order to better show the behavior at threshold. Included in Fig. 5.6 is another run (#3), from ~12μm down to eventual touching of the substrate by the LMIS. The dependence of V_t on d, was also determined for silicon and the plots are shown in Fig. 5.7. Figure 5.8 shows SEM photographs of the region on the silicon substrate where V_t versus $d^{1/2}$ data were obtained. The Auger plot in Fig. 5.9a confirms the presence of gallium in the trench, which presumably arose due to sputtering while obtaining the close spaced emission data. It is interesting to note the sizable drop of liquid near the trench which probably pulled off from the LMIS when the source was operating at close spacings. The Auger energy plot in Fig. 5.9b taken around the trench registers the presence of gallium in the drop of liquid. Also shown in Fig. 5.10 is a plot of V_t vs d on logarithmic scales, reproduced from G. B. Assayag et al.[8], for a Au LMIS and a silicon target using a mechanical method of obtaining coarse LMIS—substrate motion.

In the process of determining the dependence of the threshold voltage on

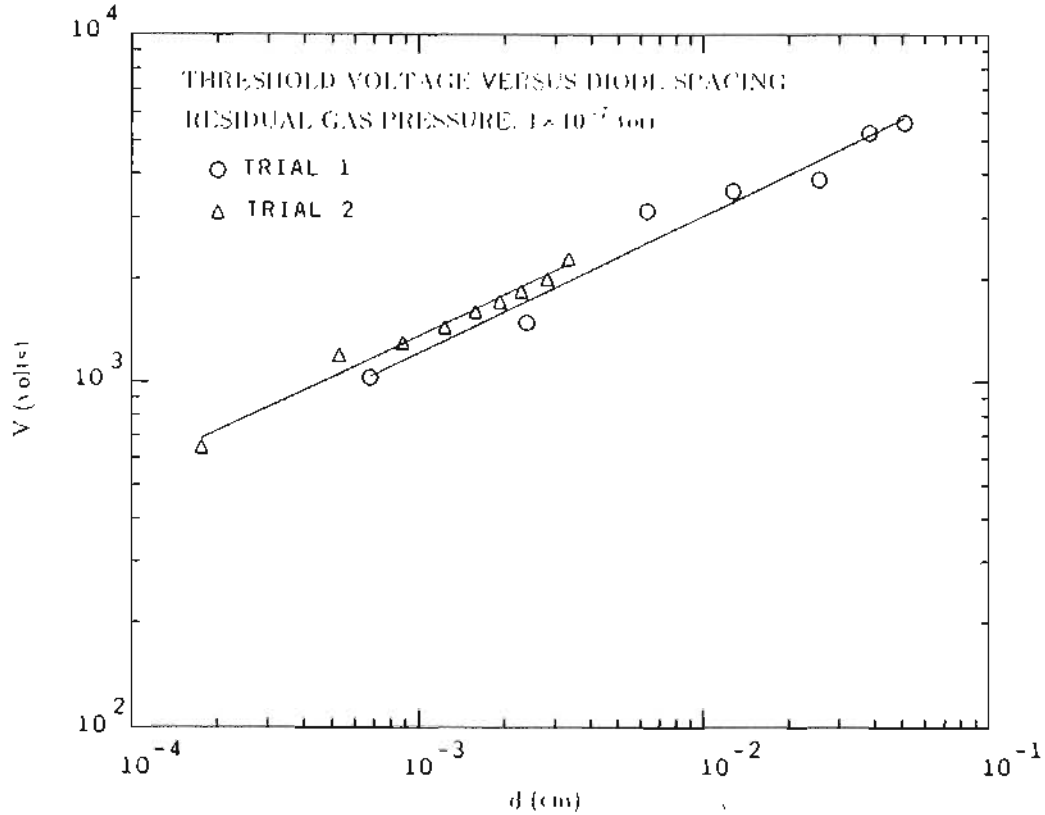

Figure 5.5 : Plots of threshold voltage versus diode spacing on logarithmic scales at a constant threshold current of 0.5 μA for GaAs substrate at a residual gas pressure of 1×10^{-7} torr.

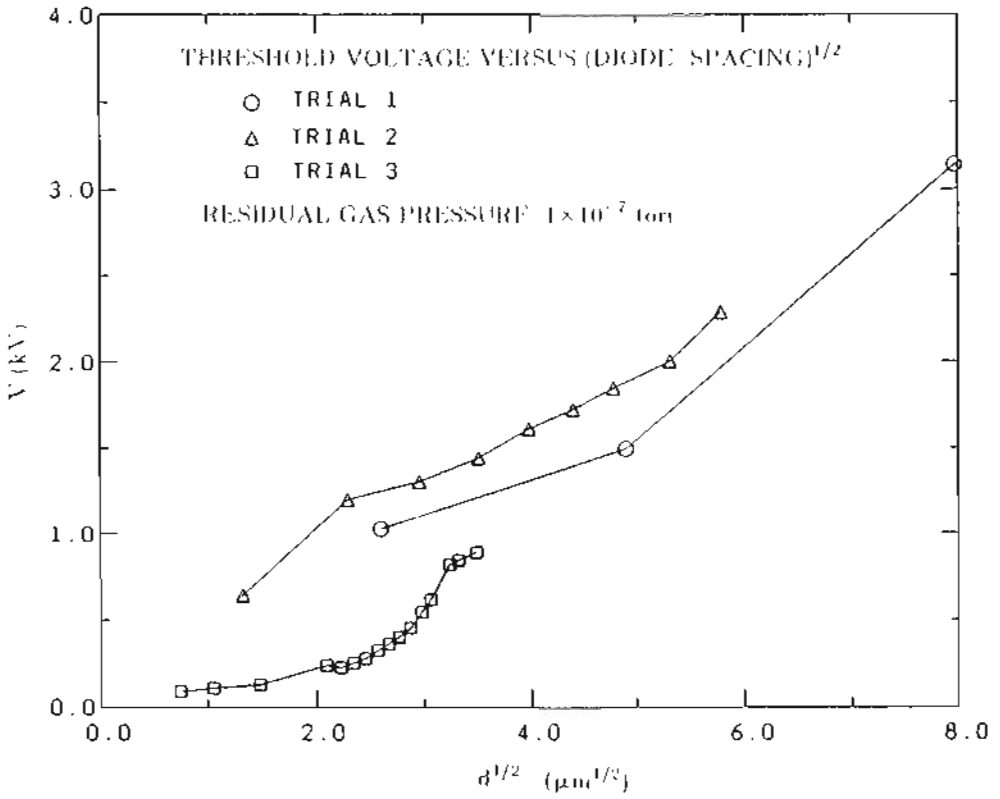

Figure 5.6 : Plots of threshold voltage versus (diode spacing)$^{1/2}$ at a constant threshold current of 0.5 μA for GaAs substrate at a residual gas pressure of 1×10^{-7} torr.

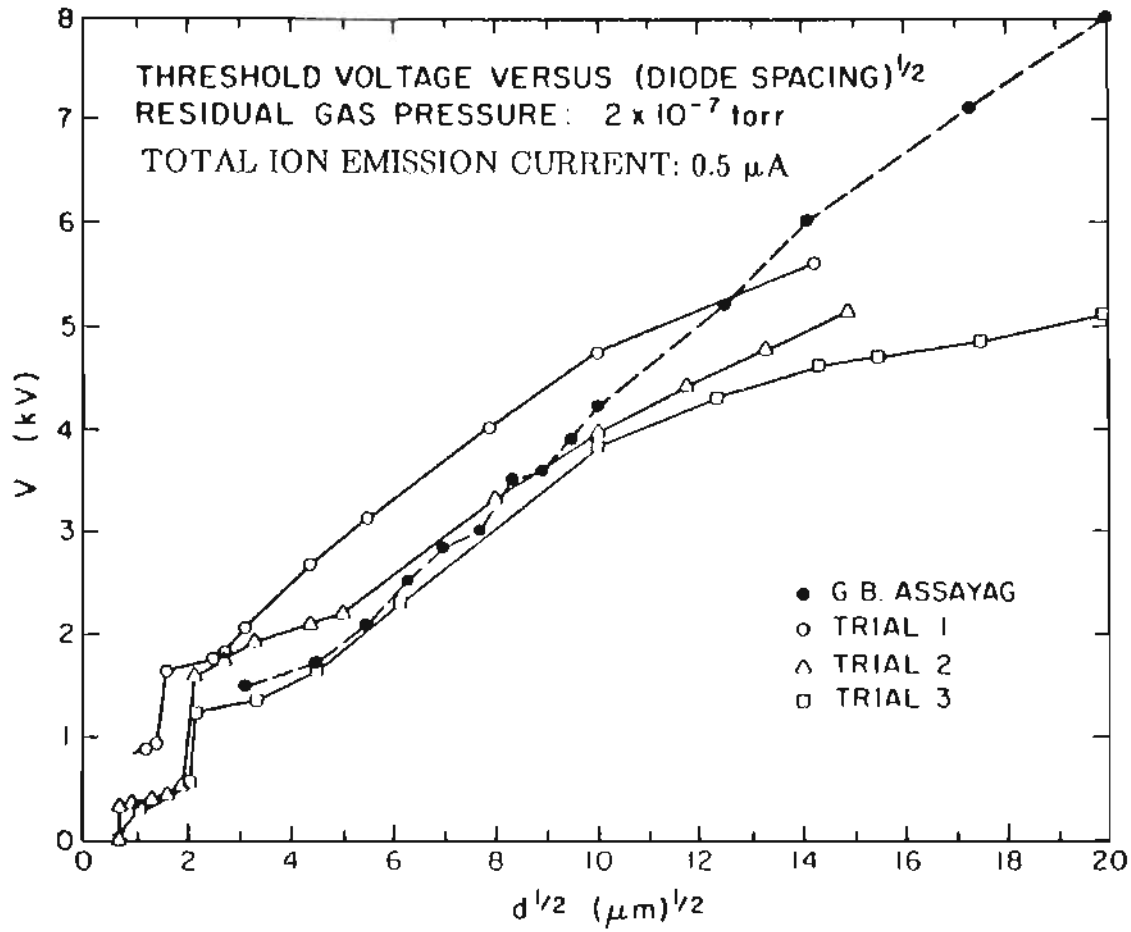

Figure 5.7 : Plots of threshold voltage versus (diodespacing)$^{1/2}$ at a constant threshold current of 0.5 μA for silicon substrate at a residual gas pressure of 2×10^{-7} torr.

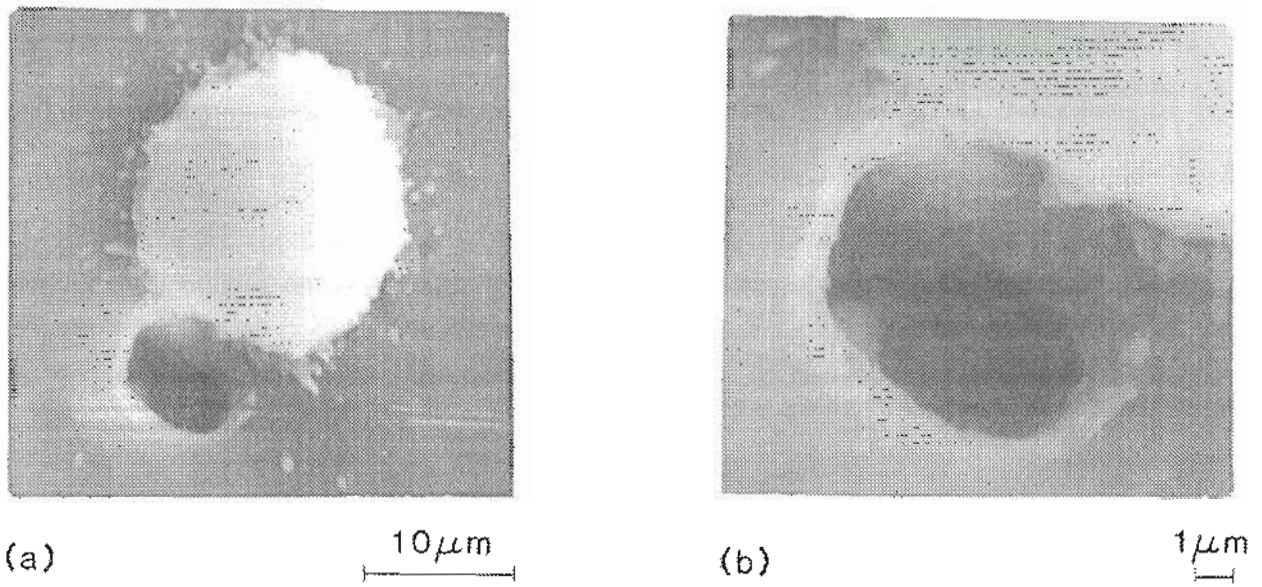

Figure 5.8 : SEM photographs of the region on the silicon substrate where the data for Fig. 5.7. were obtained. Note the sizable drop of liquid near the trench.

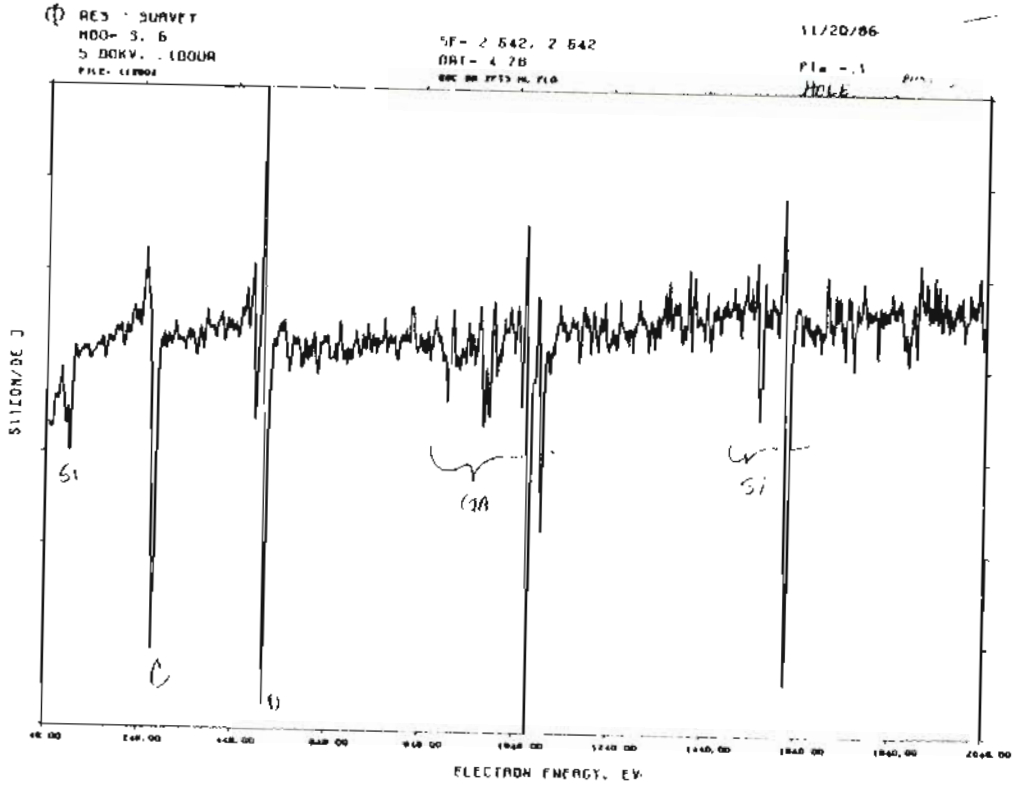

Figure 5.9(a) : Auger energy plot inside the trench shown in Fig. 5.8.

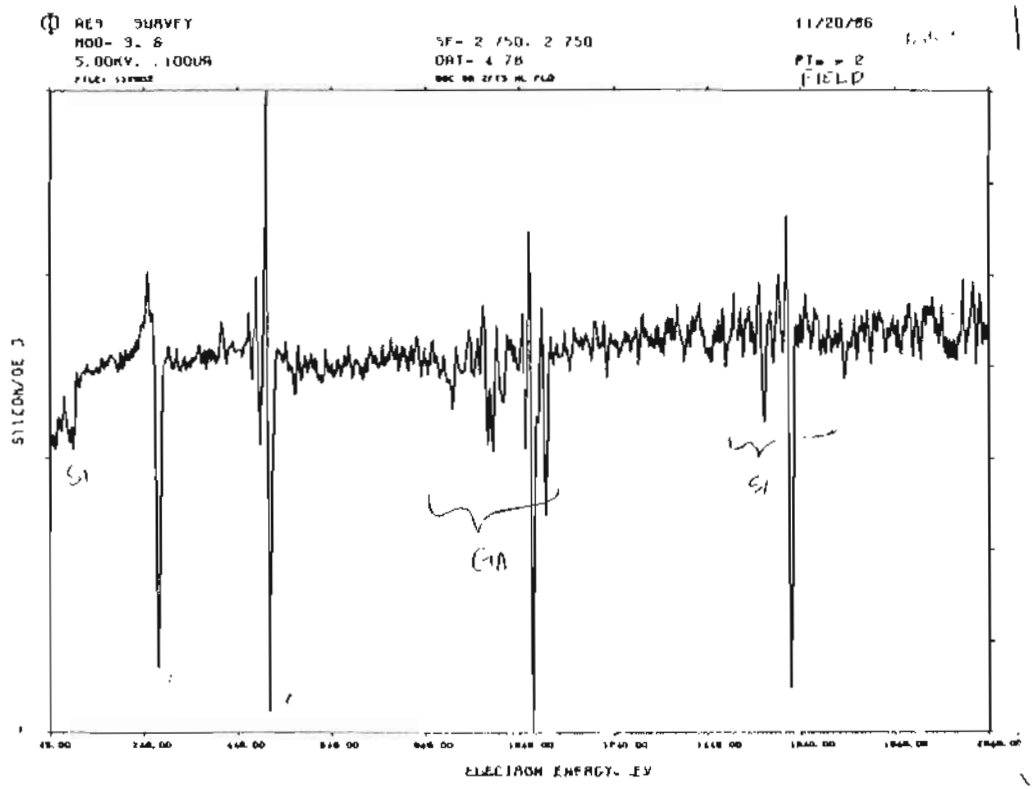

Figure 5.9(b) : Auger energy plot outside the trench shown in Fig. 5.8.

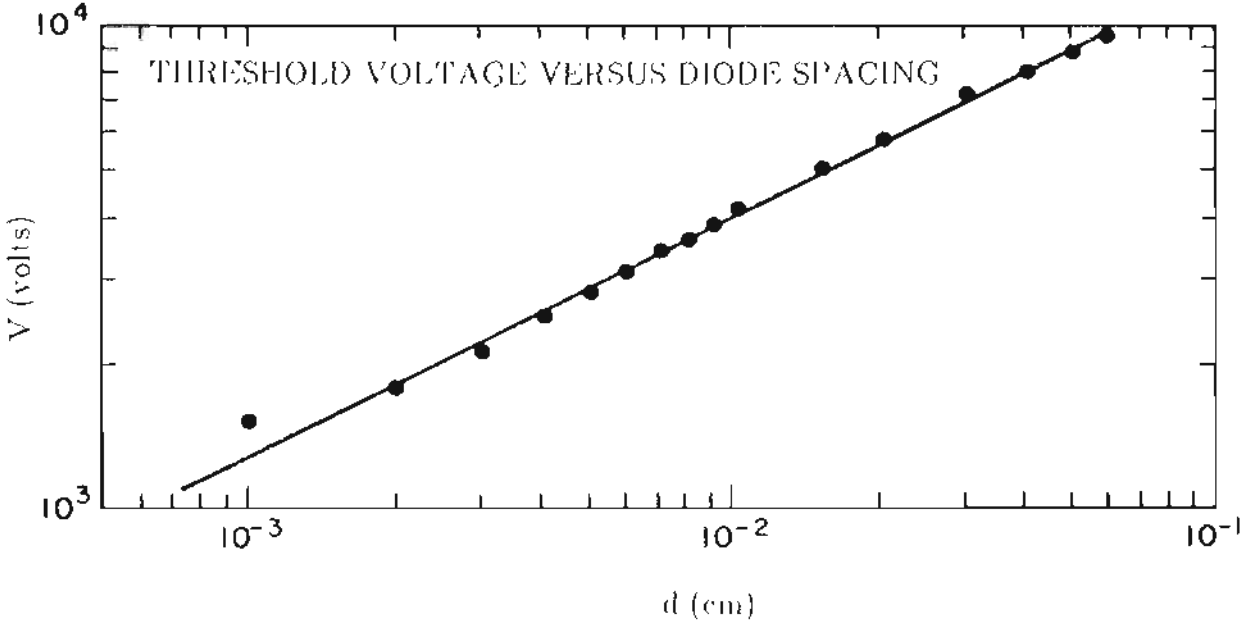

Figure 5.10 : Plot of threshold voltage versus diode spacing at a constant threshold current for silicon substrate and a Au LMIS.

the diode spacing, it was noticed that emission instability occurred in the liquid metal ion source during the proximity focusing experiments. These emission instabilities were found to be most prominent at LMIS—substrate separations of ~2 to 3 mil. The reason is believed to be due to the fact that at 2 to 3 mil separations the voltage to operate the LMIS is large enough (2 to 3 kV) that the back sputtered "neutrals" would have enough initial kinetic energy to return to the source and condense on it thereby causing instability. Figure 5.11 shows SEM micrographs of a gallium LMIS before and after use in the STM set-up. There seems to be some sputter induced deposition in the tip region as seen in the SEM photographs. Figure 5.12. is an SEM photograph of the tip in Fig. 5.11 after etching away the gallium using concentrated HCl. The damage, presumably caused by sputter induced deposition are very evident on the surface of the tip.

4. Discussion and Summary

As discussed by Bell and Swanson[9], the threshold voltage for LMIS emission from the Taylor theory is expected to be proportional to the square root of the separation, d, in the case where the collector or extractor electrode shape is generated according to Eq. (5.2).

The square root relationship holds quite well (for $d \leq 100$ μm) for all the runs 1,2 and 3 as well as for the data of Assayag[8] as shown in Fig. 5.7. At higher values of d (i.e for $d \geq 100$ μm) the square root relationship was not followed so well for runs 1,2 and 3. The sharp drop in voltage occurring below the knee in the plots shown in the Figs. 5.6 and 5.7 could be due to

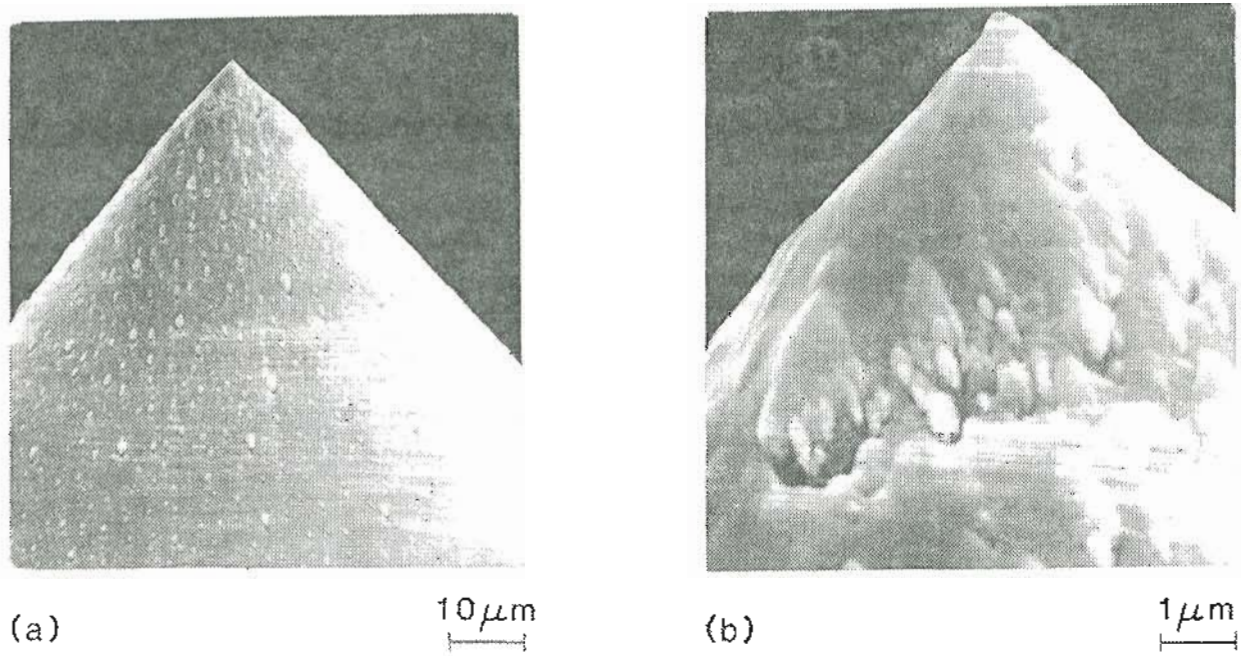

Figure 5.11 : SEM micrographs of LMIS after use in close-spaced investigations in the STM showing possible sputter induced deposition: (a) 1000X magnification; (b) 10000X magnification of region near emitter apex.

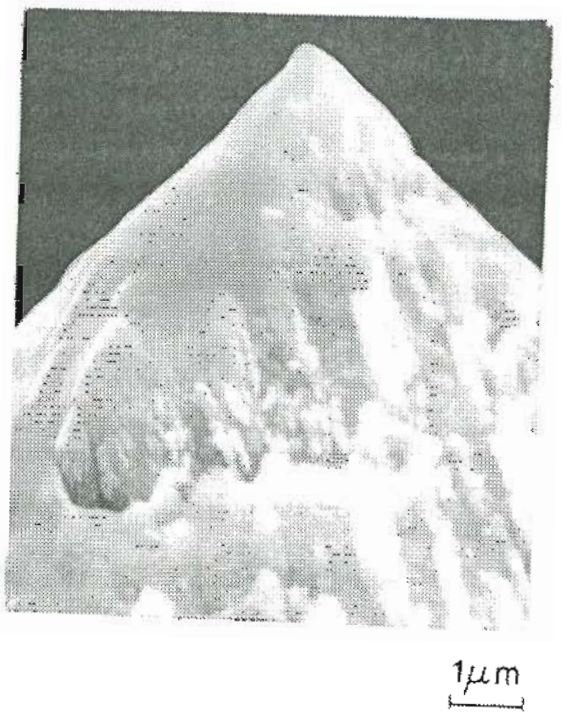

Figure 5.12 : SEM micrograph of the LMIS in Fig. 5.11 after removing the gallium with concentrated HCl.

the distortion of the liquid cone and pulling off of a drop of liquid so that the subsequent values of "d" are reduced by the presence of a liquid pool in front of the LMIS. Such liquid drops being pulled off from the LMIS have been visually noted through the binocular microscope as the LMIS approached to < 10 μm of the substrate.

The possibility of contact between the LMIS and the substrate as accounting for the knee in the plots in Figs. 5.6 and 5.7 may be ruled out because of the high resistance between the substrate and the LMIS ($\sim 10^8$ Ω). Any plausible geometry for a liquid bridge between substrate and LMIS would be of the order of 10^2 Ω. Contact did occur, at values of d less than 1 μm and is shown in the figures as a final step decline to zero.

At close-in spacings special effects come into play: the fact that the Taylor cone is probably of the order of 1 to 4 μm in length, so that the coarse movement bringing the LMIS with its underlying needle to within a few μm of the substrate followed by development of the Taylor cone as the voltage is applied is obviously fraught with the possibility of the Taylor cone spearing into the substrate as the LMIS is turned on. Another series of effects arises from the fact that the current density of the LMIS emission current rapidly reaches levels at which significant changes to the substrate geometry occur either as a result of sputter erosion of the substrate by ion bombardment or due to build up of deposits of gallium that conceivably could occur if ion bombardment occurs at energies where sputtering effects are diminished. This has been discussed in Chapter 4.C.

Because of the high current densities prevailing at close LMIS — substrate spacings and the resulting uncertainties in those spacings, it was deemed appropriate to investigate close spaced ion emission from the low current LMIS developed earlier (Chapter 4.C). This is discussed in the next section.

B. CLOSE-SPACED INVESTIGATIONS WITH A LOW CURRENT LIQUID METAL ION SOURCE

1. Introduction

The concern of operating the conventional LMIS with apex radii between 2 to 4 μm has been the significant increase in current density levels that occur as the diode spacing decreases resulting in either sputter erosion of the substrate by ion bombardment or net deposition of gallium (the principal liquid metal used for this study) at ion energies below the sputtering threshold at extremely rapid rates.

The new low current (and low voltage) Ga LMIS [10] that has been developed (See Chapter 4.C), operates at currents as low as 1 nA, instead of the usual low current threshold values of 1 μA for the larger, more conventional LMIS. The operation of these low current LMIS can be attributed to the normal Taylor cone mode of operation, by the fact that the emission was observed as a featureless bright spot on the phosphor screen of a channel plate image intensifier in a field ion microscope set-up. In addition, below a very low threshold voltage (typically, between 1 to 2 kV) the emission current was characterized by pulses, the frequency of which increased with emission current, finally merging into d.c. at the threshold voltage. This is typical of LMIS behavior.

2. Experimental

The low current LMIS used for this investigation was electrochemically etched from a 5 mil tungsten rod (spotwelded to a tantalum loop) down to a very sharp point using the d.c. drop-off process. The apex radii obtained was between 0.05 to 0.1 μm. The SEM photographs of a typical emitter used in the close spaced investigations are shown in Fig. 4.5.

After etching the tip in the d.c. drop-off process, it was wetted with gallium in a wetting chamber. The LMIS was then placed in the scanning tunneling microscope embodiment. The large separations, d, of the LMIS from the substrate were determined by use of a 30X binocular microscope with a calibrated reticule in the field of view. This was adequate down to separations of ~12 μm. Smaller distances, down to separations of 2 to 3 μm were estimated by counting the number of electromagnetic pulses delivered to the calibrated magnetic drive[11]. The separations below this were generated by using the piezodrive units for which the voltage/distance relationship was known (~ 7 nm/V).

3. Results

Figure 5.13 shows a summary of the experiments using a low current Ga LMIS and a silicon substrate where the threshold voltage V has been plotted against the diode separation d in four separate runs. The X axis represents the distance from the substrate, measured from the point at which the Taylor cone came into contact with the substrate. Figure 5.14 shows a

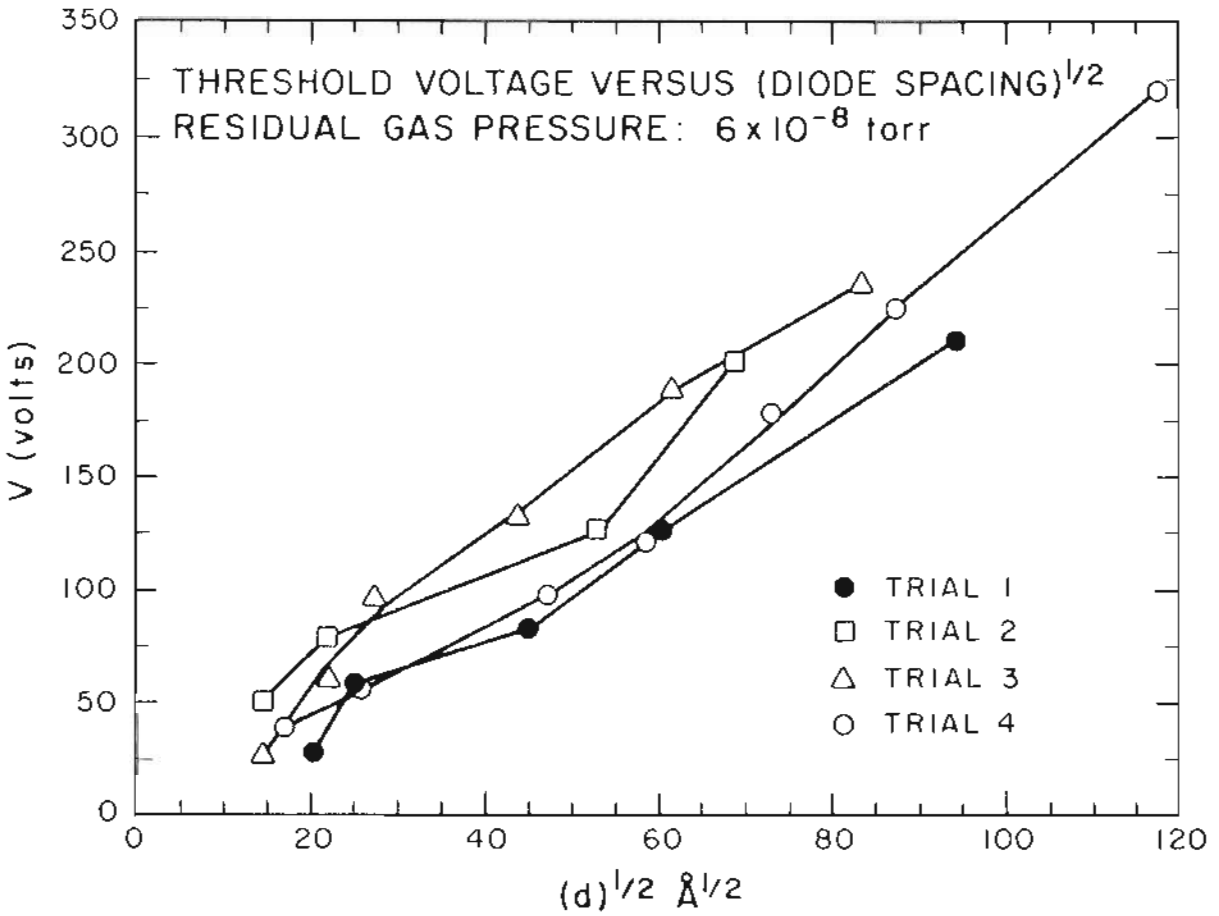

Figure 5.13 : Plots of the threshold voltage versus (diodespacing)$^{1/2}$ at a threshold current of 8.0 nA for a silicon substrate.

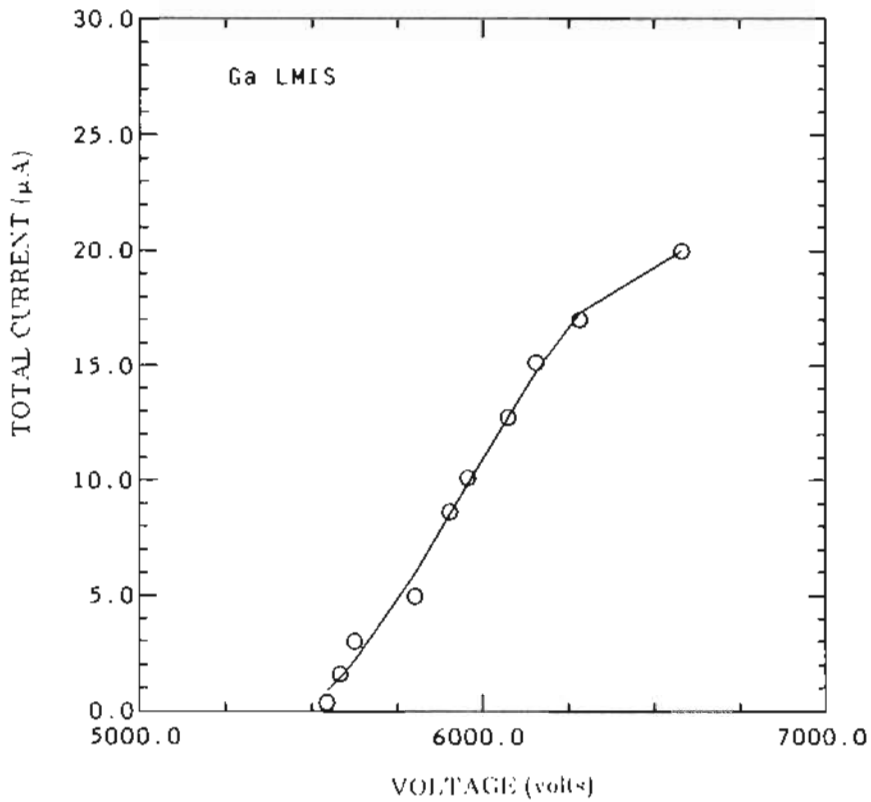

Figure 5.14 : Current-voltage plot for a gallium low current LMIS at an estimated spacing of 1500 μm.

current/voltage plot using the low current Ga LMIS at an estimated tip/substrate spacing of 1500 μm. Figure 5.15 show current/voltage plots at various close spacings using the low current LMIS and a Si substrate.

4. Discussion and Summary

The model for LMIS operation according to the Taylor theory, developed earlier[6], is that the threshold voltage is proportional to the emitter — target spacing, or

$$V = kd^{1/2} \tag{5.11}$$

where

$$k = 1.432 \times 10^3 \times \gamma^{1/2} \text{ volts/cm}^{1/2}$$

and γ is the surface tension of gallium (720 dynes/cm)

$$k_{theory} = 3.84 \text{ volts/Å}^{1/2}$$

The slopes of the V versus $d^{1/2}$ curves in Fig. 5.13. were found to be:

$$k_{experiment} = \frac{d(V)}{d(d^{1/2})} \sim 3.1 \pm 0.4 \text{ volts/Å}^{1/2}$$

Considering the fact that the LMIS is operating at spacings of the order of the Taylor cone protusion as well as the high current densities expected at

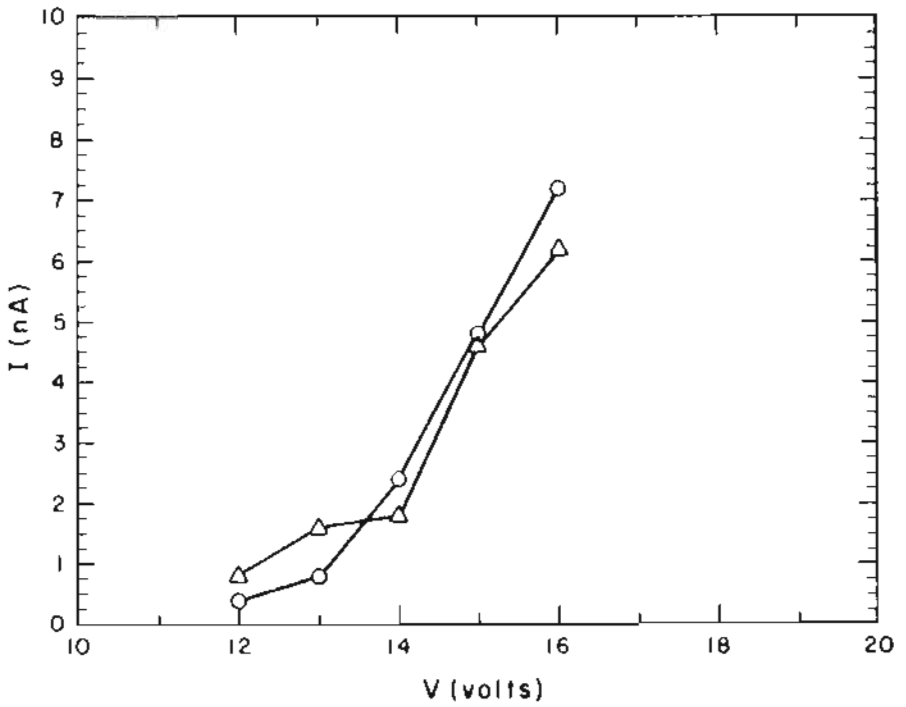

Figure 5.15(a) : Current-voltage plots for a gallium low current LMIS and silicon substrate at an estimated spacing of $\leq$ 250 Å.

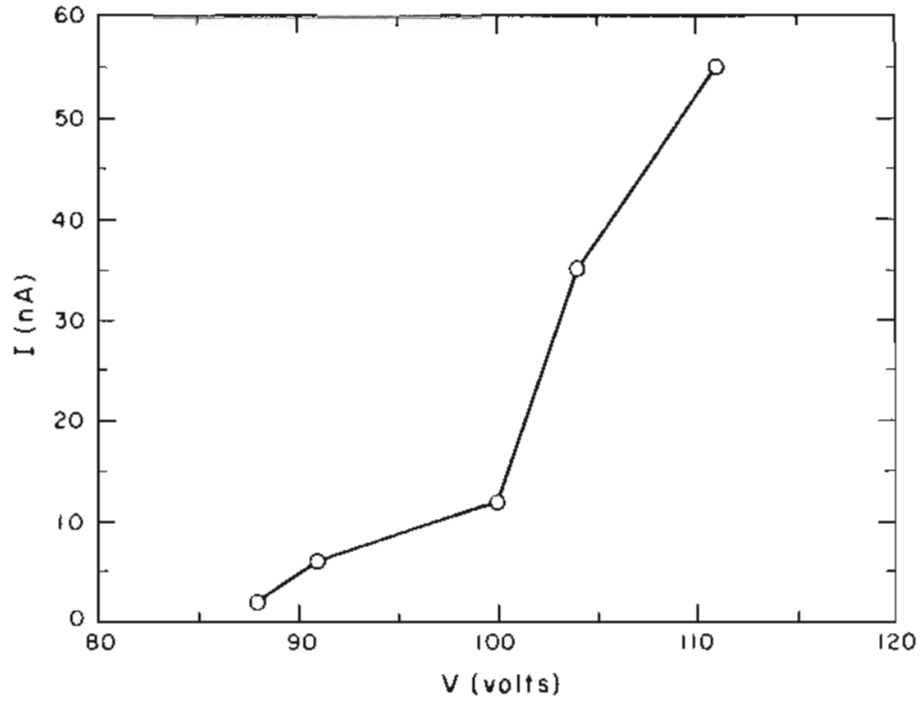

Figure 5.15(b) : Current-voltage plots for a gallium low current LMIS and silicon substrate at an estimated spacing of $\leq$ 3000 Å.

such spacings, the above values of k seem to be in relatively good agreement with one another.

The much closer approach to the substrate attained in Figs. 5.14 and 5.15, is probably due to the use of the low current LMIS which, because of its small radius, is capable of supporting a very small Taylor cone. This is estimated to be of the order of 500 Å long, as compared to the 2 to 4 μm long Taylor cones for the larger LMIS.

The fact that these low current LMIS operate at such close spacings and enable us to obtain any consistent data at all, considering the prodigious current densities expected at those spacings, would seem to mean that significant sputtering is probably absent on account of these low voltages at which these LMIS function. Significant deposition could also be ruled out because the landing ions would have enough energy to diffuse away along the plane of the substrate, from the region of impact. Further no evidence of deposition has been noted on examining the regions of impact on the substrate at the present voltages ($\sim$25 to 40 volts) at which the LMIS operate. It is concievable that at closer spacings (and consequently lower threshold voltages) there would be net deposition from the LMIS.

C. MICROMACHINING WITH THE PROXIMITY FOCUSED LMIS

1. Introduction

Microelectronic circuit fabrication is based on the ability to selectively remove (etch) material from and add (deposit) material to the surface of a suitable substrate (e.g. semiconductor wafers). The methods used at the present time to etch the desired surface structures on the substrate, range from wet chemical etching, to plasma etching and sputtering. However the drive for new devices and circuits such as gallium arsenide integrated circuits demand patterning down to submicron dimensions with highly accurate linewidth control. These materials though, are difficult to etch using chemical methods. Ion beam etching (using a well collimated beam) offers several advantages for such materials. They are (1) high etch resolution with no mask undercut, (2) the ability to etch any material or multilayer combinations, and (3) the ability to control the profiles of etched sidewalls[12].

It is quite possible to use either focused ion beams or broad-area ion beams with masks to perform ion beam etching. Ion beams have very little proximity effect and can be used down to 0.1 μm resolution or even better[13-15]. Further, ion beams can etch any material (e.g. permalloy) or combinations of materials (such as multilayer metallizations Ti, Pt, Au) that might be difficult to etch using wet or plasma chemical techniques. Chemical etch rates are often highly selective, whereas ion etch rates of most materials differ by less than an order of magnitude[12]. Hence, multilayer structures can be etched in one continuous process. Second, ion etching does not suffer from

excessive etch penetration beneath the masking layer, which leads to mask undercut or tunnel formation where lines cross over sloped surfaces (anisotropic etching).

The nature of ion etching though, has several unique problems. In the case of focused ion beams where the exposure is serial (meaning the ion beam is focused to a suitable small spot and scanned over the desired surface areas), it appears that, because of speed limitations they will be used mainly for direct (mask-less) implantation, and for repair of photo and x-ray masks[16,17] and the more recent use as an integrated circuit restructuring tool[18] and the fabrication of optical surfaces on semiconductor lasers[19,20] rather than in lithography. Broad area ion beams for projection lithography, analogous to projection lithography with light, which can cover large areas at a time and expose resists with high aspect ratios in a short time seem extremely promising. Although the problem of fabrication of high resolution masks for projection lithography is difficult, there have been significant gains made and the results appear very good.

2. Interaction of Ions with Surfaces

Before proceeding to discuss ion etching with the proximity focused liquid metal ion source (LMIS) it may be worthwhile to mention in brief the process of the interaction of an ion with the atoms of a target and the resultant modification of the surface. A parameter that follows almost naturally from the study of the interaction process is the sputtering yield of the ion on the atoms of the target and will be discussed later.

When an ion approaches the surface of a target (of the same or different material), one or more of the following phenomena[21] may occur (Fig. 5.16, reproduced from Chapman[21]).

* The ion may be reflected, probably being neutralized in the process. This reflection is the basis of an analytical technique known as *Ion Scattering Spectroscopy,* which enables us to characterize the surface layers of the material and obtain information about the fundamental ion-surface interaction.

* The impact of the ion may cause the target to eject an electron, usually referred to as a *secondary electron.*

* The ion may be buried in the target. This is the phenomenon of *ion implantation,* which is used extensively in integrated circuit technology for selectively doping silicon wafers with precisely controlled amounts and depth profiles of specific impurities.

* The ion impact may also be responsible for some structural rearrangements in the target material. Rearrangements may vary from simple vacancies (missing atoms) and interstitials (atoms out of position) to more gross lattice defects such as changes of stoichiometry (i.e. relative proportions) in alloy or compound targets, or to changes in electrical charge levels and distributions, and are usually collectively referred to as *radiation damage,* a subject of great importance, especially in relation to nuclear energy.

* The ion impact may set up a series of collisions between atoms of the

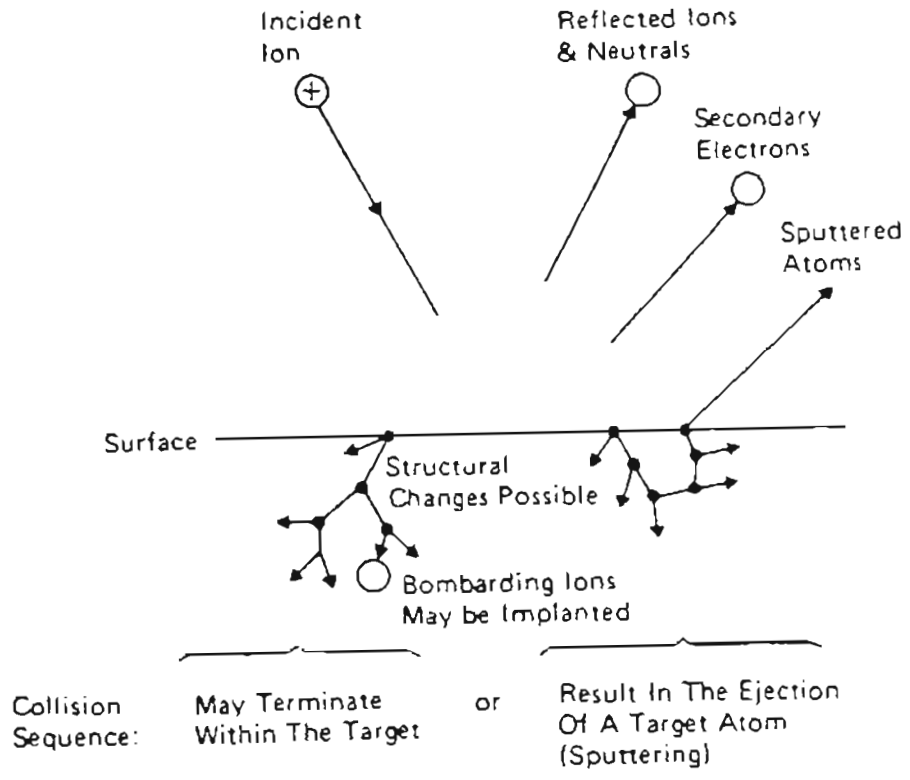

Figure 5.16 : Interactions of ions with surfaces.

target, possibly leading to the ejection of one or more of these atoms. This ejection process is known as *sputtering*.

3. The Mechanisms of Sputtering

In the energy range most relevant to sputter deposition, the interaction between the impinging ion and the target atoms, and the subsequent interactions amongst the latter, can be treated as a series of binary collisions[21]. The sputtering process is very often compared to the break in a game of atomic billiards (Fig. 5.17, reproduced from Chapman[21]) in which the cue ball (the bombarding ion) strikes the neatly arranged pack (the atomic array of the target), scattering balls (target atoms) in all directions, including some back towards the player i.e. out of the target surface. In the real process the interatomic potential function (the variation of interatomic repulsion or attraction with separation distance) is rather different from the hard sphere billiard ball case, but nevertheless the billiard ball model is not too unrealistic.

When the ion strikes the target and initiates a series of collisions known as a *collision cascade,* the cascade could lead to sputter ejection of an atom or could head off into the interior of the target dissipating the initial impact energy into lattice vibrations. To consider in detail this target collision phenomena would require the use of the interatomic potential function but the interactions, for the energies considered, being of quite short range, considerable information can be obtained by only considering interactions between immediate neighbors. Then, a binary collision can be characterized

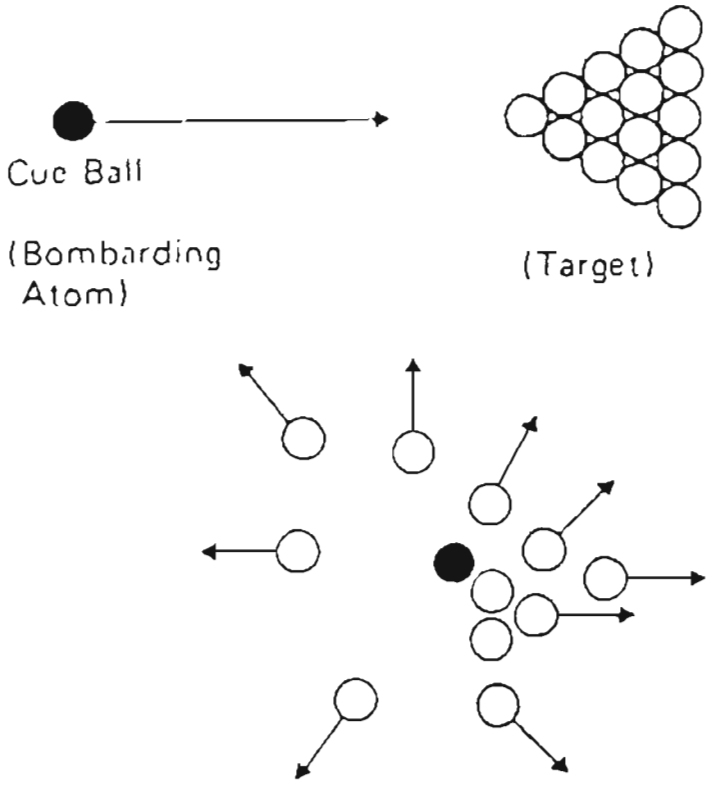

Figure 5.17 : Sputtering - the atomic billiards game.

by the energy transfer function:

$$\frac{E_t}{E_l} = \frac{4m_i m_t}{\left(m_i+m_t\right)^2} \tag{5.12}$$

where m_i and m_t are the masses of the incident ion and the target atom respectively. E_l is the energy of the incident ion and E_t is the energy transferred from the incident ion to the target atom. The sputtering process is the result of a series of such collisions.

A useful parameter encountered frequently is the *sputtering yield* S, defined as the number of target atoms (or molecules) ejected per incident ion. It is seen that the sputtering yield depends on the masses of the incident ion and the target atom, and on the energy E of the incident ion. It must be noted too that during the sputtering process the energy is transferred mostly to the surface layers of the target, and therefore the yield is seen to be proportional to the energy deposited in a thin layer near the surface and determined by the *nuclear stopping power* s(E). An expression by Sigmund[22] for s(E), involving the energy transfer function is:

$$s(E) = \frac{m_i m_t}{\left(m_i+m_t\right)^2} \frac{E}{U_0} \tag{5.13}$$

and has been used to predict the following form for the sputtering yield S:

$$S = \frac{3\,\alpha\, s(E)}{\pi^2} \tag{5.14}$$

Here U_0 is the surface binding energy of the material being sputtered, and α is a monotonic increasing function of m_t/m_i which has values of 0.17 for $m_t/m_i = 0.1$, and increasing up to 1.4 for $m_t/m_i = 10$.

Equation (5.14) for the sputtering yield predicts the yield increasing linearly with E and seems to be satisfied in practise up to above 1 keV for light projectiles and targets and where the energy densities under consideration are relatively low. Above 1 keV, S becomes relatively constant as seen in Fig. 5.18a, reproduced from Chapman[21]. At higher energies S remains constant since the higher input energies are being distributed through a larger volume, so that the energy transmitted to the surface layers remains virtually constant. At very high energies, S even decreases as ion implantation becomes dominant (Fig. 5.18b, from Chapman[21]).

Hence the expression for the sputtering yield S (Eq. 5.13) is valid only up to about 1 keV, and needs to be modified above 1 keV. The modified expression[21] yields:

$$S = 3.56\alpha \frac{Z_i Z_t}{Z_i^{2/3}+Z_t^{2/3}} \frac{m_i}{m_i+m_t} \frac{s_n(E)}{U_0} \qquad (5.15)$$

where $s_n(E)$ is the reduced stopping power and is a function of a reduced energy based on the actual energy, masses and atomic numbers Z_i and Z_t of the atoms involved. Figure 5.19, from Chapman[21] compares the theoretical result above with experimental data obtained for the case of argon on copper.

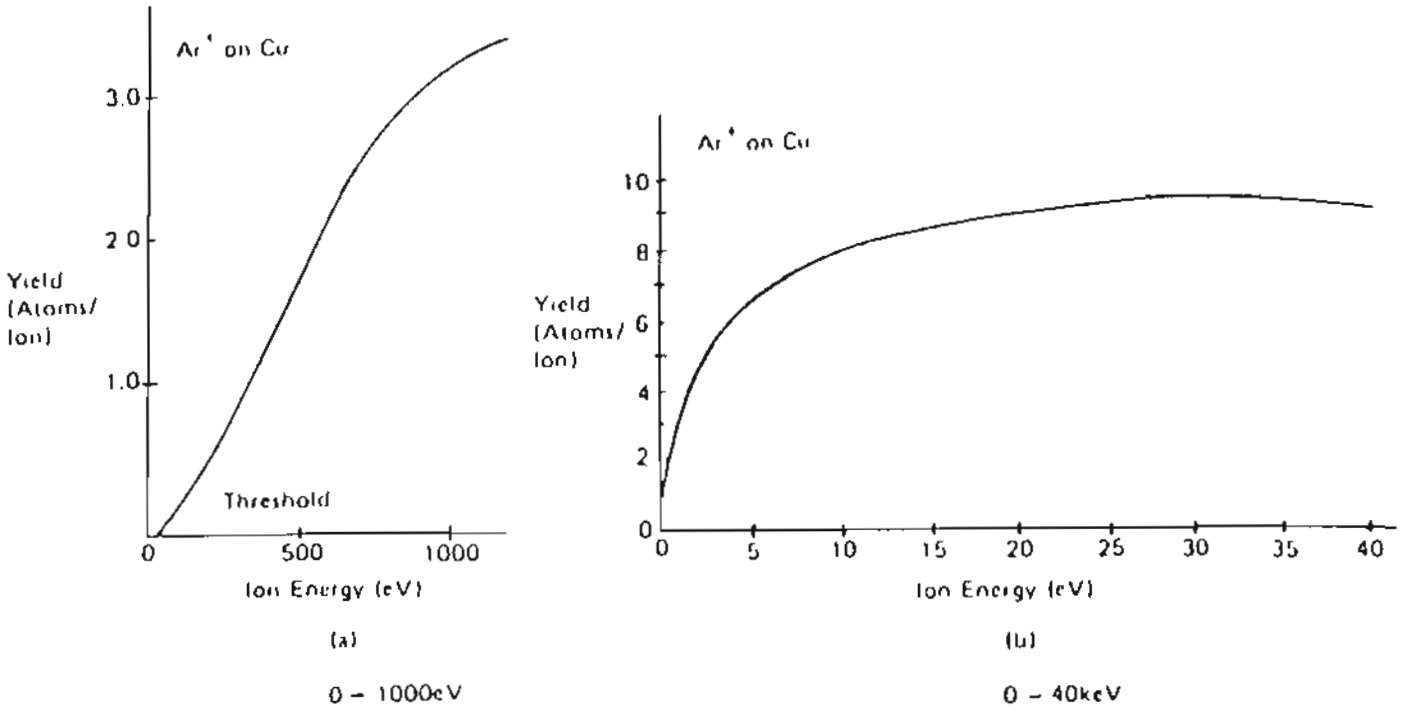

Figure 5.18 : The variation of sputtering yield, for argon ions on copper, as a function of the ion bombardment energy (a) 0 to 1000 eV (b) 0 to 40 keV.

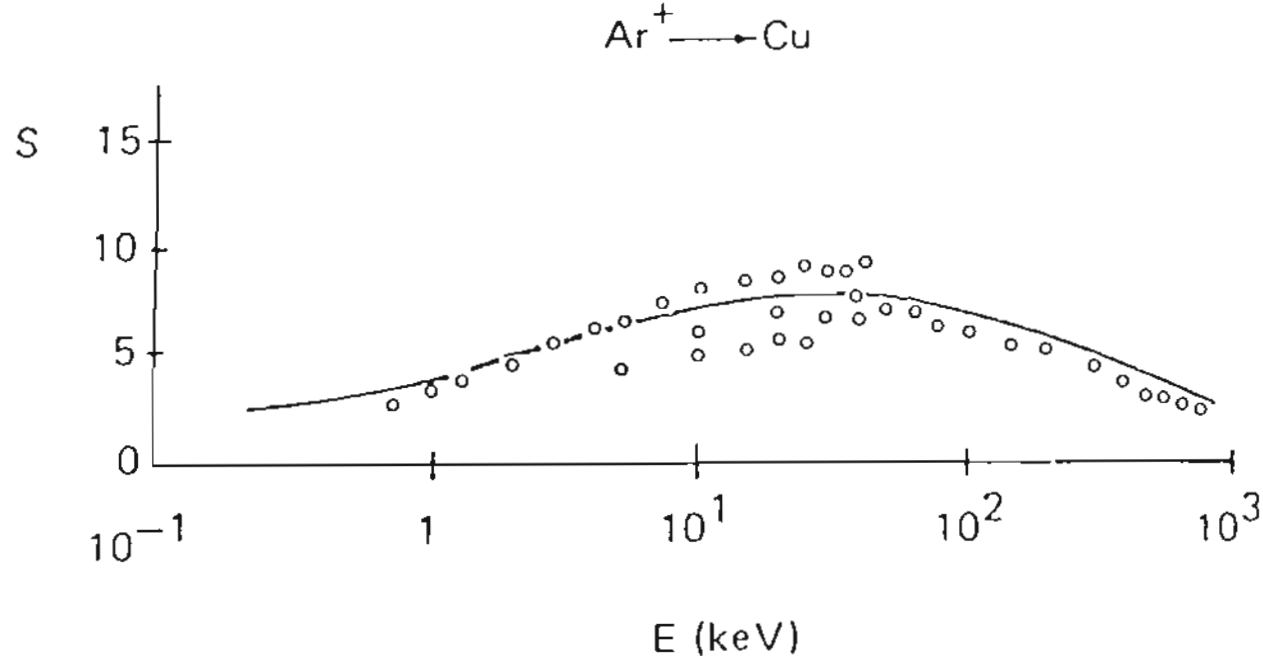

Figure 5.19 : Theoretical (solid line) and experimental values for the energy dependence of the sputtering yield of copper in argon.

4. Experimental

In the case of focused ion beams as mentioned earlier, milling or micromachining as it is often referred to, is an important application. A portion of the ions emitted from the source (as determined from an aperture) are focused using electrostatic lenses and scanned by means of a deflector (Fig. 4.39). A typical beam current density at the target is about 1 A/cm^2 since only a very small fraction ($\sim 10^{-4}$) of the available current from the source is used in the focusing process. In the LMIS-STM, micromachining with the ion beam can be achieved by the use of a close-spaced diode system comprising the source and the target, such that the beam diameter at the target could theoretically be the same order of magnitude as the Taylor cone apex ($\sim$5 nm) as discussed earlier. Also as the entire current available from the LMIS is used in the proximity focusing, this would allow exceedingly high current densities to be achieved at the target. Combining the LMIS with an STM embodiment then provides the possibility of carrying out nanometer fabrication at speeds limited only by the mechanical deflection schemes available.

5. Results

In order to determine the emission characteristics and results for a close spaced emitter-target geometry, some initial work[8,23] was done using a gold LMIS and a silicon (111) target placed close to the emitter (0.01 mm to 1 mm). The silicon target distance was changed with a micrometer.

Figure 5.20 (reproduced from Swanson et al.[23], and Assayag et al.[8],) shows holes in the Si target from the Au LMIS as a function of diode spacing. It is very interesting to note the sharpness of the edge. The exposure time was 10 secs and the emission current 1 - 2 μA. From these pictures one may plot, as shown in Fig. 5.21 (reproduced from Swanson et al.[23], and Assayag et al.[8],) the sputtered hole diameter versus emitter-target distance; the slope gives a constant emission angle of about 20°. The minimum operating distance, and hence the hole size was limited by the micrometer accuracy (0.01 mm) position. From a dektak profile shown in Fig. 5.22, (reproduced from Swanson et al.[23], and Assayag et al.[8],) the measured depth and diameter of one of the holes was found to be 0.35 and 430 μm respectively. The current density was about 0.2 A/cm^2 for the smallest diode spacing possible (0.03 mm). From this data was calculated a sputtering yield for Si of 14 atoms/ion at 6.1 kV which is unusually large when compared with the lower current density sputtering results (~1.5 for 5-10 keV Ar^+ ions on Si for a current density of about 1 mA/cm^2 or 2.6 for 30 keV Ga^+ ions on Si at a current density of 0.71 A/cm^2)[22, 24, 25].

For the next series of experiments, we constructed a STM set-up (described in Chapter 3) with a magnetically driven micropositioner for gross motion of the sample from ~1.0 cm down to about 1 - 2 μm from the LMIS. To bring the sample even closer piezoceramic drive units were used for which the voltage/distance relationship was known (~7 nm/volt). Maximum motion of about 8 to 10 μm was possible using these piezodrive units. The emission characteristics were determined this time for a close-spaced gallium

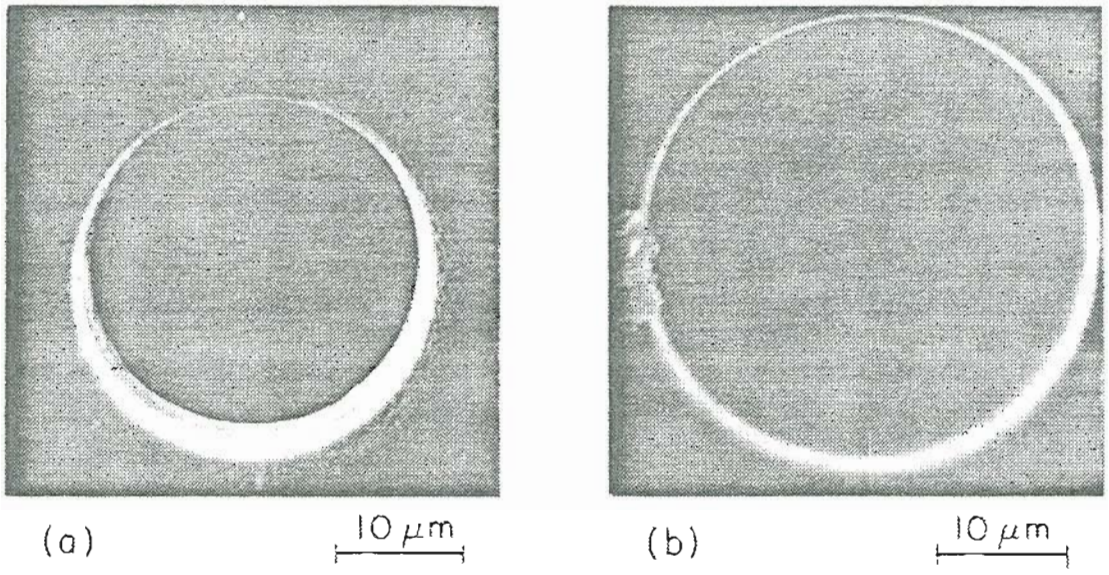

Figure 5.20 : Micrographs of holes made in a Si target with a close spaced Au LMIS and different emitter-target distances d. Exposure time was 10 secs. (a) d = 30 μm, I = 1 μA; (b) d = 50 μm, I = 1 μA.

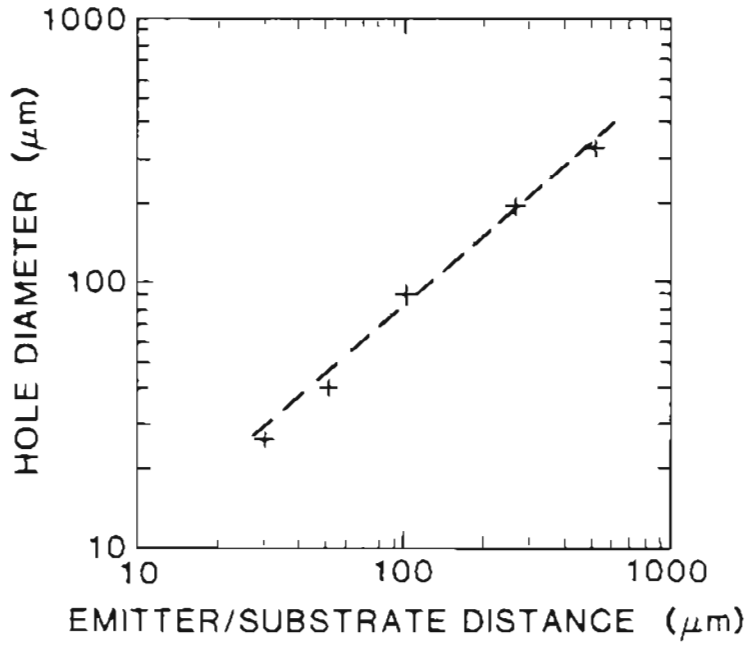

Figure 5.21 : Hole diameter versus emitter-target distance.

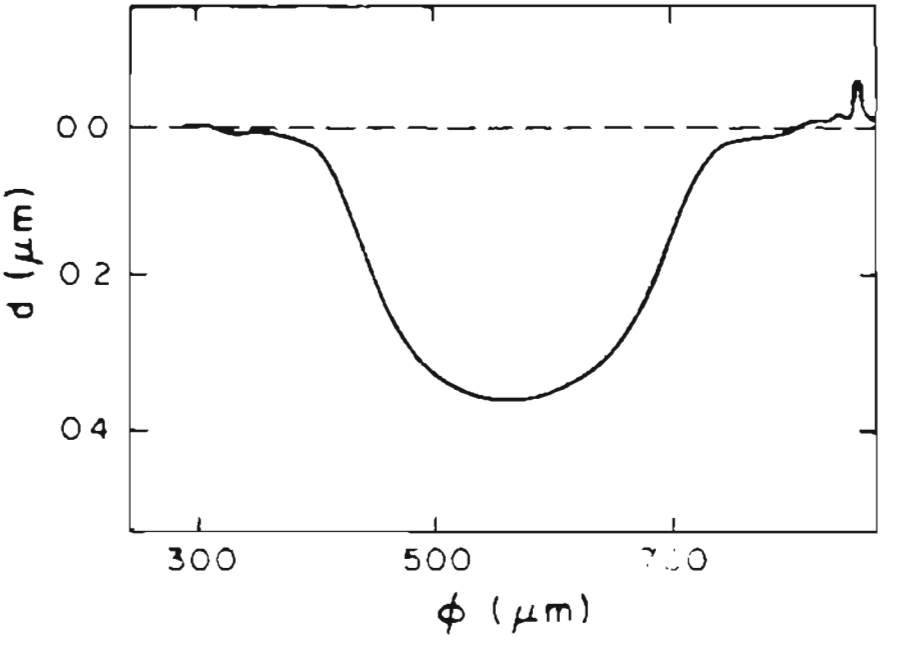

Figure 5.22 : A DEKTAK profile of a hole of diameter 430 μm and depth 0.35 μm.

LMIS with a gallium arsenide (GaAs) target. Figure 5.23 is an SEM photo of a hole made in GaAs using a Ga LMIS. The time of exposure was ~15 sec with a total current of ~0.5 μA. The sharpness of the edge is seen quite clearly in the photograph. Using a silicon target and a Ga LMIS, a hole of diameter ~120 μm was machined in ~2 min with a total current of 0.5 μA. The hole is shown in Figure 5.24a. The depth of the hole as seen in the dektak profile in Figure 5.24b is about 17 μm. The sputtering yield calculated for this, turns out to be about 17 atoms/ion. The sputtering yields calculated for the features made with the proximity focused LMIS were done without making a correction for secondary electrons, which if taken into account would increase the yield by atleast a factor of 2. Figures 5.25a and 5.25b are micrographs of holes in Si (with a Ga LMIS) of diameters 30 and 25 μm respectively with depths of about 8 to 10 μm. The exposure times were about 12 secs and 7 secs respectively with total currents of 1 - 2 μA. The sputtering yields for these are 2.1 and 2.8 atoms/ion respectively. The dektak profiles of the above holes are shown in Figs. 5.25c and 5.25d.

Holes were also made in Si with a low current Ga LMIS[10]. Figures 5.26a and 5.26b show holes of diameters 60 and 35 μm respectively. The exposure times were about 1 min with total currents of about 2 nA and 20 nA respectively. The sputtering yields for these were 14 atoms/ion and 13 atoms/ion respectively. The dektak profiles of these holes are shown in Figs. 5.26c and 5.26d.

Holes were also etched in silicon with micron and submicron dimensions. Figure 5.27a shows a hole made in Si with a Ga LMIS, of diameter ~4 μm

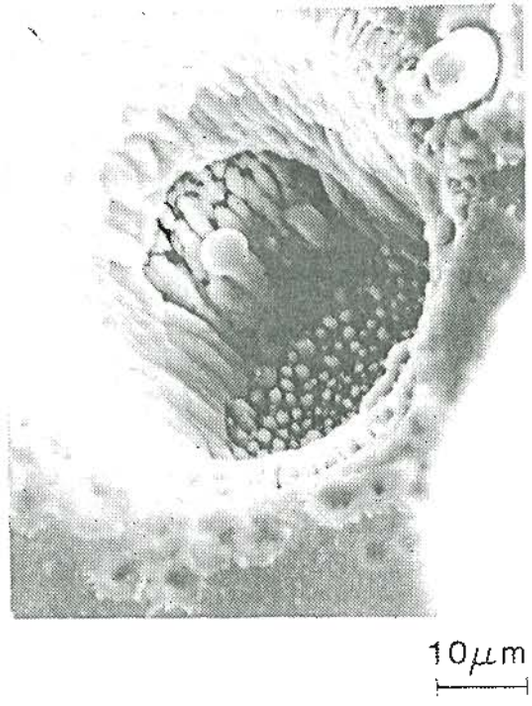

Figure 5.23 : Hole made in GaAs target with a Ga LMIS of diameter ~30 μm and depth ~20 μm at a current of 0.5 μA. The exposure time was ~15 sec.

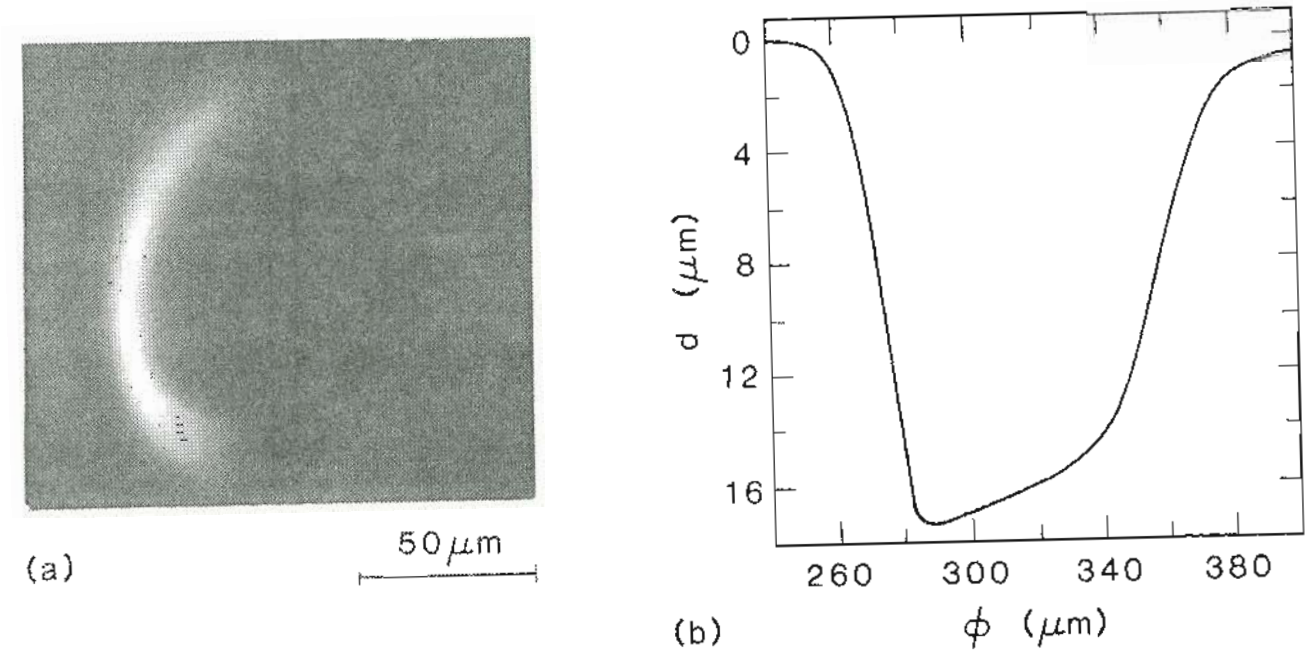

Figure 5.24 : (a) Hole made in Si target with a Ga LMIS at a current of 0.5 μA. The exposure time was ~2 min (b) a DEKTAK profile of (a). The diameter is ~100 μm and depth 17 μm.

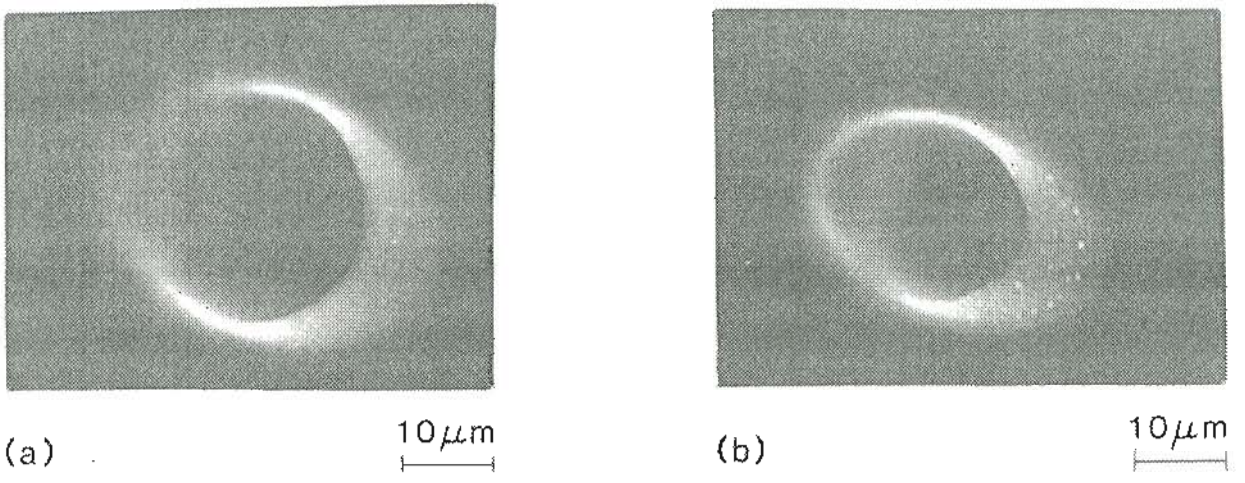

Figure 5.25(a,b) : Holes made in Si target with a Ga LMIS with a current of 1-2 μA and (a) having a diameter of 30 μm with an exposure time of about 12 secs (b) having a diameter of 25 μm with an exposure time of about 7 secs.

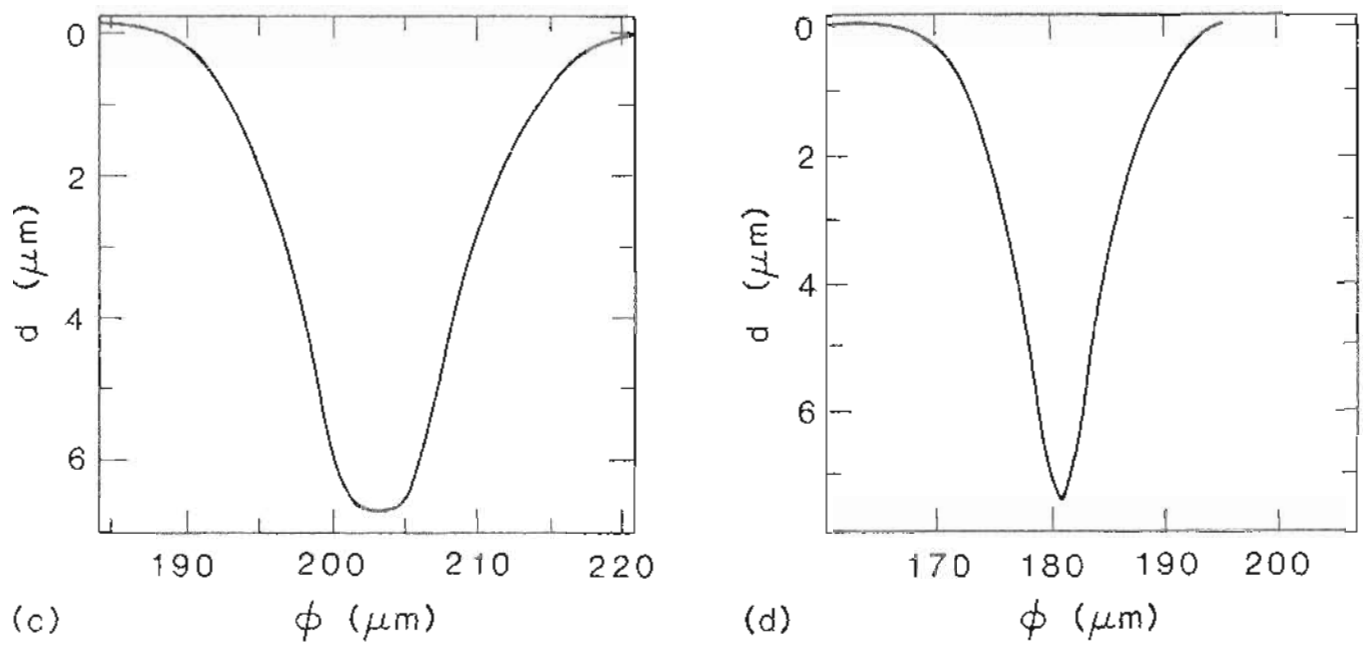

Figure 5.25(c,d) : (c) a DEKTAK profile of Fig. 5.25(a) and (d) a DEKTAK profile of Fig. 5.25(b).

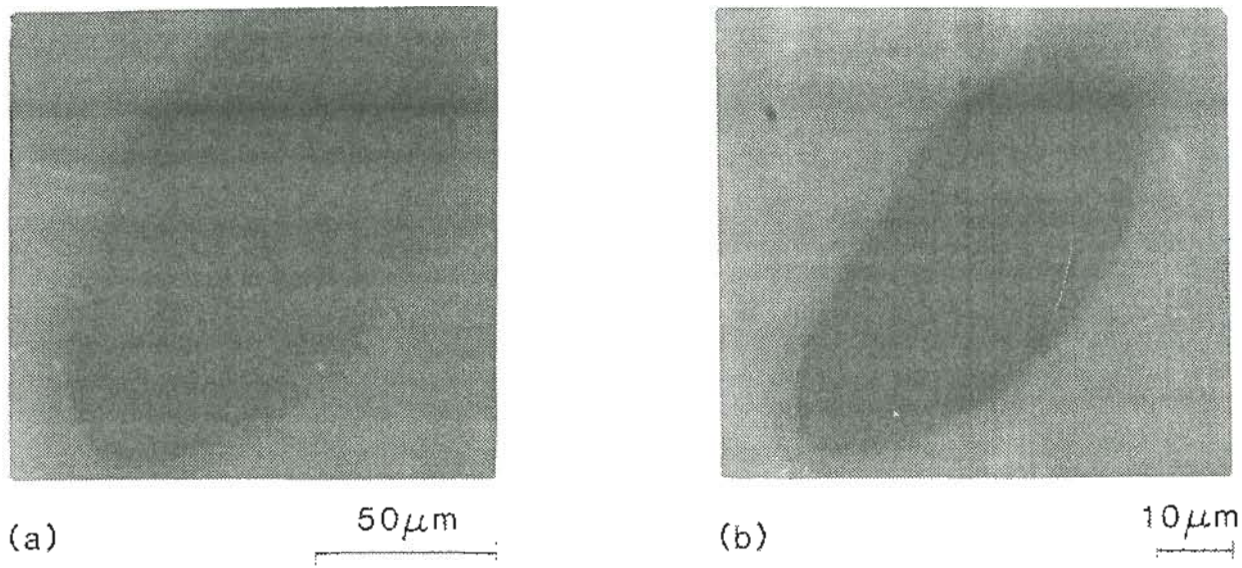

Figure 5.26(a,b) : Holes made in Si target with a Ga LMIS (a) having a diameter of 60 μm with an exposure time of about 1 min at a current of 20 nA. (b) having a diameter of 35 μm with an exposure time of about 1 min at a current of 2 nA.

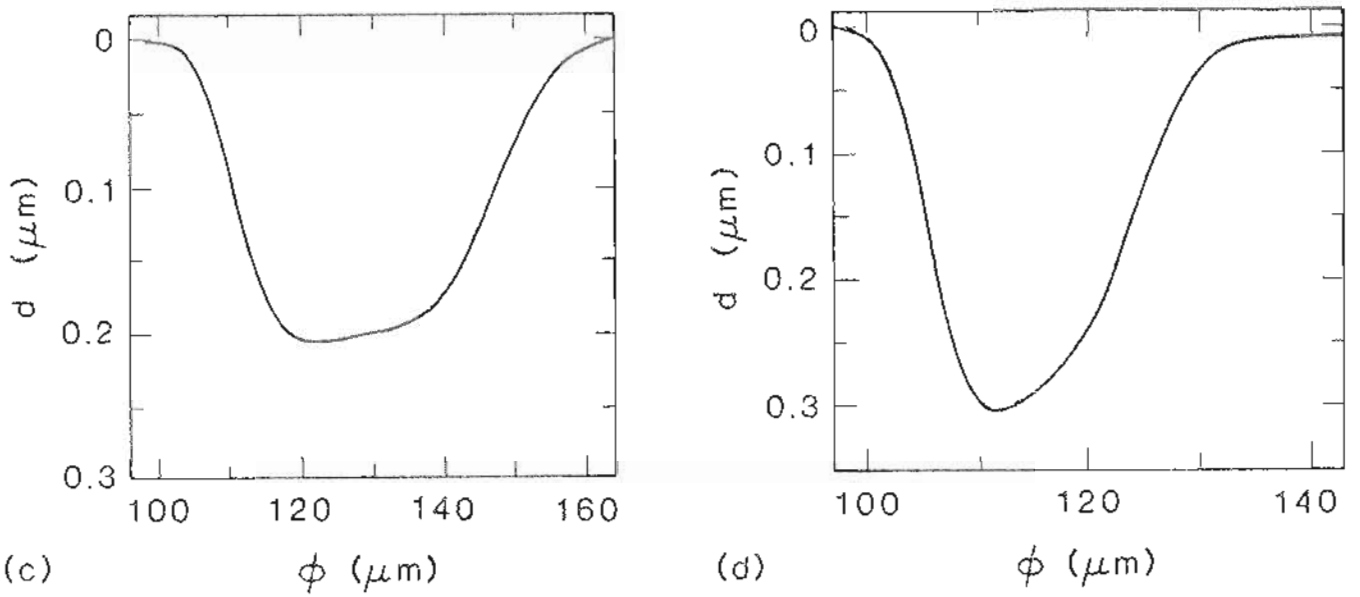

Figure 5.26(c,d) : (c) a DEKTAK profile of Fig. 5.26(a) and (d) a DEKTAK profile of Fig. 5.26(b).

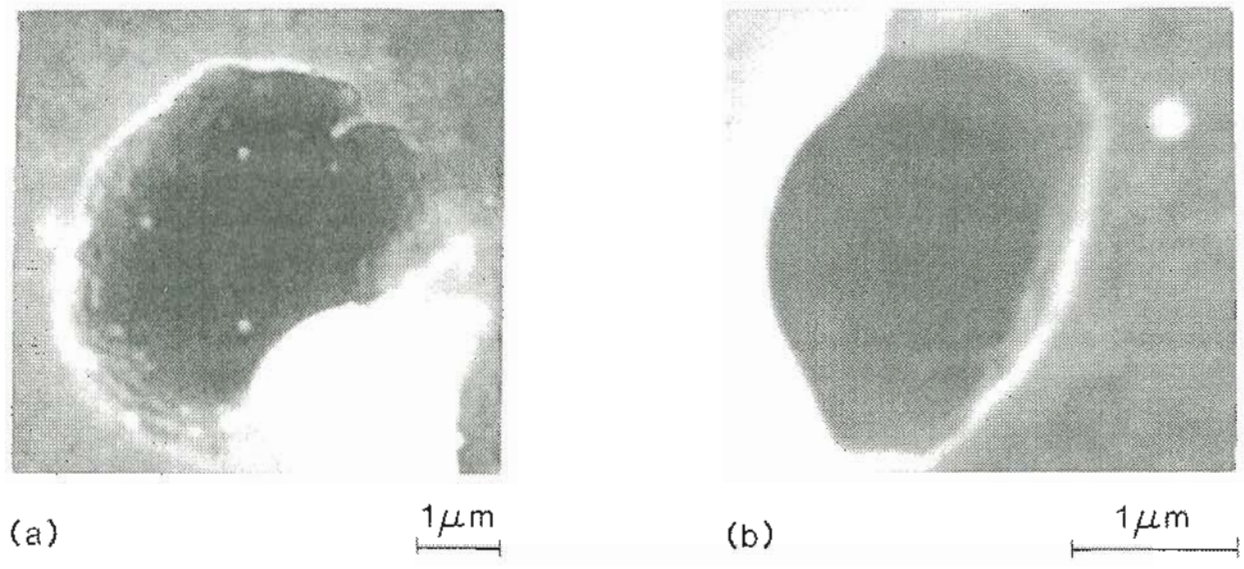

Figure 5.27(a,b) : Holes made in Si target with a Ga LMIS at a current of 0.5 μA and exposure times of 1 to 4 secs with (a) diameter ~4 μm and depth ~2 μm (b) diameter ~1.5 μm and depth ~1 μm.

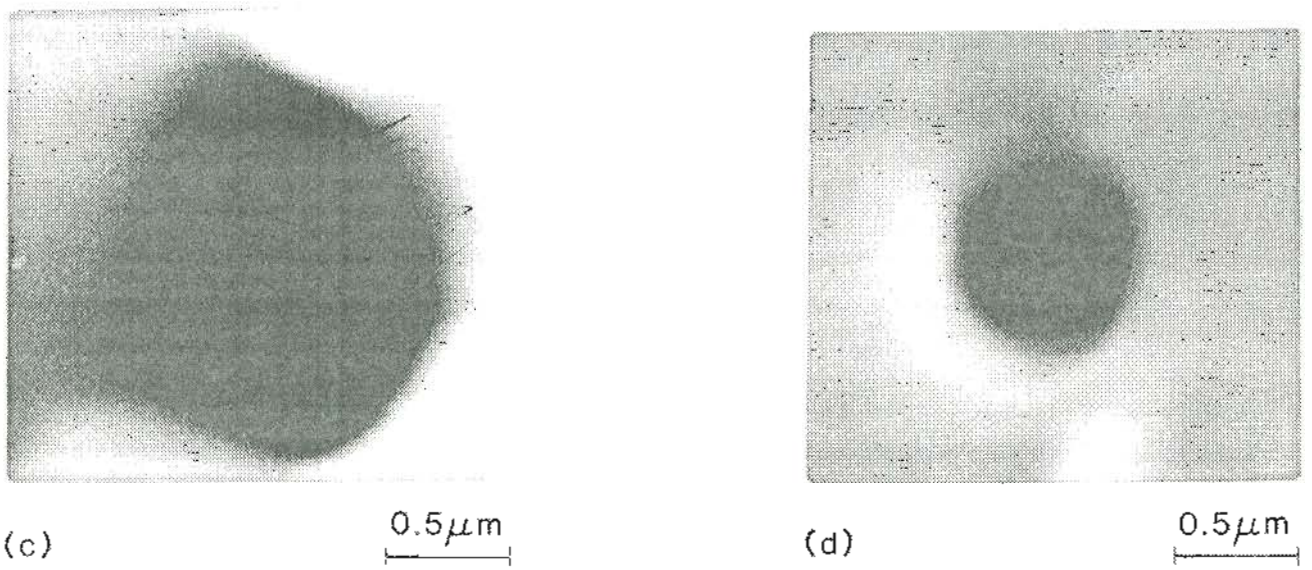

Figure 5.27(c,d) : Holes made in Si target with a Ga LMIS at a current of 0.5 μA and exposure times of 1 to 4 secs with (c) diameter ~1.25 μm (d) diameter ~0.67 μm.

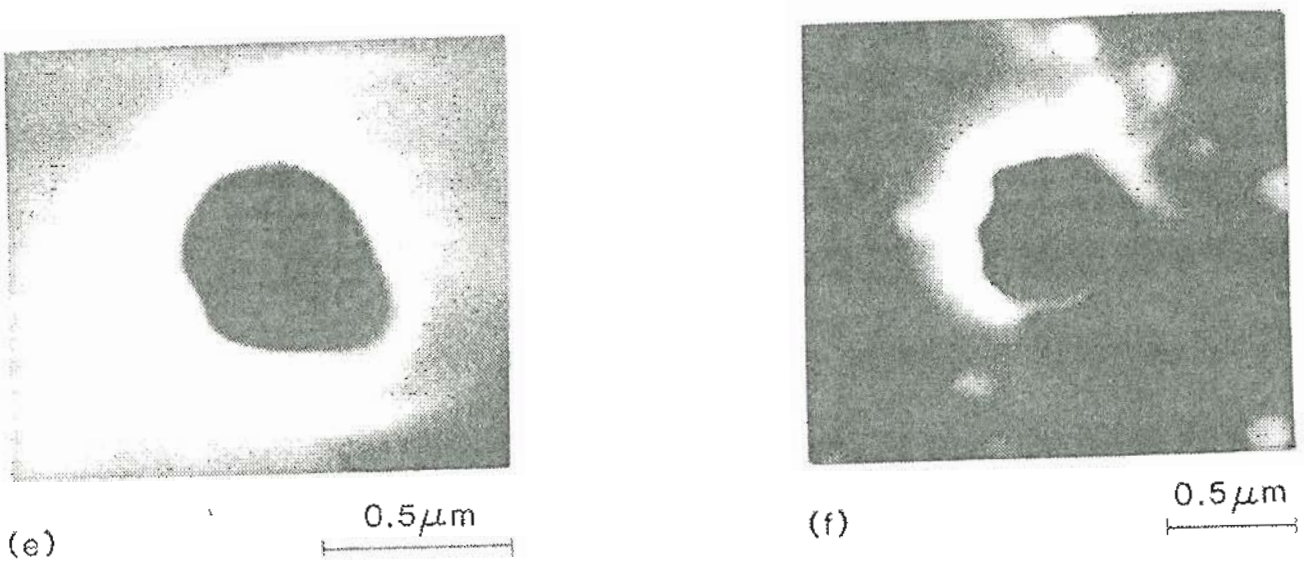

Figure 5.27(e,f) : Holes made in Si target with a Ga LMIS at a current of 0.5 μA and exposure times of 1 to 4 secs with (e) diameter ~0.5 μm (f) diameter ~0.5 μm.

and depth about 2 μm. Figure 5.27b shows a hole of diameter ~2 μm and ~1 μm deep. Figure 5.27c is a hole of diameter about 1.25 μm. Figure 5.27d is a hole of diameter about 0.67 μm. Figures 5.27e and 5.27f are holes of diameter ~0.5 μm. The ion emission current during the exposure was 0.5 μA and the exposure times were between 1 to 4 secs. Holes were also etched in Si using a low current Ga LMIS. Figure 5.28a shows a hole of diameter about 0.4 μm with a total current of 100 nA. Figure 5.28b shows a hole of diameter 0.3 μm exposed with a total current of about 20 nA.

Holes were also etched in $Cd_{0.96}Zn_{0.4}Te$ using a Ga LMIS. Figures 5.29a and 5.29b shows micrographs of two holes etched in $Cd_{0.96}Zn_{0.4}Te$ with diameters of about 200 μm and 160 μm respectively. The dektak profiles of the above holes are shown in Figs. 5.29c and 5.29d.

An attempt was also made to mill fine lines on GaAs and Si substrates. Figure 5.30 is a SEM photo of what is believed to be the result of this effort. Two lines are shown, corresponding to the two attempts made. The time for each scan was about 20 secs. The large crater evident at the beginning of each line corresponds to the deliberate initial impact of the LMIS with the substrates prior to the scans. The linewidths and lengths of the lines are ~100 nm and 10 μm respectively. Figures 5.31a and 5.31b shows line scans on Si using a low current Ga LMIS. The linewidths are ~0.2 and 0.4 μm respectively and the lines are about 5 to 6 μm long.

Table 6 gives the values of the sputtering yields in atoms/ion for the various holes etched in Si with a Ga LMIS.

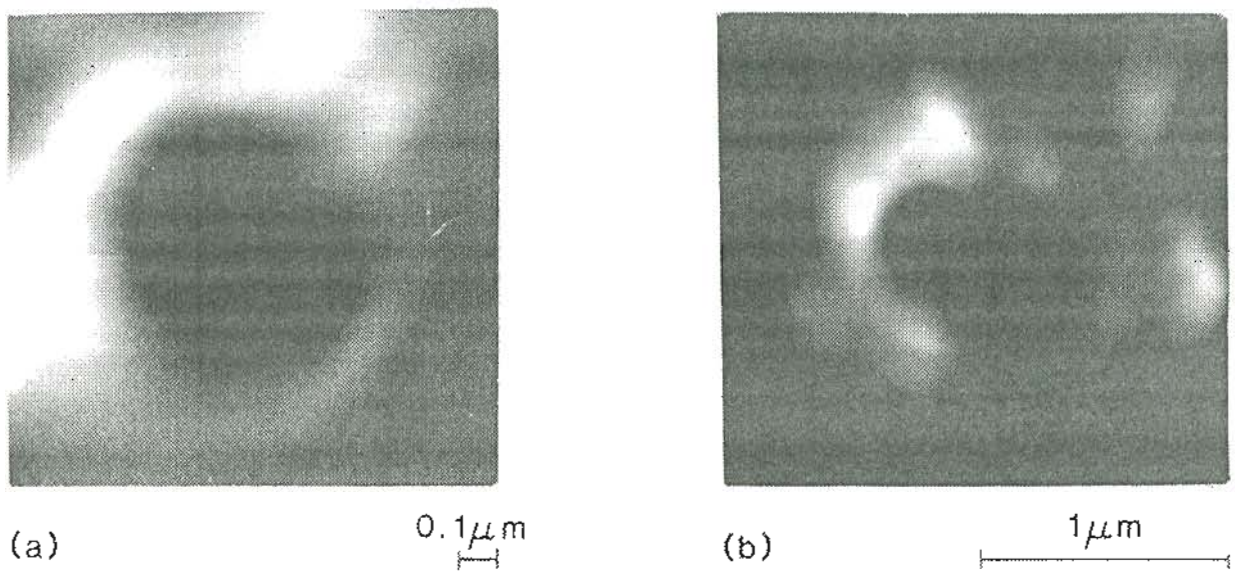

Figure 5.28 : Holes made in Si target with a Ga LMIS and exposure times of 15 to 20 secs with (a) diameter ~0.4 μm and a current of 100 nA and (b) diameter ~0.3 μm and a current of 20 nA.

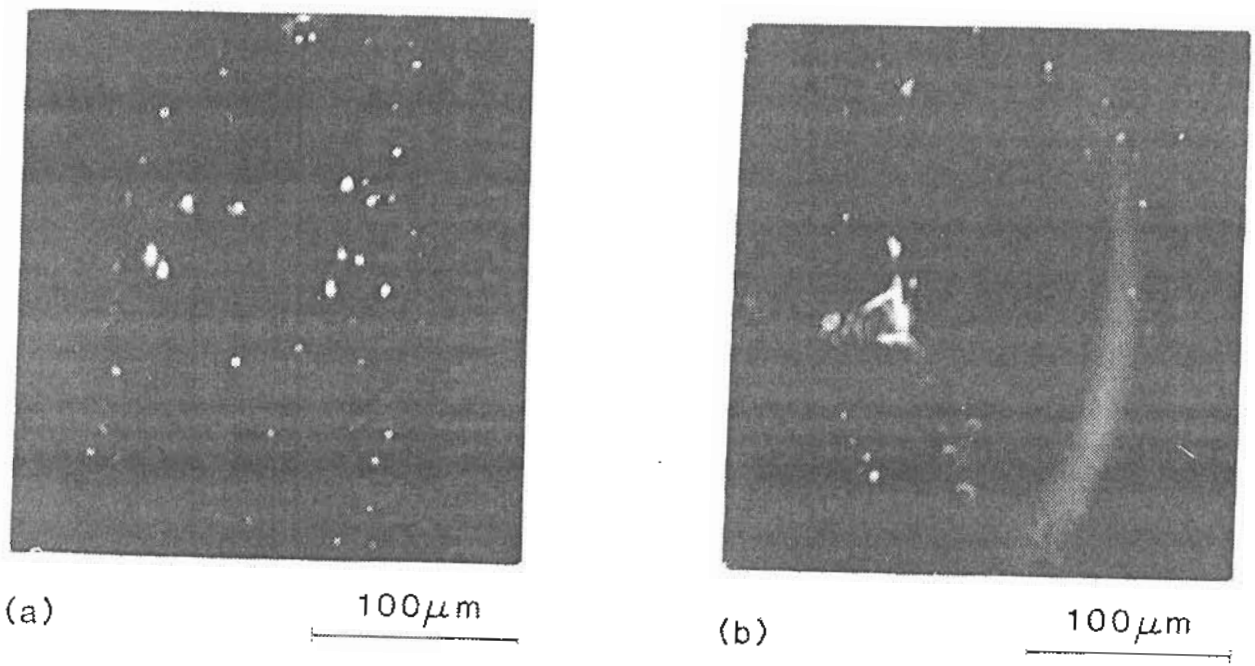

Figure 5.29(a,b) : Holes made in $Cd_{0.96}Zn_{0.4}Te$ target with a Ga LMIS with (a) diameter ~200 μm at a current of 2 μA for an exposure time of 30 secs. (b) diameter ~160 μm at a current of 4 μA for an exposure time of 30 secs.

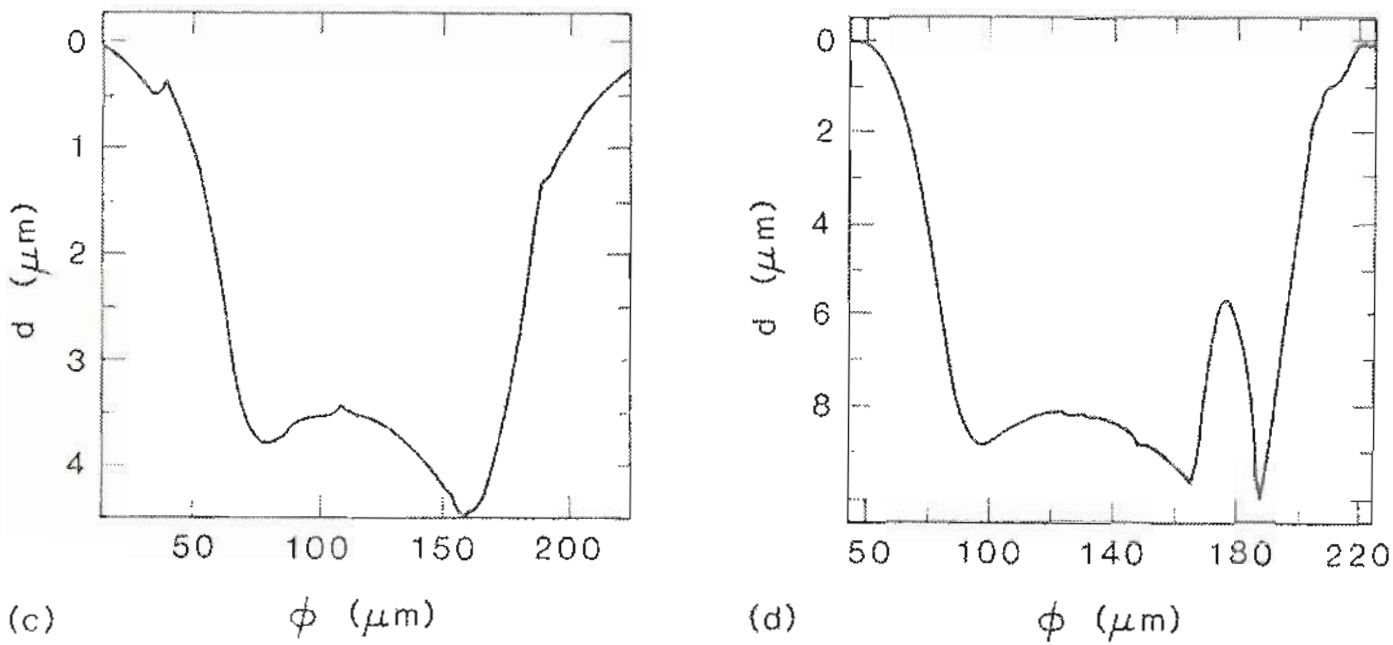

Figure 5.29(c,d) : (c) a DEKTAK profile of Fig. 5.29(a) and (d) a DEKTAK profile of Fig. 5.29(b).

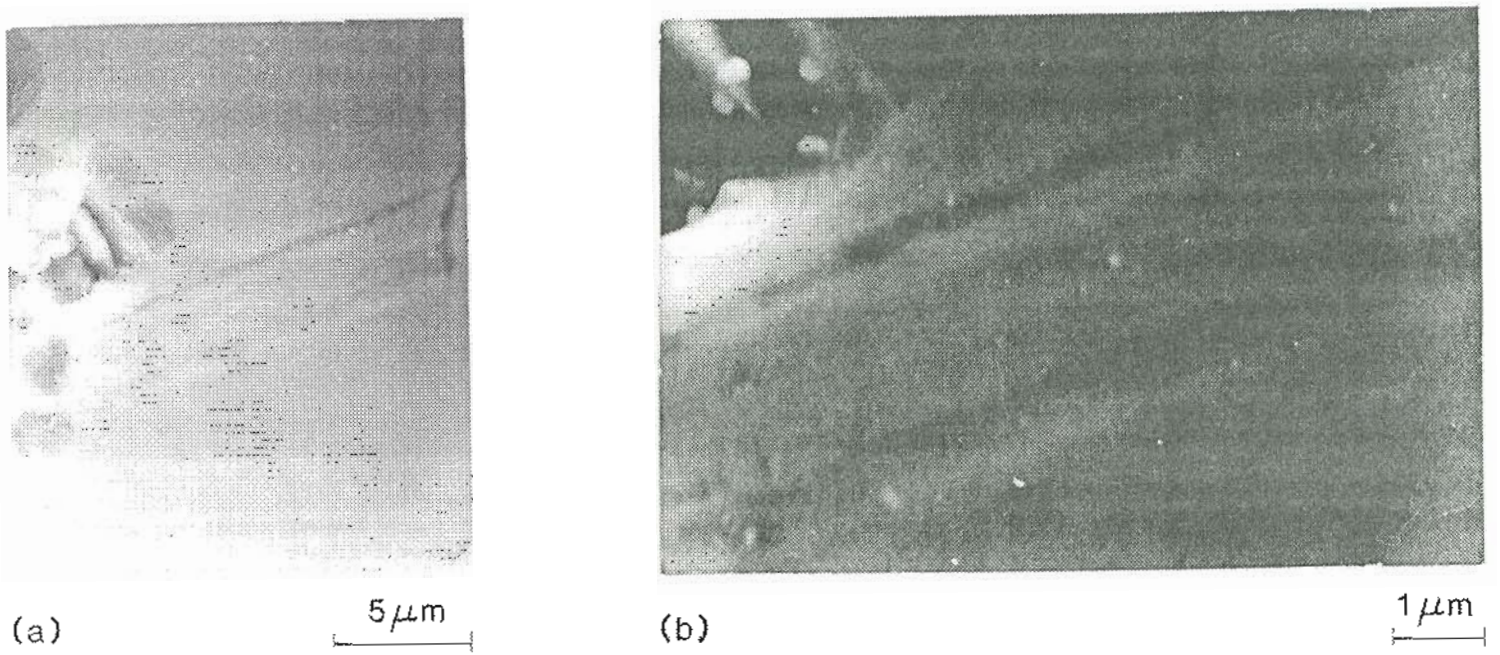

Figure 5.30 : Two parallel lines etched in GaAs with a close spaced Ga LMIS having a linewidth of ~100 nm and length ~10 μm (a) at 3600X magnification (b) at 10,000X magnification.

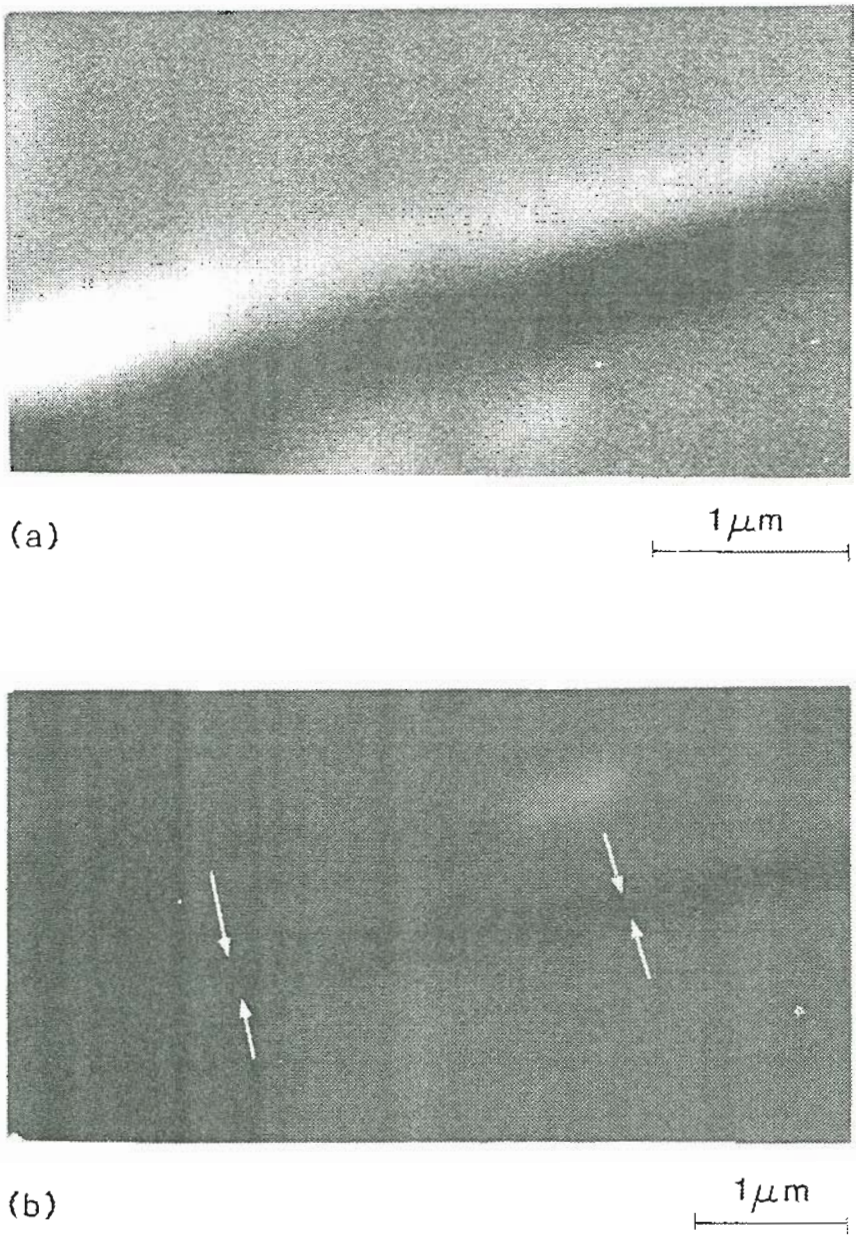

Figure 5.31 : Two lines etched in Si with a close spaced Ga LMIS having (a) a linewidth of ~200 nm and length ~5 μm and (b) a linewidth of ~400 nm and length ~5 μm.

Table 6. Sputtering yield, S, in atoms/ion for the proximity focused LMIS. (Ga^+ on Si)

Incident energy (volts)	Ion current (μA)	Current density (mA/cm^2)	Time (sec)	Volume removed ($\mu m^3 \times 10^3$)	Aspect ratio (d/h)	S
4500	1.0	10.0	120	262.00	0.125	17.45
4471	1.5	10.0	60	157.00	0.025	13.97
4000	2.5	30.0	30	43.20	0.056	4.61
3000	5.6	120.0	20	43.20	0.111	3.08
3000	1.5	310.0	7	3.68	0.333	2.81
3000	1.5	220.0	12	4.59	0.200	2.04
2261	2.0	40.0	25	13.40	0.033	2.14
2750	0.020	0.7	69	2.26	0.0033	13.11
2372	0.028	0.3	60	1.13	0.0800	5.39
2000	0.007	0.6	60	0.13	0.0025	2.39
2000	0.007	1.0	40	0.07	0.0033	2.05

The volumes removed were determined, modeling the holes as cylinders and obtaining the diameter of the holes from the SEM photographs and the depth of the holes from the DEKTAK profiles. The aspect ratio was given by d/h, where d was the depth of the sputtered hole and h was the hole diameter.

Figure 5.32 gives a plot of the sputtering yield versus the ion incident energies from the table above. Figure 5.33 gives a plot of the sputtering yield versus the volumes removed in μm^3. The currents of 2.0 μA and 10 nA recorded in Figs. 5.32 and 5.33 are the average of the currents from Table 6. We see from Fig. 5.33 that the sputtering yield varies as the square root of the volume removed, for the cases considered.

6. Discussion and Summary

This study has demonstrated the ability to operate LMIS (of gallium and gold) at close spacings for a variety of substrates, like silicon, gallium arsenide, and $Cd_{0.96}Zn_{0.4}Te$. The proximity focusing does not seem to affect the emission stability.

We have also demonstrated the ability to make holes and lines as small as 0.1 to 0.3 μm with the proximity focused LMIS. The sputtering yields calculated for the larger features are as high as 15, much larger than comparable current density results[22,24,25], and as seen from Fig. 5.33, the yield is proportional to the volume removed. We see from Table 6 that the high sputtering yields could not arise due to high energy densities within collision cascades as the energy densities in our experiments are vastly different for

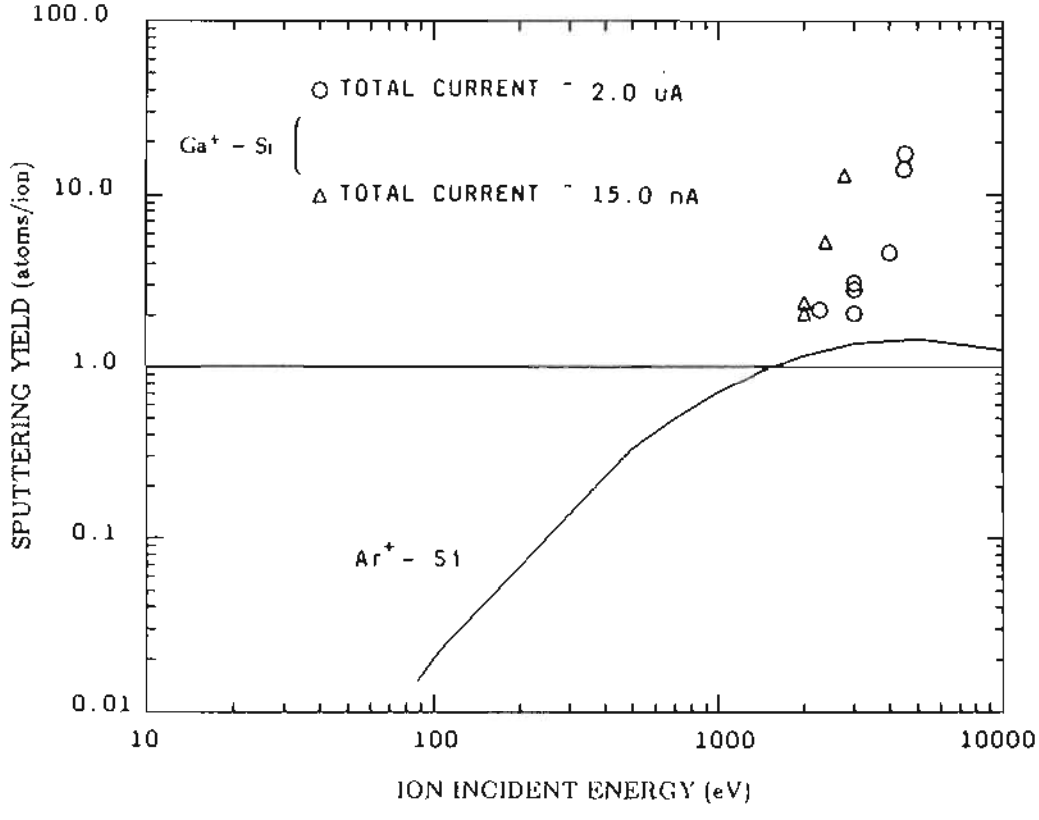

Figure 5.32 : Measured sputtering yields for Ga^+ ions on Si at normal incidence in the proximity focused mode.

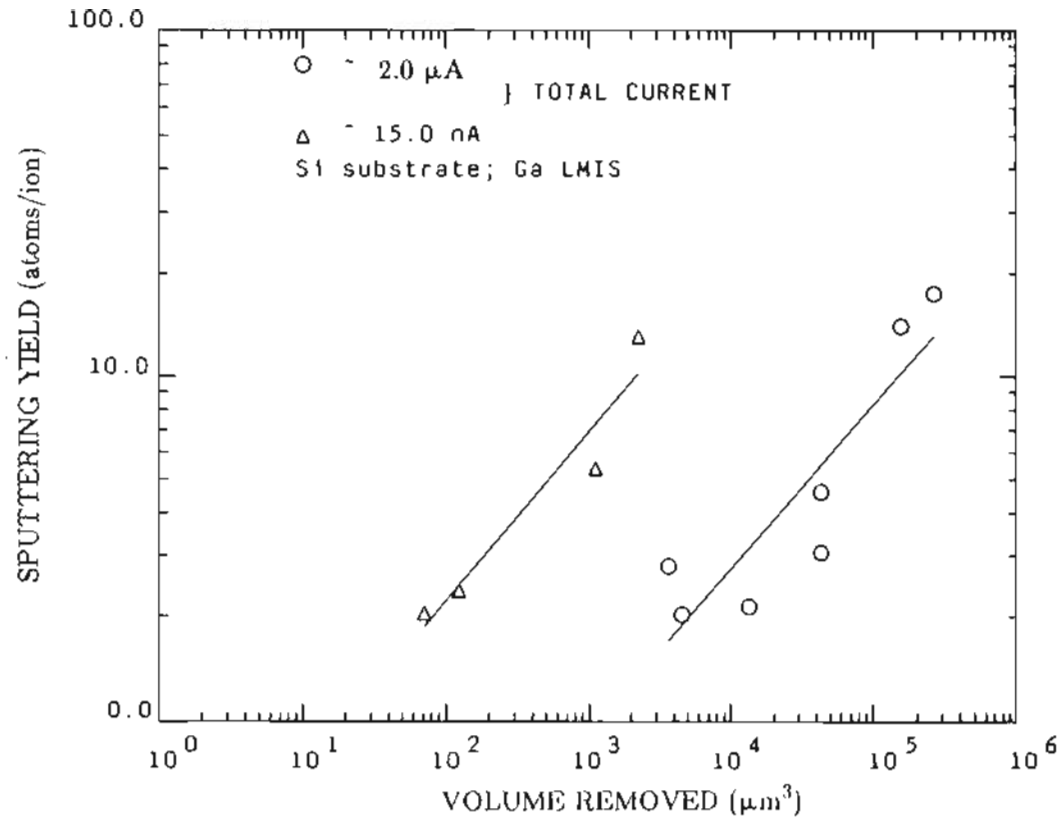

Figure 5.33 : Sputtering yield versus volume removed in μm^3 for Ga^+ ions on Si at normal incidence in the proximity focused mode.

the conventional LMIS and the low current LMIS, yet the sputtering yields are comparable. The sputtering yield is proportional to the volume removed and could be due to the evolving profile of the sputtered hole. Initially as the beam sputters the surface, the hole is gaussian in profile with the aspect ratio being low. As the sputtering continues, the aspect ratio increases as the hole gets deeper. More of the sputtering then occurs from the sloping side-walls than from the bottom of the hole. The sputtering yield being highly angular dependant, consequently increases as the volume removed increases.

The temperature rise that could be expected during micromachining with the proximity focused LMIS can be calculated using the classical theory, as given in Carslaw and Jaeger[26].

The steady state temperature rise in a semi-infinite plate due to a deposited energy of "F" watts into a spot of radius "r" and thermal conductivity "k" is:

$$T_{rise} = \frac{8F}{3\pi^2 kr} \tag{5.16}$$

For a substrate for which k ~1 watt/cm-K, F = 1 μwatt and r = 100 nm, T_{rise} ~0.03 K. This is based on a 1 nA current at 1000 eV energy. Si has a thermal conductivity of 1.5 watt/cm-K and GaAs has a value of 0.5 watt/cm-K so that at the 1 nA emission current level, the calculated temperature rise of the substrate is seen to be negligible. At 1 μA emission current, the calculated temperature rise is 30 K. At a spacing of 10 nm and 1 μA emission current, the steady state temperature rise would be ~100 K.

For the low current LMIS there would seem to be no significant thermal effects and very little even for a high current source from the proximity focusing.

Figure 5.34a shows an SEM photograph from operating a gallium LMIS at close spacing with a Si target in the LMIS-STM. The source was operated at 150 volts at ~5 nA for 90 seconds at one position after which the LMIS was moved ~1.5 μm to the right and operated again at 150 volts at 10 nA for 60 seconds. Rather than there being two neat holes separated by ~1.5 μm, the surface appears to have been damaged by a catastrophic event such an arc. Figure 5.34b shows the result of operating the gallium LMIS at another point on a Si target at 140 volts, 8 nA for 60 seconds, then moving the source ~1.5 μm to the right and operating it at 60 volts, 15 nA for 55 seconds, and moving it again ~1.5 μm to the right and operating it at 140 volts, 10 nA for 65 seconds. The surface as in the previous example appears to have again undergone a catastrophic event.

The temperature rises as calculated from the classical theory above, is negligible for the ion energies and currents considered. Hence the damage to the substrate in Figs. 5.34a and 5.34b probably arose, due to a catastrophic event such as an arc, due to a build-up of deposits during the proximity focusing operation leading to a possible "shorting" between the LMIS and the substrate.

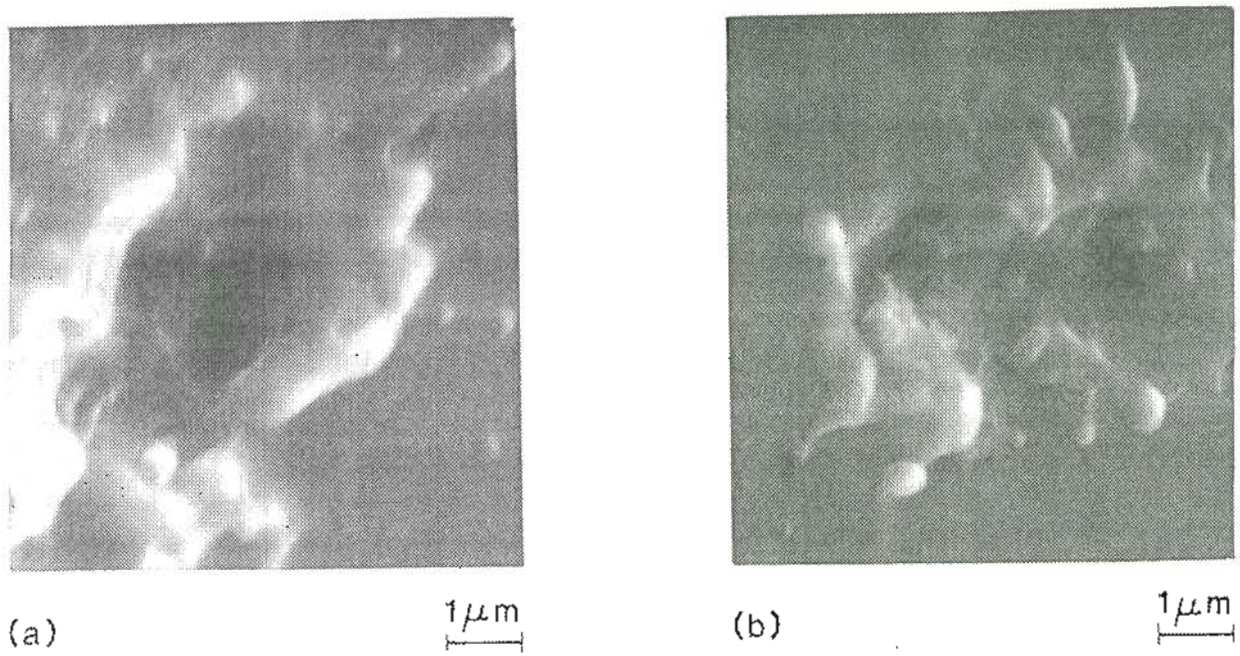

Figure 5.34 : Results obtained from operating a Ga LMIS at close spacings (a) in two regions ~1.5 μm apart at 150 volts for 90 sec and 60 sec respectively with a current between 5 to 10 nA and (b) in three regions ~1.5 μm apart at 140 volts for 60 sec with a current of 8 nA, 60 volts for 55 secs and with a current of 15 nA and at 140 volts, 10 nA for 65 sec.

References

1. N. K. Kang and L. W. Swanson, *Appl. Phys. A*, vol. 30, p. 95, 1983.
2. D. R. Kingham and L. W. Swanson, *Appl. Phys. A*, vol. 34, p. 123, 1984.
3. G. Binnig, H. Rohrer, Ch. Gerber, and E. Wiebel, *Phys. Rev. Lett.*, vol. 49, p. 57, 1982.
4. M. Ringger, H. R. Hidber, R. Schlogl, P. Oelhafen, and H.-J. Guntherodt, *Appl. Phys. Lett.*, vol. 46, p. 832, 1985.
5. M. A. McCord and R. F. W. Pease, *J. Vac. Sci. Technol. B*, vol. 4, p. 86, 1986.
6. G. I. Taylor, *Proc. R. Soc. Lond. A*, vol. 280, p. 383, 1964.
7. R. N. Hall, *Appl. Phys.*, vol. 20, p. 925, 1949.
8. G. B. Assayag, P. Sudraud, and L. W. Swanson, *Surf. Sci.*, vol. 181, p. 362, 1986.
9. A. E. Bell and L. W. Swanson, *Appl. Phys. A*, vol. 41, p. 335, 1986.
10. A. E. Bell, K. Rao, G. A. Schwind, and L. W. Swanson, *J. Vac. Sci. Technol. B*, vol. 6(3), p. 927, 1988.
11. D. P. E. Smith and S. A. Elrod, *Rev. Sci. Instr.*, vol. 56, p. 1970, 1985.
12. R. E. Lee, *J. Vac. Sci. Technol.*, vol. 16(2), p. 164, 1979.
13. H. I. Smith, *Proceedings of the Symposium on Etching for Pattern Definition*, p. 133, Electrochemical Society, Pennington, N.J., 1976.
14. S. Somekh, *J. Vac. Sci. Technol.*, vol. 13, p. 1003, 1976.

15. J. Orloff, *Microelectronics-Photonics, Materials, Sensors and Technology*, 10.

16. P. J. Heard, J. R. A. Cleaver, and H. Ahmed, *J. Vac. Sci. Technol. B*, vol. 3, 1985.

17. D. K. Atwood, G. J. Fisanick, W. A. Johnson, and A. Wagner, *SPIE*, vol. 471, p. 127, 1984.

18. J. Melngailis, C. R. Musil, E. H. Stevens, M. Utlaut, E. M. Kellogg, R. T. Post, M. W. Geis, and R. W. Mountain, *J. Vac. Sci. Technol. B*, vol. 4(1), p. 176, 1986.

19. L. R. Harriott, R. E. Scotti, K. D. Cummings, and A. F. Ambrose, *Appl. Phys. Lett.*, vol. 48, p. 1704, 1986.

20. J. Puretz, R. K. DeFreez, R. A. Elliott, and J. Orloff, *Electron Lett.*, vol. 22, p. 700, 1986.

21. B. Chapman, *Glow Discharge Processes*, John Wiley & Sons, 1980.

22. P. Sigmund, *Phys. Rev.*, vol. 184, p. 383, 1969 .

23. L. W. Swanson, A. E. Bell, and G. B. Assayag, *Quarterly R & D Report to DARPA*, 1 March to 1 June, 1985.

24. J. Melngailis, *J. Vac. Sci. Technol. B*, vol. 5(2), p. 469, 1987.

25. H. Yamaguchi, A. Shimase, S. Hiraichi, and T. Miyauchi, *J. Vac. Sci. Technol. B*, vol. 3(1), p. 71, 1985.

26. H. S. Carslaw and J. C. Jaeger, *Conduction of Heat in Solids, Chapter VIII*, Oxford University Press, 1978.

CHAPTER 6

CONCLUSIONS

The results presented in the preceding chapters can be grouped into the two sections: (1) Considerations relative to proximity focusing of the LMIS and (2) A proximity focused LMIS system. The first section can be subdivided into four categories: (a) a liquid metal electron source, (b) evaluating spacings in the LMIS-STM embodiment, (c) a low current liquid metal ion source, and (d) application of the low current LMIS to the FIB technology. In the second section, we consider (a) close-spaced investigations with a conventional LMIS, (b) close-spaced investigations with a low current LMIS and (c) micromachining with the proximity focused LMIS system. The following paragraphs summarize the results obtained for each of these categories.

The development of the liquid metal electron source showed that it was possible to obtain d.c. electron emission from the solid substrate covered with a layer of the liquid metal or by freezing in the Taylor cone shape and doing a field build-up process to obtain a highly confined beam. The electron emission from the solid needle covered with a liquid layer was classic field emission from a small radii emitter and not from a field stabilized Taylor cone. Operating the emitter above the critical Taylor voltage resulted in a pulsed explosive emission process and for these small radii emitters, the destruction of the underlying substrate. It was possible to obtain d.c. electron emission from freezing in the Taylor cone and doing a field build-up process. The optimum radius for doing this was between 0.5 to 1.0 μm. The electron

emission area obtained from the Fowler Nordheim equation, using the Fowler-Nordheim plot was of the order of $10^{-13}cm^2$ with the emission believed to arise from the same geometrical area as the ion emission.

The electron emission from the LMIS could also be used to determine source-target separations. The polar model, after solving Laplace's equation in polar coordinates, provided reasonably accurate values for the diode separations and corresponded well with the separations determined using the magnetically driven micropositioner and the piezoceramic tubes for spacings $\leq$ 25 μm. Larger separations could be determined quite easily by using a 30X microscope with a calibrated reticule in the field of view. This was adequate down to separations between the source and the target of $\sim$12 μm.

It was found possible to operate the Ga LMIS in the Taylor cone mode at currents down to a few nA using small radii emitters ($<$ 0.5 μm). However, off-axis emission and multiple Taylor cone emission is more prevalent. The fact that one is able to achieve a much lower value of the d.c. current threshold is surprising, but may be due to the very small size of the Taylor cone and to its location, perched on the apex of a very small radius - $\sim$25 to 500 nm needle. For an emitter of radius 200 nm and cone half-angle of 9°, the Taylor cone radius must be $\sim$6 nm, perhaps even smaller, to achieve a field of $\sim$2 V/Å for field evaporation at the observed threshold voltage of 3000 V for the LMIS. It is also conceivable that the susceptibility of the Taylor cone to surface instabilities at voltages close to the normally observed threshold is diminished when the cone dimensions are much smaller than normal and, in addition, flow impedances may be altered due to the smaller

emitter cone angles associated with smaller emitter radii.

The Full Width at Half Maximum (FWHM) of the total energy distribution, also known as the energy spread levels out at 4.5 eV as the current is decreased below 1 μA using the low current LMIS. The figure of merit, $\frac{dI}{d\Omega\ \Delta V^2}$, maximizes at or near 1 μA total current. This leads to a motivation to choose an emitter radius and shape so as to give stable operation at ~1 μA. In this way emitter life and focused ion beam current density is maximized.

The proximity focused LMIS investigation demonstrated the ability to operate the LMIS at very close spacings for a variety of targets, including silicon and gallium arsenide. The proximity focusing did not seem to affect the emission stability of the LMIS and seemed to be in good agreement with the Taylor theory model. It was found possible to create microfeatures as small as 0.1 μmon various targets. The current densities at very close spacings in the proximity focused mode are orders of magnitude higher than presently available in a FIB system.

APPENDIX A

DERIVATION OF THE TUNNEL CURRENT EQUATION BETWEEN SIMILAR ELECTRODES SEPERATED BY A THIN INSULATING LAYER

1. Introduction

The study of the tunnel effect wherein flow of current takes place between two "metallic" electrodes seperated by a thin insulating film was investigated theoretically by Sommerfeld and Bethe for very low voltages and for high voltages; and later extended to include intermediate voltages by Holm. The present derivation from Simmons[1], utilizes the WKB approximation to present the theory for current flow through a generalized barrier.

2. Notation

m = mass of the electron

e = charge of the electron

h = Plank's constant

s = thickness of insulating film

s_1, s_2 = limits of barrier at Fermi level

Δs = $s_2 - s_1$

J = tunnel current density

V = voltage across film

V_i = image potential

η = Fermi level

$f(E)$ = Fermi-Dirac function

ψ = work function of metal electrode

ϕ_0 = height of rectangular barrier

$\bar{\phi}$ = mean barrier height

ϵ = permittivity of insulating film

K = dielectric constant

σ = tunnel resistivity ($\Omega-cm^2$)

3. The Tunnel Equation

When two metallic electrodes are separated by an insulating layer, the equilibrium conditions require that the top of the energy gap of the insulator be positioned above the Fermi level of the electrodes. This is akin to introducing a potential barrier between the electrodes which impedes the flow of electrons between the electrodes.

The flow of electrons between the two electrodes will then take place if: (a) The electrons have enough thermal energy to surmount the potential barrier and flow in the conduction bands of the electrodes or (b) The barrier is made thin enough to permit the electrons to tunnel through it.

The derivation of the tunnel equations below is done in similar fashion to that carried out by Sommerfeld, Bethe and Holm assuming low temperatures, hence restricting the transport of electrons to tunneling only.

The probability $D(E_x)$ of an electron penetrating a potential barrier of height V(x) as shown in Fig. A.1 (reproduced from Simmons[1]) is given by

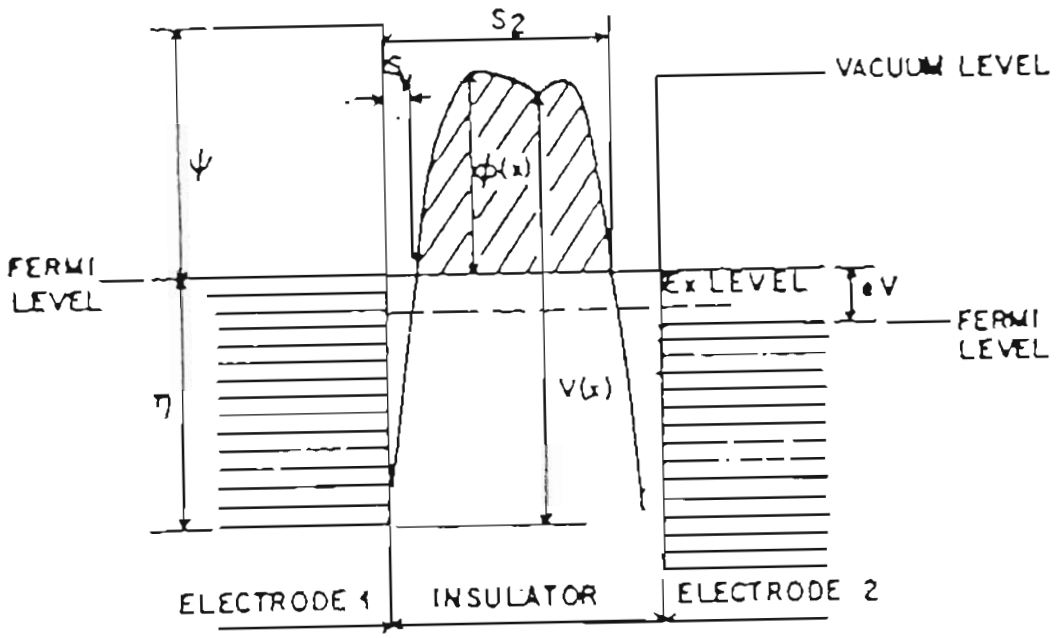

Figure A.1 : General barrier in insulating film between two metal electrodes.

the well-known WKB approximation:

$$D(E_x) = \exp\left\{-\frac{4\pi}{h}\int_{s_1}^{s_2} [2m(V(x)-E_x)]^{1/2}\, dx\right\} \tag{A.1}$$

where $E_x = mv_x^2/2$ is the energy component of the electron in the x direction. The number N_1 of the electrons tunneling through the barrier from electrode 1 to electrode 2 is given by

$$N_1 = \int_0^{v_m} v_x\, n(v_x)\, D(E_x)\, dv_x = \frac{1}{m}\int_0^{E_m} n(v_x)\, D(E_x)\, dE_x \tag{A.2}$$

where E_m is the maximum energy of the electrons in the electrodes, and $n(v_x)\, dv_x$ is the number of electrons per unit volume with velocity distribution between v_x and v_x+dv_x. For an isotropic velocity distribution, assumed to exist within the electrodes, the number of electrons per unit volume with velocity between the usual infinitesimal limits is given by

$$n(v)\, dv_x dv_y dv_z = (2m^4/h^3)\, f(E)\, dv_x dv_y dv_z \tag{A.3}$$

where f(E) is the Fermi-Dirac distribution function. Hence from Eq. (A.3),

$$n(v_x) = \frac{2m^4}{h^3}\int_{-\infty}^{\infty}\int f(E)\, dv_y dv_z$$

Expressing the integrand in polar coordinates;

$$v_r^2 = v_y^2 + v_z^2$$
$$E_r = m v_r^2/2$$

which then gives us

$$n(v_x) = \frac{4\pi m^3}{h^3} \int_0^\infty f(E)\, dE_r \qquad (A.4)$$

Using (A.4) in (A.2) we get:

$$N_1 = \frac{4\pi m^2}{h^3} \int_0^{E_m} D(E_x)\, dE_x \int_0^\infty f(E)\, dE_r \qquad (A.5)$$

The number N_2 of electrons tunneling from electrode 2 to electrode 1 is determined in a similar manner, since the tunneling probability $D(E_x)$ is the same in either direction. The Fermi-Dirac function is written as f(E+eV) to account for the second electrode being at a positive potential V with respect to electrode 1; and so

$$N_2 = \frac{4\pi m^2}{h^3} \int_0^{E_m} D(E_x)\, dE_x \int_0^\infty f(E+eV)\, dE_r \qquad (A.6)$$

The net flow of electrons N ($= N_1 - N_2$) through the barrier is

$$N = \int_0^{E_m} D(E_x)\, dE_x \times \left\{ \frac{4\pi m^2}{h^3} \int_0^{\infty} | f(E) - f(E+eV) |\, dE_r \right\} \qquad (A.7)$$

Representing

$$\zeta_1 = \frac{4\pi m^2 e}{h^3} \int_0^{\infty} f(E)\, dE_r$$

and

$$\zeta_2 = \frac{4\pi m^2 e}{h^3} \int_0^{\infty} f(E+eV)\, dE_r$$

and $\zeta = \zeta_1 - \zeta_2$. Eq. (A.7) then becomes

$$J = \int_0^{E_m} D(E_x)\, \zeta\, dE_x \qquad (A.8)$$

For a generalized barrier as in Fig. A.1 we can write $V(x) = \eta + \phi(x)$ which in Eq. (A.1) becomes:

$$D(E_x) = \exp\left\{ -\frac{4\pi}{h}(2m)^{1/2} \int_{s_1}^{s_2} |\eta + \phi(x) - E_x|^{1/2}\, dx \right\} \qquad (A.9)$$

which is:

$$D(E_x) \sim \exp\left\{ -A(\eta+\bar{\Phi}-E_x)^{1/2} \right\} \tag{A.10}$$

where $\bar{\Phi}$ is the mean barrier height above the Fermi level of the negatively biased electrode and is defined by:

$$\bar{\Phi} = \frac{1}{\Delta s} \int_{s_1}^{s_2} \Phi(x)\, dx$$

and

$$A = \left\{ \frac{4\pi\beta\Delta s}{h} \right\} (2m)^{1/2}$$

where β is a correction factor. At 0°K, ζ_1 and ζ_2 are given by

$$\zeta_1 = (4\pi me/h^3)\,(\eta-E_x)$$

and

$$\zeta_2 = (4\pi me/h^3)\,(\eta-E_x-eV)$$

Hence,

$$\zeta = \begin{Bmatrix} (4\pi me/h^3)(eV) & 0<E_x<\eta-eV \\ (4\pi me/h^3)(\eta-E_x) & \eta-eV<E_x<\eta \\ 0 & E_x>\eta \end{Bmatrix} \tag{A.11}$$

Substituting Eqs. (A.10) and (A.11) in Eq. (A.8) gives us

$$J = (4\pi me/h^3) \left\{ eV \int_0^{\eta-eV} \exp[-A(\eta+\bar{\phi}-E_x)^{1/2}]\, dE_x + \int_{\eta-eV}^{\eta} (\eta-E_x) \exp[-A(\eta+\bar{\phi}-E_x)^{1/2}]\, dE_x \right\} \quad (A.12)$$

To facilitate integration, Eq. (A.12) can be written as

$$J = (4\pi me/h^3) \left\{ eV \int_0^{\eta-eV} \exp[-A(\eta-\bar{\phi}-E_x)^{1/2}]\, dE_x - \bar{\phi} \int_{\eta-eV}^{\eta} \exp[-A(\eta+\bar{\phi}-E_x)^{1/2}]\, dE_x + \int_{\eta-eV}^{\eta} (\eta+\bar{\phi}-E_x) \times \exp[-A(\eta+\bar{\phi}-E_x)^{1/2}]\, dE_x \right\} \quad (A.13)$$

The first of the integrals in Eq. (A.13) results in:

$$(8\pi mV/h^3)\,(e/A)^2 \left\{ [A(\bar{\phi}+eV)^{1/2}+1] \exp[-A(\bar{\phi}+eV)^{1/2}] - |A(\bar{\phi}+\eta)^{1/2}+1|\, \exp[-A(\bar{\phi}+\eta)^{1/2}| \right\} \quad (A.14)$$

The second term in the braces can be neglected in comparison to the first and, also, $[A(\bar{\phi}+eV)^{1/2}] >> 1$; and so Eq. (A.14) reduces to

$$(8\pi me^2/h^3A)\ V(\bar{\phi}+eV)^{1/2}\ \exp[-A(\bar{\phi}+eV)^{1/2}] \tag{A.15}$$

The second integral is of the same form as the first and hence taking advantage of the approximations that led to Eq. (A.15) we get, for the second integral

$$-(8\pi me/h^3A^2)\ \bar{\phi}\ \Big\{\ [A\bar{\phi}^{1/2}+1]\ \exp(-A\bar{\phi}^{1/2})$$

$$-\ [A(\bar{\phi}+eV)^{1/2}+1]\ \exp[-A(\bar{\phi}+eV)^{1/2}]\Big\} \tag{A.16}$$

The third integral of Eq. (A.13) has the form

$$\int z^3 e^{-Az} dz = -\ e^{-Az}\ \left\{\frac{z^3}{A}+\frac{3z^2}{A^2}+\frac{6z}{A^3}+\frac{6}{A^4}\right\} \tag{A.17}$$

where

$$z^2 = \eta+\bar{\phi}-E_x$$

The third and fourth terms in Eq. (A.17) are negligible in comparison to the first two; therefore the third integral in Eq. (A.13) integrates to

$$(8\pi me/h^3A)\left\{ \bar{\phi}^{3/2} \exp(-A\bar{\phi}^{1/2}) - (\bar{\phi}+eV)^{3/2} \exp[-A(\bar{\phi}+eV)^{1/2}] \right\}$$

$$+ (8\pi me/h^3A)\,(3/A) \left\{ \bar{\phi} \exp(-A\bar{\phi}^{1/2}) \right.$$

$$\left. - (\bar{\phi}+eV) \exp[-A(\bar{\phi}+eV)^{1/2}] \right\} \qquad (A.18)$$

Summing Eqs. (A.15), (A.16) and (A.18) yields

$$J = (e/2\pi h)\,(\beta\Delta s)^{-2} \left\{ \bar{\phi} \exp(-A\bar{\phi}^{1/2}) \right.$$

$$\left. - (\bar{\phi}+eV) \exp[-A(\bar{\phi}+eV)^{1/2}] \right\} \qquad (A.19)$$

Equation (A.19) can be expressed in the following form:

$$J = J_0 \left\{ \bar{\phi}\exp(-A\bar{\phi}^{1/2}) - (\bar{\phi}+eV) \exp|-A(\bar{\phi}+eV)^{1/2}| \right\} \qquad (A.20)$$

where

$$J_0 = \frac{e}{2\pi h(\beta\Delta s)^2}$$

The advantage of using Eq. (A.20) is that it can be applied to a poten-

tial barrier of any shape provided the mean barrier height is known, or, alternatively, if the current-voltage characteristics of a tunnel junction is known, the mean barrier height can be determined.

Equation (A.20) can be interpreted as a current density $J_0\ \bar{\phi}\ \exp(-A\bar{\phi}^{1/2})$ flowing from electrode 1 to electrode 2 and a current density $J_0\ (\bar{\phi}+eV)\ \exp[-A(\bar{\phi}+eV)^{1/2}]$ flowing from electrode 2 to electrode 1, resulting in a net current density J, given by Eq. (A.20). (See Fig. A.2, reproduced from Simmons[1]). When V is zero, a state of dynamic equilibrium can be considered to exist, that is, a current density of magnitude $J_0\ \bar{\phi}\ \exp(-A\bar{\phi}^{1/2})$ flowing in either direction.

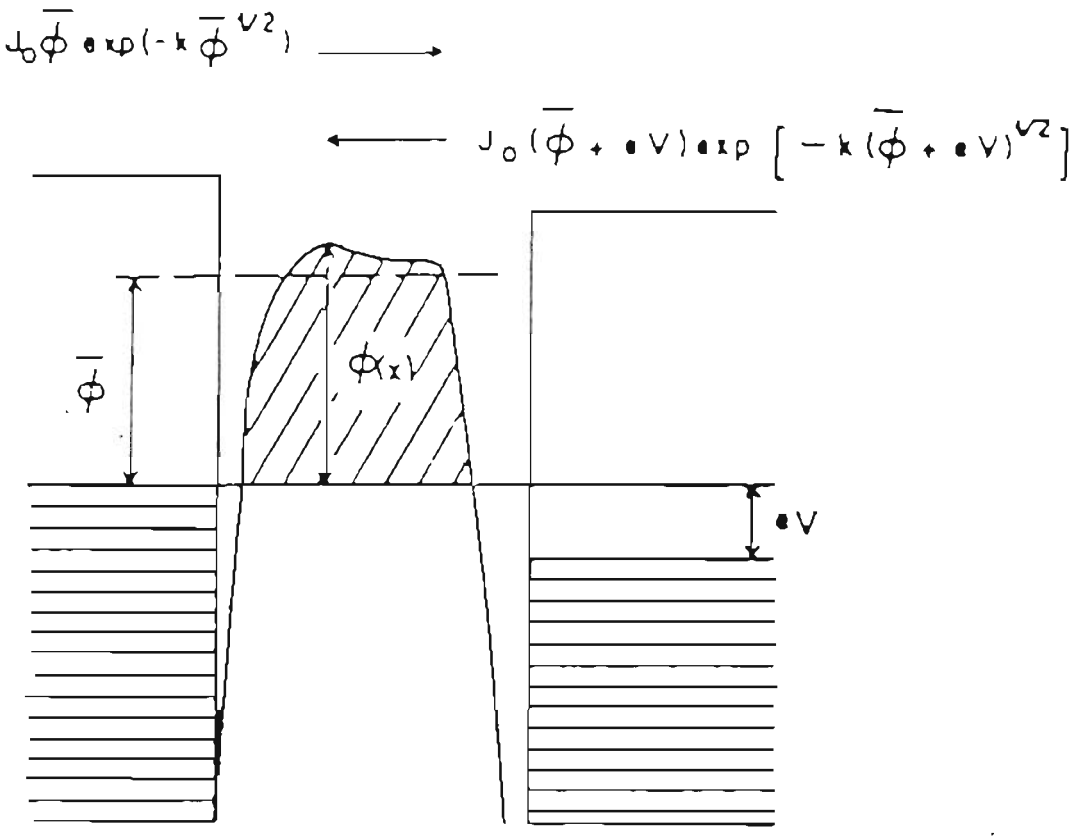

Figure A.2 : Pictorial illustration of Eq. (A.20), showing current flow between the electrodes.

APPENDIX B

ELECTROCHEMICAL ETCHING OF TUNGSTEN EMITTERS

1. Introduction

The production of a very sharp point from a cylindrical wire blank depends on the establishment of a non-uniform rate of metal dissolution along the blank. The necessary selectivity is achieved by either physically confining the reaction to a specific zone or by setting up convection currents in the electrolyte. We have used two methods to produce the tungsten emitters[2]

The D.C. Method of Emitter Shaping.

The A.C. Method of Emitter Shaping.

2. The D.C. Method of Emitter Shaping

(a). Intermittent Polishing

The first step in the d.c. electropolishing technique is the uniform removal of metal from the surface of an emitter blank of diameter 20 mil down to approximately 5 mil using a d.c. voltage between 5 to 10 volts, before producing the sharp tip required. The process is shown in Fig. B.1.

The natural convection currents in the electrolyte set up by the streaming of the reaction products downward along the surface of the emitter blank are useful in promoting the tapered shape, desirable in point formation. If

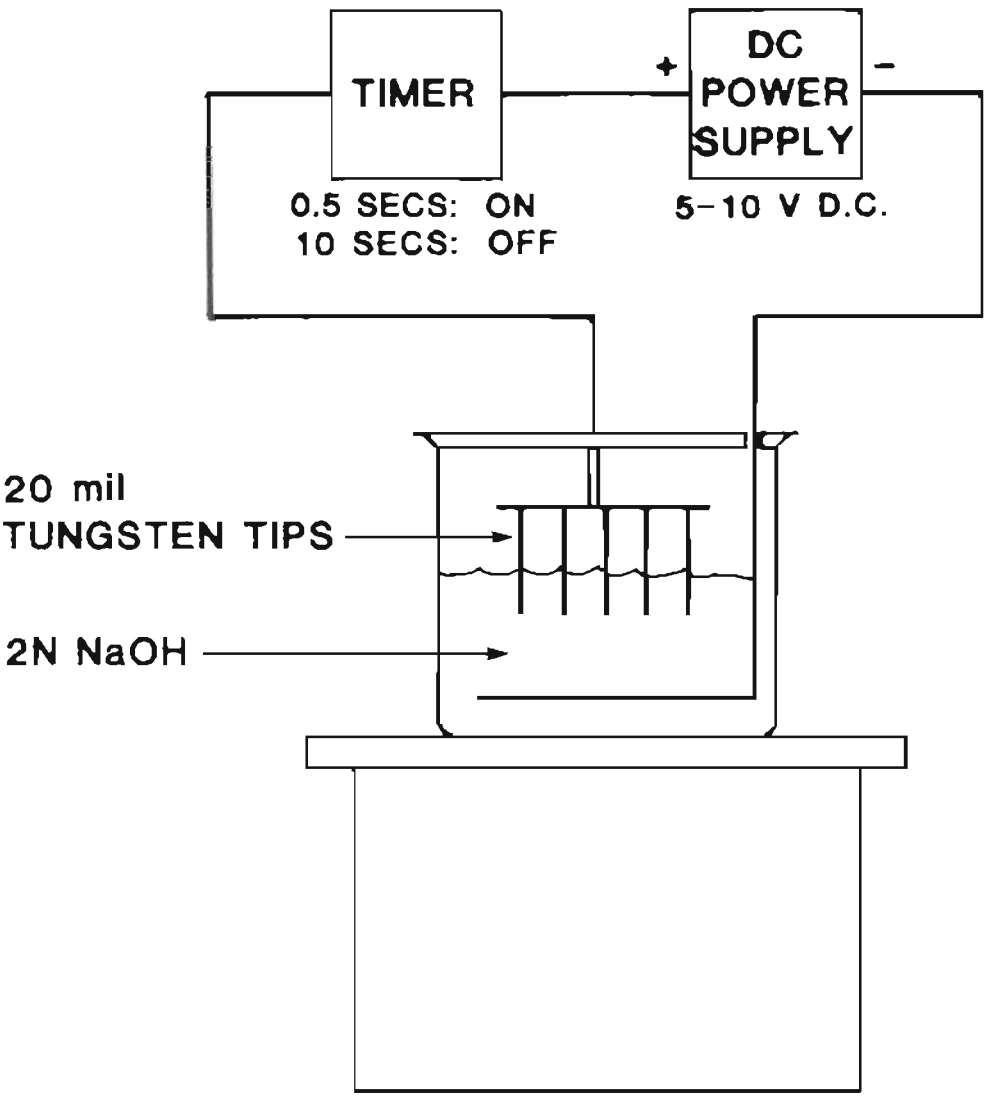

Figure B.1 : Schematic diagram for the parallel production of emitter filaments by the intermittent polishing technique.

such convection currents can be avoided, the rate of removal of metal from the anode (i.e. the emitter blank) is uniform over the entire immersed portion. To remove the effects of convection currents one applies the voltage in short bursts instead of continuously. When the "on" period is of the order of one-half second or less and the "off" period several seconds, the effect of natural convection is greatly reduced and the metal is removed uniformly over the entire surface of the anode. To avoid discontinuous etching due to the level of liquid falling during the period of the intermittent polishing which usually stretches to a few hours, a few drops of oil are added to the liquid. The addition of the oil prevents the liquid from evaporating and helps in maintaining the desired level of liquid. An advantage of the intermittent process is the simultaneous reduction of many emitter filaments supported in parallel in the NaOH solution. The intermittent polishing technique is carried on for about 4 to 5 hours using 5 to 10 volts d.c. with a timer, providing an "on-time" of 0.5 sec and an "off-time" of 5 to 10 secs, until the 20 mil diameter of the emitter blank has been reduced to between 2 to 5 mil in diameter.

(b). The D.C. Drop-off Process

The emitter blank reduced to between 2 to 5 mil in diameter from 20 mil is immersed in the electrolyte (2N NaOH) and a steady d.c. voltage of 5 to 15 volts is applied as shown in Fig. B.2 The production of a sharp point from a cylindrical wire blank depends on the establishment of a non-uniform rate of metal dissolution along the blank. The necessary selectivity is

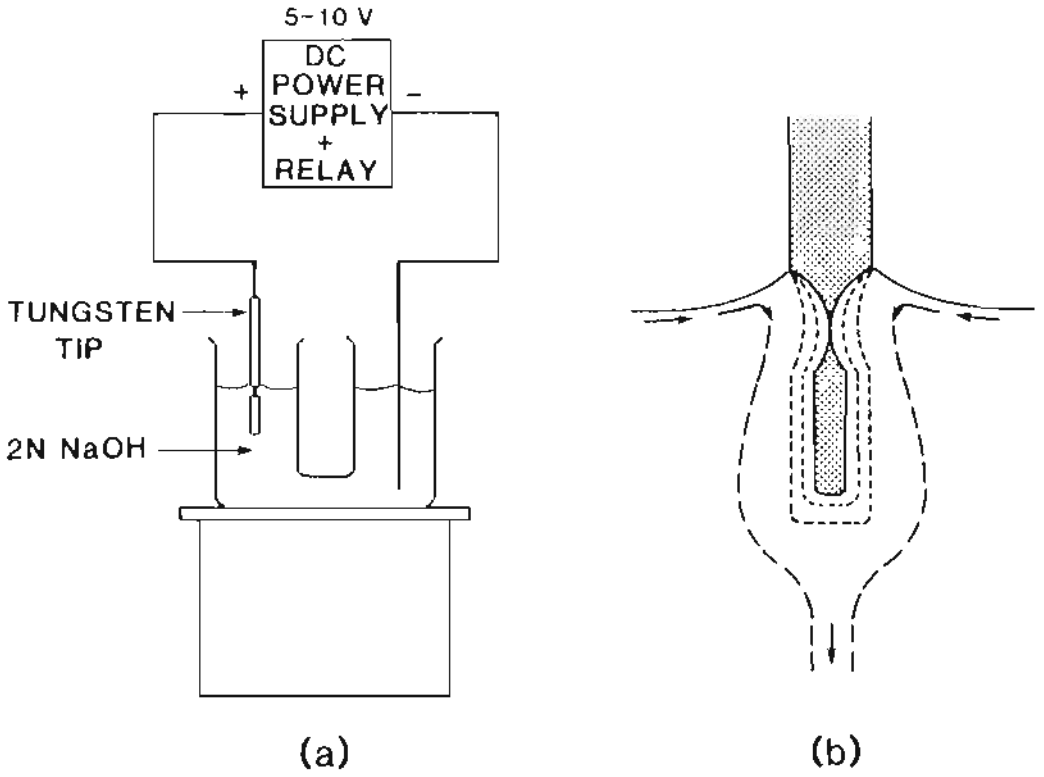

Figure B.2 : Schematic diagram for the d.c. drop-off technique for producing emitter filaments.

attained by setting up convection currents in the electrolyte. These convection currents, caused by the downward streaming of the tungstate ion produced in the anodic dissolution process, brings fresh electrolyte to the top of the submerged portion of the blank, the metal accordingly dissolving faster in this region. Continuation of this process causes the blank to become narrower near the surface, and ultimately when the weight of the lower portion exceeds the tensile strength, it drops off, leaving a sharp point of radius $\leq$ 500 Å attached to the filament. Removal of the lower portion of the blank causes considerable reduction in the reacting area and hence a discontinuous reduction in the cell current. A simple relay utilizes this discontinuous change in cell current for the purpose of terminating the process automatically. Results obtained using the d.c. drop-off process is shown in the SEM photographs in Fig. B.3.

3. The A.C. Method of Emitter Shaping

Although the d.c. drop-off method results in the production of extremely sharp emitters with narrow cone angles ($\sim 5^\circ$) the a.c. approach provides a method of producing emitters of greater apex half-angle of about 15° and hence of greater rigidity.

During the a.c. shaping of an emitter, Fig. B.4., strong convection currents carrying reaction products upward along the blank are caused by hydrogen gas evolved from the blank during the cathodic half cycle of the impressed alternating voltage; metal removal takes place during the anodic half cycle. Since fresh electrolyte is continuously brought to the lower portion

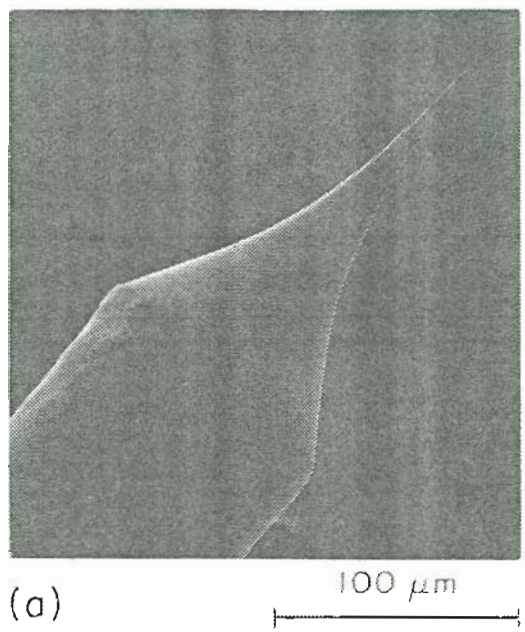

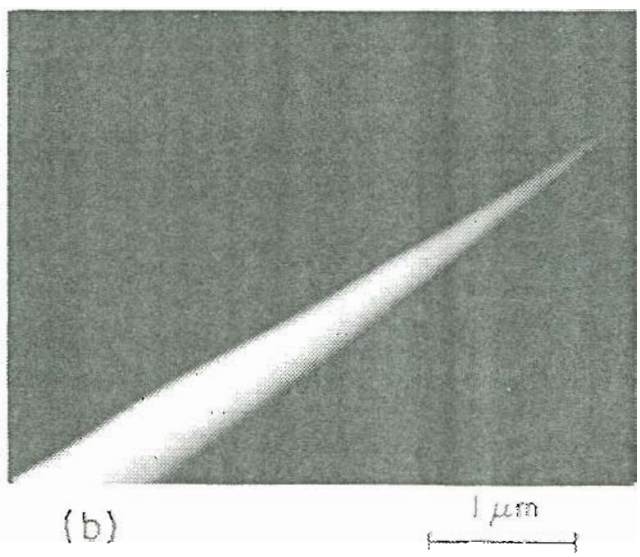

Figure B.3 : SEM profiles of tungsten emitters shaped by the d.c. drop-off process.

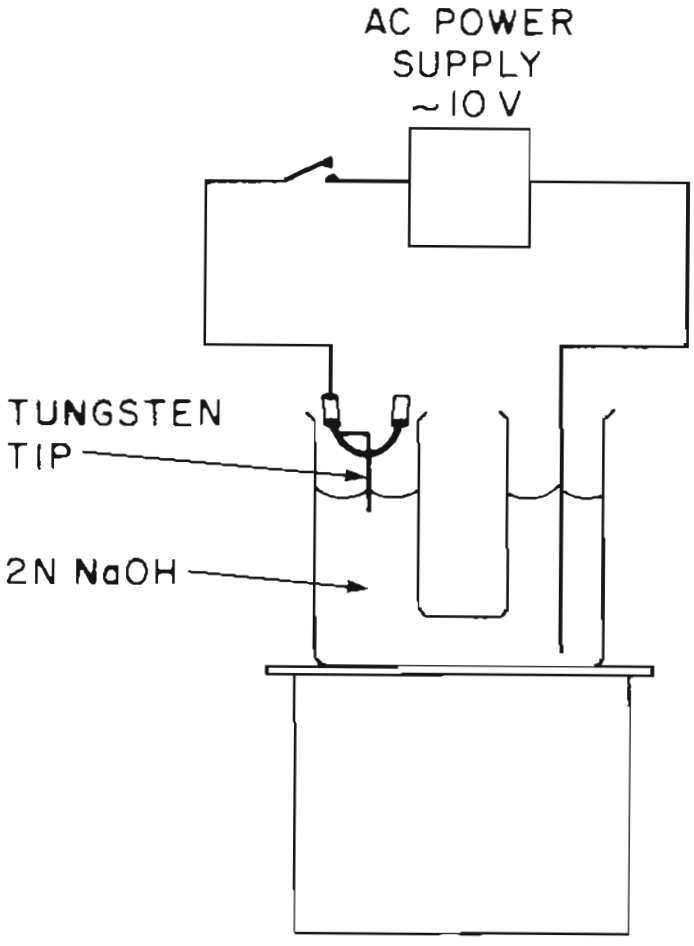

Figure B.4 : Schematic diagram for the a.c. self-termination technique for producing emitter filaments.

of the blank, the dissolution of metal is more rapid in this region, and is just the opposite of the preferential dissolution observed during the d.c. process. Continuation of this process results in an overall thinning of the blank and eventual point formation at the lower end. Within certain limits, continued a.c. polishing after initial point formation results in a decrease in length of the emitter, but a sharp point is maintained. A useful point of radius approximately 1000 Å is obtained even when the process is allowed to go to self-termination; that is, until the current is interrupted when the lower portion of the blank is completely dissolved and the surface of the electrolyte breaks away from the remainder of the blank. This automatic termination involves no special circuitry and is especially advantageous in the shaping of a number of emitters on a common supporting filament, a circumstance which precludes the use of the electrically terminated d.c. process since drop-off very rarely occurs simultaneously for all blanks. Provided the emitter structures are spaced such that there is little meniscus interaction between the individual blanks, multiple emitter structures may be fabricated which have quite uniform envelopes and tip geometries.

We have been able to achieve a.c etched emitters of radii between 500 to 1000 Å by controlling the immersion depth of the 5 mil emitter blank (obtained after the intermittent polishing technique). For immersion depths less than a mm below the surface and hence much lower reaction currents, the resulting a.c. etched emitters proved to be very sharp with radii between 500 and 1000 Å while for greater immersion depths and so greater reaction currents the radii of the emitters were greater than 1000 Å up to 1 μm. The

reason for this is probably due to the fact that during the intermittent polishing technique the diameter of the reduced emitter blank is not uniform throughout, sometimes varying as much as 2 to 3 mil over the entire length of the reduced blank, being narrower near the end of the blank and broader as we proceed up the shank. Hence during the a.c. self termination process on the emitter blanks, the radius of the resulting end form depends to a great degree on the initial diameter of the emitter blank that is immersed under the electrolyte. For low immersion depths the emitter blank to be etched is usually much narrower than the emitter blank etched with greater immersion depths. Figure B.5 shows SEM photographs of various a.c etched emitters with varying radii depending on the depth of immersion of the tungsten blank. It is worthwhile to note that the a.c etched emitters of radii $\leq$ 500 Å in Fig. B.5. resemble d.c etched emitters to a great degree.

4. Roughening of Etched Emitters

It is sometimes necessary to roughen the emitters obtained after the etching process. For use of these emitters as substrates for liquid metal ion sources it becomes imperative to roughen them so as to produce smooth flow of the liquid from the shank to the apex of the emitter. Roughening can be accomplished by dipping the emitter apex in 2N NaOH and applying an a.c. voltage of 1 to 2 volts for about 1 sec. Care must be taken to immerse only the apex and not the shank under the surface of the liquid as this gives rise to more pronounced roughening of the emitter as can be seen from Fig. B.6.

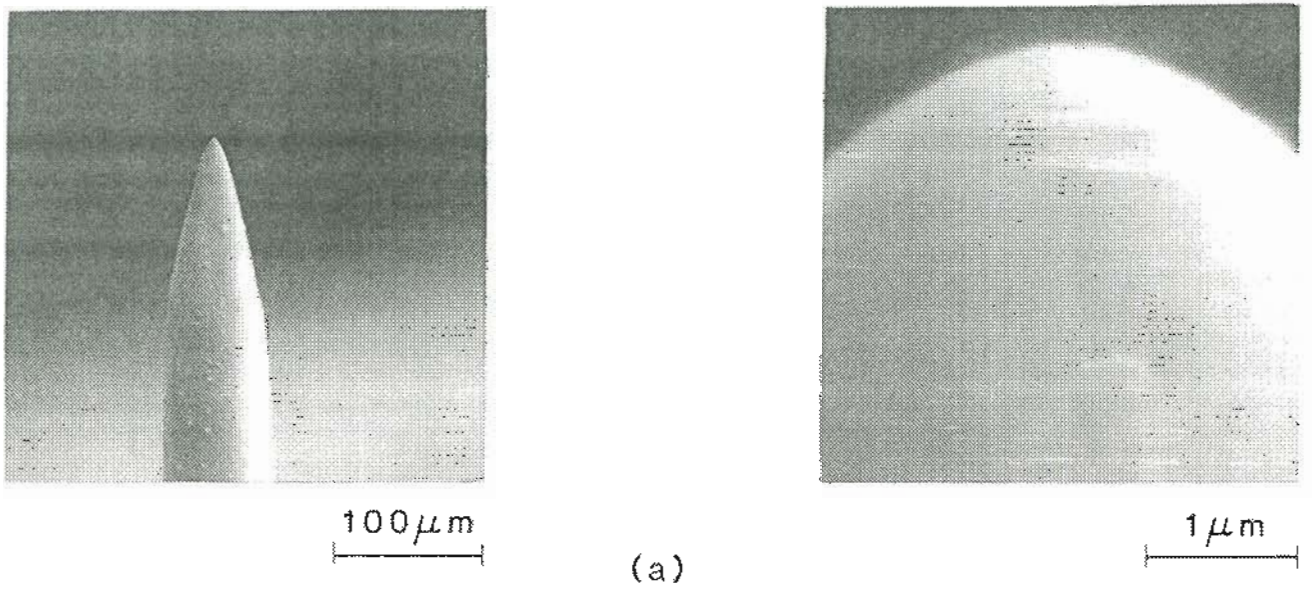

Figure B.5(a) : SEM profiles of tungsten emitter shaped by the a.c. self-termination process. Etching done with an initial reaction current of 200 mA

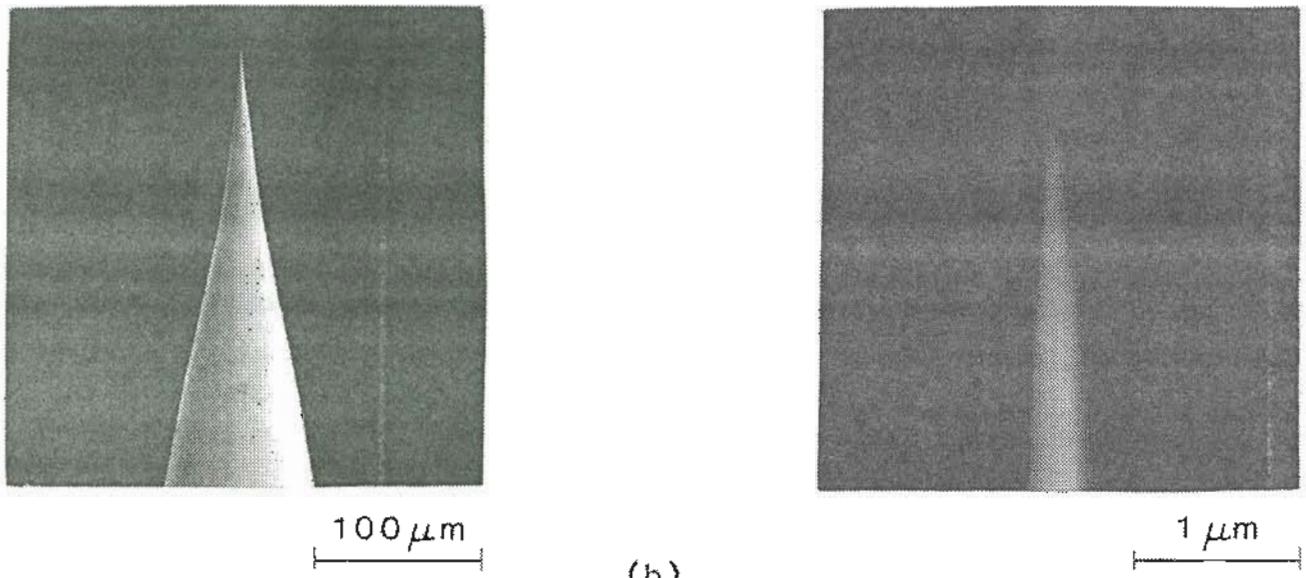

Figure B.5(b) : SEM profiles of tungsten emitter shaped by the a.c. self-termination process. Etching done with an initial reaction current of 57 mA.

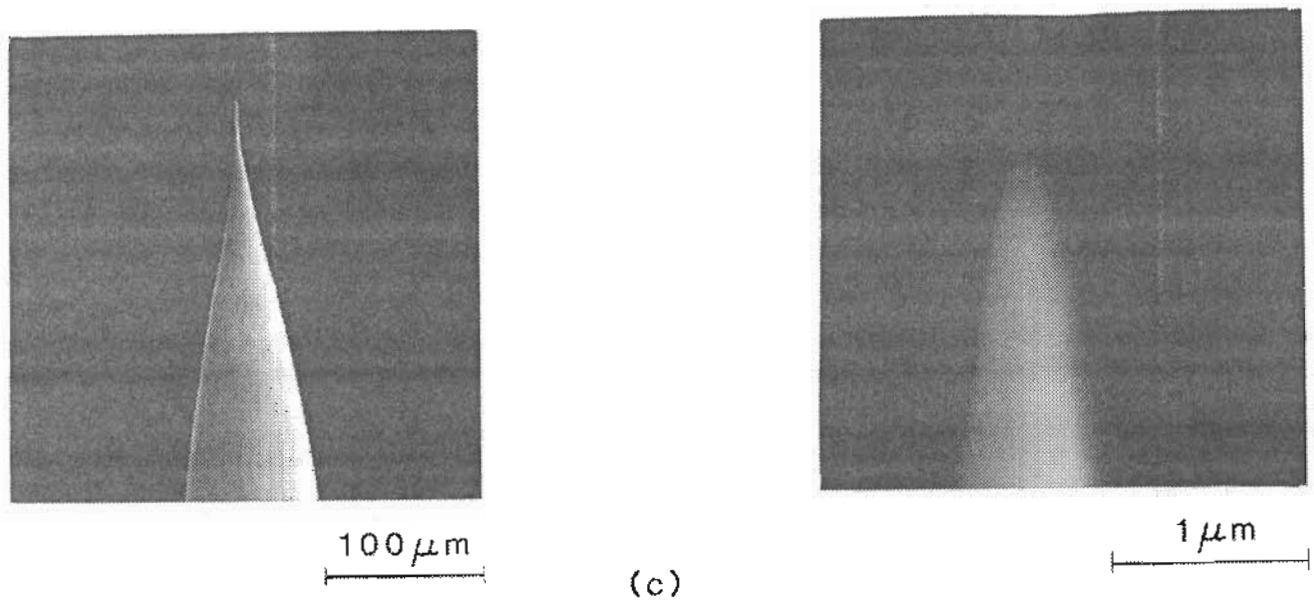

Figure B.5(c) : SEM profiles of tungsten emitter shaped by the a.c. self-termination process. Etching done with an initial reaction current of 43 mA.

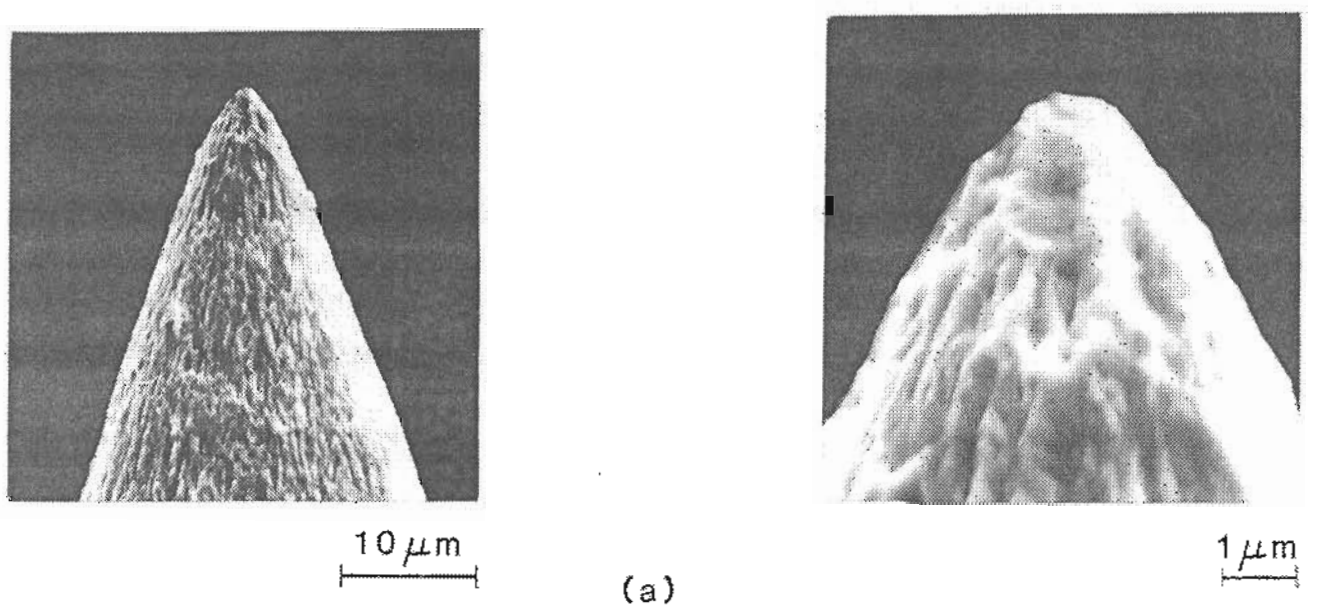

Figure B.6(a) : Roughening of etched emitters in 2N NaOH at 1-2 volts for ~ 1 sec. Roughening done with apex and part of shank of emitter under liquid.

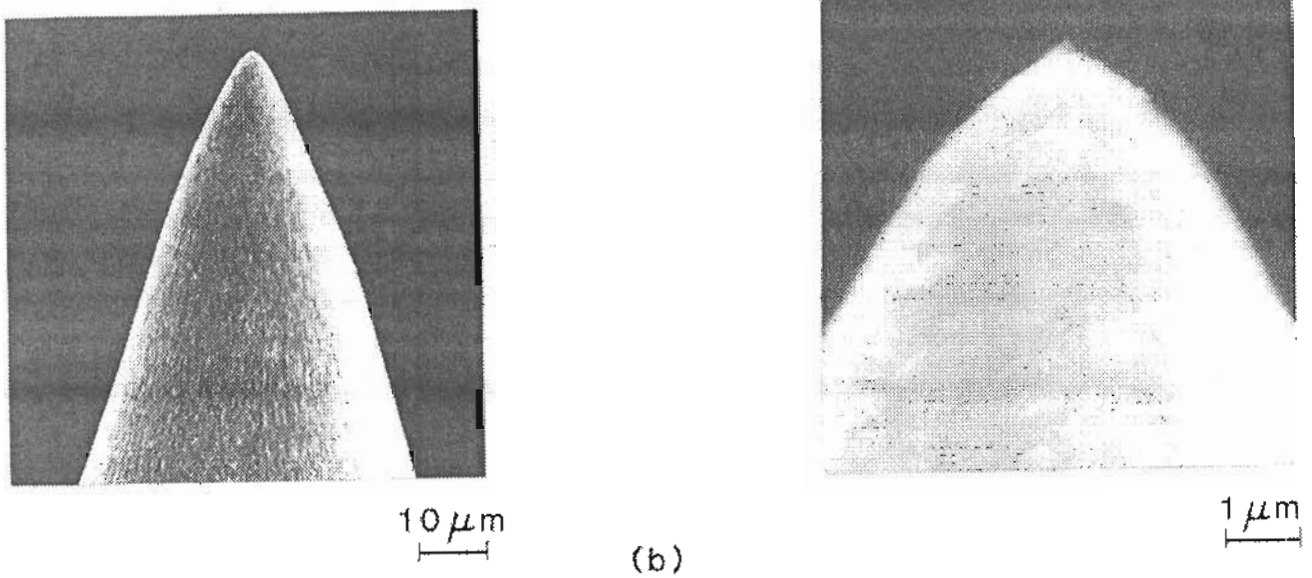

Figure B.6(b) : Roughening of etched emitters in 2N NaOH at 1-2 volts for ~ 1 sec. Roughening done only with apex of the emitter under liquid.

A = area of cross section

γ = specific weight of the beam

and EI is known as the flexural rigidity of the beam, with I the moment of inertia of the cross section with respect to the longitudinal axis x. Here partial derivatives are used because y is a function of x and t.

Since $a^2 = EIg/A\gamma$, Eq. (C.1) becomes

$$EI\frac{\partial^4 y}{\partial x^4} = -\frac{\gamma A}{g}\frac{\partial^2 y}{\partial x^2} \tag{C.2}$$

where for free transverse vibration of beams without external loading, we have considered the inertia forces, $f_I(x) = -(\gamma A/g)\frac{\partial^2 y}{\partial x^2}$, as the load intensity along the entire length of the beam.

Eq. (C.2) can then be written as:

$$EI\frac{d^4 y}{dx^4} = -\frac{dQ}{dx} = -f_I(x) \tag{C.3}$$

Assuming EI is a constant and integrating Eq. (C.3) twice, we obtain:

$$EI\frac{d^3 y}{dx^3} = -Q = -\frac{dM}{dx} \tag{C.4}$$

$$EI\frac{d^2 y}{dx^2} = -M \tag{C.5}$$

where Q is the shearing force and M is the bending moment at a cross section located a distance x from the origin of coordinates (see Fig. C.1, reproduced from Jacobsen and Ayre[3]). This then, is the well known differential equation of the static deflection curve of a beam.

We have calculated the lateral deflection, y, due to an external force for needles of cross section represented by $r = kz^m$ where r is the diameter of cross section and z is the axial distance from the apex of the needle. The lateral deflection force was applied at a distance $z = x$ from the needle apex and k and x were chosen so that a, R_0 and L were the same for various needles where $r = a$ is the diameter of the needle at the point where the deflection force is applied, R_0 is the maximum radius of cross section of the needle and L is the tapered section of the needle. The lateral deflection, y, was calculated for $m = 1$ and $m = 2$ and a ratio of $L/R_0 = 3$. The case of $m = 1$ is typical of W needles made by the "a.c. self- termination" technique and the $m = 2$ case is more like that of an extremely sharp "d.c. drop-off" needle as can be seen from Fig. C.2.

Case 1 ($m = 1$).

As shown in Fig. C.3a. and from the relation between similar triangles, we have

$$\frac{a}{R_0} = \frac{x}{L}$$

which becomes

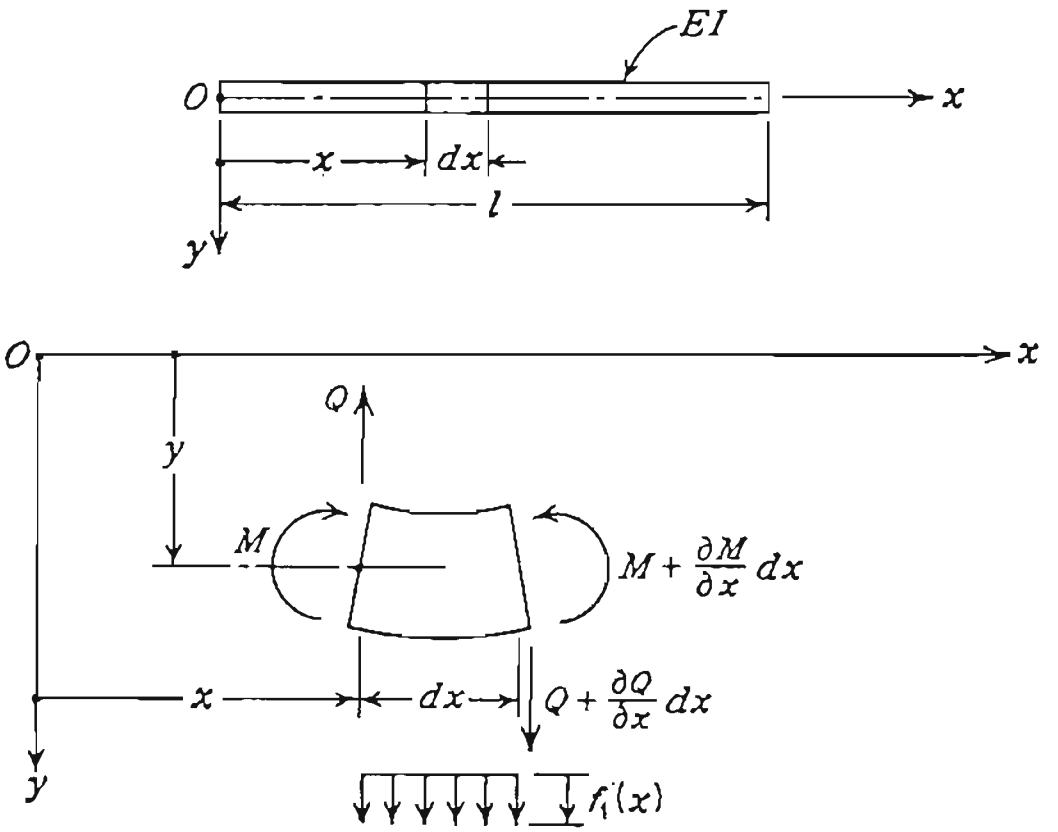

Figure C.1 : Beam in flexure; transverse vibration.

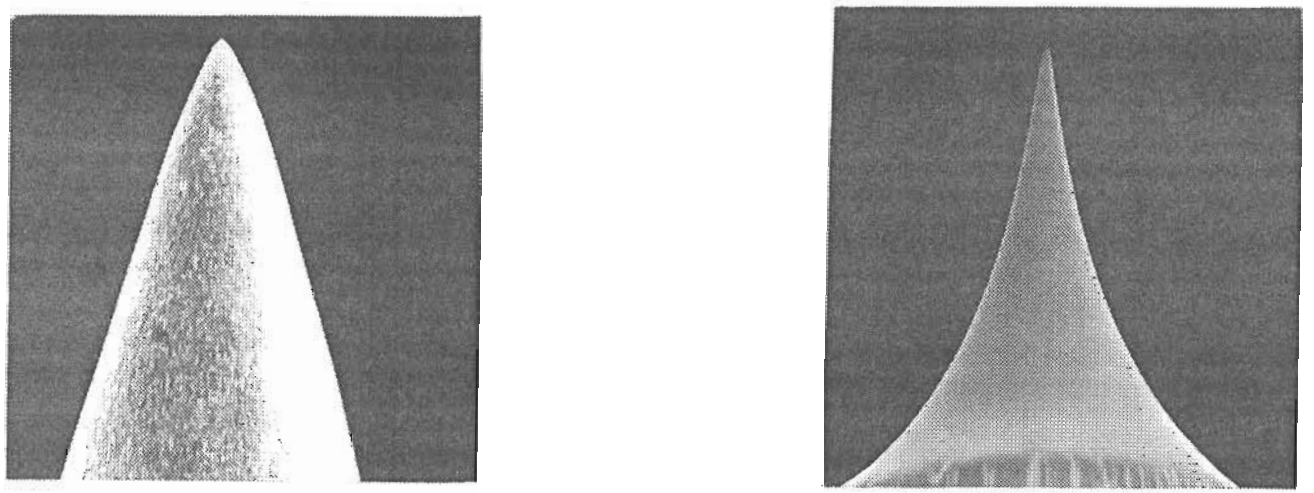

(a)

(b)

Figure C.2 : Photomicrographs (a) and (b) show emitters fabricated by the a.c. self-termination (m = 1) and d.c. drop-off (m = 2) methods respectively. Magnification approximately 170 X.

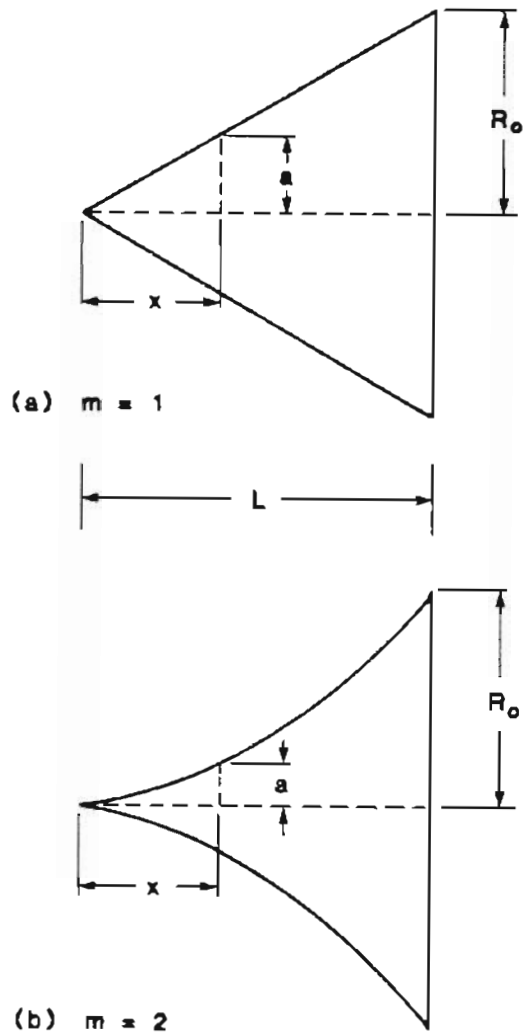

Figure C.3 : Simple taper beam (a) for the case m = 1, and (b) for the case m = 2, for evaluating the lateral deflections.

$$a = x\left(\frac{R_0}{L}\right)$$

The moment of inertia of the cross section at a, with respect to x is then

$$I = \frac{\pi}{4}a^4 = \frac{\pi R_0^4}{4L^4}x^4$$

From Eq. (C.5) for the deflection curve of a beam, we have

$$\frac{d^2y}{dx^2} + \left(\frac{M}{E}\right)\frac{4L^4}{\pi R_0^4 x^4} = 0$$

Solving for y, we then have, for small x:

$$y_{(m=1)} = -\left(\frac{4M}{\pi E}\right)\frac{L^2}{6R_0^2 a^2} \qquad (C.6)$$

where L, R_0 and a are in centimeters.

Case 2 (m = 2)

As shown in Fig. C.3b, we have, using the relation between similar triangles:

$$\frac{a}{R_0} = \left(\frac{x}{L}\right)^2$$

which then becomes

$$a = x^2 \left(\frac{R_0}{L^2} \right)$$

The moment of inertia of the cross section at a, with respect to x, is

$$I = \frac{\pi}{4} a^4 = \frac{\pi x^8 {R_0}^4}{4L^8}$$

From Eq. (C.5) for the deflection curve of a beam, we have

$$\frac{d^2y}{dx^2} + \left(\frac{4M}{\pi E} \right) \frac{L^8}{{R_0}^4 x^8} = 0$$

Solving for y, we have for small x:

$$y_{(m=2)} = \left(\frac{4M}{\pi E} \right) \frac{L^2}{42 R_0 a^3} \tag{C.7}$$

For a ratio of $L/R_0 = 3$, and assuming $a = 10^{-6}$ cm and $L = 3 \times 10^{-6}$ cm, we obtain for the ratios of the lateral deflection in the $m = 1$ and $m = 2$ cases, (Eqs. C.6, C.7):

$$\frac{y_{(m=2)}}{y_{(m=1)}} = \frac{42 R_0 a^3}{6 {R_0}^2 a^2} = \frac{7a}{R_0}$$

which for the values given above, becomes:

$$\frac{y_{(m=2)}}{y_{(m=1)}} = \frac{6.25\times10^{-3}}{7\times10^{-6}} \sim 1000$$

We therefore see that the d.c. drop off needles (m=2) deflect a factor of approximately 1000 times more than that of the a.c. self termination needles (m=1) for a given lateral force applied to the needle apex.

3. Frequencies of Lateral Vibrations of Taper Beams

In his treatise on the theory of sound, Lord Rayleigh showed that the fundamental natural frequency as calculated from the assumed shape of a dynamic-deflection curve of a system will be equal to or higher than the system's true natural frequency. Moreover if the assumed shape of the deflection curve is a close approximation to that of the true curve, the calculated frequency will be a very close approximation of the true one. In other words, small departures from the shape of the true dynamic-deflection curve will not be critical in the determination of the system's fundamental natural frequency.

For a conservative system, the total energy of the system is unchanged at all times. If the total kinetic energy of the system is zero at the maximum displacement but is a maximum at the static equilibrium point and the reverse is true for the potential energy, then:

$$(K.E)_{max} = (P.E)_{max} = \text{total energy of the system}$$

This is known as Rayleigh's method. The resulting equation will readily yield the natural frequency of the system.

The lowest mode frequencies of the lateral vibrations for the two needle shapes calculated using Rayleigh's method are then given by:

$$\omega = \left(\frac{U}{T}\right)^{1/2}$$

where T is the kinetic energy and U the strain energy for the member of length L, and are given by:

$$T = \frac{1}{2}\int_{l_0}^{L} \gamma \left(\frac{\partial y}{\partial x}\right)^2 dx$$

$$U = \frac{1}{2}\int_{l_0}^{L} EI \left(\frac{\partial^2 y}{\partial x^2}\right)^2 dx$$

where $\gamma = \pi a^2 \rho$, and ρ is the mass density.

Case 1 (m = 1)

From the deflection curve of a beam (Eq. (C.5)),

$$EI\frac{d^2y}{dx^2} = -M \qquad (C.5)$$

where $I_{(m=1)} = \frac{\pi a^4}{4} = \frac{\pi x^4 R^4{}_0}{4L^4}$ and so

$$EI\left(\frac{d^2y}{dx^2}\right)^2 = \left(\frac{4M}{\pi E}\right)\frac{L^4}{x^4R^4_0}$$

The strain energy U then is

$$U = \frac{1}{2}\int_x^L EI\left(\frac{\partial^2 y}{\partial x^2}\right)^2 dx = \frac{4ML^4}{2\pi ER^4_0}\int_x^L \frac{dx}{x^4}$$

which then becomes:

$$U = -\frac{4ML^4}{6\pi ER^4_0}\left(\frac{1}{L^3} - \frac{1}{x^3}\right) = -\frac{4ML^4}{6\pi x^3 ER^4_0}$$

and the kinetic energy T is

$$T = \frac{1}{2}\int_x^L \gamma\left(\frac{\partial y}{\partial x}\right)^2 dx = \frac{1}{2}\int_x^L \pi a^2\rho\frac{b^2}{36}\left(\frac{3}{L^2} - \frac{2x}{L^3} - \frac{1}{x^2}\right)^2 dx$$

which becomes

$$T = \frac{4\rho M^2L^6}{9x\pi E^2R_0{}^6}$$

Hence the lowest mode frequency is:

$$\omega_{(m=1)} = \left(\frac{U}{T}\right)^{1/2} = \left(\frac{3E}{\rho}\right)\frac{R_0}{xL}$$

which for values of $E = 50\times10^6$ psi, $\rho = 19.35$ g/cc, $L/R_0 = 3$, and $x = 10^{-6}$ cm, gives us:

$$\omega_{(m=1)} = 7.59 \text{ GHz}$$

Case 2 (m = 2)

For m = 2, the strain energy U is

$$U = \frac{1}{2}\int_x^L EI\left(\frac{\partial^2 y}{\partial x^2}\right)^2 dx = \left(\frac{4M^2}{7\pi E}\right)\frac{L^8}{x^7 R_0^4}$$

and the kinetic energy T is

$$T = \frac{1}{2}\int_x^L \gamma\left(\frac{\partial y}{\partial x}\right)^2 dx = \frac{1}{2}\int_x^L \pi a^2\rho\left(\frac{d}{42}\left\{-\frac{1}{x^6}-\frac{6x}{L^7}+\frac{7}{L^6}\right\}\right)$$

which then becomes:

$$T = \left(\frac{16M^2}{12348E^2}\right)\frac{\rho L^{12}}{\pi R_0^6 x^7}$$

and the lowest mode frequency is then

$$\omega_{(m=2)} = \left(\frac{21E}{\rho}\frac{R_0}{L^2}\right)^{1/2}$$

which for values of $E = 50\times10^6$ psi, $\rho = 19.35$ g/cc, $L/R_0 = 3$, and $x =$

10^{-6} cm, gives us:

$$\omega_{(m=2)} = 1098 \text{ kHz}$$

4. Summary

From the analysis of the vibration characteristics viz. the lateral deflections and the lowest mode frequencies for the two types of emitters, the a.c. etched emitter and the d.c. etched emitter, it is clearly evident that the a.c. etched emitters are superior. They deflect a factor of $\sim$1000 less than the d.c. etched emitters and their lowest mode frequencies of lateral vibrations are much higher.

References

1. J. G. Simmons, *J. Appl. Phys.*, vol. 34, p. 1793, 1963.

2. L. W. Swanson, A. E. Bell, and K. Rao, *Quarterly R & D report to DARPA*, 1 December 1985 to 28 February 1986.

3. L. S. Jacobsen and R. S. Ayre, *Engineering Vibrations*, McGraw Hill, New York, 1958.

BIOGRAPHICAL NOTE

The author was born on 14 July 1960, in Bombay, India. He graduated from the Cathedral High School in December 1975. He pursued two years of Pre-University education at the St. Aloysius College before joining the Karnataka Regional Engineering College at the University of Mysore where he recieved a Bachelor of Technology degree in Electrical Engineering in June 1983.

After a year in the Department of Electrical and Computer Engineering at Oregon State University, the author joined the Department of Applied Physics and Electrical Engineering at the Oregon Graduate Center and recieved the Master of Science degree in Electrical Engineering in 1986.

The author continued towards his Ph.D at the Oregon Graduate Center and completed all requirements for the Doctor of Philosophy degree in Electrical Engineering in December 1988.

The author has been married to Suman Rao since December 1986. He is leaving the Oregon Graduate Center to accept a joint appointment with the National Nanofabrication Facility and the Department of Applied and Engineering Physics at Cornell University in Ithaca, New York.